Supramolecular Quantum Dot–Porphyrin Assemblies for Biological Oxygen Sensing

by

Christopher M. Lemon

B. S., Biochemistry and Physics
B. A., Mathematical Statistics
Ohio Northern University (2008)

BSc(Hons), Chemistry
University of Auckland (2010)

ARCHIVES
MASSACHUSETTS INSTITUTE OF TECHNOLOGY
APR 16 2013
LIBRARIES

Submitted to the Department of Chemistry
in Partial Fulfillment of the Requirements for the Degree of

Master of Science in Inorganic Chemistry
at the
MASSACHUSETTS INSTITUTE OF TECHNOLOGY

February 2013

© 2013 Massachusetts Institute of Technology. All Rights Reserved.

Signature of Author: ______________________________
Department of Chemistry
January 18, 2013

Certified by: ______________________________
Daniel G. Nocera
The Henry Dreyfus Professor of Energy and Professor of Chemistry
Thesis Supervisor

Accepted by: ______________________________
Robert W. Field
Haslam and Dewey Professor of Chemistry
Chairman, Departmental Committee on Graduate Students

To my Family and Friends
for all of their Love and Support

Supramolecular Quantum Dot–Porphyrin Assemblies for Biological Oxygen Sensing

by

Christopher M. Lemon

Submitted to the Department of Chemistry
on January 18, 2013 in Partial Fulfillment of the
Requirements for the Degree of Master of Science in
Inorganic Chemistry

Abstract

Generating metabolic profiles of tumors provides a spatiotemporal map of the concentration of key species to assess and quantify tumor growth, metabolism, and response to therapy. Because the tumor microenvironment is characterized by hypoxia, the concentration of oxygen is an important indicator of tumor health. Understanding how this parameter changes as a function of disease progression is critical to develop novel targeted therapeutics. New non-invasive sensors must be developed that are small enough to penetrate into the tumor and monitor dynamic changes with high resolution.

To this end, this thesis presents new oxygen sensors that are a supramolecular assemblies of a quantum dot (QD) and a palladium(II) porphyrin. High spectral overlap between QD emission and porphyrin absorption results in efficient Förster resonance energy transfer (FRET) for signal transduction in these sensors. Porphyrins with *meso* pyridyl substituents bind to the surface of the QD to produce self-assembled nanosensors. Since these macrocycles are sensitive in the 0–160 torr range, they are ideal phosphors for *in vivo* biological oxygen quantification. The QD serves as a two-photon antenna to enable sensing under two-photon excitation. Multiphoton imaging is a powerful technique that is nondestructive to tissue and provides high-resolution images of live tissue at depths of several hundred microns with submicron spatial resolution.

Having studied the photohysical properties of these sensors under both one- and two-photon excitation in organic solvents, these sensors were then encapsulated in lipid micelles to quantify oxygen in aqueous media. In these constructs, the quantum dot also serves as an internal intensity standard, furnishing a ratiometric oxygen sensor. Preliminary *in vivo* multiphoton imaging and oxygen measurements were conducted using mice with chronic dorsal skinfold chambers or cranial windows. Together, the properties of this sensor establish a ratiometric two-photon oxygen sensor for applications in probing biological microenvironments.

Thesis Supervisor: Daniel G. Nocera
Title: The Henry Dreyfus Professor of Energy and Professor of Chemistry

Table of Contents

Table of Contents 7

List of Figures 10

List of Schemes 17

List of Tables 19

List of Charts 20

List of Abbreviations 21

Chapter 1. Introduction 27

1.1 Introduction: Sensing on the Nanoscale 28

1.2 Survey of Optical Sensing Mechanisms 29

1.3 Biological Sensing: Metabolic Profiling 35

1.4 Overview of Oxygen Sensing Methodologies 37

1.5 Phosphorescence Quenching 40

1.6 Förster Resonance Energy Transfer 43

1.7 Multiphoton Spectroscopy and Imaging 46

1.8 Quantum Dots and Sensing 50

1.9 Two-Photon Oxygen Sensors 52

1.10 Scope of Thesis 54

1.11 References 55

Chapter 2. Porphyrin Synthesis 73

2.1 Background 74

2.2 Statistical Porphyrin Synthesis 74

2.3 Semi-Rational and Rational Porphyrin Synthesis ... 82

2.4 Water Solubilization of Pyridyl Porphyrins ... 97

2.5 Porphyrins for *Tt* H-NOX ... 100

2.6 Discussion and Conclusions ... 101

2.7 Experimental Details ... 107

2.8 References ... 146

Chapter 3. Quantum Dot–Porphyrin Assemblies as O_2 Sensors ... 151

3.1 Background ... 152

3.2 Photophysical Studies of **Pd-1** and **Pt-1** ... 155

3.3 Photophysical Studies of Palladium Pyridyl Porphyrins ... 159

3.4 FRET Experiments ... 164

3.5 Characterization of QD Assemblies ... 175

3.6 Discussion and Conclusions ... 186

3.7 Experimental Details ... 187

3.8 References ... 192

Chapter 4. Micelle Encapsulation of Assemblies for O_2 Sensing ... 199

4.1 Background ... 200

4.2 Preparation of Micelles ... 200

4.3 Photophysical Properties of Micelles ... 204

4.4 Oxygen Sensitivity and Quenching Kinetics ... 215

4.5 Preliminary *In Vivo* Imaging ... 235

4.6 Discussion and Conclusions ... 238

4.7 Experimental Details ... 239

4.8 References 246

Acknowledgements 253

Curriculum Vitae 255

List of Figures

Figure 1.1 Schematic representation of the five primary optical sensing strategies exploiting a nanoparticle scaffold: (A) nucleic acid recognition, (B) analyte displacement of a quencher, (C) analyte displacement of a terminal energy acceptor, (D) analyte-induced binding of two nanoparticles, and (E) conjugation of analyte-sensitive chromophores. Reproduced from Ref. 74 30

Figure 1.2 The components of the RRE–Rev sensor: a biotinylated RRE RNA mimic (a) and a Cy5 conjugated peptide as a Rev mimic (b). (c) A schematic of the sensor, depicting the RRE–Rev interaction and the resultant emission of both the QD and Cy5. Reproduced from Ref. 75 31

Figure 1.3 Schematic representation of a maltose sensor exploiting analyte displacement of quencher. In the presence of maltose, the β–cyclodextrin modified QSY-9 is displaced, resulting in emission of the QD as a turn-on sensor. Reproduced from Ref. 76.......... 32

Figure 1.4 Schematic representation of a maltose sensor exploiting analyte displacement of a secondary fluorophore. In the presence of maltose, the β–cyclodextrin modified Cy3.5 is displaced, resulting in emission of Cy3 as a turn-on sensor. Reproduced from Ref. 76.......... 33

Figure 1.5. a) Schematic representation of a QD-based pH sensor. b) Changes in the emission spectrum of the construct as a function of pH: 6.0 (—), 7.0 (—), 8.0 (—), 9.0 (—), and 10 (—). Reproduced from Ref. 78.......... 34

Figure 1.6 Schematic representation (above) and two-photon images (below) of tumor vasculature at various stages of anti-angiogenic therapy. In normal tissue, the vasculature is well ordered and delivery of blood and oxygen is efficient. In tumors, the vasculature is leaky and distended, resulting in inefficient blood flow and giving rise to hypoxia. After treatment with anti-angiogenic therapy, the vasculature is repaired and restructured, resembling normal vessels. With aggressive anti-angiogenic therapy, the vessels are eventually pruned, resulting in inadequate delivery of oxygen or drugs. Reproduced from Ref. 79.......... 36

Figure 1.7 Jablonski diagram outlining the various photophysical processes that can occur with a given fluorophore. Processes that involve a photon (absorbance, fluorescence, phosphorescence) are highlighted in color, while nonradiative processes are illustrated with black arrows: internal conversion (IC), intersystem crossing (ISC), vibrational relaxation (VR), and non-radiative decay (NRD). A fluorophore in a triplet excited state can interact with triplet oxygen, generating singlet oxygen and returning the fluorophore to its ground electronic state *via* collisional quenching... 42

Figure 1.8 a) Schematic representation of a donor nanoparticle (D) and an acceptor fluorophore (A), which is promoted to an excited electronic state *via* FRET. b) An illustration of spectral overlap in this model system. The emission spectrum of the donor D (—) largely overlaps with the absorbance of the acceptor A (—); the spectral overlap is highlighted in yellow 44

Figure 1.9 Comparison of one and two-photon processes. Panels a) and b) compare one- and two-photon excitation, respectively, from the ground state of a molecular fluorophore. c) Single photon excitation of fluorescein, demonstrating that fluorescence is detected throughout the sample. d) Two-photon excitation of the same fluorescein sample, exhibiting fluorescence only in the focal volume, which is highlighted with a yellow circle 48

Figure 2.1 a) Solid-state structure of compound **18**. Thermal ellipsoids are drawn at the 50% probability level and hydrogen atoms have been removed for clarity. b) Solid-state packing of **18** in infinite chains *via* hydrogen bonding, as viewed down the crystallographic *c** axis 85

Figure 2.2 Solid-state structure of compound **Pd-37**. Thermal ellipsoids are drawn at the 50% probability level and hydrogen atoms have been removed for clarity 93

Figure 2.3 Illustration of **Pd-37** where the 4 position of each *meso* ring has been refined as a carbon atom. The ten largest residual density peaks (Q peaks) are shown as green spheres. Thermal ellipsoids are drawn at the 50% probability level and hydrogen atoms have been removed for clarity 94

Figure 3.1 Comparison of the steady state absorption (—) and emission spectra of (a) **Pd-1** (λ_{ex} = 525 nm) and (b) **Pt-1** (λ_{ex} = 510 nm). While the emission intensity of the phosphor is almost completely quenched in the presence of air (~160 torr O_2) (—), it is greatly enhanced under vacuum (—) 157

Figure 3.2 Schematic representation of the sensing methodology. The quantum dot (**QD**) is irradiated under two-photon excitation using NIR (700-1000 nm) light. QD emission is quenched in the presence of a surface-bound porphyrin (**3**) and through FRET promotes the porphyrin to an excited electronic state. The phosphorescence is then quenched in the presence of oxygen; the lifetime and intensity of the emission is a quantitative measure of O_2 concentration........ 159

Figure 3.3 Comparison of the steady state absorption (—) and emission spectra (λ_{ex} = 525 nm) of **2** (a), **3** (b), and **4** (c) in toluene. While the emission intensity of the phosphor is almost completely quenched in the presence of air (~160 torr O_2) (—), it is greatly enhanced under vacuum (—) 161

Figure 3.4 Comparison of the steady state absorption (—) and emission spectra (—) of **QD** (λ_{ex} = 450 nm) in toluene 165

Figure 3.5 Titration of 1 (—), 2 (—), 5 (—), and 10 (—) equivalents of **2** (a–c), **3** (d–f), or **4** (g–i) into a toluene solution of **QD** (—). The absorbance spectrum shows an increase in the Soret and Q bands with increasing porphyrin concentration (left). The emission spectrum (λ_{ex} = 450 nm) exhibits quenching of **QD** emission with increasing porphyrin concentration (center). Additionally, the **QD** lifetime (λ_{ex} = 450 nm) decreases as a function of increasing porphyrin concentration (right). 167

Figure 3.6 Normalized **QD** emission (—) (λ_{ex} = 450 nm) and absorption of **2** (—), illustrating spectral overlap that accounts for the high FRET efficiency in **QD2** 173

Figure 3.7 Comparison of the absorption spectra of **2** (—), **QD** (—), and **QD2** (—) in toluene. The spectrum of **QD2** represents a composite of the two constituent spectra. The increased absorbance due to **QD** is pronounced in the 300-400 nm region.. 175

Figure 3.8 Comparison of the steady state absorption (—) and emission spectra (λ_{ex} = 450 nm) of **QD2** (a), **QD3** (b), and **QD4** (c) in toluene. While the emission intensity of the phosphor is almost completely quenched in the presence of air (~160 torr O_2) (—), it is greatly enhanced under vacuum (—) 177

Figure 3.9 Excitation spectra of concentration-matched evacuated toluene solutions of **QD2** (—), **QD3** (—), and **QD4** (—) monitoring the emission at 685 nm; excitation light was removed using a 590 nm long pass filter. The increased emission of these species in the 300-400 nm region is due to **QD** absorbance at these wavelengths... 178

Figure 3.10 Emission spectra (λ_{ex} = 450 nm) of concentration-matched toluene solutions of **2** (—) and **QD2** (—) under vacuum. The enhancement of the emission intensity of **QD2** is attributed to FRET excitation of the porphyrin, as the QD has a greater absorbance at 450 nm relative to **2**........ 179

Figure 3.11 Two-photon emission spectra (λ_{ex} = 800 nm) of concentration-matched toluene solutions of **QD** (—) and evacuated samples of **2** (—) and **QD2** (—) in three different spectral windows: 500 nm (a), 550 nm (b), and 650 nm (c). The emission intensity of the dot is quenched in the presence of porphyrin, as observed in (b). **2** does not emit under two-photon excitation and emission is only observable in the presence of **QD**, as shown in (c). (d) Qualitative two-photon emission spectra constructed by concatenating (a), (b), and (c) and rescaling the emission intensity. This is a qualitative representation of the data so that all of the data may be visualized in a single plot.. 180

Figure 4.1 Schematic representation of the sensing methodology. The quantum dot–porphyrin assembly, encapsulated in a lipid micelle is irradiated under two-photon excitation using NIR (700-1000 nm) light. Through FRET, the porphyrin is promoted to an excited electronic state. Oxygen can freely diffuse into the micelle and reversibly quench porphyrin emission; the lifetime and intensity of the emission is a quantitative measure of O_2 concentration.. 201

Figure 4.2 A typical GFC trace of the **QD1-MC** assembly. The eluent of the column was monitored by recording the absorbance at 280 nm 202

Figure 4.3 Representative DLS traces of **QD-MC** (a) and **QD1-MC** (b). Based on data, the diameter of these particles is 16.8 nm and 18.2 nm, respectively... 203

Figure 4.4 The steady state absorption (—) and emission spectra of **QD1-MC** (λ_{ex} = 450 nm) in PBS buffer. While the emission intensity of the phosphor is almost completely quenched in the presence of air (~160 torr O_2) (—), it is greatly enhanced under vacuum (—). The emission of the QD in **QD1-MC** is unchanged in air and vacuum, thereby establishing a ratiometric sensor.. 205

Figure 4.5 Comparison of the steady state absorption (—) and emission spectra (—) (λ_{ex} = 450 nm) of **QD-MC** in PBS solution... 206

Figure 4.6 Excitation spectrum of **QD1-MC** in PBS solution, monitoring the emission at 685 nm. Excitation light was removed using a 590 nm long-pass filter.. 207

Figure 4.7 Normalized **QD-MC** emission (—) (λ_{ex} = 450 nm) and absorption of **1** (—), illustrating the spectral overlap that accounts for high FRET efficiency in **QD1-MC**.. 207

Figure 4.8 Steady state emission spectrum of **QD-MC** in PBS solution under two-photon excitation (λ_{ex} = 800 nm).. 211

Figure 4.9 (a) The steady state emission spectra of **QD1-MC** (λ_{ex} = 450 nm) in PBS buffer with various oxygen concentrations: 0 (—), 5 (—), 20 (—), 55 (—), 145 (—), and 260 (—) μM O_2. (b) An intensity Stern-Volmer plot constructed from the data obtained in (a) at 682 nm. The data was fit (—) to a two-component model 216

Figure 4.10 (a) A plot of the ratio of porphyrin emission at 682 nm to quantum dot emission at 528 nm (I_{682}/I_{528}) as a function of oxygen concentration. (b) The raw data obtained from the oxygen-dependent emission spectra presented in Figure 4.9b. (c) A plot of $\left[\frac{I_0}{I}-1\right]/[O_2]$ versus $[O_2]$ to determine if static quenching is present in **QD1-MC**. (d) A plot of $\frac{I_0}{\Delta I}$ versus $[O_2]^{-1}$ to determine if a two-component system is a sufficient means of explaining the nonlinearity of (b).. 217

Figure 4.11 Representative series of lifetime decay traces of **QD1-MC** as a function of oxygen concentration. The lifetime of the porphyin emission was monitored at 685 nm.. 220

Figure 4.12 Representative analysis of a set of lifetime data of **QD1-MC** as a function of oxygen concentration at 25°C. (a) A plot of the lifetime components (τ_i) as a function of $[O_2]$ (b) A plot of the pre-exponential factors (a_i) as a function of $[O_2]$. Ideally, the contribution of each component of the fit should not exhibit a dependence on $[O_2]$. (c) A plot of τ_{M0}/τ_M as a function of $[O_2]$, illustrating the upward curvature (toward the y-axis) of the data at high $[O_2]$. (d) A plot of $1/\tau_i$ as a function of $[O_2]$, illustrating that long component exhibits a linear dependence while the short component shows an exponential dependence. 221

Figure 4.13 Representative analysis of a set of lifetime data of **QD1-MC** as a function of oxygen concentration at 37°C. (a) A plot of the lifetime components (τ_i) as a function of $[O_2]$. It should be noted that, while the long component decreases monotonically with increasing oxygen concentration, the short component does not; this is more clearly illustrated in (d). (b) A plot of the pre-exponential factors (a_i) as a function of $[O_2]$. Ideally, the contribution of each component of the fit should not exhibit a dependence on $[O_2]$. (c) A plot of τ_{M0}/τ_M as a function of $[O_2]$, illustrating the upward curvature (toward the y-axis) of the data at high $[O_2]$. (d) A plot of $1/\tau_i$ as a function of $[O_2]$, demonstrating that while the long component exhibits a linear dependence on oxygen concentration, the short component shows an exponential dependence.. 222

Figure 4.14 A Stern-Volmer plot using an alternative fitting regime in which it is assumed that the porphyrin phosphor interacts with the micelle, giving a distribution of lifetimes. Each decay trace with fit to Eq. 9. The above plot is derived from the τ parameter of each decay trace (the raw data is illustrated in Figure 4.11). Based on the theory behind this model, the *a* and τ should be constant and only the *c* term, which represents the quenching parameter, should exhibit an oxygen dependence. Despite these limitations and unexpected results, a reasonable Stern-Volmer plot could be obtained ($R^2 = 0.98741$) that does not exhibit an upward curvature at high oxygen concentrations and is wholly representative of all the data, rather than just a single component of a biexponential fit. However, the deviation from theory and the inferior fits relative to the biexponential decay discredit this model to explain the data 225

Figure 4.15 A representative example of the long lifetime component of the biexponential fit as a function of [O_2] for one sample of **QD1-MC** at (a) 25°C and (b) 37°C. (a) The line of best fit ($R^2 = 0.98839$) gives $K_{SV} = 0.400\ \mu M^{-1}$ and $k_q = 9.73 \times 10^8\ M^{-1}\ s^{-1}$ at 25°C. (b) The line of best fit ($R^2 = 0.98728$) gives $K_{SV} = 0.794\ \mu M^{-1}$ and $k_q = 1.84 \times 10^9\ M^{-1}\ s^{-1}$ at 37°C...... 226

Figure 4.16 Global fits of the long lifetime component of the biexponential fit as a function of [O_2] for five independent samples of **QD1-MC** at (a) 25°C and (b) 37°C. (a) The line of best fit ($R^2 = 0.97354$) gives $K_{SV} = 0.410\ \mu M^{-1}$ and $k_q = 9.96 \times 10^8\ M^{-1}\ s^{-1}$ at 25°C. (b) The line of best fit ($R^2 = 0.96525$) gives $K_{SV} = 0.723\ \mu M^{-1}$ and $k_q = 1.67 \times 10^9\ M^{-1}\ s^{-1}$ at 37°C 227

Figure 4.17 A representative example of the short lifetime component of the biexponential fit as a function of [O_2] for one sample of **QD1-MC** at (a) 25°C and (b) 37°C. (a) The curve of best fit ($R^2 = 0.98731$) yields $V = 0.0127\ \mu M^{-1}$ and $K_{SV} = 0.0129\ \mu M^{-1}$, which translates to $k_q = 4.45 \times 10^8\ M^{-1}\ s^{-1}$ at 25°C. (b) The curve of best fit ($R^2 = 0.994$) yields $V = 0.00889\ \mu M^{-1}$ and $K_{SV} = 0.168\ \mu M^{-1}$, which translates to $k_q = 2.95 \times 10^9\ M^{-1}\ s^{-1}$ at 37°C.. 229

Figure 4.18 A plot of the short component of the biexponential decay as a function of oxygen concentration at 37°C. This represents the full set of data that is presented in Figure 4.17b. The curve of best fit ($R^2 = 0.87353$) yields $V = 0.00512\ \mu M^{-1}$ and $K_{SV} = 0.368\ \mu M^{-1}$, which corresponds to $k_q = 6.45 \times 10^9\ M^{-1}\ s^{-1}$ 229

Figure 4.19 Schematic representation of the proposed structure of **QD1-MC**. The hydrophobic QD, represented in green, is encapsulated by phospholipids, to give a hydrophobic interior (yellow) and a hydrophilic exterior (blue). It is proposed that the long lifetime component, which exhibits well-behaved Stern-Volmer kinetics, is due to **1** dispersed in the oleate groups of the phospholipids. Alternatively, the short component is attributed to **1** bound to the QD surface.. 231

Figure 4.20 Two-photon images of a SCID mouse with a dorsal skinfold chamber (DSC) at a depth of 70 μm, comparing the vasculature without the sensor (a–c) and with **QD1-MC** (d–f). Collected light was separated into three channels: green (a & d) for **QD** emission using a 565 nm dichroic mirror and a 535/40 bandpass filter, yellow (b & e) for autofluorescence using a 585 nm dichroic mirror, and red (c & f) for emission of **1** using a 690/90 bandpass filter 233

Figure 4.21 Three-dimensional projections of brain vasculature under two-photon excitation of a SCID mouse with a cranial window (CW). Images were collected over a depth of 200 μm in 10 μm increments and combined into a projection using the ImageJ software package. Collected light was separated into three channels: green (a) for **QD** emission using a 570 nm dichroic mirror and a 535/40 bandpass filter, yellow (not pictured) for autofluorescence using a 585 nm dichroic mirror, and red (b) for emission of **1** using a 690/90 bandpass filter........ 235

Figure 4.22 Composite two-photon images of SCID mice with either (a) a dorsal skinfold chamber (DSC) at a depth of 70 μm or (b) a cranial window (CW) at a depth of 115 μm. Collected light was separated into three channels: green for **QD** emission using a 565 nm or 570 nm dichroic mirror, for (a) and (b), respectively and 535/40 bandpass filter, yellow for autofluorescence using a 585 nm dichroic mirror, and red for emission of **1** using a 690/90 bandpass filter. These images are an overlay of all three optical channels. The indicated points (1–8) represent locations at which *in vivo* lifetimes were measured and the associated data is presented in Table 4.5 237

List of Schemes

Scheme 2.1 Synthesis of A_3B porphyrins with *meso*-aryl substitutents *via* a mixed-aldehyde condensation under standard Lindsey conditions 76

Scheme 2.2 Synthesis of A_3B metalloporphyrins and subsequent basic ester hydrolysis; both reactions are facilitated by microwave irradiation 77

Scheme 2.3 Synthesis of A_3B porphyrins *via* the addition of a functional handle to H_2TPP (**4**) and subsequent sulfonation to afford water-soluble derivatives.. 78

Scheme 2.4 Synthesis of a water-soluble A_3B porphyrin *via* sulfonation of **1**............ 80

Scheme 2.5 Statistical synthesis of porphyrin **10** under Adler-Longo conditions; compounds **11–13** were identified as the other major porphyrin isomers isolated from this reaction 81

Scheme 2.6 Retrosynthetic analysis of compound **10**, outlining different synthetic routes that can be exploited in the rational synthesis of porphyrins 83

Scheme 2.7 Preparation of the 1-acyldipyrromethane **25** and attempted *in situ* formation of the 9-BBN complex to facilitate chromatography.............. 89

Scheme 2.8 Preparation of the 1,9-diacyldipyrromethane **34** and attempted *in situ* formation of the tin complex to facilitate chromatography...................... 92

Scheme 2.9 Preparation of the 1,9-diacyldipyrromethane **35** and subsequent condensation with **16** to form the A_3B porphyrin **37** 92

Scheme 2.10 Preparation of bilane **40** and subsequent cyclization under microwave irradiation to afford porphyrin **10** 96

Scheme 2.11 Preparation of water-soluble porphyrin derivatives of compound **Pd-10**..... 98

Scheme 2.12 Preparation of water-soluble porphyrin derivatives of compound **10** *via* a zinc(II) intermediate 99

Scheme 2.13 Preparation of a zwitterionic water-soluble porphyrin **Pd-44** 100

Scheme 2.14 Synthesis of palladium(II) and platinum(II) complexes of Mesoporphyrin IX dimethyl ester **45** and subsequent basic ester hydrolysis; both reactions are facilitated by microwave irradiation... 101

Scheme 2.15 Proposed reaction mechanism illustrating potential intermediates in the bilane to porphyrin conversion 105

List of Tables

Table 2.1 Synthesis of 5-Aryl Dipyrromethanes 84

Table 2.2 Summary of Crystallographic Data for **18** 86

Table 2.3 Synthesis of *S*-2-Pyridyl Thioates (Mukaiyama Reagents) 87

Table 2.4 Synthesis of 1-Acyl Dipyrromethanes 88

Table 2.5 Metal-Mediated [2+2] Porphyrin Synthesis Under Microwave Irradiation 90

Table 2.6 Summary of Crystallographic Data for **Pd-37** 95

Table 3.1 Summary of Spectroscopic Data for **Pd-1** and **Pt-1** 157

Table 3.2 Summary of Linear Spectroscopic Data for Pd Porphyrins and QD Assemblies 161

Table 3.3 Summary of Lifetime Data for Pd Porphyrins 164

Table 3.4 Lifetime data for QD titration with Pd Porphyrins **2–4** 171

Table 3.5 Summary of Förster Energy Transfer Parameters 174

Table 3.6 Summary of Lifetime Data for QD Assemblies 183

Table 4.1 Comparison of Linear Spectroscopic Data for **1**, **QD1**, and **QD1-MC** .. 205

Table 4.2 Comparison of QD Lifetime Data for Micelles in PBS 209

Table 4.3 Comparison of Förster Energy Transfer Parameters 209

Table 4.4 Comparison of Porphyrin Lifetimes for **QD1-MC** 213

Table 4.5 *In vivo* Lifetime Measurements 237

List of Charts

Chart 3.1 Molecular structure of the metalloporphyrins studied herein 155

Chart 3.2 Porphyrins bearing *meso*-pyridyl substituents that bind to the surface of CdSe quantum dots 160

Chart 4.1 Molecular structure of porphyrin **1** incorporated into lipid micelles 201

List of Abbreviations

9-BBN	9-Borabicyclo[3.3.1]nonane
A	Absorbance, acceptor
Å	Angstrom
A_i	Amplitude of the *i*th component of multiexponential fit
acac	Acetylacetonate
aq	Aqueous
Ar	Aryl
AU	Arbitrary units
BBO	β-Barium borate
bm	Broad multiplet
bpy	2,2′-Bipyridine
bs	Broad singlet
Bu	*n*-Butyl
Bz	Benzyl
C	Celsius
CCD	Charge-coupled device
cm	Centimeter
CW	Cranial window
cw	Continuous wave
Cy3, Cy3.5, Cy5	Cyanine dyes
D	Donor
d	Doublet

DBU	1,8-diazabicyclo[5.4.0]undec-7-ene
DDQ	2,3-dichloro-5,6-dicyano-1,4-benzoquinone
DLS	Dynamic light scattering
DHLA	Dihydrolipoic acid
DPSS	Diode-pumped solid-state
DSC	Dorsal skinfold chamber
E	FRET efficiency
EPR	Electron paramagnetic resonance
EQ	Equivalents
Eq	Equation
Et	Ethyl
FRET	Förster resonance energy transfer
g, mg	gram, milligram
GFC	Gel filtration chromatography
GM	Göppert-Mayer
HIV	Human immunodeficiency virus
H-NOX	Heme nitric oxide/oxygen binding (protein domain)
HOMO	Highest occupied molecular orbital
Hz, KHz, MHz, GHz	Hertz, kilohertz, megahertz, gigahertz
I	Intensity
IC	Internal conversion
ISC	Intersystem crossing
J	NMR coupling constant, spectral overlap integral

K	Kelvin
k_q	Bimolecular quenching constant
K_{SV}	Stern-Volmer quenching constant
L, dL, mL, μL	Liter, deciliter, milliliter, microliter
LUMO	Lowest unoccupied molecular orbital
M	Metal
M, μM	Molar, micromolar
m	Multiplet
m, mm, nm	Meter, millimeter, nanometer
m	Number of acceptor molecules per donor
MC	Micelle
Me	Methyl
MeCN	Acetonitrile
mes	Mesityl
mJ	Millijoule
mol, mmol	Mole, millimole
MPLSM	Multiphoton laser-scanning microscope
MRI	Magnetic resonance imaging
N	Avogadro's number
n, η	Refractive index
NBS	*N*-Bromosuccinimide
NC	Nanocrystal
Nd:YAG	Neodymium-doped yttrium aluminum garnet

Nd:YLF	Neodymium-doped yttrium lithium fluoride
NIR	Near infrared
NMR	Nuclear magnetic resonance
NRD	Nonradiative decay
OAc	Acetate
OPA	Optical parametric amplifier
OPO	Optical parametric oscillator
OTf	Triflate
PBS	Phosphate-buffered saline
PEG	Poly(ethylene glycol)
PET	Positron emission tomography
Ph	Phenyl
PhCN	Benzonitrile
PIL	Polymeric imidazole ligand
pO_2	Partial pressure of oxygen
q	Quartet
QD	Quantum dot
QSY-9	Fluorescence quenching dye
R^2 or R_{adj}^2	Correlation coefficient
R_0	Förster distance
r	Donor-acceptor distance
RAFT	Reversible addition-fragmentation chain transfer
Rev	Regulator of virion expression

RNA	Ribonucleic acid
RRE	Rev responsive element
S_n	Excited singlet state
S_0	Singlet ground state
s	Singlet
s, ms, μs, ns, ps, fs	Second, millisecond, microsecond, nanosecond, picosecond, femtosecond
SCID	Severe combined immunodeficient
STP	Standard temperature and pressure
t	Triplet
T_n	Excited triplet state
T_1	Longitudinal (spin-lattice) relaxation time
T_2	Transverse (spin-spin) relaxation time
$T_2{}^*$	Transverse relaxation time with gradient-echo sequences
TFA	Trifluoroacetic acid
THF	Tetrahydrofuran
TLC	Thin-layer chromatography
TOPO	Tri-*n*-octylphosphine oxide
TPP	Dianion of 5,10,15,20-tetraphenyl porphyrin
Tt	*Thermoanaerobacter tengcongensis*
UV	Ultraviolet
vis	Visible
VR	Vibrational relaxation
W, mW	Watt, milliwatt

δ	NMR chemical shift
ε	Dielectric constant, molar absorptivity
κ	Relative dipole orientation factor
λ	Wavelength
λ_{ex}	Excitation wavelength
σ_2	Two-photon absorption cross-section
τ_{air}	Lifetime in air
τ_{avg}	Average lifetime of a multiexponential fit
τ_i	Lifetime of the *i*th component of multiexponential fit
τ_0	Natural radiative lifetime
Φ	Quantum yield
ϕ_f	Fluorescence quantum yield
ϕ_p	Phosphorescence quantum yield

Chapter 1

Introduction

1.1 Introduction: Sensing on the Nanoscale

The field of sensor development and design remains an important area of chemical research, as the demand for novel sensors for biological and chemical analytes is increasing. Sensors in the disciplines of chemistry, biology, and materials science have found application in areas as diverse as medicine,[1–6] national security,[7–13] and environmental science.[14–22] Chemosensing involves the recognition of an analyte by either a physical or chemical process followed by a modulation of an output signal to report the detection of the analyte on a molecular scale.[23–33] Signal transduction occurs in response to analyte binding, resulting in a "3R" sensing mechanism: recognize, relay, and report. The result is a modulation of the physical or chemical properties of the sensor in the presence of analyte, such as oxidation-reduction, electon transfer, colorimetric changes, or optical changes. In terms of optical sensing, there are a variety of methods for analyte reporting including modulation of excited state lifetime, energy transfer efficiency, or emission intensity.[34] Fluorescence based sensors offer many advantages over other methods of signal transduction. Compared to other sensing mechanisms, fluorescent sensors typically have low background signal.[35] Such sensors can exploit a nanoparticle scaffold and thus be noninvasive for biological sensing applications.[36,37] Due to the small size of the sensors, analyte reporting is achieved at nanometer length scales with nanosecond time responses.[38–40] Because of the rapid time scale for reporting, the analyte concentration may be monitored continuously in real time.[41,42] This method of sensing is robust and can even detect the presence of analyte at the single molecule limit.[43–48] Such sensors may be incorporated into a variety of imaging techniques including optical fibers and waveguides.[49–52] Together, these properties make fluorescent nanosensors ideal platforms for sensing, particularly for chemical detection in biological media.

Recently, there has been an explosion of novel nanoparticle-based sensors for biological applications. A wide variety of nanoparticles may serve as scaffolds for sensor assemblies including metal oxide nanostructures,[53] nanostructured carbon (such as graphene[54] or single-wall carbon nanotubes[55]), noble metal nanoparticles (such as gold[56–63] and silver[64]), polymer nanoparticles,[65] magnetic nanoparticles[66,67] (such as lanthanide oxides and iron oxide), silica nanoparticles,[68] and semiconductor quantum dots.[69,70] Several reviews have been recently published that discuss biological sensing with these scaffolds and provide a comprehensive discussion of various nanoparticle-based sensors.[71–73] Given these recent reports and reviews, sensors for a wide range of analytes have been prepared: biological metabolites,[53] proteins,[56,58,62,67] cancer cells and their volatile organic metabolites,[58,59,61,63,67,69] amino acids,[57,64] nucleic acids and DNA,[53,67] viruses and bacteria,[67] heavy metals,[64] and pH.[65,68] Nanoparticle scaffolds enable noninvasive sensing in biological media. Also, the particles, particularly gold nanoparticles and quantum dots, have tunable optical properties with high luminescence quantum yields. Together, these properties make nanoscale sensors ideal for *in vivo* chemosensing.

1.2 Survey of Optical Sensing Mechanisms

While a variety of mechanisms for optical analyte detection with nanoparticle sensors exist, there are five major methodologies[74] (Figure 1.1): (A) nucleic acid recognition, (B) analyte displacement of a quencher, (C) analyte displacement of a terminal energy acceptor, (D) analyte-induced binding of two nanoparticles, and (E) conjugation of analyte-sensitive chromophores. Rather than a comprehensive review of these mechanisms, a single representative example of each sensing methodology will be presented to highlight and explain the mechanism. While the schemes of Figure 1.1 depict the nanoparticle as a semiconductor nanocrystal (NC), or quantum dot, any fluorescent nanoparticle could, in principle, be used as the sensor scaffold. In each of the

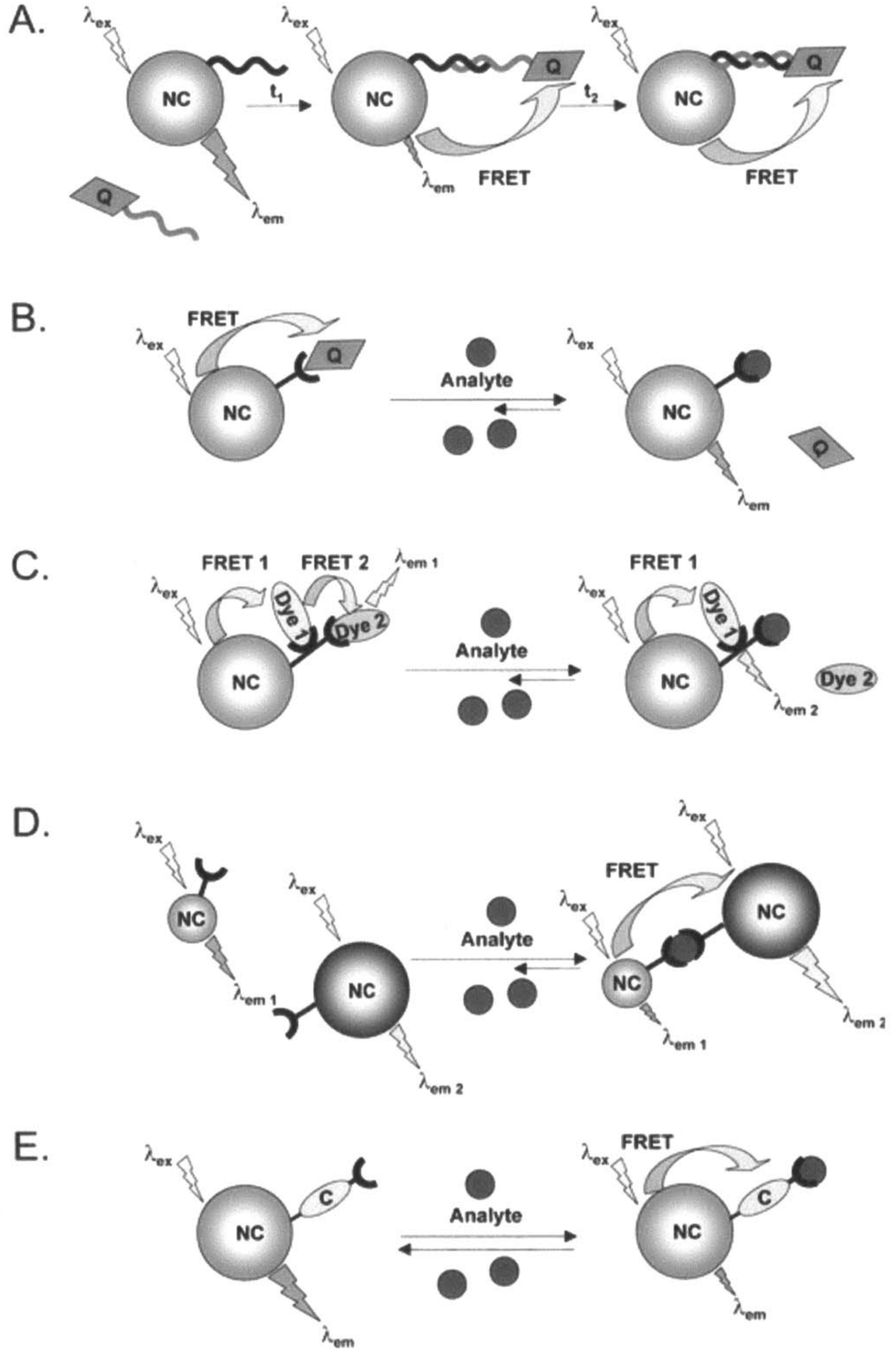
A.
λ_{ex}
NC
Q
t_1
λ_{em}
FRET
t_2
B.
Analyte
C.
FRET 1
FRET 2
$\lambda_{em\,1}$
Dye 1
Dye 2
$\lambda_{em\,2}$
D.
E.
C

Figure 1.1. Schematic representation of the five primary optical sensing strategies exploiting a nanoparticle scaffold: (A) nucleic acid recognition, (B) analyte displacement of a quencher, (C) analyte displacement of a terminal energy acceptor, (D) analyte-induced binding of two nanoparticles, and (E) conjugation of analyte-sensitive chromophores. Reproduced from Ref. 74.

examples presented herein, Förster resonance energy transfer, or FRET, is exploited as a means of signal transduction. The theory and mathematical description of FRET will be detailed in Section 1.6. This section serves to provide an overview of optical sensor design strategies.

Sensors based on nucleic acid recognition (Figure 1.1A) rely on modulating the distance between the nanoparticle and an acceptor dye Q upon detection of the analyte. As a means of reporting, a change in emission lifetime or intensity may be detected. Using this sensing methodology, Zhang and Johnson reported a sensor to detect the interaction of Rev (regulator of virion expression), a HIV-1 regulatory protein, with the corresponding Rev responsive element (RRE).[75] An *in vitro* system to model the protein-RNA interaction was designed: the stem-loop of RRE (Figure 1.2A) and a 17 amino acid peptide to mimic Rev (Figure 1.2B). The stem-loop was modified with biotin at the 5′ end to attach the RNA to streptavidin-coated quantum dots (QDs) (Figure 1.2C). A fluorescent dye (Cy5) was conjugated to the peptide to serve as the reporter signal.

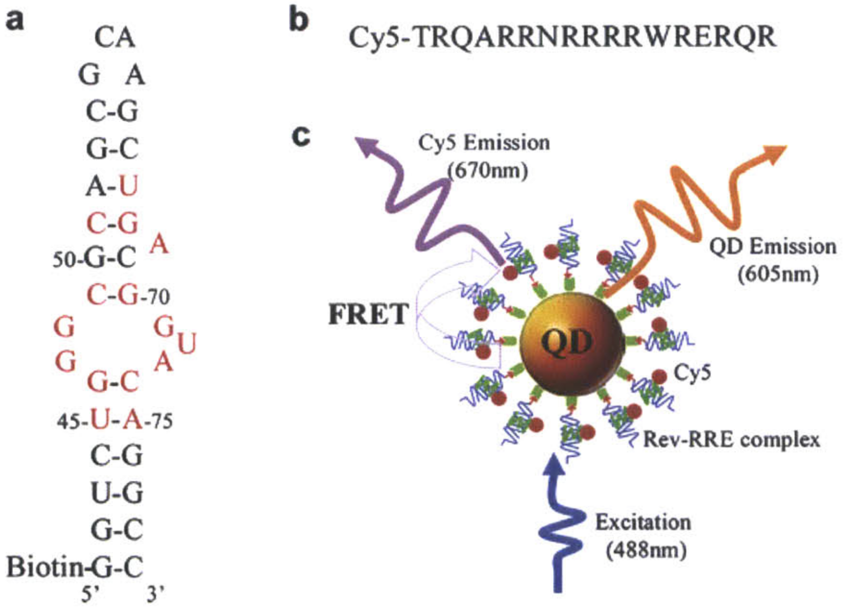
a
CA
G A
C-G
G-C
A-U
C-G
A
50-G-C
C-G-70
G
G
G
U
A
G-C
45-U-A-75
C-G
U-G
G-C
Biotin-G-C
5'
3'
b
Cy5-TRQARRNRRRRWRERQR
c
Cy5 Emission
(670nm)
QD Emission
(605nm)
FRET
QD
Cy5
Rev-RRE complex
Excitation
(488nm)

Figure 1.2. The components of the RRE–Rev sensor: a biotinylated RRE RNA mimic (a) and a Cy5 conjugated peptide as a Rev mimic (b). (c) A schematic of the sensor, depicting the RRE–Rev interaction and the resultant emission of both the QD and Cy5. Reproduced from Ref. 75.

The RRE-modifed QDs were titrated with the Rev peptide and upon excitation with 488 nm light where Cy5 does not absorb, both QD and Cy5 emission were visible. This is due to the biding of the Rev peptide to the RRE RNA on the QD surface; energy transfer occurs because the QD serves as an energy donor to excite the Cy5 dye.

Alternatively, sensing can be accomplished by analyte-induced displacement of a quencher (Figure 1.1B) or displacement of a terminal fluorophore (Figure 1.1C) to give a turn-on sensor. In the first scenario, a quencher molecule prevents emission of the nanoparticle. In the presence of analyte, the quencher is replaced by the analyte resulting in nanoparticle emission. In the second scenario (Figure 1.1C), the nanoparticle is functionalized with two separate fluorophores: Dye 1 and Dye 2. In the absence of analyte, a cascade of energy transfer occurs, resulting in the emission of Dye 2. When the analyte is present, Dye 2 is displaced by the analyte, resulting in emission of Dye 1. Mattoussi, Mauro, and co-workers reported two strategies for maltose sensing that exploit both analyte-displacement strategies.[76] In the first sensor (Figure 1.3), maltose-binding protein is bound to the surface of a QD using a polyhistidine tag (5HIS). The sugar binding pocket of the protein is blocked with β–cyclodextrin modified QSY-9, resulting in quenching of QD emission. In the presence of maltose, the sugar displaces QSY-9 and results in QD emission.

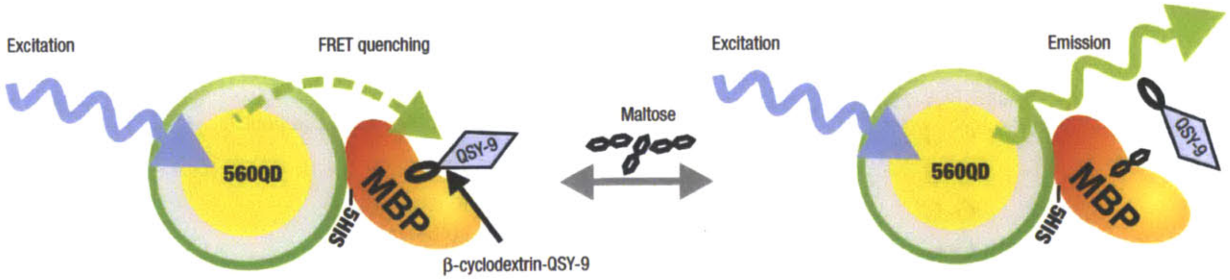

Figure 1.3. Schematic representation of a maltose sensor exploiting analyte displacement of quencher. In the presence of maltose, the β–cyclodextrin modified QSY-9 is displaced, resulting in emission of the QD as a turn-on sensor. Reproduced from Ref. 76.

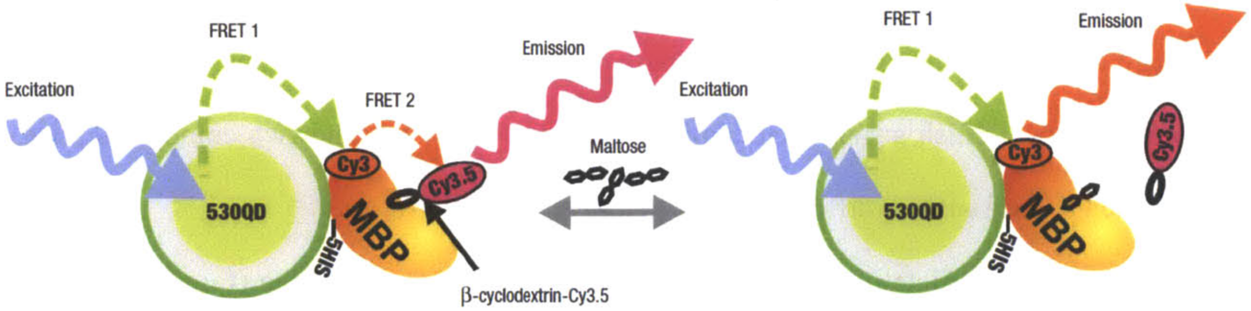

Figure 1.4. Schematic representation of a maltose sensor exploiting analyte displacement of a secondary fluorophore. In the presence of maltose, the β–cyclodextrin modified Cy3.5 is displaced, resulting in emission of Cy3 as a turn-on sensor. Reproduced from Ref. 76.

In the second sensor (Figure 1.4), Cy3-modified maltose-binding protein is bound to the surface of a QD using a polyhistidine tag (5HIS). The Cy3 fluorophore serves as a bridging acceptor/donor and its emission ultimately serves to signal the presence of analyte. The sugar binding pocket of the protein is blocked with β–cyclodextrin modified Cy3.5, resulting in quenching of Cy3 emission. In the absence of analyte, only Cy3.5 emission is observed, as a cascade of energy transfer occurs to enable emission of the terminal fluorophore. In the presence of maltose, the sugar displaces the β–cyclodextrin modified dye in the protein binding pocket, displacing Cy3.5 and enabling Cy3 emission.

The presence of analyte can induce the assembly of dyads consisting of two different nanoparticles (Figure 1.1D). Both particles are emissive in the absence of analyte. In the presence of analyte, however, two particles come together, resulting in energy transfer that causes a decrease in emission intensity of the donor particle and an enhancement of the emission of the acceptor particle. Chou and co-workers reported a potassium ion sensor consisting of both green- and red-emitting QDs.[77] Both colors of QDs were modified with 15-crown-5 as the potassium chelator; as $KClO_4$ is titrated into the QD mixture, the green emission of the smaller dots decreased while the red emission of the large dots increased. This phenomenon is attributed to an energy transfer mechanism caused by QD aggregation, due to recognition of K^+ ions by two crown ethers to furnish a sandwich complex. It is unclear if the sandwich complexes arise from the same QD or from two different QDs.

Finally, a nanoparticle may be appended with an analyte-sensitive dye (Figure 1.1E). In the presence of analyte, energy transfer occurs, resulting in a decrease of nanoparticle emission. If the dye were emissive, the presence of analyte would modulate the emission of both the nanoparticle and dye. Nocera, Bawendi, and co-workers reported a sensor that uses a fluorescent pH indicator as a means of optically measuring pH.[78] In this construct (Figure 1.5a), a QD is appended with a pH-sensitive squarine dye. Since this compound is emissive, the emission intensity from the dye serves as a measure of pH. It was found that as the pH increases, the QD emission also increases while the dye emission decreases (Figure 1.5b). This is due to changes in the absorption spectrum of the dye, which in turn modulates the energy transfer efficiency in the construct. The presence of an isosbestic point at 640 nm enables a self-referencing (ratiometric) pH sensor, allowing pH to be determined by the QD to dye emission ratio.

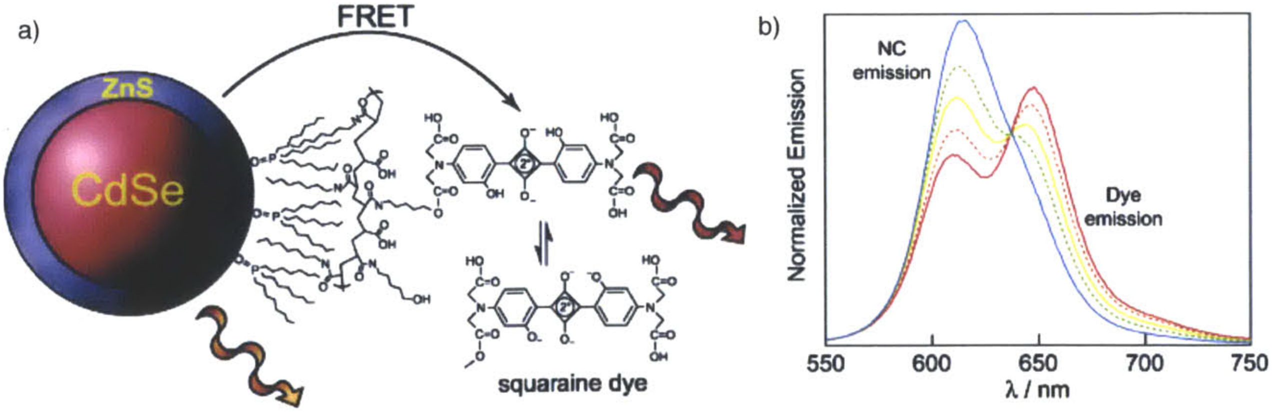

Figure 1.5. a) Schematic representation of a QD-based pH sensor. b) Changes in the emission spectrum of the construct as a function of pH: 6.0 (—), 7.0 (—), 8.0 (—), 9.0 (—), and 10 (—). Reproduced from Ref. 78.

1.3 Biological Sensing: Metabolic Profiling

Tumor biology is one discipline that can greatly benefit from new sensors and probes to answer fundamental questions about cancer development and disease progression.[79] Two key parameters that serve to define the metabolic profile of a tumor are pH and oxygen.[80,81] The concentration of these species affects tumor cell metabolism, tumor cell proliferation and viability, and glucose and oxygen consumption rates.[81] Tumor vasculature is comprised of dilated and leaky heterogeneous vessels, resulting in inefficient delivery of blood and oxygen (Figure 1.6).[82,83] As a result, the tumor is characterized by hypoxia ($pO_2 \leq 5$ torr), which stimulates angiogenesis (the formation of new blood vessels), can induce tumor cell apoptosis (programmed cell death), and select for tumor cells with defects in apoptosis pathways.[81] Additionally, the tumor environment is characterized by low extracellular pH (6.6–6.8)[81] due to the presence of lactic acid as a product of anaerobic glycolysis and carbonic acid, which is derived from dissolved CO_2 as a product of aerobic respiration; these species tend to accumulate in the tumor due to inefficient removal pathways.[84] Together, tumor acidity and hypoxia incapacitate immune cells, render tumor cells invasive and metastatic, and induce the expression of angiogeneic factors, which trigger and stimulate tumor growth.[85–87]

One emerging strategy to treat cancer is to target angiogenesis, as tumors require blood vessels for growth and metastasis.[88–93] In 2005, Carmeliet postulated that "angiogenesis research will probably change the face of medicine in the next decades, with more than 500 million people worldwide predicted to benefit from pro- or anti-angiogenesis treatments."[94] While anti-angiogeneic therapy has provided short-term benefits,[95,96] it has been demonstrated with long-term studies that the tumors grow back more aggressively.[97–99] However, the combination of anti-angiogeneic therapy and chemotherapy has been shown to be effective in the long term.[100]

This combination of therapies raises a paradox: chemotherapy attacks malignant tissue directly while anti-angiogeneic therapy destroys the very vessels required to deliver drugs. Thus, one might expect that anti-angiogeneic therapy may hinder the efficacy of chemotherapeutics.[101–103]

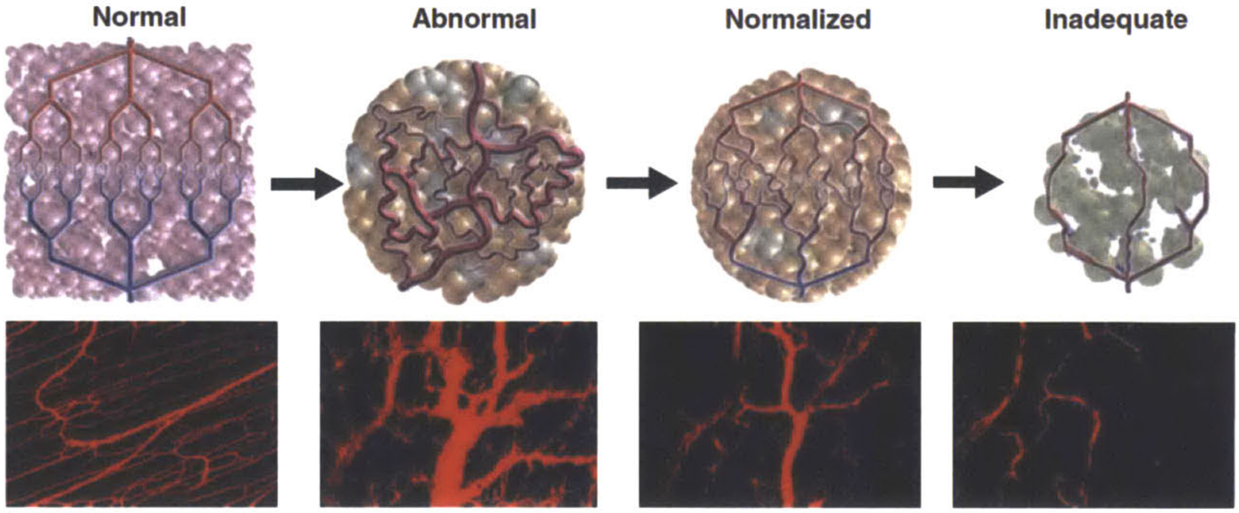

Figure 1.6. Schematic representation (above) and two-photon images (below) of tumor vasculature at various stages of anti-angiogenic therapy. In normal tissue, the vasculature is well ordered and delivery of blood and oxygen is efficient. In tumors, the vasculature is leaky and distended, resulting in inefficient blood flow and giving rise to hypoxia. After treatment with anti-angiogenic therapy, the vasculature is repaired and restructured, resembling normal vessels. With aggressive anti-angiogenic therapy, the vessels are eventually pruned, resulting in inadequate delivery of oxygen or drugs. Reproduced from Ref. 79.

Jain has hypothesized that certain anti-angiogenic therapies can transiently “normalize” the distended tumor vasculature, resulting in the more efficient delivery of oxygen and drugs.[79] In this “Normalization Hypothesis,” there is a time window in which tumor vasculature resembles normal vessels after the administration of an anti-angiogenic drug (Figure 1.6). Since the normal tissue is less leaky and dilated, the transport of nutrients, waste, oxygen, and drugs is greatly enhanced. However, excessive dosage of anti-angiogenic drugs results in the destruction of vessels, making them inadequate to deliver drugs. It has been demonstrated that such therapies improve tumor oxygenation over brief periods of time, thereby suggesting the presence of a so-called vasculature normalization window.[96,104] However, the functional parameters of pH and pO_2 have not been efficiently characterized as this process occurs. As a result, novel nano-sized sensors are needed to probe changes in these analyte concentrations in real time. Ideally, one could monitor the normalization process by monitoring how the oxygen level changes over the course of anti-angiogenic therapy. Once the oxygen level of the tumor resembles that of normal tissue, the tumor could then be treated with a high dose of chemotherapy or radiation, as the circulation of drugs and oxygen would be most efficient to destroy the tumor. Alternatively, such oxygen sensors could be used to determine the oxygen level in a tumor (anoxic, hypoxic, or normoxic) so that an appropriate course of therapy could be administered given the tumor type, thus resulting in "personalized medicine." For example, radiation therapy relies on high oxygen content to produce and propagate reactive oxygen species to destroy tumor cells,[105] but hypoxic tumors are much less sensitive to radiation.[82] The ability to rapidly determine and monitor changes in tumor oxygenation could help determine the best course of therapy and improve patient outcomes.

1.4 Overview of Oxygen Sensing Methodologies

Having demonstrated the importance of oxygen as a key parameter for tumor health and progression, various methods of measuring oxygen in biological media have been developed: polarographic microelectrodes,[106,107] magnetic resonance imaging (MRI),[108,109] electron paramagnetic resonance (EPR),[110] positron emission tomography (PET),[111,112] hemoglobin saturation spectrometry,[113–115] and phosphorescence quenching.[116–118] Of these methodologies, phosphorescence quenching is noninvasive and offers high-resolution measurement of oxygen levels; this technique will be thoroughly discussed in Section 1.5. In 2007, a comprehensive review comparing different methods of measuring oxygen levels was published.[119]

Polargraphic microelectrodes have been long considered the standard in biological oxygen measurements. These Clark-type electrodes quantify dissolved oxygen by modulating the current in a platinum cathode due to the four-electron, four-proton reduction of oxygen to water.[106] As a result, this method consumes oxygen during the measurement process. To obtain accurate measurements, the electrode must be maintained in a stable environment, rendering it unable to make dynamic measurements.[120] While advancements have been made to minimize the electrode size and amount of oxygen consumption,[121] it is an invasive means of quantifying oxygen, as it perturbs the microenvironment of the tissue and measured values are typically not reproducible. Microelectrodes are less sensitive at low oxygen pressures (< 10 torr)[122] and are thus not conducive to measuring tumor hypoxia. However, due to the minimal probe volume and resolution (typically 0.01–1 μM $[O_2]$), microelectrodes are often used as a reference for the development of other oxygen measurement techniques.[107]

Since MRI is a popular noninvasive diagnostic technique, it has used as a method of quantifying oxygen in tissues *in vivo*.[108] The most popular nucleus to study using this technique is ^{19}F, as this isotope has 100% natural abundance and has a resonant frequency 94% of ^{1}H, enabling the use of standard MRI instruments to probe ^{19}F.[109] Typical agents for ^{19}F oxygen measurements are perfluorocarbons as they are biologically inert, exhibit minimal toxicity, and are commercially available, with hexafluorobenzene being the most common.[123–125] Oxygen is quantified by measuring the ^{19}F spin-lattice relaxation rate ($R_1 = 1/T_1$), which is modulated by the concentration of paramagnetic oxygen. At a given magnetic field and temperature, the two parameters are related using the following equation:

$$R_1 = a + b[O_2] \tag{1}$$

where *a* is the relaxation rate in the absence of oxygen, *b* is the relaxation rate contribution from oxygen, and $[O_2]$ is the oxygen concentration.[108] Using this nucleus, the spatial resolution is on the order of μm–mm with an oxygen resolution of 1–8 torr.[119] Using the same principle as above, oxygen levels have been measured using ^1H MRI with hexamethyldisiloxane as the probe.[108,126] One other popular MRI technique for O_2 sensing is blood oxygenation level-dependent (BOLD) contrast.[108,127,128] In this method, changes in the blood concentration of deoxyhemoglobin are monitored to quantify oxygen levels. Since deoxyhemoglobin is paramagnetic, it affects the relaxation rate of water. Blood oxygen levels are measured using gradient echo sequences that are sensitive to the T_2* relaxation rate.[108]

While both EPR and PET have been used clinically to measure oxygen levels, these two techniques are less prevalent.[129] Indirect measurement of oxygen levels by EPR are accomplished using a paramagnetic probe, which interacts with molecular oxygen and modulates its electron relaxation properties. Typically, changes in T_2 are measured as well as the broadening of hyperfine lines of the paramagnetic probe.[108] The most common probes are lithium phthalocyanine, nitroxoides, trityl radicals, and India ink.[110] Since the spatial resolution of this technique is low (on the order of mm),[110] EPR is often used in conjunction with another technique such as MRI to enhance the image resolution.[130] In terms of PET imaging of hypoxia, this technique is primarily used for the qualitative identification of hypoxic tissue. Radioactive dyes such as ^{18}F-fluoromisonidazole or radioactive copper ^{62}Cu or ^{64}Cu dithiosemicarbazones complexes undergo a chemical or redox reaction, resulting in the accumulation of these species in hypoxic tissue.[129]

One final oxygen measurement technique is the use of hemoglobin saturation spectrometry. In this technique, changes in the optical absorbance features of hemoglobin due to oxygen binding are monitored.[113,114] Since this method relies on hemoglobin concentration, oxygen measurements are only reflective of vascular oxygen levels. It has been applied to studying breast cancer as a noninvasive means of differentiating tumors from normal tissue.[115] However, the relationship between hemoglobin oxygen saturation and oxygen levels is complicated and requires accurate knowledge of the oxyhemoglobin dissociation curve as well as local concentrations of carbon dioxide and pH in order to properly quantify oxygen levels.[107] While this technique is noninvasive, the spatial resolution is on the order of mm and suffers from the interference of myoglobin as well.[119]

1.5 Phosphorescence Quenching

While other methods of oxygen detection utilize existing imaging and detection strategies, these methods lack the spatiotemporal resolution necessary to probe the tumor microenvironment and monitor small, dynamic changes in oxygen with accuracy. Phosphorescence quenching offers a viable alternative that circumvents the limitations of the techniques outlined in Section 1.4. This method has been used to probe oxygen levels in vessels, tissues, and tumors.[107,121,131] A dye molecule in its triplet excited state undergoes collisional quenching with molecular oxygen (a ground state triplet) to return the fluorophore back to its ground electronic state and generate singlet oxygen (Figure 1.7). This phenomenon of triplet quenching is well-established[116–118] and is described mathematically by the Stern-Volmer equation:[132]

$$\frac{I_0}{I} = \frac{\tau_0}{\tau} = 1 + k_q \tau_0[\mathrm{Q}] = 1 + K_{SV}[\mathrm{Q}] \tag{2}$$

where I_0 and τ_0 are the intensity and lifetime of the excited state in the absence of quencher, I and τ are the intensity and lifetime of the excited state at a given concentration of quencher, k_q is the bimolecular quenching constant, $[Q]$ is the concentration of quencher Q, and K_{SV} is known as the

Stern-Volmer quenching constant. Using Eq. 2, the oxygen concentration in a given sample may be determined by measuring the emission intensity or the excited state lifetime of a molecular probe.

Such a molecular probe is subject to a variety of photophysical processes, as illustrated in Figure 1.7. Upon absorption of a photon, a fluorophore is promoted from its ground singlet state (S_0) to an excited single state (S_1, S_2). Internal conversion (IC), a radiationless transition, can occur between isoenergetic vibrational levels (v and v') of different electronic states (m and n) of the same multiplicity: $S_n^v \rightarrow S_m^{v'}$ or $T_n^v \rightarrow T_m^{v'}$. If the molecule is in a higher vibrational state, it relaxes back to the ground vibrational state through a nonradiative process called vibrational relaxation (VR). Transitions between the singlet and triplet manifolds can be accomplished through spin inversion. The radiationless deactivition of the lowest singlet and triplet states is known as intersystem crossing: $S_1 \rightarrow T_1$ and $T_1 \rightarrow S_0$. This occurs by either direct spin-orbit coupling of S_1 to a higher vibrational level of T_1 or by spin-orbit coupling to a higher triplet state followed by rapid internal conversion to T_1. Radiative deactivation of excited electronic states (luminescence) occurs though either the lowest singlet (S_1) or triplet (T_1) state; this is known as Kasha's rule. Nonradiative decay (NRD) of these states is generally slow relative to the corresponding emission of a photon: fluorescence $S_1 \rightarrow S_0$ or phosphorescence $T_1 \rightarrow S_0$. Transitions of the same multiplicity are spin allowed, while those involving states of different multiplicity are spin forbidden. Thus, phosphorescence is a spin-forbidden process, manifesting in a long excited state lifetimes (ms–s) relative to fluorescence (ns or faster).[133]

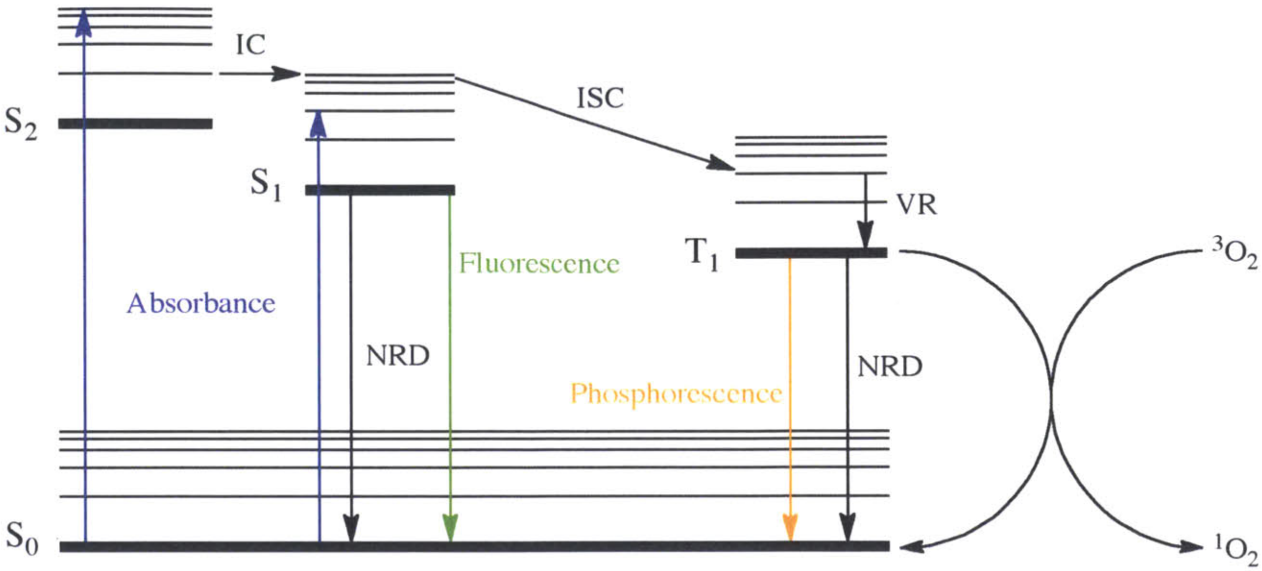

Figure 1.7. Jablonski diagram outlining the various photophysical processes that can occur with a given fluorophore. Processes that involve a photon (absorbance, fluorescence, phosphorescence) are highlighted in color, while nonradiative processes are illustrated with black arrows: internal conversion (IC), intersystem crossing (ISC), vibrational relaxation (VR), and non-radiative decay (NRD). A fluorophore in a triplet excited state can interact with triplet oxygen, generating singlet oxygen and returning the fluorophore to its ground electronic state *via* collisional quenching.

Phosphors that are used as oxygen sensors are typically metal polypyridine or porphyrin complexes.[134,135] Typically, second and third row transition metals are use, as they exhibit sufficient spin-orbit coupling so that intersystem crossing to the triplet manifold is efficient.[136] Varying the metal and synthetically tailoring the ligand scaffold can readily tune the photophysical properties of the molecule: absorption and emission wavelengths, quantum yield, excited state lifetimes, and oxygen sensitivity range. The most common fluorophores are ruthenium(II) bipyridine and phenanthroline complexes and are often incorporated into a polymer matrix to furnish an optical sensor device.[137–144] As an alternative, palladium(II) and platinum(II) porphyrin complexes have been used because of their high phosphorescence quantum yields and long lifetimes.[145–148] Most reported examples of sensors that use these porphyrins incorporate them into polymer matrices, thin films, or attach them to solid substrates.[149–151] While some recent examples with platinum(II) porphyrins utilize a nanoparticle scaffold, the nanosensor is still embedded in a polymer matrix.[152,153] Since there are few examples of nanoparticle-based oxygen sensors suitable for biological applications,[154,155] more research is necessary to develop novel sensors for *in vivo* oxygen sensing. The next several sections will discuss the design principles and concepts that will be incorporated into these new sensors: Förster resonance energy transfer (Section 1.6), multiphoton spectroscopy (Section 1.7), quantum dots as sensor scaffolds (Section 1.8).

1.6 Förster Resonance Energy Transfer

One of the most common methods of signal transduction in nanoparticle-based sensors is Förster resonance energy transfer or FRET. In this mechanism, energy is transferred nonradiatively from a donor (D) fluorophor to an acceptor (A) molecule (Figure 1.8a).[156] In a FRET-based sensor, the donor is selected such that is has favorable absorption properties in the desired optical range while the acceptor is selected for analyte sensitivity and emission properties (*i.e.* optical readout of analyte concentration). Additionally, the FRET pair must be judiciously selected such that the emission of the donor is energetically similar to the absorption of the acceptor so that efficient energy transfer can occur (*vide infra*).

FRET decreases the emission intensity of the donor and transfers the energy to an acceptor molecule. Initially, both the donor and acceptor have two electrons in their HOMO (*i.e.* a ground state singlet). Upon absorption of a photon, one of the electrons in the HOMO of the donor is promoted to the LUMO. During FRET, the excited electron in the donor returns to the ground state without emitting a photon while, simultaneously, an electron in the acceptor is promoted from the HOMO to the LUMO. The excited acceptor may then relax back down to the ground state either by fluorescence or by nonradiative decay. This energy transfer mechanism is a through-space interaction that involves long-range dipole-dipole interactions and does not require molecular contact between the donor and acceptor, making FRET independent of steric and electrostatic interactions. Instead, the rate of energy transfer depends on the spectral overlap between donor emission and acceptor absorption, the quantum yield of the donor, the relative orientation of the donor and acceptor transition dipoles, and the distance between the donor and acceptor molecules.[35]

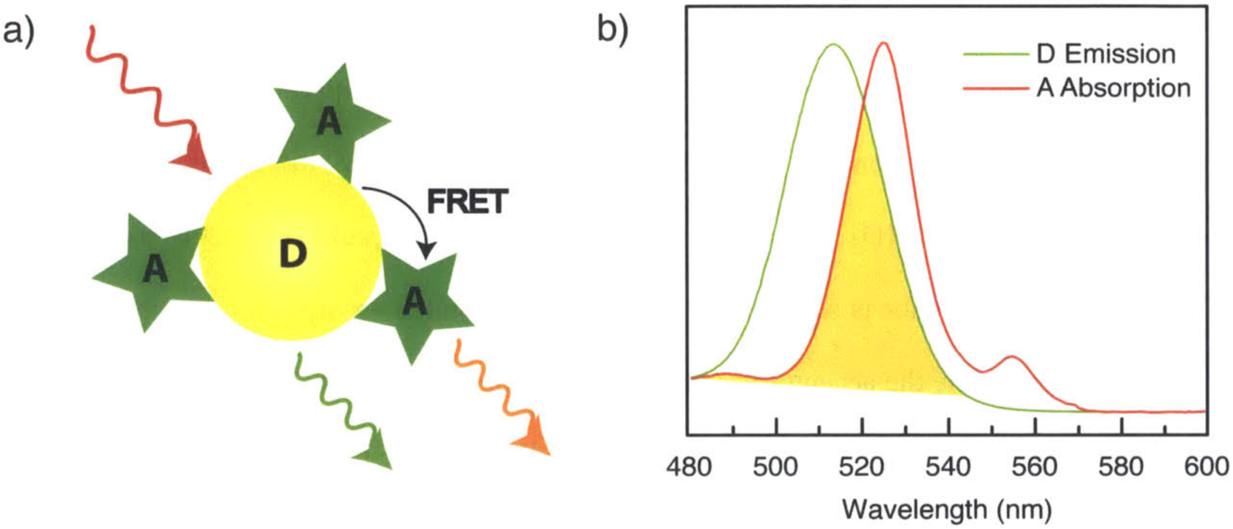

Figure 1.8. a) Schematic representation of a donor nanoparticle (D) and an acceptor fluorophore (A), which is promoted to an excited electronic state *via* FRET. b) An illustration of spectral overlap in this model system. The emission spectrum of the donor D (—) largely overlaps with the absorbance of the acceptor A (—); the spectral overlap is highlighted in yellow.

In order to mathematically describe the efficiency (E) of energy transfer between a donor and a single acceptor *via* FRET, the following equation is used to express this quantity in terms of donor-acceptor distances or energy transfer rates:

$$E = \frac{1}{1+\left(\frac{r}{R_0}\right)^6} = \frac{R_0^6}{R_0^6 + r^6} = \frac{k_{D-A}}{k_{D-A} + \tau_D^{-1}} \qquad (3)$$

where r is the distance between the donor and acceptor, R_0 is the Förster distance or the distance at which the energy transfer efficiency is 50%, k_{D-A} is the rate of energy transfer, and τ_D is the lifetime of the donor in the absence of acceptor. If there are multiple acceptors per donor molecule, then Eq. 3 is modified to account for m acceptors per donor:

$$E = \frac{mk_{D-A}}{mk_{D-A} + \tau_D^{-1}} = \frac{mR_0^6}{mR_0^6 + r^6} \tag{4}$$

The Förster distance (R_0) can be calculated from the spectral overlap integral (J) of donor emission and acceptor absorption (Figure 1.8b):

$$J = \int_0^\infty F_D(\lambda)\varepsilon_A(\lambda)\lambda^4 d\lambda \tag{5}$$

where $F_D(\lambda)$ is the normalized emission intensity of the donor and $\varepsilon_A(\lambda)$ is the extinction coefficient of the acceptor at wavelength λ. Having determined the overlap integral for a given donor-acceptor pair, the Förster distance may now be calculated:

$$R_0^6 = \frac{9000(\ln 10)\kappa^2 \Phi_D J}{128\pi^5 N n^4} \tag{6}$$

where κ^2 is the relative orientation factor of the transition dipoles, Φ_D is the quantum efficiency of the donor, N is Avogadro's number, and n is the index of refraction of the medium. Typically, critical FRET length scales for R_0 range from 2–9 nm.[35] While J and R_0 can be calculated from the static emission and absorption spectra of the system components and a series of constants, more information is necessary in order to determine both r and E. The FRET efficiency E can be determined experimentally:

$$E = 1 - \frac{\tau_{D-A}}{\tau_D} \tag{7}$$

where τ_{D-A} is the lifetime of the donor in the presence of acceptor. After this series of calculations, the donor-acceptor distance r may now be determined using Eq. 3 or 4.

Alternatively, energy transfer can occur *via* a direct electron transfer in a Dexter[157] mechanism rather than a dipolar Förster interaction. In Dexter energy transfer, an excited electron in the LUMO of the donor is transferred to the acceptor molecule. The acceptor then transfers an electron from its HOMO back to the donor HOMO, leaving the acceptor in an excited state and the donor in the ground state. Typically, the Dexter interaction is associated with fluorescence quenching and can be observed if the spectral overlap is small so that large electron exchange rates become significant. If there is good spectral overlap, FRET usually occurs before Dexter transfer can occur. Finally, high concentrations of both donor and acceptor are necessary for significant Dexter transfer to occur, whereas FRET can be accomplished at much lower concentrations.[35]

1.7 Multiphoton Spectroscopy and Imaging

Having established that phosphorescence quenching is a suitable method of measuring oxygen levels and FRET is a viable technique for signal transduction, the absorption properties of the donor molecule must be considered. If a sensor is to be used *in vivo*, sufficient excitation light must penetrate the tissue to excite the donor. However, biological tissue is not very transparent to visible light; instead red or near infrared light must be used. Indeed, the so-called "tissue transparency window" is in the 600–1100 nm region where absorption of endogenous fluorophores, particular hemoglobin and melanin, is minimal and the penetration depth of these wavelengths is on the order of millimeters in most tissues.[158]

In order to exploit these wavelengths, one can utilize multiphoton spectroscopy, a nonlinear optical technique that involves the simultaneous absorption of two or more photons. The idea of two-photon absorption was first proposed by Maria Göppert-Mayer in 1931.[159] It was not until 30 years later that this concept was experimentally verified when Kaiser and

Garrett used red light from a ruby laser and detected blue fluorescence from a sample of $CaF_2:Eu^{2+}$.[160] Under linear or one-photon excitation, a fluorescent molecule is promoted to its excited state by the absorption of a single photon, with energy approximately equal to the separation of the ground and excited states (Figure 1.9a). Multiphoton processes require two or more photons to interact with the molecule simultaneously. In a two-photon process, the "first" photon excites the molecule to an intermediate state while the "second" photon promotes the molecule to its final state (Figure 1.9b). The intermediate state can either be an eigenstate of the molecule or a superposition of molecular states; therefore, it is usually referred to as a virtual intermediate state.[161] While the strength of a two-photon transition is due to contributions from all eigenstates as intermediate states, the two-photon absorption cross-section (σ_2) can be estimated using a single intermediate state approximation:[162]

$$\sigma_2 = \sigma_{ij}\sigma_{jf}\tau_j \tag{8}$$

where σ_{ij} is the one-photon absorption cross-section for the transition from the initial state i to the intermediate state j, σ_{jf} is the one-photon absorption cross-section for the transition from the intermediate state j to the final state f, and τ_j is the lifetime of the intermediate state. The parameter τ_j determines the time scale for photon coincidence and is 10^{-15} s or less for a virtual state (*i.e.* simultaneous photon absorption). Alternatively, a process may be a true sequential multiphoton excitation if the intermediate state is a real state with a lifetime of 10^{-9} to 10^{-12} s. A one-photon absorption cross-section (σ_1) may be estimated using the length of the transition dipole. For a typical organic fluorophore with a 10^{-8} cm dipole transition, σ_1 is approximately 10^{-16} or 10^{-17} cm^2. Using these values and Eq. 8, one may estimate a two-photon absorption cross-section of 10^{-49} cm^4 s/photon or 10 Göppert-Mayer (GM), where 1 GM = 10^{-50} cm^4 s/photon.[161]

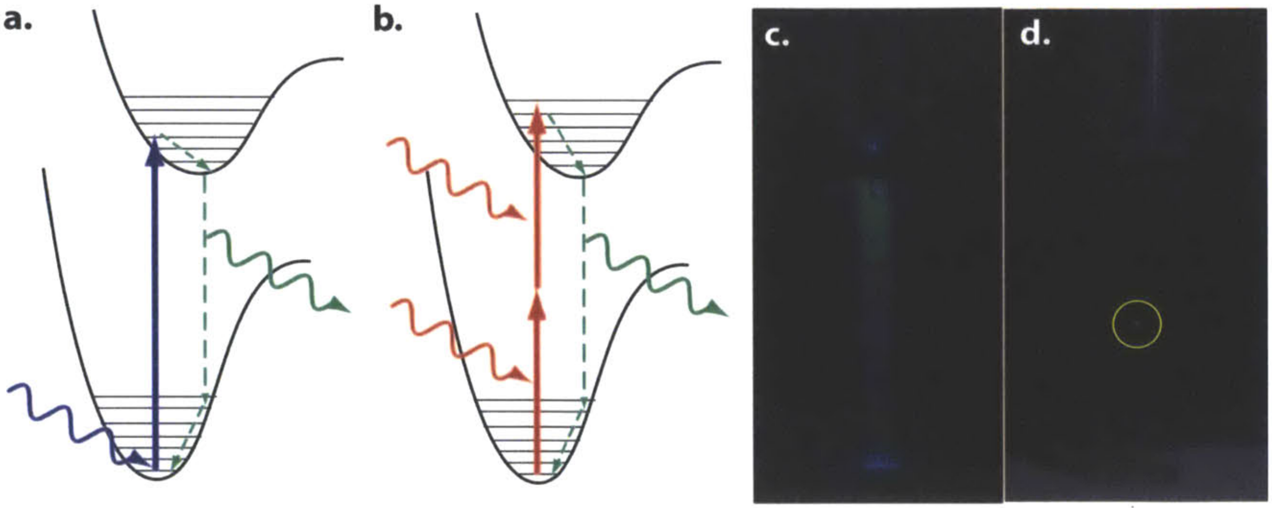

Figure 1.9. Comparison of one and two-photon processes. Panels a) and b) compare one- and two-photon excitation, respectively, from the ground state of a molecular fluorophore. c) Single photon excitation of fluorescein, demonstrating that fluorescence is detected throughout the sample. d) Two-photon excitation of the same fluorescein sample, exhibiting fluorescence only in the focal volume, which is highlighted with a yellow circle.

If a molecular absorption uses a single photon, the excitation density in the focal region is proportional to the intensity of the incident light. However, for a two-photon process, the excitation density depends on the square of the intensity and rapidly decays as the distance from the focal point increases. As a result, the two-photon excitation volume is much smaller than an analogous one-photon excitation volume and increases the spatial resolution of the signal. Indeed, the two-photon excitation densities are 10^4 and 10^8 smaller in the axial and radial directions respectively, than at the focus, resulting in the excitation of a small volume element.[163] This phenomenon is illustrated in Figure 1.9, where a sample of fluorescein is irradiated under one (c) and two photon (d) excitation conditions. The observed emission under one-photon excitation exhibits an hour-glass shape, generating a streak of emission along the beam path. This is in stark contrast to the two-photon excitation, which exhibits a sharp point of emission at the focus of the excitation source. As a result, two-photon excitation minimizes photobleaching and thermal degradation of the sample.

Until 1990, multiphoton spectroscopy was considered an exotic technique that was limited to the fields of optical spectroscopy and chemical physics. This was because photon sources that could provide appropriately high peak power to increase the probability of multiphoton absorption were limited.[35] With the advent of mode-locked solid-state femtosecond lasers, such as Ti:sapphire, the accessibility of multiphoton spectroscopy has dramatically increased.[161] In 1990, the first two-photon imaging of biological samples was reported using an ultrafast laser source.[164] Since then, multiphoton laser scanning microscopy (MPLSM) has become a powerful, routine imaging technique. It uses NIR light in the 600–1100 nm region to exploit the tissue transparency window and allow for greater depth penetration and deep tissue imaging. MPLSM provides noninvasive three-dimensional optical imaging with significant depth penetration (450–600 μm) and approximately 1 μm of spatial resolution.[158,165–168] Given the small focal volume of two-photon excitation, one can minimize the amount of bleaching and photodamage while generating high-resolution images to accurately map the heterogeneity of the tumor microenvironment.[169–171]

While MPLSM is a powerful imaging technique, there is a dearth of fluorescence dyes, that have significant two-photon absorption cross-sections, as $\sigma_2 \sim 10–100$ GM for most typical fluorophores (*vide supra*).[161,172–174] For example, fluorescein, a popular fluorescent dye commonly used in biological labeling, exhibits σ_2 varies from 8 GM to 37 GM in the 690–960 nm range, with the absorption maximum observed at 780 nm.[173] Some conventional fluorophores exhibit notably high σ_2 values: Cy3 with 140 GM and Rhodamine 6G with 150 GM, both at 700 nm.[173] More recently, design principles have been devised to prepare organic molecules with large (1000–10,000 GM) two-photon absorption cross-sections.[163,175] While these developments have been made, most analyte-sensitive dyes have low two-photon absorption cross-sections and cannot be used directly for MPLSM applications. Instead, a two-photon antenna must be coupled with an analyte-sensitive dye so that biological sensing can be accomplished under multiphoton excitation.

1.8 Quantum Dots and Sensing

Inorganic semiconductor nanocrystals, also known as quantum dots, are an important class of fluorophores that exhibit unique photophysical properties.[176–189] When a semiconductor absorbs a photon with energy greater the band gap, an electron is promoted from the valence band to the conduction band. If the photon has energy slightly less than the band gap by an amount equal to the phonon energy, an exciton will form. An exciton is a bound electron-hole pair that is held together by Coulombic interactions.[190] When the size of the exciton is on the order of the dimensions of the semiconductor, quantum confinement occurs.[191] As a result, the energy of confinement of the exciton in the crystal exceeds the Coulomb energy, resulting in molecule-like states rather than bands in the bulk material. Such nano-sized crystalline particles are known as quantum dots. The size of the particle is directly related to its optical properties; the effective band gap of a quantum dot increases with decreasing size.[176] QDs have broad absorption profiles with high extinction coefficients that are complemented by narrow, Gaussian-shaped emission features that are tunable with size. For CdSe QDs, small dots with a ~2 nm diameter exhibit blue emission under near UV excitation whereas larger dots with a ~5 nm diameter emit red light. Typically, QDs also exhibit high luminescence quantum yields; overcoating the QD with a higher band gap semiconductor (such as ZnS or CdZnS overcoats for CdSe) in a core/shell motif improves the emission quantum yield. Presumably, the shell passivates sites on the surface of the core that would otherwise lead to nonradiative excition recombination.[192,193] Recently, it has been demonstrated that quantum yields can be near unity for CdSe/CdS dots.[194] Additionally, QDs exhibit large two-photon absorption cross-sections,[195–199] with values of σ_2 as high as 47,000 GM for CdSe/ZnS QDs.[196] Together, the optical properties of QDs are in stark contrast to those of traditional organic fluorophores, which are prone to photobleaching as well as exhibit narrow absorption profiles and broad emission features that tend to tail into the red,[200] and have low σ_2 values (Section 1.7). As a result, QDs have become popular fluorophores for biological imaging[201,202] and have found application as fluorescent tracers in microscopy,[203,204] imaging molecular targets,[205] cell tracking,[202,206] and tumor pathophysiology.[207]

As synthesized, QDs are hydrophobic with tri-*n*-octylphosphine oxide (TOPO) as the capping lignad.[176] In order to utilize them for biological applications, the surface of the QD must be modified in order to impart water solubility and biocompatibility. An additional concern in utilizing QDs for biological studies is the potential toxicity in using cadmium-containing substances. However, live animal studies have demonstrated that toxicity is not observed, even four months after injection under standard conditions.[208] Both air and UV light can oxidize CdSe QDs, resulting in leaching of toxic Cd^{2+} ions.[209] It has been shown that the use of a ZnS overcoat on CdSe QDs significantly mitigates cell death in embryo studies.[210] However, long-term toxicity studies have not yet been performed to investigate chronic cadmium toxicity.

One method to confer water solubility is to coat a CdSe/CdS or CdSe/ZnS core/shell structure with a layer of silica,[211] while another is to use mercaptoacetic acid to passivate the surface.[212] The surfaces of QDs have been modified with phospholipids,[203] amphipilic polymers,[205] dendrimers,[213–218] and oligomeric phosphines[219] to make them water-soluble. A more elegant approach is to exchange the hydrophobic capping ligand for a multidentate hydrophilic ligand.[220–222] One such ligand example is a block copolymer prepared by RAFT polymerization[223] that consists of three monomers: imidazole for QD surface binding, PEG for water-solubility, and a terminal amine for derivitization.[222] Biotin was conjugated to this PIL ligand for HeLa cell labeling *via* biotin-streptavidin binding in cell cultures. Additionally, these QDs have been utilized *in vivo* to image the tumor vasculature. It was found that these constructs extravasate into the tumor tissue, enabling one to study the microenvironment. [222] Using this construct, one can utilize the terminal amine to conjugate a responsive dye to study dynamic changes of key analytes, such as pH and pO_2, in the tumor microenvironment.

1.9 Two-Photon Oxygen Sensors

By combining the principles of phosphorescence quenching, FRET, and multiphoton spectroscopy, one may develop novel oxygen sensors with a QD scaffold for *in vivo* biological applications using MPLSM. As outlined in Section 1.8, QDs have tunable photophysical properties that make them desirable for biological imaging. Because of their high quantum yields, they are ideal FRET donors for an appended analyte-sensitive fluorophore. Additionally, the high two-photon absorption cross-sections of QDs make them superior two-photon antennas for multiphoton-based sensing applications. Typically, the photophysical properties of QDs are unperturbed by changes in their environment (*i.e.* they are constant in both the presence and absence of an analyte, such as oxygen),[224] rendering them a suitable framework for ratiometric sensors, which rely on signal changes relative to an internal standard to quantify the amount of analyte. In such a construct, a QD is appended with an oxygen-sensitive phosphor; the QD is judiciously selected to maximize the spectral overlap with the conjugated phosphor for high FRET efficiency. In terms of the sensing strategy, the construct is irradiated under two-photon excitation conditions. Due to the high spectral overlap, FRET occurs from the QD to the attached phosphor, promoting it to an excited electronic state. The phosphor serves as an oxygen reporter, as its lifetime and emission intensity are sensitive to the amount of oxygen in the sample. Since the QD also emits and its luminescence is unaffected by oxygen, it serves as an intensity standard, making ratiometric sensing possible by using the ratio of porphyrin to QD emission intensity.

Vinogradov and co-workers have reported a series of two-photon FRET-based oxygen sensors in which a platinum or platinum porphyrin is covalently linked with coumarin dyes.[225–228] In these systems, the coumarin dye serves as both the two-photon antenna and FRET donor for the porphyrin phosphor. The Vinogradov design, while circumventing the use of potentially toxic QD's, suffers from several design limitations. The photophysical properties, namely the emission wavelength, of QDs are tunable, enabling the optimization of spectral overlap with the appended phosphor and maximizing FRET efficiency; such tunability is not possible with conventional organic fluorophores, which are quite limited in both spectral features and quantum yield. QDs are superior two-photon sensitizers ($\sigma_2 \sim 10^4$ GM than most conventional fluorophores like coumarins ($\sigma_2 = 20$ GM for Coumarin-343).[226] The Vinogradov sensors utilize many donors per acceptor, whereas the QD scaffold utilizes a single donor with many acceptors, thereby producing more signal on a per sensor basis, which is advantageous for biological applications.

While ruthenium bipyridine complexes[229] and platinum porphyrins[230,231] have been used as oxygen sensors in conjunction with QDs, the QD merely serves as an internal intensity standard (nether a FRET donor nor a two-photon antenna) in these systems. There are only three examples of authentic FRET-based oxygen sensors with a QD serving as the FRET donor and either pyrene,[232] platinum octaethylporphine ketone,[233] or osmium bipyridine complexes[234] serving as the FRET acceptor. Of these, only the osmium example reported by Nocera, Bawendi, and co-workers has been studied under two-photon excitation. This sensor, while exploiting the QD scaffold design principles outlined above, suffers from low dynamic range at biologically relevant oxygen pressures (0–160 torr), although it is sensitive for higher oxygen pressures.[234] The optical response of the pyrene-based sensor is in the 350–400 nm range, which is outside the tissue transparency window and is not an ideal candidate for biological imaging.[232] The platinum octaethylporphine ketone sensor is embedded in a polyvinyl chloride matrix and coated on a micropipette; this is an invasive means of oxygen detection and cannot be translated to *in vivo* applications.[233] As a result, new optical oxygen sensors must be designed to harness the benefits of QDs as biological fluoropores.

1.10 Scope of Thesis

In general, it is quite difficult to quantify an analyte concentration based on a simple change in emission intensity alone. Accurate measurements are unattainable if the background intensity changes, the dye emission is sensitive to environmental interferents, or there is emission from background fluorophores in the sensor environment (*i.e* autofluorescence in biological sensing.) This thesis presents oxygen-sensing constructs that are ratiometric, reversible, and stable. Chapter 2 describes the synthesis of free-base porphyrins and surveys various methods (statistical, semi-rational, and rational) to synthesize these fluorophores. The preparation of palladium(II) and platinum(II) complexes is also presented, as these are the oxygen-sensitive phosphors that are used throughout the thesis. In Chapter 3, the photophysical properties of these compounds are explored. Additionally, supramolecular assemblies consisting of *meso*-pyridyl palladium(II) porphyrins and a quantum dot are prepared in toluene, furnishing self-assembled oxygen sensors. These assemblies have been fully characterized optically, using both linear and two-photon spectroscopy. Chapter 4 reports the water-solubilization of these hydrophobic assemblies by exploiting micelle encapsulation. After full characterization and calibration of the sensor *in vitro*, preliminary imaging and oxygen quantification was performed using murine models.

1.11 References

1. Arnold, M. A.; Small, G. W. *Anal. Chem.* **2005**, *77*, 5429–5439.
2. Aslan, K.; Zhang, J.; Lackowicz, J. R.; Geddes, C. D. *J. Fluoresc.* **2004**, *14*, 391–400.
3. Ballerstadt, R.; Evans, C.; McNichols, R.; Gowda, A. *Biosens. Bioelectron.* **2006**, *22*, 275–284.
4. Kondepati, V. R.; Heise, H. M. *Anal. Bioanal. Chem.* **2007**, *388*, 545–563.
5. Pickup, J. C.; Hussain, F.; Evans, N. D.; Rolinski, O. J.; Birch, D. J. S. *Biosens. Bioelectron.* **2005**, *20*, 2555–2565.
6. Wang, J. *Chem. Rev.* **2008**, *108*, 814–825.
7. Cable, M. L.; Kirby, J. P.; Sorasaenee, K.; Gray, H. B.; Ponce, A. *J. Am. Chem. Soc.* **2007**, *129*, 1474–1475.
8. Yung, P. T.; Lester, E. D.; Bearman, G.; Ponce, A. *Biotechnol. Bioeng.* **2007**, *98*, 864–871.
9. Royo, S.; Martinez-Manez, R.; Sancenon, F.; Costero, A. M.; Parra, M.; Gil, S. *Chem. Commun.* **2007**, 4839–4847.
10. Jiang, Y.; Zhao, H.; Zhu, N.; Lin, Y.; Yu, P.; Mao, L. *Angew. Chem. Int. Ed.* **2008**, *47*, 8601–8604.
11. Gao, D.; Wang, Z.; Liu, B.; Ni, L.; Wu, M,; Zhang, Z. *Anal. Chem.* **2008**, *80*, 8545–8553.
12. Ai, K.; Zhang, B.; Lu, L. *Angew. Chem. Int. Ed.* **2009**, *48*, 304–308.
13. Oh, W. K.; Jeong, Y. S.; Song, J.; Jang, J. *Biosens. Bioelectron.* **2011**, *29*, 172–177.
14. Niessner, R. *Trends Anal. Chem.* **1991**, *10*, 310–316.

15. Scully, P.; Chandy, R.; Edwards, R.; Merchant, D.; Morgan, R. *Environ. Sci. Res.* **2001**, *56*, 175–199.

16. Szmacinski, H.; Lakowicz, J. R. *Sens. Actuators, B* **1995**, *B29*, 16–24.

17. Wang, L.; Wang, L.; Xia, T.; Dong, L.; Bian, G.; Chen, H. *Anal. Sci.* **2004**, *20*, 1013–1017.

18. Ma, C.; Zeng, F.; Huang, L.; Wu, S. *J. Phys. Chem. B* **2011**, *115*, 874–882.

19. Su, S.; Wu, W.; Gao, J.; Lu. J.; Fan, C. *J. Mater. Chem.* **2012**, *22*, 18101–18110.

20. Kim, H. N.; Ren, W. X.; Kim, J. S.; Yoon, J. *Chem. Soc. Rev.* **2012**, *41*, 3210–3244.

21. Dosev, D.; Nichkova, M.; Kennedy, I. M. in *Environmental Applcations of Nanomateris*, 2nd ed.; Fryxel. G. E.; Cao, G., Eds.; Imperial College Press: London, 2012; pp 561–619.

22. Du, D. in *Environmental Applcations of Nanomateris*, 2nd ed.; Fryxel. G. E.; Cao, G., Eds.; Imperial College Press: London, 2012; pp 621–645.

23. Bell, T.; Hext, N. M. *Chem. Soc. Rev.* **2004**, *33*, 589–598.

24. de Silva, A. P.; Gunaratne, H. Q. N.; Gunnlaugsson, T.; Huxley, A. J. M.; McCoy, C. P.; Rademacher, J. T.; Rice, T. E. *Chem. Rev.* **1997**, *97*, 1515–1566.

25. *Chemosensors of Ion and Molecular Recognition*; Kluwer Academic Publishers: Dordrecht, The Netherlands, 1997; Vol. 492.

26. *Fluorescent Chemosensors for Ion and Molecule Recognition*; American Chemical Society: Washington, D. C., 1993.

27. Czarnik, A. W. *Acc. Chem. Res.* **1994**, *27*, 302–308.

28. Rudzinski, C. M.; Hartmann, W. K.; Nocera, D. G. *Coord. Chem. Rev.* **1998**, *171*, 115–123.

29. Rudzinski, C. M.; Nocera, D. G. in *Optical Sensors and Switches*, Ramamurthy, V.; Schanze, K. S., Eds.; Marcel Dekker: New York, 2001, pp 1–91.

30. Rudzinski, C. M.; Young, A. M.; Nocera, D. G. *J. Am. Chem. Soc.* **2002**, *124*, 1723–1727.

31. Swager, T. M. *Acc. Chem. Res.* **1998**, *31*, 201–207.

32. Mohr, G. J. *Chem. Eur. J.* **2004**, *10*, 1082–1090.

33. de Silva, A. P.; Fox, D. B.; Moody, T. S.; Weir, S. M. *Trends Biotechnol.* **2001**, *19*, 29–34.

34. Wolfbeis, O. S. *J. Mater. Chem.* **2005**, *15*, 2657–2669.

35. Lakowicz, J. R.; *Principles of Fluorescence Spectroscopy*, 3rd ed.; Springer: New York, 2006.

36. Buck, S. M.; Xu, H.; Brasuel, M.; Philbert, M. A.; Kopelman, R. *Talanta* **2004**, *63*, 41–59.

37. Peng, J.; He, X.; Wang, K.; Tan, W.; Wang, Y.; Liu, Y. *Anal. Bioanal. Chem.* **2007**, *388*, 645–654.

38. Verhey, H. J.; Gebben, B.; Hofstraat, J. W.; Verhoeven, J. W. *J. Polym. Sci., Part A: Polym. Chem.* **1995**, *33*, 399–405.

39. Tan, W.; Shi, Z. Y.; Smith, S.; Bimbaum, D.; Kopelman, R. *Science* **1992**, *258*, 778–781.

40. Sharp, S. L.; Warmack, R. J.; Goudinnet, J. P.; Lee, I.; Ferrell, T. L. *Acc. Chem. Res.* **1993**, *26*, 377–382.

41. Campbell, C. G.; Ghodrati, M.; Garrido, F. *Soil Sci.* **1999**, *164*, 156–170.

42. O'Connell, K. P.; Valdes, J. J.; Azer, N. L.; Schwartz, R. P.; Wright, J. Eldefrawi, M. E. *J. Immunol. Methods* **1999**, *225*, 157–169.

43. Dahan, M.; Levi, S.; Luccardini, C.; Rostaing, P.; Riveau, B.; Triller, A. *Science* **2003**, *302*, 442–445.

44. Shimizu, K. T.; Neuhauser, R. G.; Leatherdale, C. A.; Empedocies, S. A.; Woo, W. K.; Bawendi, M. G. *Phys. Rev. B* **2001**, *63*, 205316-1–205316-5.

45. Xie, X. S.; Lu, H. P. *Springer Ser. Chem. Phys.* **2001**, *67*, 227–240.

46. Deniz, A. A.; Dahan, M.; Grunwell, J. R.; Ha, T.; Faulhaver, A. E.; Chemla, D. S.; Weiss, S.; Schultz, P. G. *Proc. Natl. Acad. Sci. USA* **1999**, *96*, 3670–3675.

47. Weiss, S. *Science* **1999**, *283*, 1676–1683.

48. Ha, T.; Ting, A. Y.; Liang, J.; Caldwell, W. B.; Deniz, A. A.; Chemla, D. S.; Schultz, P. G.; Weiss, S. *Proc. Natl. Acad. Sci. USA* **1999**, *96*, 893–898.

49. Chan, Y.; Snee, P. T.; Caruge, J. M.; Yen, B. K.; Nair, G. P.; Nocera, D. G.; Bawendi, M. G. *J. Am. Chem. Soc.* **2006**, *128*, 3146–3147.

50. Sundar, V. C.; Eisler, H. J.; Deng, T.; Chan, Y.; Thomas, E. L.; Bawendi, M. G. *Adv. Mater.* **2004**, *16*, 2137–2141.

51. Vezenov, D. V.; Mayers, B. T.; Conroy, R. S.; Whitesides, G. M.; Snee, P. T.; Chan, Y.; Nocera, D. G.; Bawendi, M. G. *J. Am. Chem. Soc.* **2005**, *127*, 8952–8953.

52. Wun, A. W.; Snee, P. T.; Chan, Y.; Bawendi, M. G.; Nocera, D. G. *J. Mater. Chem.* **2005**, *15*, 2697–2706.

53. Hahn, Y. B.; Ahmad, R.; Tripathy, N. *Chem. Commun.* **2012**, *48*, 10369–10385.

54. Yao, J.; Sun, Y.; Yang, M.; Duan, Y. *J. Mater. Chem.* **2012**, *22*, 14313–14329.

55. Valentini, F.; Carbone, M.; Palleschi, G. *Anal. Bioanal. Chem.* **2013**, *405*, DOI: 10.1007/s00216-012-6351-6.

56. Jans, H.; Huo, Q. *Chem. Soc. Rev.* **2012**, *41*, 2849–2866.

57. Gates, A. T.; Fakayode, S. O.; Lowry, M.; Ganea, G. M.; Murufeshu, A.; Robinson, J. W.; Strongin, R. M.; Warner, I. M. *Langmuir* **2008**, *24*, 4107–4113.

58. Perfézou, M.; Turner, A.; Merkoçi, A. *Chem. Soc. Rev.* **2012**, *41*, 2606–2622.

59. Barash, O.; Peled, N.; Tisch, U.; Bunn, P. A.; Hirsch, F. R.; Haick, H. *Nanomed. Nanotechnol. Biol. Med.* **2012**, *8*, 580–589.

60. Dreaden, E. C.; El-Sayed, M. A. *Acc. Chem. Res.* **2012**, *45*, 1854–1865.

61. Hakim, M.; Billan, S.; Tisch, U.; Peng, G.; Dvrokind, I.; Marom, O.; Abdah-Bortnyak, R.; Kuten, A.; Haick, H. *Br. J. Cancer* **2011**, *104*, 1649–1655.

62. Miranda, O. R.; Chen, H. T.; You, C. C.; Mortenson, D. E.; Yang, X. C.; Bunz, U. H. F.; Rotello, V. M. *J. Am. Chem. Soc.* **2010**, *132*, 5285–5289.

63. Marom, O.; Nakhoul, F.; Tisch, U.; Shiban, A.; Abassi, Z.; Haick, H. *Nanomedicine* **2012**, *7*, 639–650.

64. Choi, S.; Dickson, R. M.; Yu, J. *Chem. Soc. Rev.* **2012**, *41*, 1867–1891.

65. Benjaminsen, R. V.; Sun, H.; Henriksen, J. R.; Christensen, N. M.; Almadl, K.; Andresen, T. L. *ACS Nano* **2011**, *5*, 5864–5873.

66. Sharma, P. K.; Dutta, R. K.; Pandey, A. C. *Adv. Mater. Lett.* **2011**, *2*, 246–263.

67. Koh, I.; Josephson, L. *Sensors* **2009**, *9*, 8130–8145.

68. Burns, A.; Sengupta, P.; Zedayko, T.; Baird, B.; Wiesner, U. *Small* **2006**, *2*, 723–726.

69. Liu, Q.; Yeh, Y. C.; Rana, S.; Jiang, Y.; Guo, L.; Rotello, V. M. *Cancer Lett.* **2013**, *329*, DOI: 10.1016/j.canlet.2012.09.013.

70. Yan, S.; Shi, Y.; Xiao, Z.; Mhou, M.; Yan, W.; Shen, H., Hu, D. *J. Nanosci. Nanotechnol.* **2012**, *12*, 6873–6879.

71. Mout, R.; Moyano, D. F.; Rana, S.; Rotello, V. M. *Chem. Soc. Rev.* **2012**, *41*, 2539–2544.

72. Swierczewska, M.; Liu, G.; Lee, S.; Chen, X. *Chem. Soc. Rev.* **2012**, *41*, 2641–2655.

73. Ruedas-Rama, M. J.; Walters, J. D.; Orte, A.; Hall, E. A. H. *Anal. Chim. Acta* **2012**, *751*, 1–23.

74. Somers. R. C.; Bawendi, M. G.; Nocera, D. G. *Chem. Soc. Rev.* **2007**, *36*, 579–591.

75. Zhang, C. Y.; Johnson, L. W. *J. Am. Chem. Soc.* **2006**, *128*, 5324–5325.

76. Medintz, I. L.; Clapp, A. R.; Mattoussi, H.; Goldman, E. R.; Fisher, B.; Mauro, J. M. *Nat. Mater.* **2003**, *2*, 630–638.

77. Chen, C. Y.; Cheng, C. T.; Lai, C. W.; Wu, P. W.; Wu, K. C.; Chou, P. T.; Chou, Y. H.; Chiu, H. T. *Chem. Commun.* **2006**, 263–265.

78. Snee, P. T.; Somers, R. C.; Nair, G.; Zimmer, J. P.; Bawendi, M. G.; Nocera, D. G. *J. Am. Chem. Soc.* **2006**, *128*, 13320–13321.

79. Jain R. K. *Science* **2005**, *307*, 58–62.

80. Vaupel, P.; Kallinowski, F.; Okunieff, P. *Cancer Res.* **1989**, *49*, 6449–6465.

81. Helmlinger, G.; Yuan, F.; Dellian, M.; Jain, R. K. *Nat. Med.* **1997**, *3*, 177–182.

82. Fukumura, D.; Jain, R. K. *Microvasc. Res.* **2007**, *74*, 72–84.

83. Fukumura, D.; Jain, R. K. *J. Cell. Biochem.* **2007**, *101*, 937–949.

84. Helmlinger, G.; Sckell, A.; Dellian, M.; Forbes, N. S.; Jain, R. K. *Clin. Cancer Res.* **2002**, *8*, 1284–1291.

85. Erler, J. T.; Bennewith, K. L.; Nicolau, M.; Dornhoefer, N.; Kong, C.; Le, Q. T.; Chi, J. T.; Jeffrey, S. S.; Giaccia, A. J. *Nature* **2006**, *440*, 1222–1226.

86. Pennacchietti, S.; Michieli, P.; Galluzzo, M.; Mazzone, M.; Giordano, S.; Comoglio P. M. *Cancer Cell* **2003**, *3*, 347–361.

87. Rofstad, E. K.; Mathiesen, B.; Kindem, K.; Galappathi, K. *Cancer Res.* **2006**, *66*, 6699–6707.

88. Folkman, J. *N. Engl. J. Med.* **1971**, *285*, 1182–1186.

89. Carmeliet, R.; Jain, R. K. *Nature* **2000**, *407*, 249–257.

90. Jain, R. K. *Nat. Med.* **2001**, *7*, 987–989.

91. Folkman, J. *Nat. Rev. Drug Discovery* **2007**, *6*, 273–286.

92. Chauhan, V. P.; Stylianopoulos, T.; Boucher, Y.; Jain, R. K. *Annu. Rev. Chem. Biomol. Eng.* **2011**, *2*, 281–298.

93. Carmeliet, P.; Jain, R. K. *Nat. Rev. Drug Discovery* **2011**, *10*, 417–427.

94. Carmeliet, P. *Nature* **2005**, *438*, 932–936.

95. Yuan, F.; Chen, Y.; Dellian, M.; Safabakhsh, N.; Ferrara, N.; Jain, R. K. *Proc. Natl. Acad. Sci. USA* **1996**, *93*, 14765–14770.

96. Lee, C. G.; Heijn, M.; di Tomaso, E.; Griffon-Etienne, G.; Ancukiewicz, M.; Koike, C.; Park, K. R.; Ferrara, N.; Jain, R. K.; Suit, H. D.; Boucher, Y. *Cancer Res.* **2000**, *60*, 5565–5570.

97. Yang, J. C.; Haworth, L.; Sherry, R. M.; Hwu, P.; Schwartzentruber, D. J.; Topalian, S. L.; Steinberg, S. M.; Chen, H. X.; Rosenberg, S. A. *N. Engl. J. Med.* **2003**, *349*, 427–434.

98. Cobleigh, M.; Langmuir, V. K.; Sledge, G. W.; Miller, K. D.; Haney, L.; Novotny, W. F.; Reimann, J. D.; Vassel, A. *Semin. Oncol.* **2003**, *30*, 117–124.

99. Mayer, R. *N. Engl. J. Med.* **2004**, *350*, 2406–2408.

100. Hurwitz, H.; Fehrenbacher, L.; Novotny, W.; Cartwright, T.; Hainsworth, J.; Heim, W.; Berlin, J.; Baron, A.; Griffing, S.; Holmgren, E.; Ferrara, N.; Fyfe, G.; Rogers, B.; Ross, R.; Kabbinavar, F. *N. Engl. J. Med.* **2004**, *350*, 2335–2342.

101. Ma, J.; Pulfer, S.; Li, S.; Chu, J.; Reed, K.; Gallo, J. M. *Cancer Res.* **2001**, *61*, 5491–5498.

102. Murata, R.; Nishumura, Y.; Hiraoka, M. *Int. J. Radiat. Oncol.* **1997**, *37*, 1107–1113.

103. Fenton, B. M.; Paoni, S. F.; Ding, I. *Radiother. Oncol.* **2004**, *72*, 221–230.

104. Hansen-Algenstaedt, N.; Stoll, B. R.; Padera, T. P.; Dolmans, D. E. J. G. J.; Hicklin, D. J.; Fukumura, D.; Jain, R. K. *Cancer Res.* **2000**, *60*, 4556–4560.

105. Brown, J. M. *Cancer Res.* **1999**, *59*, 5863–5870.

106. Clark, L. C.; Wolf, R.; Granger, D.; Taylor, Z. *J. Appl. Physiol.* **1953**, *6*, 189–193.

107. Swartz, H. M.; Dunn, J. F. *Adv. Exp. Med. Biol.* **2003**, *530*, 1–12.

108. Pacheco-Torres, J.; López-Larrubia, P.; Ballesteros, P.; Cerdán, S. *NMR Biomed.* **2011**, *24*, 1–16.

109. Ruiz-Cabello, J.; Barnett, B. P.; Bottomley, P. A.; Bulte, J. W. M. *NMR Biomed.* **2011**, *24*, 114–129.

110. Khan, N.; Williams, B. B.; Hou, H.; Li, H.; Swartz, H. M. *Antioxid. Redox Signaling* **2007**, *9*, 1169–1182.

111. Bruehlmeier, M.; Roelcke, U.; Schubiger, P. A.; Ametamey, S. M. *J. Nucl. Med.* **2004**, *45*, 1851–1859.

112. Mortensen, L. S.; busk, M.; Nordsmark, M.; Jakobsen, S.; Theil, J.; Overgaard, J.; Horsman, N. R. *Radiother. Oncol.* **2011**, *99*, 418–423.

113. Pittman, R. N.; Duling, B. R. *J. Appl. Physiol.* **1975**, *38*, 315–320.

114. Pittman, R. N.; Duling, B. R. *J. Appl. Physiol.* **1975**, *38*, 321–327.

115. Srinivasan, S.; Pogue, B. W.; Carpenter, C.; Jiang, S.; Wells, W. A.; Poplack, S. P.; Kaufman, P. A.; Paulsen, K. D. *Antioxid. Redox Signaling* **2007**, *9*, 1143–1156.

116. Kautsky, H.; Hirsch, A. *Ber. Dtsch, Chem. Ges.* **1931**, *64*, 2677–2683.

117. Kautsky, H.; Muller, G. O. *Z. Naturforsch., A: Phys. Sci.* **1947**, *2a*, 167–172.

118. Vanderkooi, J. M.; Maniara, G.; Green, T. J.; Wilson, D. F. *J. Biol. Chem.* **1987**, *262*, 5476–5482.

119. Springett, R.; Swartz, H. M. *Antioxid. Redox Signaling* **2007**, *9*, 1295–1301.

120. Whalen, W. J.; Riley, J.; Nair, P. *J. Appl. Physiol.* **1967**, *23*, 798–801.

121. Tsai, A. G.; Johnson, P. C.; Intaglietta, M. *Physiol. Rev.* **2003**, *83*, 933–963.

122. Kallinowski, F.; Zander, R.; Hoeckel, M.; Vaupel, P. *Int. J. Radiat. Oncol. Biol. Phys.* **1990**, *19*, 953–961.

123. Mason, R. P.; Rodbumrung, W.; Antich, P. P. *NMR Biomed.* **1996**, *9*, 125–134.

124. Diepart, C.; Magat, J.; Jordan, B. F.; Gallez, B. *NMR Biomed.* **2011**, *24*, 458–463.

125. Liu, S.; Shah, S. J.; Wilmes, L. J.; Feiner, J.; Kodibagkar, V. D.; Wendland, M. F.; Mason, R. P.; Hylton, N.; Hopf, H. W.; Rollins, M. D. *Magn. Reson. Med.* **2011**, *66*, 1722–1730.

126. Kodibagkar, V. D.; Wang, X.; Pacheco-Torres, J.; Gulaka, P.; Mason, R. P. *NMR Biomed.* **2008**, *21*, 899–907.

127. Ogawa, S.; Lee, T. M.; Kay, A. R.; Tank, D. W. *Proc. Natl. Acad. Sci. USA* **1990**, *87*, 9868–9872.

128. Gloviczki, M. L.; Glockner, J. F.; Crane, J. A.; McKusick, M. A.; Misra, S.; Grande, J. P.; Lerman, L. O.; Textor, S. C. *Hypertension* **2011**, *58*, 1066–1072.

129. Krohn, K. A.; Link, J. M.; Mason, R. P. *J. Nucl. Med.* **2008**, *49*, 129S–148S.

130. Yasui, H.; Matsumoto, S.; Devasahayam, N.; Munasinghe, J. P.; Choudhuri, R.; Saito, K.; Subramanian, S.; Mitchell, J. B.; Krishna, M. C. *Cancer Res.* **2010**, *70*, 6427–6436.

131. Filho, I. P. T.; Leunig, M.; Yuan, F.; Intaglietta, M.; Jain, R. K. *Proc. Natl. Acad. Sci. USA* **1994**, *91*, 2081–2085.

132. Stern, O.; Volmer, M. *Z. Phys.* **1919**, *20*, 183–188.

133. Klessinger, M.; Michl, J. *Excited States and Photochemistry of Organic Molecules*; VCH Publishers: New York, 1995.

134. Kalyanasundaram, K. *Photochemistry of Polypyridine and Porphyrin Complexes*; Academic Press: San Diego, CA, 1992.

135. Papkovsky, D. B. *Methods Enzymol.* **2004**, *381*, 715–735.

136. Figgis, B. N.; Hitchman, M. A. *Ligand Field Theory and Its Applications*; Wiley-VCH: New York, 2000.

137. Bacon, J. R.; Demas, J. N. *Anal. Chem.* **1987**, *59*, 2780–2785.

138. Carraway, E. R.; Demas, J. N.; Degraff, B. A.; Bacon, J. R. *Anal. Chem.* **1991**, *63*, 337–342.

139. Li, X. M.; Ruan, F. C.; Wong, K. Y. *Analyst* **1993**, *118*, 289–292.

140. Xu, W.; McDonough, R. C.; Langsdorf, B.; Demas, J. N.; DeGraff, B. A. *Anal. Chem.* **1994**, *66*, 4133–4141.

141. Klimant, I.; Wolfbeis, O. S. *Anal. Chem.* **1995**, *67*, 3160–3166.

142. Hartmann, P.; Leiner, M. J. P.; Lippitsch, M. E. *Anal. Chem.* **1995**, *67*, 88–93.

143. Hartmann, P.; Leiner, M. J. P.; Lippitsch, M. E. *Sens. Actuators, B* **1995**, *29*, 251–257.

144. Draxler, S.; Lippitsch, M. E.; Klimant, I.; Kraus, H.; Wolfbeis, O. S. *J. Phys. Chem.* **1995**, *99*, 3162–3167.

145. Li, X. M.; Wong, K. Y. *Anal. Chim. Acta* **1992**, *262*, 27–32.

146. Lee, S. K.; Okura, I. *Anal. Commun.* **1997**, *34*, 185–188.

147. Eaton, K.; Douglas, P. *Sens. Actuators, B* **2002**, *82*, 94–104.

148. Amao, Y.; Okura, I. *J. Porphyrins Phthalocyanines* **2009**, *13*, 1111–1122.

149. Zhang, H.; Sun, Y.; Ye, K.; Zhang, P.; Wang, Y. *J. Mater. Chem.* **2005**, *15*, 3181–3186.

150. Tripathi, V. S.; Lakshminarayana, G.; Nogami, M. *Sens. Actuators, B* **2010**, *147*, 741–747.

151. Amao, Y.; Miyakawa, K.; Okura, I. *J. Mater. Chem.* **2000**, *10*, 305–308.

152. Chu, C. S.; Lo, Y. L.; Sung, T. W. *Talanta* **2010**, *82*, 1044–1051.

153. Collier, B. B.; Singh, S.; McShane, M. *Analyst* **2011**, *136*, 962–967.

154. Wu, C.; Bull, B.; Christensen, K.; NcNeill, J. *Angew. Chem. Int. Ed.* **2009**, *48*, 2741–2745.

155. Fercher, A.; Borisov, S. M.; Zhdanov, A. V.; Klimant, I.; Papkovsky, D. B. *ACS Nano* **2011**, *5*, 5499–5508.

156. Förster, T. *Ann. Phys.* **1948**, *437*, 55–75.

157. Dexter, D. L. *J. Chem. Phys.* **1953**, *21*, 836–850.

158. König, K. *J. Microsc.* **2000**, *200*, 83–104.

159. Göppert-Mayer, M. *Ann. Phys.* **1931**, *401*, 273–294.

160. Kaiser, W.; Garrett, C. G. B. *Phys. Rev. Lett.* **1961**, *7*, 229–231.

161. Xu, C.; Zipfel, W. R. Multiphoton Excitation of Fluorescent Probes. In *Handbook of Biomedical Nonlinear Optical Microscopy*; Masters, B. R.; So, P. T. C., Eds.; Oxford University Press: New York, 2008; pp 311–333.

162. Birge, R. R. One-Photon and Two-Photon Excitation Spectroscopy. In *Ultrasensitive Laser Spectroscopy*; Klinger, D. S., Ed.; Academic Press: New York, 1983; pp 109–174.

163. Pawlicki, M.; Collins, H. A.; Denning, R. G.; Anderson, H. L. *Angew. Chem. Int. Ed.* **2009**, *48*, 3244–3266.

164. Denk, W.; Strickler, J. H.; Webb, W. W. *Science* **1990**, *248*, 73–76.

165. Xu, C.; Zipfel, W.; Shear, J. B.; Williams, R. M.; Webb, W. W. *Proc. Natl. Acad. Sci. USA* **1996**, *93*, 10763–10768.

166. Jain, R. K.; Booth, M. F.; Padera, T. P.; Munn, L. L.; Fukumura, D.; Brown, E. Applications of Nonlinear Intravital Microscopy in Tumor Biology. In *Handbook of Biomedical Nonlinear Optical Microscopy*; Masters, B. R.; So, P. T. C., Eds.; Oxford University Press: New York, 2008; pp 735–756.

167. Zipfel, W. R.; Williams, R. M.; Webb, W. W. *Nat. Biotechnol.* **2003**, *21*, 1369–1377.

168. Helmchen, F.; Denk, W. *Nat. Methods* **2005**, *2*, 932–940.

169. Squirrell, J. M.; Wokosin, D. L.; White, J. G.; Bavister, B. D. *Nat. Biotechnol.* **1999**, *17*, 763–767.

170. Brown, E. B.; Campbell, R. B.; Tsuzuki, Y.; Xu, L.; Carmeliet, P.; Fukumura, D.; Jain, R. K. *Nat. Med.* **2001**, *7*, 864–868.

171. Jain, R. K.; Munn, L. L.; Fukumura, D. *Nat. Rev. Cancer* **2002**, *2*, 266–276.

172. Xu, C.; Webb, W. W. *J. Opt. Soc. Am. B* **1996**, *13*, 481–491.

173. Albota, M. A.; Xu, C.; Webb, W. W. *Appl. Opt.* **1998**, *37*, 7352–7356.

174. Oulianov, D. A.; Tomov, I. V.; Dvornikov, A. S.; Rentzepis, P. M. *Opt. Commun.* **2001**, *191*, 235–243.

175. Albota, M.; Beljonne, D.; Brédas, J. L.; Ehrlich, J. E.; Fu, J. Y.; Heikal, A. A.; Hess, S. E.; Kogej, T.; Levin, M. D.; Marder, S. R.; McCord-Maughon, D.; Perry, J. W.; Röckel, H.; Rumi, M.; Subramaniam, G.; Webb, W. W.; Wu, X. L.; Xu, C. *Science* **1998**, *281*, 1653–1656.

176. Murray, C. B.; Norris, D. J.; Bawendi, M. G. *J. Am. Chem. Soc.* **1993**, *115*, 8706–8715.

177. Bawendi, M. C.; Steigerwald, M. L.; Brus, L. E. *Annu. Rev. Phys. Chem.* **1990**, *41*, 477–496.

178. Kastner, M. A. *Phys. Today* **1993**, *46*, 24–31.

179. Anscombe, N. *N. Photonics* **2007**, *1*, 360–361.

180. Azzazy, H. M. E.; Mansour, M. M. H.; Kazmierczak, S. C. *Clin. Biochem.* **2007**, *40*, 917–927.

181. Hammer, N. I.; Emrick, T.; Barnes, M. D. *Nanosc. Res. Lett.* **2007**, *2*, 282–290.

182. Coe-Sullivan, S. *Mater. Matters* **2007**, *2*, 13–14.

183. Corbin, J. G.; Haydar, T. F. *Nanomedicine* **2007**, *2*, 579–581.

184. Guyot-Sionnest, P. *Mater. Matters* **2007**, *2*, 10–12.

185. Pinaud, F.; Michalet, X.; Bentolila, L. A.; Tsay, J. M.; Doose, S.; Li, J. J.; Iyer, G.; Weiss, S. *Biomaterials* **2006**, *27*, 1679–1687.

186. Reithmaier, J. P.; Somers, A.; Kaiser, W.; Deubert, S.; Gerschuetz, F.; Forchel, A.; Parillaud, O.; Krakowski, M.; Alizon, R.; Hadass, D.; Bilenca, A.; Dery, H.; Mikhelashvili, V.; Eisenstein, G.; Gioannini, M.; Montrosset, I.; Berg, T. W.; van der Poel, M.; Mork, J.; Tromborg, B. *Phys. Status Solidi B* **2006**, *243*, 3981–3987.

187. Samia, A. C. S.; Dayal, S.; Burda, C. *Photochem. Photobiol.* **2006**, *82*, 617–625.

188. Scholz, M.; Aichele, T.; Benson, O. *Adv. Solid State Phys.* **2008**, *46*, 3–14.

189. Wu, M. H.; Ueda, A.; Mu, R. *Opt. Sci. Eng.* **2005**, *99*, 331–350.

190. Kittel, C. *Introduction to Solid State Physics*, 8th ed.; John Wiley & Sons: Hoboken, NJ, 2005.

191. Brus, L. E. *J. Chem. Phys.* **1983**, *79*, 5566–5571.

192. Hines, M. A.; Guyot-Sionnest, P. *J. Phys. Chem.* **1996**, *100*, 468–471.

193. Dabbousi, B. O.; Rodriguez-Viejo, J.; Mikulec, F. V.; Heine, J. R.; Mattoussi, H.; Ober, R.; Jensen, K. F.; Bawendi, M. G. *J. Phys. Chem. B* **1997**, *101*, 9463–9475.

194. Greytak, A. B.; Allen, P. M.; Liu, W.; Zhao, J.; Young, E. R.; Popovic, Z.; Walker, B. J.; Nocera, D. G.; Bawendi, M. G. *Chem. Sci.* **2012**, *3*, 2028–2034.

195. Blanton, S. A.; Dehestani, A.; Lin, P. C.; Guyot-Sionnest, P. *Chem. Phys. Lett.* **1994**, *229*, 317–322.

196. Larson, D. R.; Zipfel, W. R.; Williams, R. M.; Clark, S. W.; Bruchez, M. P.; Wise, F. W.; Webb, W. W. *Science* **2003**, *300*, 1434–1436.

197. Pu, S. C.; Yang, M. J.; Hsu, C. C.; Lai, C. W.; Hsieh, C. C.; Lin, S. H.; Cheng, Y. M.; Chou, P. T. *Small* **2006**, *2*, 1308–1313.

198. Schmidt, M. E.; Blanton, S. A.; Hines, M. A.; Guyot-Sionnest, P. *Phys. Rev. B* **1996**, *53*, 12629–12632.

199. Blanton, S. A.; Hines, M. A.; Schmidt, M. E.; Guyot-Sionnest, P. *J. Lumin.* **1996**, *70*, 253–268.

200. Jaiswal, J. K.; Simon, S. M. *Trends Cell Biol.* **2004**, *14*, 497–504.

201. Medintz, I. L.; Uyeda, H. T.; Goldman, E. R.; Mattoussi, H. *Nat. Mater.* **2005**, *4*, 435–446.

202. Michalet, X.; Pinaud, F. F.; Bentolila, L. A.; Tsay, J. M.; Doose, S.; Li, J. J.; Sundaresan, G.; Wu, A. M.; Gambhir, S. S.; Weiss, S. *Science* **2005**, *307*, 538–544.

203. Dubertret, B.; Skourides, P.; Norris, D. J.; Noireaux, V.; Brivanlou, A. H.; Libchaber, A. *Science* **2002**, *298*, 1759–1762.

204. Jain, R. K.; Stroh, M. *Nat. Biotechnol.* **2004**, *22*, 959–960.

205. Wu, X.; Liu, H.; Liu, J.; Haley, K. N.; Treadway, J. A.; Larson, J. P.; Ge, N.; Peale, F.; Bruchez, M. P. *Nat. Biotechnol.* **2003**, *21*, 41–46.

206. Gao. X.; Cui, Y.; Levenson, R. M.; Chung, L. W.; Nie, S. *Nat. Biotechnol.* **2004**, *22*, 969–976.

207. Stroh, M.; Zimmer, J. P.; Duda, D. G.; Levchenko, T. S.; Cohen, K. S.; Brown, E. B.; Scadden, D. T.; Torchilin, V. P.; Bawendi, M. G.; Fukumura, D.; Jain, R. K. *Nat. Med.* **2005**, *11*, 678–682.

208. Ballou, B.; Lagerholm, B. C.; Ernst, L. A.; Bruchez, M. P.; Waggoner, A. S. *Bioconj. Chem.* **2004**, *15*, 79–86.

209. Derfus, A. M.; Chan, W. C. W.; Bhatia, S. N. *Nano. Lett.* **2004**, *4*, 11–18.

210. Chan, W. H.; Shiao, N. H. *Acta Pharmacol. Sin.* **2008**, *29*, 259–266.

211. Bruchez, M.; Moronne, M.; Gin, P.; Weiss, S.; Alivisatos, A. P. *Science* **1998**, *281*, 2013–2016.

212. Chan, W. C.; Nie, S. *Science* **1998**, *281*, 2016–2018.

213. Guo, W.; Li, J. J.; Wang, Y. A.; Peng, X. *Chem. Mater.* **2003**, *15*, 3125–2133.

214. Guo, W.; Li, J. J.; Wany, Y. A.; Peng, X. *J. Am. Chem. Soc.* **2003**, *125*, 3901–3909.

215. Huang, B.; Tomalia, D. A. *Inorg. Chem. Acta* **2006**, *359*, 1961–1966.

216. Liu, Y.; Kim, M.; Wang, Y.; Wang, Y. A.; Peng, X. *Langmuir* **2006**, *22*, 6341–6345.

217. Wang, Y. A.; Li, J. J.; Chen, H.; Peng, X. *J. Am. Chem. Soc.* **2002**, *124*, 2293–2298.

218. Wisher, A. C.; Bronstein, I.; Chechik, V. *Chem. Commun.* **2006**, 1637–1639.

219. Kim, S.; Bawendi, M. G. *J. Am. Chem. Soc.* **2003**, *125*, 14652–14653.

220. Uyeda, H. T.; Medintz, I. L.; Jaiswal, J. K.; Simon, S. M.; Mattoussi, H. *J. Am. Chem. Soc.* **2005**, *127*, 3870–3878.

221. Liu, W.; Howarth, M.; Greytak, A. B.; Zheng, Y.; Nocera, D. G.; Ting, A. Y.; Bawendi, M. G. *J. Am. Chem. Soc.* **2008**, *130*, 1274–1284.

222. Liu, W.; Greytak, A. B.; Lee, J.; Wong, C. R.; Park, J.; Marshall, L. F.; Jiang, W.; Curtin, P. N.; Ting, A. Y.; Nocera, D. G.; Fukumura, D.; Jain, R. K.; Bawendi, M. G. *J. Am. Chem. Soc.* **2010**, *132*, 472–483.

223. Moad, G.; Rizzardo, E.; Thang, S. H. *Aust. J. Chem.* **2005**, *58*, 379–410.

224. Walker, G. W.; Sundar, V. C.; Rudzinski, C. M.; Wun, A. W.; Bawendi, M. G.; Nocera, D. G. *Appl. Phys. Lett.* **2003**, *83*, 3555–3557.

225. Briñas, R. P.; Troxler, T.; Hochstrasser, R. M.; Vinogradov, S. A. *J. Am. Chem. Soc.* **2005**, *127*, 11851–11862.

226. Finikova, O. S.; Troxler, T.; Senes, A.; DeGrado, W. F.; Hochstrasser, R. M.; Vinogradov, S. A. *J. Phys. Chem. A* **2007**, *111*, 6977–6990.

227. Finikova, O. S.; Lebedev, A. Y.; Aprelev, A.; Troxler, T.; Gao, F.; Garnacho, C.; Muro, S.; Hochstrasser, R. M.; Vinogradov, S. A. *ChemPhysChem* **2008**, *9*, 1673–1679.

228. Sinks, L. E.; Robbins, G. P.; Roussakis, E.; Troxler, T.; Hammer, D. A.; Vinogradov, S. A. *J. Phys. Chem. B* **2010**, *114*, 14373–14382.

229. Jorge, P. A. S.; Mayeh, M.; Benrashid, R.; Caldas, P.; Santos, J. L.; Farahi, F. *Appl. Opt.* **2006**, *45*, 3760–3767.

230. Collier, B. B.; Singh, S.; McShane, M. *Analyst* **2011**, *136*, 962–967.

231. Wang, X.; Chen, X.; Xie, Z.; Wang, X. *Angew. Chem. Int. Ed.* **2008**, *47*, 7450–7453.

232. Amelia, M.; Lavie-Cambot, A.; McClenaghan, N. D.; Credi, A. *Chem. Commun.* **2011**, *47*, 325–327.

233. Zhang, C.; Ingram, J.; Schiff, S.; Xu, J.; Xiao, M. *Proc. SPIE* **2011**, *7947*, 79470B-1–79470B-6.

234. McLaurin, E. J.; Greytak, A. B.; Bawendi, M. G.; Nocera, D. G. *J. Am. Chem. Soc.* **2009**, *131*, 12994–13001.

Chapter 2

Porphyrin Synthesis

2.1 Background

Many oxygen sensitive phosphors have been reported in the literature including osmium,[1] iridium,[2] and ruthenium[3] polypyridine complexes. However, these molecules generally exhibit small differences between the lifetime of aerated and evacuated samples, thereby limiting the range over which these molecules are sensitive to oxygen concentration. Indeed, only a 1–2 μs difference in the lifetime was observed for a ruthenium polypyridine complex[3] while a related osmium complex[1] exhibited only 100–150 ns lifetime difference. The osmium example, however, was suitable for high pressure oxygen sensing (0–760 torr). An alternative phosphor is necessary to probe hypoxia in the tumor microenvironment. To this end, platinum and palladium porphyrins are best suited for biological applications due to their strong room temperature phosphorescence in the 650–800 nm range and long (~10^2 μs) triplet lifetimes.[4] The long lifetimes of palladium porphyrins make them ideal for oxygen sensing in the biologically relevant 0–160 torr range. Upon optical excitation of the porphyrin, rapid intersystem crossing to a long-lived triplet state occurs. Molecular oxygen (a ground state triplet) deactivates the excited state through collisional quenching, following Stern-Volmer kinetics.[5] By monitoring the intensity or lifetime of the triplet state of the phosphor, the amount of oxygen in a sample is quantified.[6] This chapter describes the synthesis of free-base porphyrins, using statistical, semi-rational, and rational methodologies, as well as their palladium and platinum porphyrin complexes for oxygen sensing applications.

2.2 Statistical Porphyrin Synthesis

Early methods of porphyrin synthesis typically involve forcing conditions in which pyrrole and an aryl aldehyde are refluxed in an organic acid, such as propionic or acetic acid. These methods were developed by Adler and Longo in the 1960's.[7,8] While this procedure can reproducibly provide prophyrins in high yields for certain substituents under highly optimized conditions (20% yield for H_2TPP),[8] the harsh reaction conditions results in the access to many reaction pathways, resulting in large amounts of polypyrrolic byproducts. Additionally, the corresponding chlorins (tetrapyrrolic macrocycles in which one of the pyrrole rings has been reduced, making the 2 and 3 positions sp^3 hybridized carbons) are produced in approximately 3% yield.[8] In 1989, Lindsey and Wagner published a facile method to synthesize *meso*-substituted porphyrins under gentle, room-temperature conditions.[9] These so-called Lindsey conditions involve a $BF_3{\bullet}OEt_2$-catalyzed condensation between pyrrole and an aryl aldehyde in $CHCl_3$. This results in the formation of linear condensation products which cyclize to give a porphyrinogen, a non-aromatic tetrapyrrolic macrocycle in which the *meso* positions are sp^3 hybridized. This intermediate then undergoes a six-electron, six-proton oxidation to afford the corresponding porphyrin, using 2,3-dichloro-5,6-dicyano-1,4-benzoquinone (DDQ) as the oxidant. Since this reaction is performed at room temperature under mild conditions, the formation of polypyrrolic byproducts is minimized and chlorin impurities are not formed, giving porphyrins in high yield (29% yield for 5,10,15,20-tetramesitylporphyrin).[9]

Given the advantages of the Lindsey porphyrin synthesis, this methodology was employed for the synthesis of A_3B porphyrins. These asymmetric porphyrins, which represent an appreciable synthetic challenge, are required so that a point of attachment may be built into the molecule, enabling a covalent linkage of the porphyrin to a polymer-coated quantum dot (See Chapter 1). Since the PIL polymer features terminal amines for fluorophor attachment,[10] these porphyrin features a methyl ester, which can then be hydrolyzed to form a carboxylic acid. This functional group can then react with the terminal amine of the PIL polymer *via* amide bond formation.

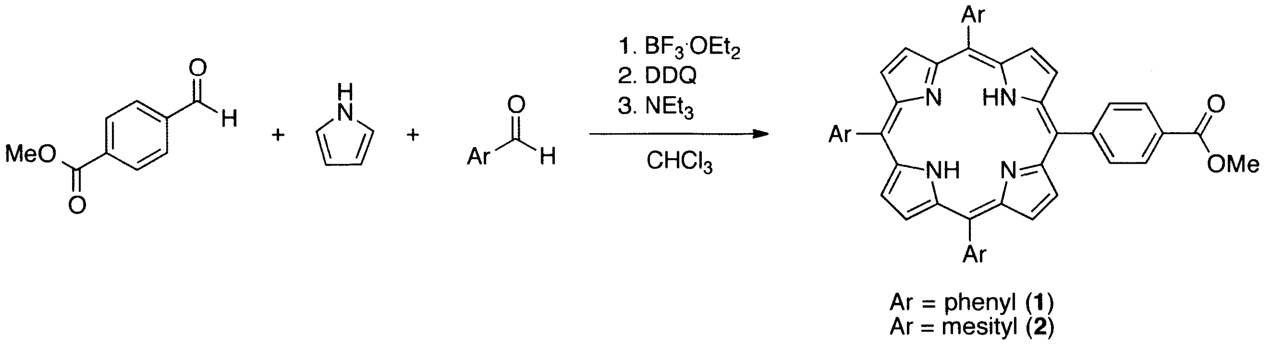

Scheme 2.1. Synthesis of A_3B porphyrins with *meso*-aryl substitutents *via* a mixed-aldehyde condensation under standard Lindsey conditions.

Using a mixed aldehyde condensation under standard Lindsey conditions (Scheme 2.1), porphyrins **1** and **2** were isolated in 11% and 8% yield, respectively. In both syntheses, the symmetric A_4 porphyrin was obtained in 7% yield as the only macrocyclic byproduct. The free-base porphyrin **1** was metallated using either Pd(acac)$_2$ in pyridine or Pt(acac)$_2$ in benzonitrile under microwave irradiation.[11] The complexes **Pd-1** and **Pt-1** were isolated as red-orange solids in 99% and 66% yield, respectively (Scheme 2.2). Ideally, these reactions should be quantitative, as indicated by literature reports.[11] Perhaps the lower yield of **Pt-1** is due to precipitation of metallic platinum at high temperatures (250 °C) relative to the palladium insertion conditions, which are conducted at 180 °C. Ester hydrolysis was performed using basic conditions under microwave irradiation[12] to reduce the reaction time relative to conventional heating protocols.[13] The complexes **Pd-3** and **Pt-3** were isolated as red-orange solids in 66% and 89% yield, respectively. It should be noted that hydrolysis was not conducted on the free base porphyin **1** because subsequent metallation with platinum or palladium under microwave irradiation resulted in partial decarboxylation, giving the corresponding tetraphenylporphyrin complex.[14] The photophysical properties of both **Pd-3** and **Pt-3** are presented in Chapter 3.

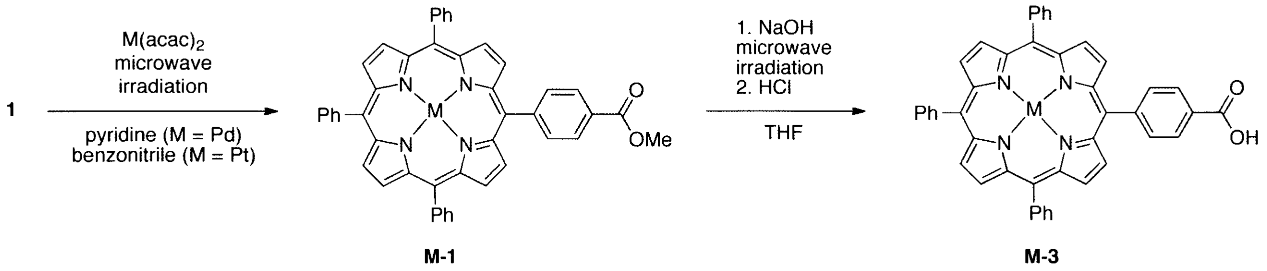

Scheme 2.2. Synthesis of A_3B metalloporphyrins and subsequent basic ester hydrolysis; both reactions are facilitated by microwave irradiation.

With the complexes **Pd-3** and **Pt-3** that are appropriately functionalized for quantum dot attachment, attempts were made to conjugate **Pd-3** to water-soluble dots coated with PIL (see Chapter 1). The addition of THF as a co-solvent was required to keep the porphyrin in solution. However, the presence of organic solvents induces precipitation of dots that have already been brought into water. As a result, coupling was inefficient and an alternative approach to prepare porphyrin-quantum dot conjugates is necessary. The use of water-soluble porphyrins would circumvent these limitations and enable facile coupling in aqueous media.

One approach to preparing water-soluble porphyrins is through the addition of sulfonate groups. This has been accomplished by refluxing 5,10,15,20-tetraphenyl porphyrin (**4**) in concentrated sulfuric acid.[15–18] However, a functional handle must be built into the porphyrin to enable conjugation of the porphyrin to a quantum dot. To this end, a single nitro group was added (Scheme 2.3) by treating **4** with sodium nitrite for three minutes to minimize the formation of products with multiple nitro groups.[19] This results in regiospecific nitration of the *para* position of the *meso* phenyl substituent to afford porphyrin **5**. The nitro group was then reduced to an amine using $SnCl_2$ in concentrated hydrochloric acid to give porphyrin **6** in 42% yield, based on the amount of **4** used in the initial nitration step. Additionally, complexes **Pd-4** and **Pd-6** have been prepared using microwave irradiation[11] in 94% and 75% yield, respectively.

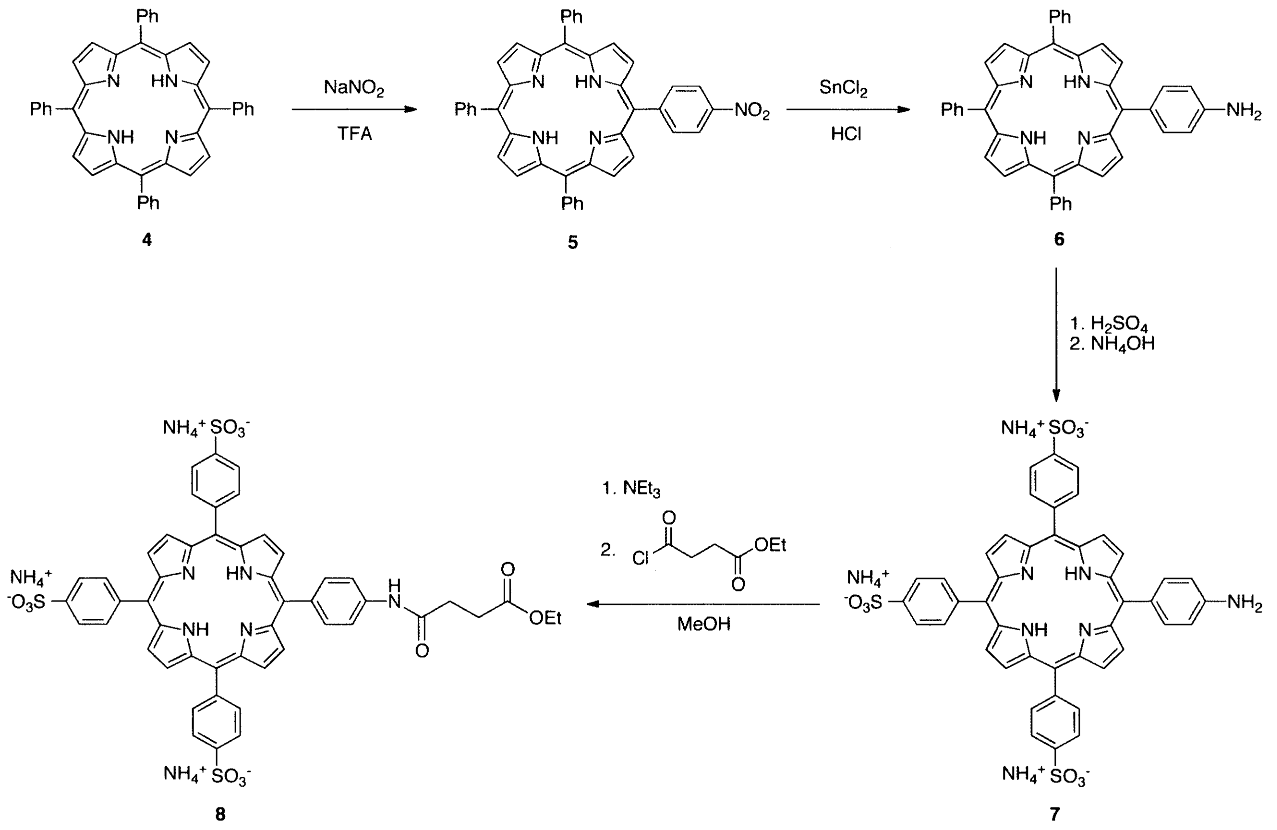

Scheme 2.3. Synthesis of A_3B porphyrins *via* the addition of a functional handle to H_2TPP (**4**) and subsequent sulfonation to afford water-soluble derivatives.

After the incorporation of an amine for quantum dot conjugation, porphyrin **6** was treated with refluxing sulfuric acid and subsequently neutralized with aqueous ammonia to give the sulfonate porphyrin **7** as the ammonium salt (Scheme 2.3). The ^1H NMR of compound **7** in CD_3OD is dominated by a broad resonances at $\delta = 8.84, 8.94$ that are attributed to the *β*-pyrrolic protons and a complex multiplet centered at $\delta = 8.27$ that is due to the aryl protons of the 4-sulfonatophenyl substituents. These features are not the well-resolved doublets that were expected based on literature reports.[15] Using the well-resolved doublets of the 4-aminophenyl substituent as an integration standard, both the *β*-pyrrolic and 4-sulfonatophenyl resonances integrate for more than the expected number of protons, suggesting that there are multiple products present in the sample. A broad singlet at δ 4.60 was identified as the amine protons, suggesting that this functional group was unchanged in the reaction. To make porphyrin **7** compatible with amine-functionalized quantum dots, the amino porphyrin was treated with ethyl 4-chloro-4-oxobutyrate to form an amide bond, giving porphyrin **8**. The terminal ethyl ester of this compound could then be hydrolyzed to give a carboxylic acid that is suitable for conjugation to PIL-coated QDs. The ^{1}H NMR of compound **8** in CD_3OD suggests that the coupling reaction was successful, due to the disappearance of the amine signal and the addition of four peaks attributed to the 3-(ethoxycarbonyl)propionylamido group. The integration of this moiety and the 4-aminophenyl doublets suggests that these two functional groups are present in a 1:1 ratio, suggesting complete conversion of the amine to the amide. However, the integration of both the *β*-pyrrolic and 4-sulfonatophenyl signals are inconsistent, indicating that multiple sulfonated porphyrins are present in the sample. The sulfonatino reaction was also performed on porphyrin **1**, which was treated in an identical manner to porphyrin **6** (Scheme 2.4). The ^{1}H NMR of compound **9** in CD_3OD indicates a loss of the methyl ester signal, indicating that the ester was hydrolyzed to the carboxylate during the course of the reaction. The only well-resolved features of the spectrum are the doublets of the 4-carbonylphenyl group at $\delta = 8.20, 8.37$. Signals attributed to the *β*-pyrrolic and 4-sulfonatophenyl appear as a very broad singlet ($\delta = 8.63$–9.17) and a complex multiplet ($\delta = 8.27$), respectively, instead of the expected series of doublets. As observed for compound **7**, the integration of these signals does not correspond to the appropriate number of protons based on the integration of the well-resolved doublets, suggesting that there are multiple species present in the sample. Based on these observations, it is clear that the harsh reaction conditions for sulfonation result in the formation of several sulfonated products; the reaction is indiscriminate and is not as selective as literature reports have indicated.[15–18]

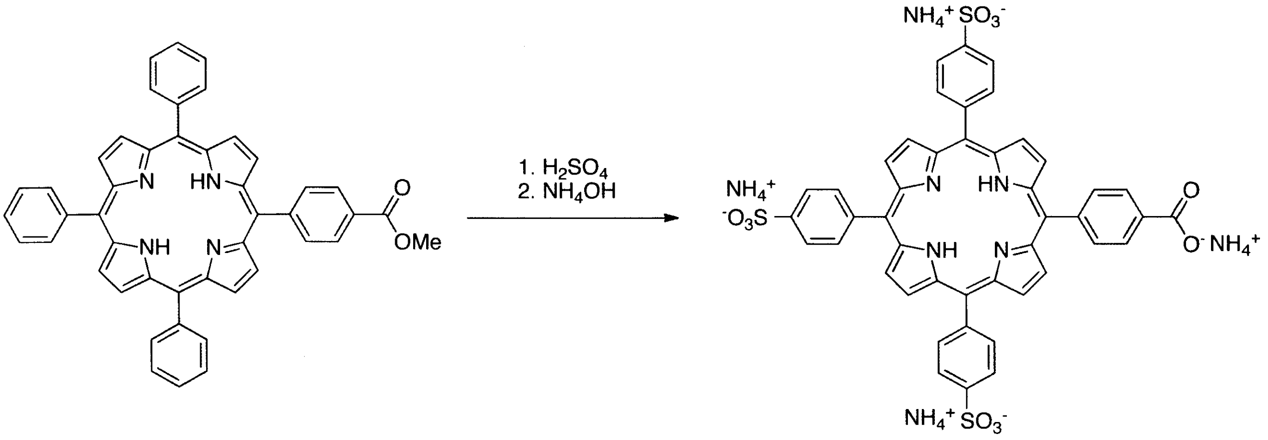

1 **9**

Scheme 2.4. Synthesis of a water-soluble A_3B porphyrin *via* sulfonation of **1**.

Since the synthesis of sulfonated porphyrins proved to be a challenge, an alternative approach to synthesizing water-soluble porphyrins is necessary. Porphyrins bearing pyridyl substituents offer an alternative to sulfonate groups, as these moieties can subsequently be N-alkylated to confer water solubility. Since this reaction is nearly quantitative and can be performed in the last synthetic step, difficult chromatographic separations of water-soluble compounds is avoided, making the route to clean products much easier than in the case of sulfonated porphyrins **7–9**.

To this end, the synthetic target is porphyrin **10**, which features three 4-pyridyl substituents that can be N-alkylated for water-solubility and a 4-methoxycarbonylphenyl group which can be hydrolyzed to the carboxylic acid for conjugation to an amine-functionalized QD. Initially, a mixed aldehyde condensation under standard Lindsey conditions[9] was attempted, as this synthesis is well-known and works for a wide variety of *meso* substituents. However, in the attempted synthesis of **10**, only an insoluble black material was obtained, likely due to the formation of polypyrrolic species. In an attempt to avoid these side reactions, a mixed aldehyde/dipyrromethane condensation[20] of 5-(4-pyridyl)dipyrromethane, 4-

pyridinecarboxaldehyde, and methyl 4-formylbenzoate was performed under Lindsey conditions; no macrocyclic products were identified in this reaction. The failure of these reactions is presumably due to coordination of $BF_3•OEt_2$ to the nitrogen of a pyridyl ring, thereby sequestering the Lewis acid catalyst. Literature reports[21–24] for the preparation of **10** employ Adler-Longo[7,8] conditions (Scheme 2.5) in refluxing propionic acid. While this method is synthetically facile, this protocol suffers from difficult and repetitive chromatographic separations as all six possible porphyrin isomers (A_4, A_3B, *cis*-A_2B_2, *trans*-A_2B_2, AB_3, and B_4) are formed in addition to other tetrapyrrolic products, resulting in low yields (4.3–5.9 %)[21–24] of the target A_3B product.

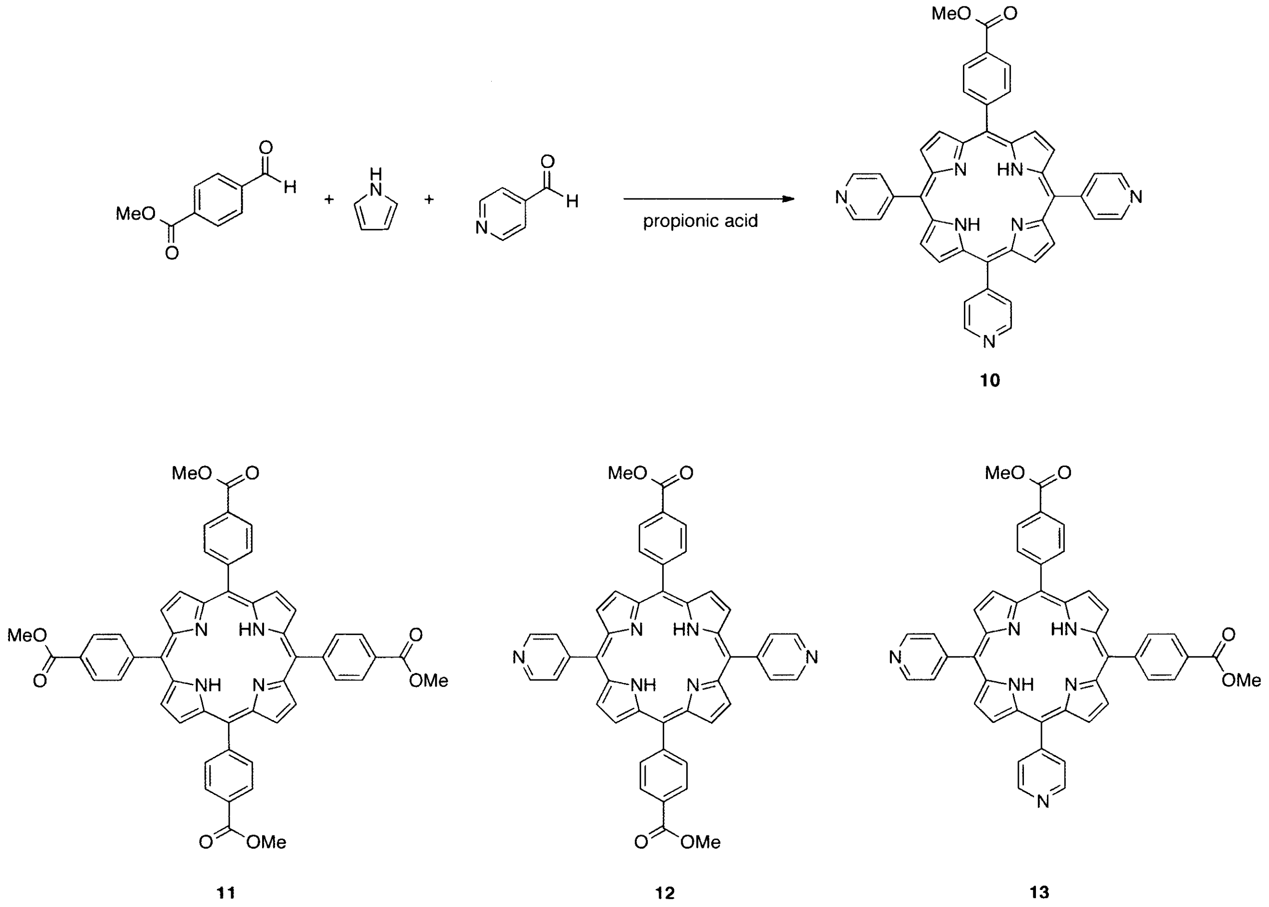

Scheme 2.5. Statistical synthesis of porphyrin **10** under Adler-Longo conditions; compounds **11**–**13** were identified as the other major porphyrin isomers isolated from this reaction.

Following this literature precedent, porphyrin **10** was prepared under Adler-Longo conditions, purified using a series of three chromatography steps, and isolated in 3.9% yield. In addition to the porphyrin producs, which display red fluorescence, products that exhibit green or blue fluorescence were also observed. Porphyrins **11** (B_4), **12** (*trans*-A_2B_2), and **13** (*cis*-A_2B_2) were isolated as the major porphyrin byproducts of this reaction. The symmetric A_4 porphyrin 5,10,15,20-tetraks(4-pyridyl)porphyrin was also formed during the course of the reaction, but this product is so polar that it remained at the top of the column and was not isolated. While compounds **12** and **13** display nearly identical ^{1}H NMR spectra, these compounds were differentiated on the basis of their polarity; compound **12** eluted with a 1:1 mixture of CH_2Cl_2 and EtOAc while compiund **13** eluted with 10% MeOH in EtOAc. This difference in polarity was compared to a literature report in which these two isomers were unambiguously differentiated using Ru(CO)(TPP) as a chemical shift reagent.[23] In an effort to increase the yield of porphyrin **10** under statistical conditions, the reaction was performed in a 1:1 mixture of toluene and propionic acid and the reagents were slowly added as toluene solutions to the refluxing reaction mixture. Although these modifications increase the yield from 3.9% to 5.8%, several chromatograph steps were necessary to obtain pure product.

2.3 Semi-Rational and Rational Porphyrin Synthesis

An alternative to statistical methods is rational porphyrin synthesis, which involves the synthesis of a linear tetrapyrrole (*i.e.* bilane) that is cyclized and subsequently oxidized to afford the corresponding porphyrin.[25,26] This method has the advantage of forming a single porphyrin product, thereby circumventing difficult chromatographic separations. It also allows for the synthesis of porphyrin isomers that are difficult to isolate or differentiate under statistical conditions (*e.g.* *cis*-A_2B_2 versus *trans*-A_2B_2). Additionally, up to four different *meso* substituents can be incorporated, enabling the formation of precise porphyrin isomers that are inaccessible with statistical methods (*e.g.* *cis*-A_2BC and ABCD). Many of the early steps (synthesis of dipyrromethanes and Mukaiyama reagents) can be performed on a multi-gram scale and employ crystallization rather than chromatography as the primary means of purification. Many of the later steps are very efficient and are performed *in situ* to minimize difficult chromatographic separations.

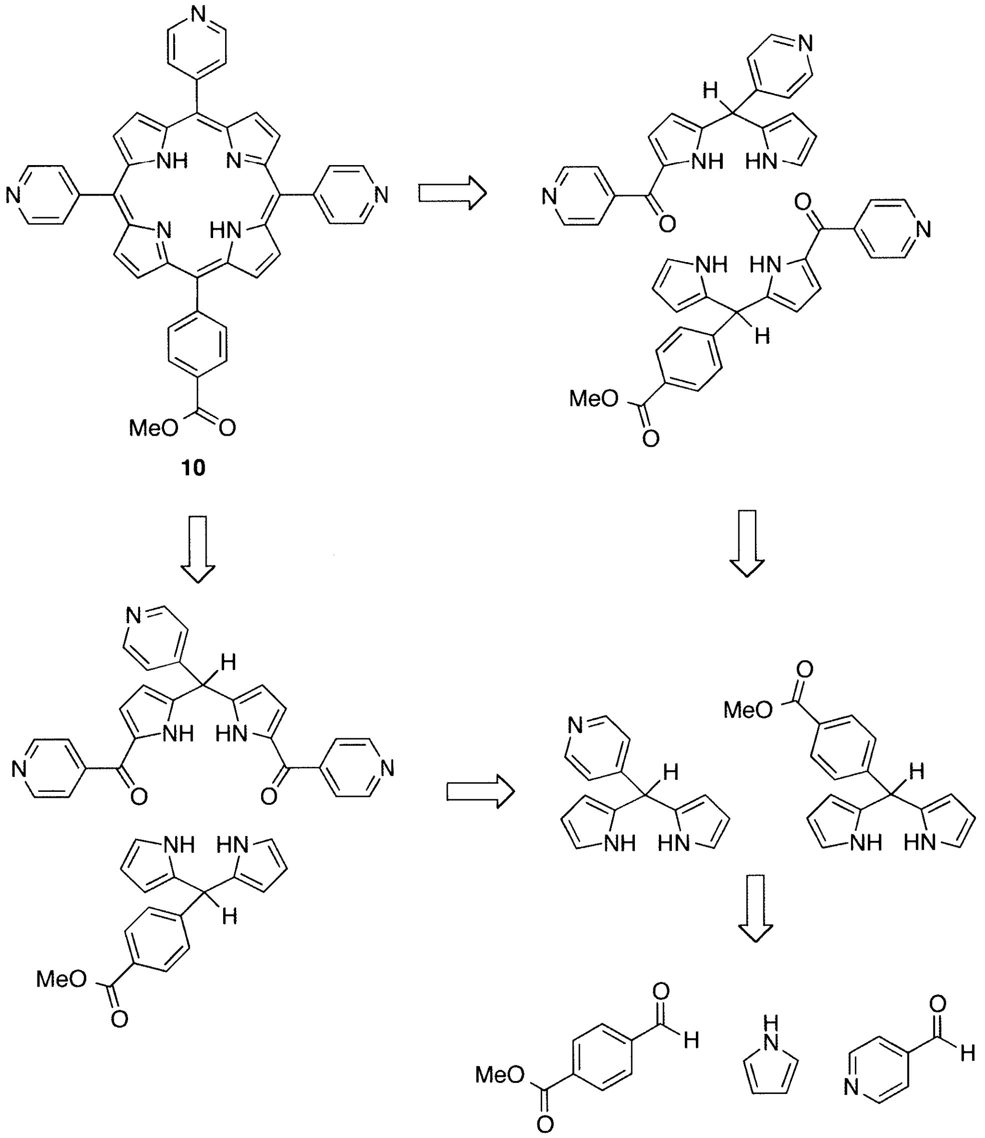

Scheme 2.6. Retrosynthetic analysis of compound **10**, outlining different synthetic routes that can be exploited in the rational synthesis of porphyrins.

In order to devise a synthetic route for the preparation of pyridyl porphyrins, exemplified by compound **10**, a retrosynthetic analysis of this compound was performed (Scheme 2.6). One approach involves the condensation of two 1-acyldipyrromethanes, compounds which are equivalent to one half of a porphyrin. Such a [2+2] cycloaddition is a statistical reaction, as self-condensations are also possible to form both the A_4 and *trans*-A_2B_2 isomers in addition to the desired A_3B porphyrin. To form a single porphyrin species, two 1-acyldipyrromethanes could be condensed to form a linear species (bilane) that is subsequently cyclized to form the porphyrin. Alternatively, the porphyrin may be formed by a [2+2] cycloaddition between a 1,9-diacyldipyrromethane (two pyrrole units and three *meso* carbons) and a dipyrromethane. In either case, these precursors are prepared from dipyrromethanes, which in turn are prepared from commercially available reagents: aryl aldehydes and pyrrole. Each of these synthetic methodologies is presented below.

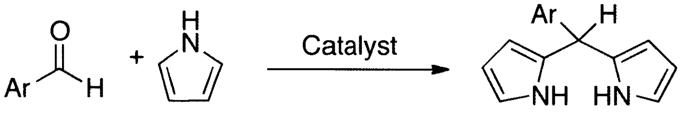

Table 2.1. Synthesis of 5-Aryl Dipyrromethanes

Compound	Ar	Catalyst	Yield
14	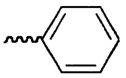	$InCl_3$	89%
15	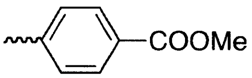	$InCl_3$	63%
16	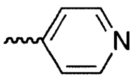	Heat	51%
17	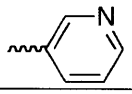	Heat	51%
18	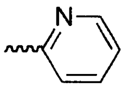	Heat	24%

First, dipyrromethanes were prepared from a condensation reaction between pyrrole and an aryl aldehyde (Table 2.1). Compounds bearing a heteroaryl substituent (**16**–**18**) were heated to promote the reaction[27] whereas $InCl_3$ was used as the catalyst in the case of the phenyl and 4-methoxycarbonylphenyl substituents.[28,29] These last two compounds were purified by crystallization, whereas the forcing conditions necessary to prepare the heteroaryl compounds required chromatography. After chromatography, it was found that compound **18** readily crystallized from CH_2Cl_2, yielding crystals that were suitable for x-ray diffraction. The solid state structure of the compound is presented in Figure 2.1 and the crystallographic data is summarized in Table 2.2.

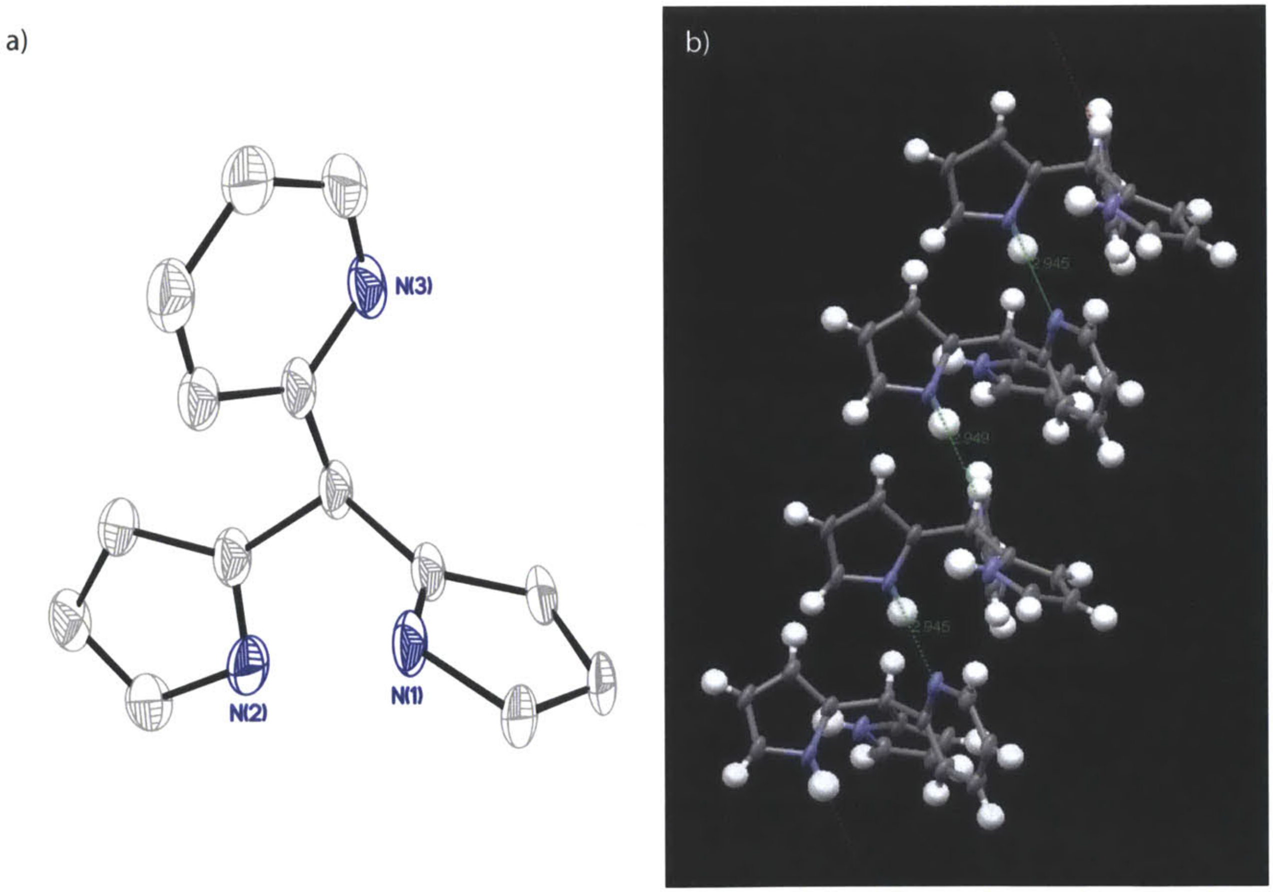

Figure 2.1. a) Solid-state structure of compound **18**. Thermal ellipsoids are drawn at the 50% probability level and hydrogen atoms have been removed for clarity. b) Solid-state packing of **18** in infinite chains *via* hydrogen bonding, as viewed down the crystallographic c^* axis.

Table 2.2. Summary of Crystallographic Data for **18**

	18
Formula	$C_{14}H_{13}N_3$
Formula weight (g/mol)	223.27
Temperature (K)	100(2)
Crystal System	Triclinic
Space Group	$P\bar{1}$
Color	Tan
a (Å)	9.148(2)
b (Å)	9.812(2)
c (Å)	14.070(3)
α (°)	90.28(3)
β (°)	105.32(3)
γ (°)	108.23(3)
V (Å^3)	1151.6(4)
Z	4
No. Reflections	11797
No. Unique Reflections	3289
R_{int}	0.0771
$R1^a$ (all data)	0.0997
$wR2^b$ (all data)	0.2013
$R1$ [(I > 2σ)]	0.0712
$wR2$ [(I > 2σ)]	0.1766
GOF^c	1.056

$^a R1 = (\Sigma||F_o| - |F_c||)/\Sigma|F_o|$, $^b wR2 = [\Sigma w(F_o^2 - F_c^2)^2/\Sigma wF_o^2]^{1/2}$, ^{c} GOF $= [\Sigma w(F_o^2 - F_c^2)^2/(n-p)]^{1/2}$, where n is the number of independent reflections and p is the number of refined parameters

The molecule crystallizes in the triclinic space group $P\bar{1}$ with unit cell parameters nearly identical to those previously reported.[30] The solid-state structure shows that the molecule packs in an infinite chain *via* hydrogen bonding interactions between the pyridyl group of one molecule and the pyrrole ring of an adjacent molecule, with N–H···N distances of 2.945 and 2.949 Å.

In order to synthesize the 1-acyldipyrromethanes identified in the retrosynthetic analysis (Scheme 2.6), the dipyrromethanes (**14**–**18**) must be acylated. To this end, *S*-2-pyridyl thioates, also known as Mukaiyama reagents, were used as the acylating reagent, as these provide cleaner reactions than using an aryl acid chloride directly.[31] These compounds (Table 2.3) were prepared from 2-mercaptopyridine and an aryl acid chloride; purification was accomplished by filtration and extraction rather than chromatography.[32]

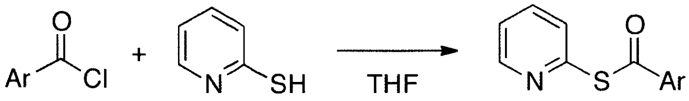

Table 2.3. Synthesis of *S*-2-Pyridyl Thioates (Mukaiyama Reagents)

Compound	Ar	Yield
19	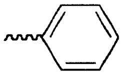	56%
20	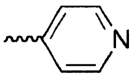	60%
21	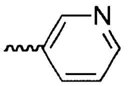	37%
22	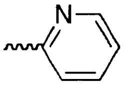	66%

To prepare the 1-acyl dipyrromethanes (Table 2.4), a dipyrromethane is first treated with ethyl magnesium bromide (EtMgBr) to protect the N-pyrrolic protons from acylation.[31,32] Instead of adding the Mukaiyama reagent to the dipyrromethane as a solution, it was added as a solid in one portion. This new procedural modification resulted in overall cleaner reactions. Only three products were observed by TLC upon bromine staining: unreacted dipyrromethane (pink), 1-acyldipyrromethane (yellow-orange), and 1,9-diacyldipyrromethane (brown). This modification resulted in higher yields for compounds **26** and **28** than literature reports; they were isolated in

61% and 60% yield, respectively, whereas the literature report yields are 34% and 29%, respectively.[32]

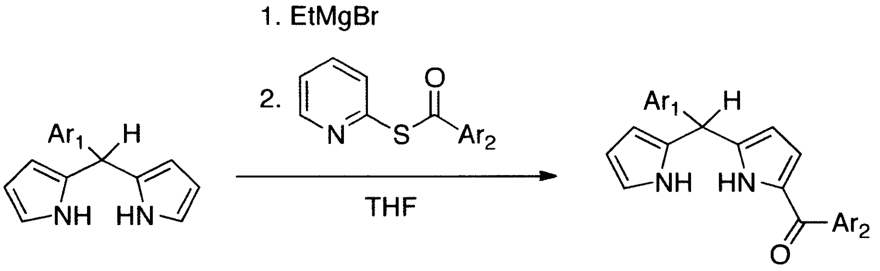

Table 2.4. Synthesis of 1-Acyl Dipyrromethanes

Compound	Ar1	Ar2	Yield
23	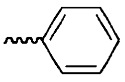	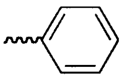	11%
24	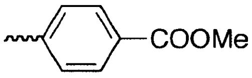	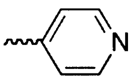	65%
25	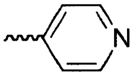	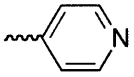	30%
26	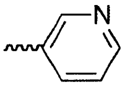	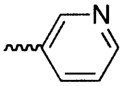	61%
27	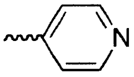	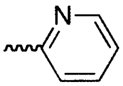	39%
28	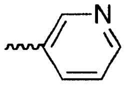	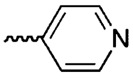	60%
29	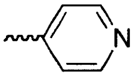	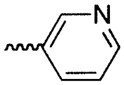	35%
30	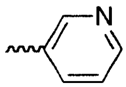	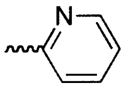	35%
31	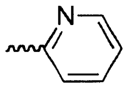	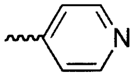	19%

Since these compounds are rather polar, one way to facilitate their purification is through the formation of a dialkyl boron complex with 9-borabicyclo[3.3.1]nonane (9-BBN).[33] The addition of alkyl chains and the masking of the carbonyl should drastically reduce the polarity of the molecule and minimize the time it takes to purify the compound. A crude solution of **25** was treated with 9-BBN-OTf in an attempt to make the boron complex **25-9BBN** (Scheme 2.7). However, only decomposition products were identified by TLC. It is likely that the presence of pyridyl substitutents sequestered the 9-BBN and subsequently promoted decomposition pathways in the crude reaction mixture.

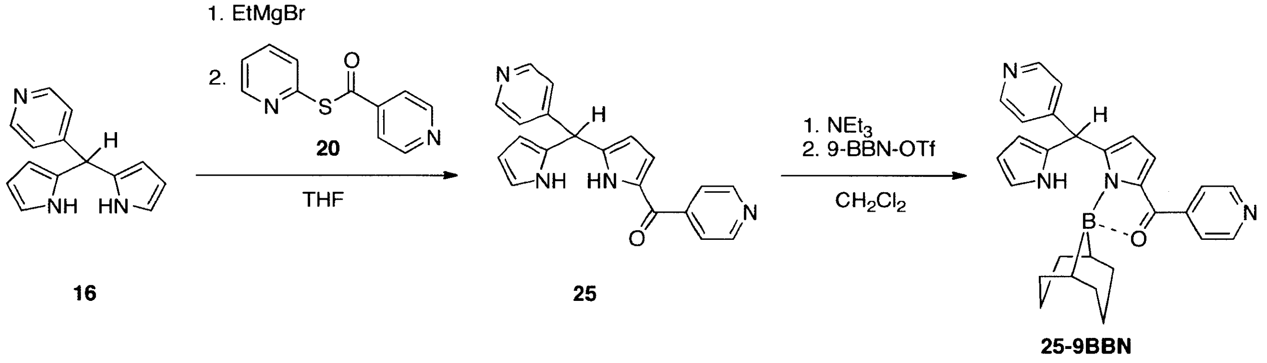

Scheme 2.7. Preparation of the 1-acyldipyrromethane **25** and attempted *in situ* formation of the 9-BBN complex to facilitate chromatography.

With the 1-acyldipyrromethanes in hand, these compounds were used directly in a metal-mediated [2+2] condensation under microwave irradiation. In this reaction, the 1-acyldipyrromethanes are treated with $MgBr_2$ and DBU in toluene (Table 2.5).[32] It is postulated that magnesium(II) cations serve as a template to bring the two halves of the porphyrin together and facilitate cyclization. Since this reaction is performed in aerobic conditions, it is believed that oxygen may serve as the oxidant to afford the magnesium(II) porphyrin complex. This species was then demetallated with TFA and subsequently neutralized with NEt_3 to give the free-base porphyrin in good yield. It should be noted that this reaction is still statistical, giving rise to three porphyrin isomers (*trans*-A_2B_2, A_3B, and A_4 in the case of **10**). The term "semi-rational" may be appropriate, as only three of six possible porphyrin isomers with two different substitutents (A_4, A_3B, *cis*-A_2B_2, *trans*-A_2B_2, AB_3, and B_4) can be formed in the course of the reaction. In particular, this route is amenable to the synthesis of *cis*-A_2B_2 porphyrins such as **32** and **33** (Table 2.5) and the separation of the three porphyrin isomers in these cases is exceptionally facile, as these three species have drastically different polarities.

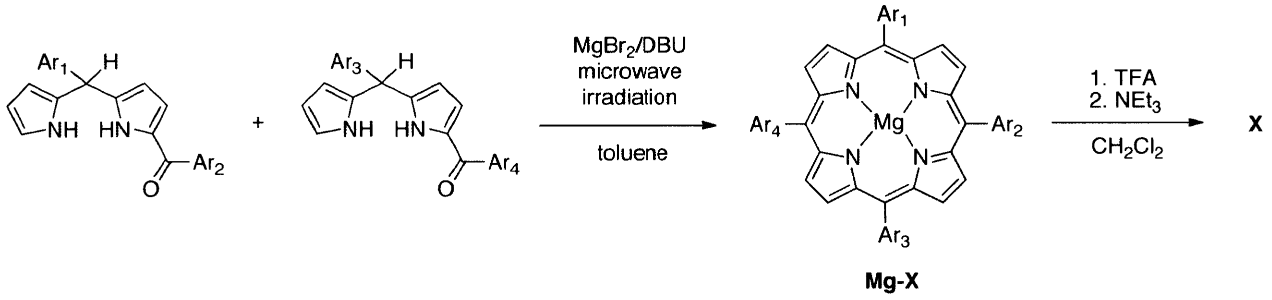

Table 2.5. Metal-Mediated [2+2] Porphyrin Synthesis Under Microwave Irradiation

Compound	Ar_1	Ar_2	Ar_3	Ar_4	Yield
10	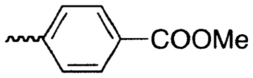	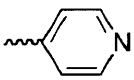	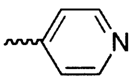	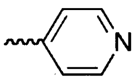	11%
32	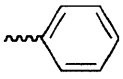	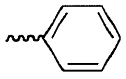	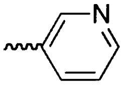	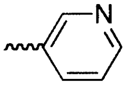	24%
33	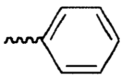	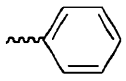	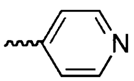	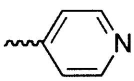	23%*

* Isolated as the Mg(II) complex

This methodology provides sufficient quantities of free-base porphyrins to prepare various metal complexes. Using the aforementioned microwave-mediated metal insertion protocol,[11] the following complexes have been prepared: **Pd-10** (50% yield), **Pt-10** (42% yield), **Pd-32** (32% yield), and **Pd-33** (40% yield). The yields of these reactions are markedly lower than the previously discussed metal insertion reactions. Indeed, the yields of **Pd-1** and **Pt-1** were 99% and 66%, respectively. The low yields for the complexes with *meso*-pyridyl substituents is attributed to the formation of insoluble coordination oligomers in which the metal coordinates to pyridyl groups of two different porphyrins. Such a coordination motif is precedented in the literature.[34–37]

As outlined in the retrosynthetic analysis of Scheme 2.6, the reaction between a 1,9-diacyldipyrromethane and a dipyrromethane is a viable method of porphyrin synthesis.[38] It should be noted that this is a completely rational synthesis, as the formation of only one porphyrin product is possible. While the preparation of 1,9-diacyldipyrromethanes is similar to the methods used for synthesizing 1-acyldipyrromethanes, there are a few key differences.[29] A bulky Grignard reagent, such as mesityl magnesium bromide, is used to favor the formation of the diacylated product over the monoacylated species. Additionally, an acid chloride is used directly as the acylating reagent. The synthesis of the 1,9-diacyldipyrromethane **34** is presented in Scheme 2.8. The product was identified by TLC and continued elution of the column for several days primarily afforded the monoacylated species **25**. After drastically increasing the polarity of the solvent, **34** began to elute, but **25** was identified as the major product, as it co-eluted with compound **34**. Based on ^{1}H NMR, only a trace amount of the desired product was obtained, as the spectrum was dominated by signals from **25**. In an effort to facilitate purification of **34**, an attempt was made to prepare the dibutyltin(IV) complex of the compound.[39] This is analogous to the formation of alkylboron complexes to simplify the purification of 1-acyldipyrromethanes. A crude solution of **34** was treated with Bu_2SnCl_2 in an attempt to make the tin complex **Sn-34** (Scheme 2.8). However, only decomposition products were identified by TLC. It is likely that the presence of pyridyl substitutents sequestered the Bu_2SnCl_2 and subsequently promoted decomposition pathways in the crude reaction mixture.

Although the preparation of **10** was not viable using this method, it remains a useful protocol for the synthesis of A_3B porphyrins bearing a single pyridyl substituent.[27] To this end, the 1,9-diacyldipyrromethane **35** was prepared from **14** and benzoyl chloride in 20% yield (Scheme 2.9). Prior to the porphyrin-forming reaction, compound **35** was reduced to the corresponding dicarbinol **36**. Since this intermediate is not very stable, the crude solution of **36** was treated with **16** to give porphyrin **37** *via* a [2+2] cycloaddition in which Yb(OTf)$_3$ served as the acid catalyst. The literature preparation of compound **37**,[27] used TFA as the acid catalyst to give the compound in 3.9% yield, whereas the use of Yb(OTf)$_3$ dramatically increases the yield to 24%.

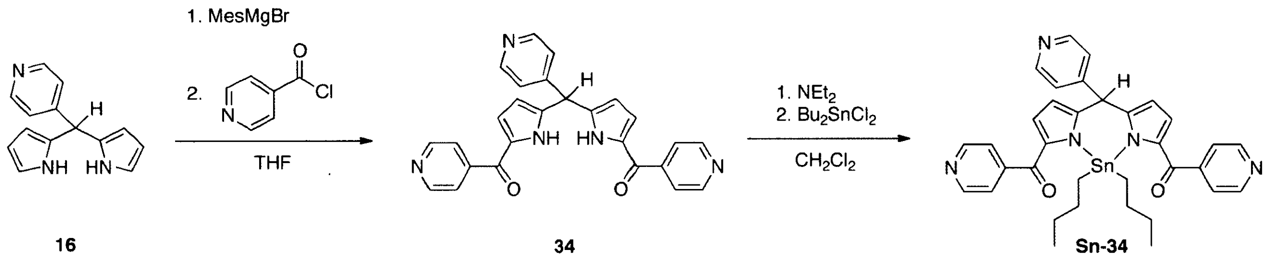
1. MesMgBr
2.
Cl
THF
16
34
1. NEt$_2$
2. Bu$_2$SnCl$_2$
CH$_2$Cl$_2$
Sn-34

Scheme 2.8. Preparation of the 1,9-diacyldipyrromethane **34** and attempted *in situ* formation of the tin complex to facilitate chromatography.

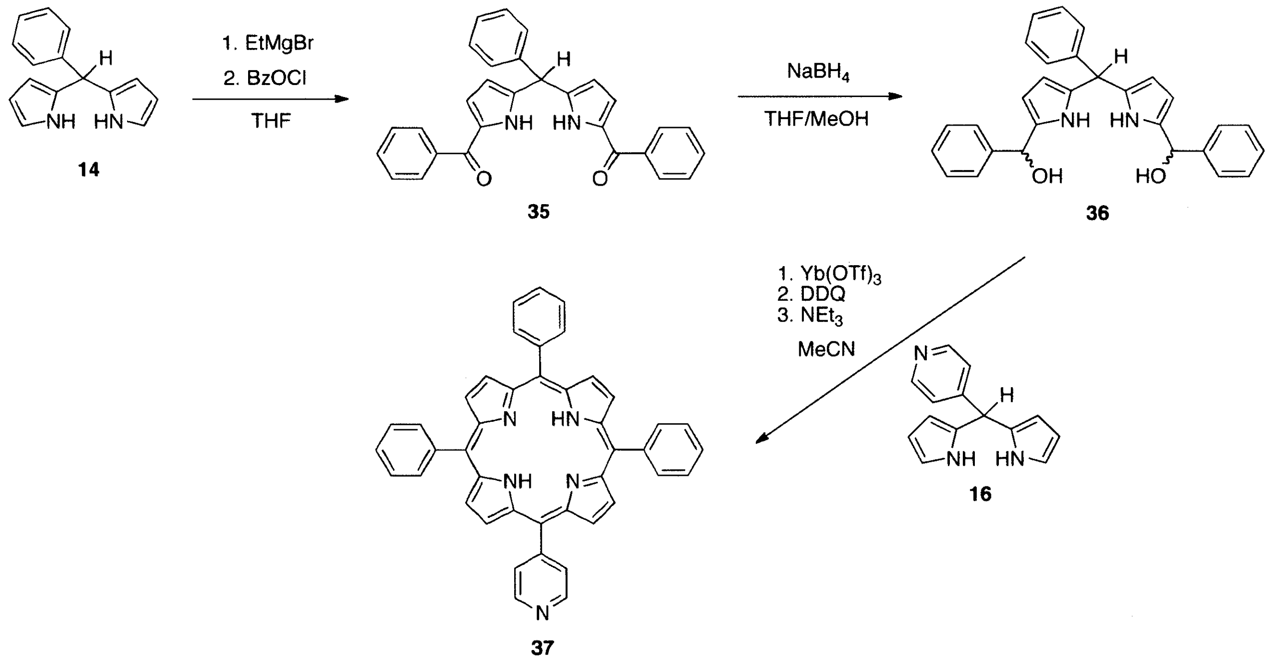
14
1. EtMgBr
2. BzOCl
THF
35
NaBH$_4$
THF/MeOH
36
1. Yb(OTf)$_3$
2. DDQ
3. NEt$_3$
MeCN
16
37

Scheme 2.9. Preparation of the 1,9-diacyldipyrromethane **35** and subsequent condensation with **16** to form the A$_3$B porphyrin **37**.

Following the aforementioned microwave-mediated metal insertion protocol,[11] the palladium(II) complex **Pd-37** was prepared in 17% yield; the low yield is attributed to the formation of insoluble coordination oligomers (*vide supra*). Diffraction quality crystals of **Pd-37** were obtained *via* slow vapor diffusion of heptane into a toluene solution of the compound, affording the crystals as orange blocks. The thermal ellipsoid plot of the refined structure is illustrated in Figure 2.2 and a summary of the crystallographic data is of presented in Table 2.6.

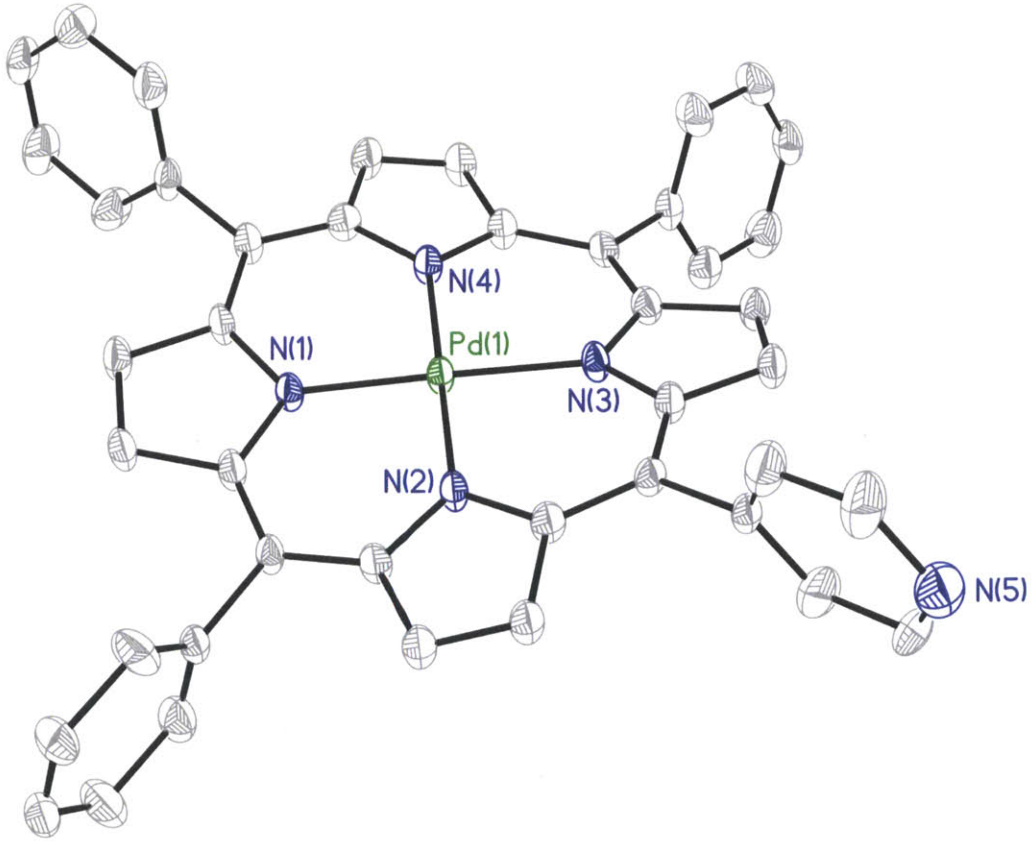

Figure 2.2. Solid-state structure of compound **Pd-37**. Thermal ellipsoids are drawn at the 50% probability level and hydrogen atoms have been removed for clarity.

In order to identify the unique 4-pyridyl group of the structure, the 4 position of each *meso* subsitutent was refined as a carbon atom and the resultant electronic density difference map was examined. The ten largest residual density peaks (Q peaks) of this refinement cycle are shown in

Figure 2.3. Three of the four *meso* substituents show a Q peak adjacent to the 4 position of the ring, indicating the presence of a hydrogen atom, while the fourth does not, thereby differentiating the 4-pyridyl ring from the phenyl rings. Qualitatively, the structure is very similar to other palladium porphyrin complexes, such as 5,10,15,20-tetrakis(4-carboxyphenyl) porphyrinatopalladium(II).[40] The palladium atom resides in the center of the mean 24 atom macrocycle plane with an average Pd–N distance of 2.011 Å (compare to 2.009 Å for TPP).[41] The porphyrin plane exhibits an S_4 ruffle with an average deviation of 0.196 Å from the mean 24 atom plane. Such non-planarity is also observed in the solid state structure of PdTPP. Each of the pyrrole nitrogen atoms deviates from the mean N_4 plane by 0.030 Å, a displacement that is identical to that observed for PdTPP.[41]

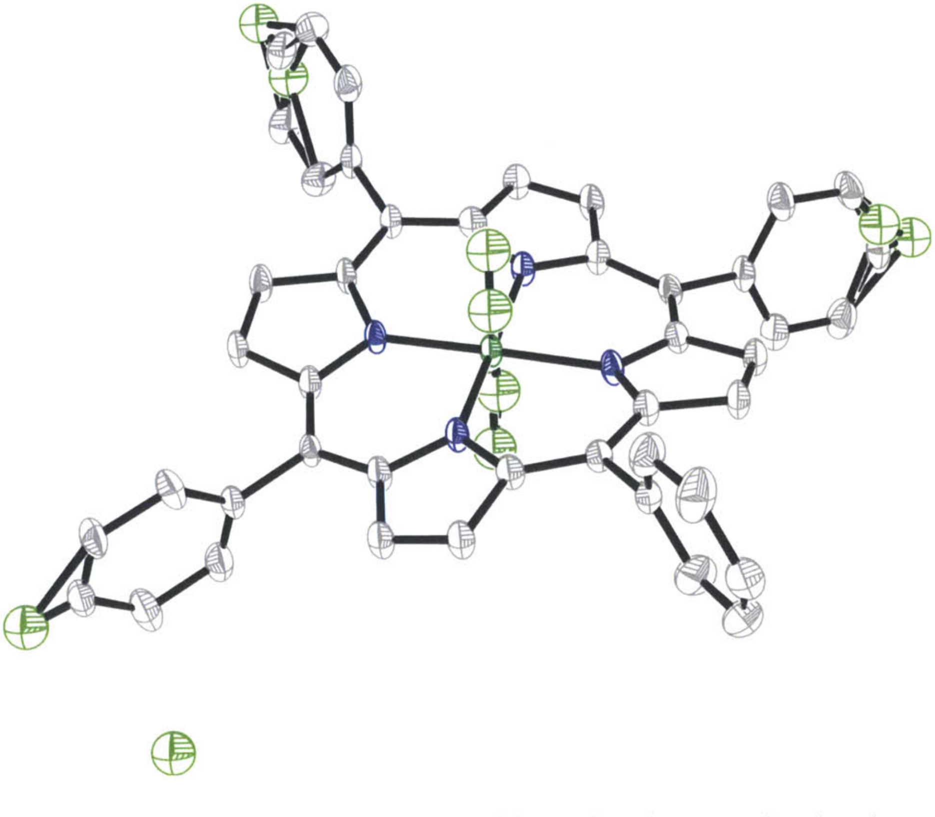

Figure 2.3. Illustration of **Pd-37** where the 4 position of each *meso* ring has been refined as a carbon atom. The ten largest residual density peaks (Q peaks) are shown as green spheres. Thermal ellipsoids are drawn at the 50% probability level and hydrogen atoms have been removed for clarity.

Table 2.6. Summary of Crystallographic Data for **Pd-37**

	Pd-37
Formula	$C_{43}H_{27}N_5Pd$
Formula weight (g/mol)	720.10
Temperature (K)	100(2)
Crystal System	Monoclinic
Space Group	Cc
Color	Orange
a (Å)	13.736(3)
b (Å)	21.167(3)
c (Å)	12.464(2)
α (°)	90
β (°)	121.980(4)
γ (°)	90
V (Å^3)	3074.1(10)
Z	4
No. Reflections	27676
No. Unique Reflections	7607
R_{int}	0.0602
$R1^a$ (all data)	0.0518
$wR2^b$ (all data)	0.1087
$R1$ [(I > 2σ)]	0.0425
$wR2$ [(I > 2σ)]	0.1021
GOF^c	1.127

^{a} $R1 = (\Sigma||F_o| - |F_c||)/\Sigma|F_o|$, ^{b} $wR2 = [\Sigma w(F_o^2 - F_c^2)^2/\Sigma wF_o^2]^{1/2}$, ^{c} $\text{GOF} = [\Sigma w(F_o^2 - F_c^2)^2/(n - p)]^{1/2}$, where n is the number of independent reflections and p is the number of refined parameters

An alternative to a [2+2] condensation of a 1,9-diacyldipyrromethane and a dipyrromethane is the formation and subsequent cyclization of a linear tetrapyrrole, known as a bilane (Scheme 2.10).[25,26] The bilane is prepared from the condensation of two 1-acyldipyrromethanes. However, one of these reactants must be protected with an α-bromide to prevent self-condensation so that this method yields a single porphyrin product. Regioselective

α-bromination of compound **25** was accomplished using *N*-bromosuccinide to afford the 1-bromo-9-acyldipyrromethane **38**.

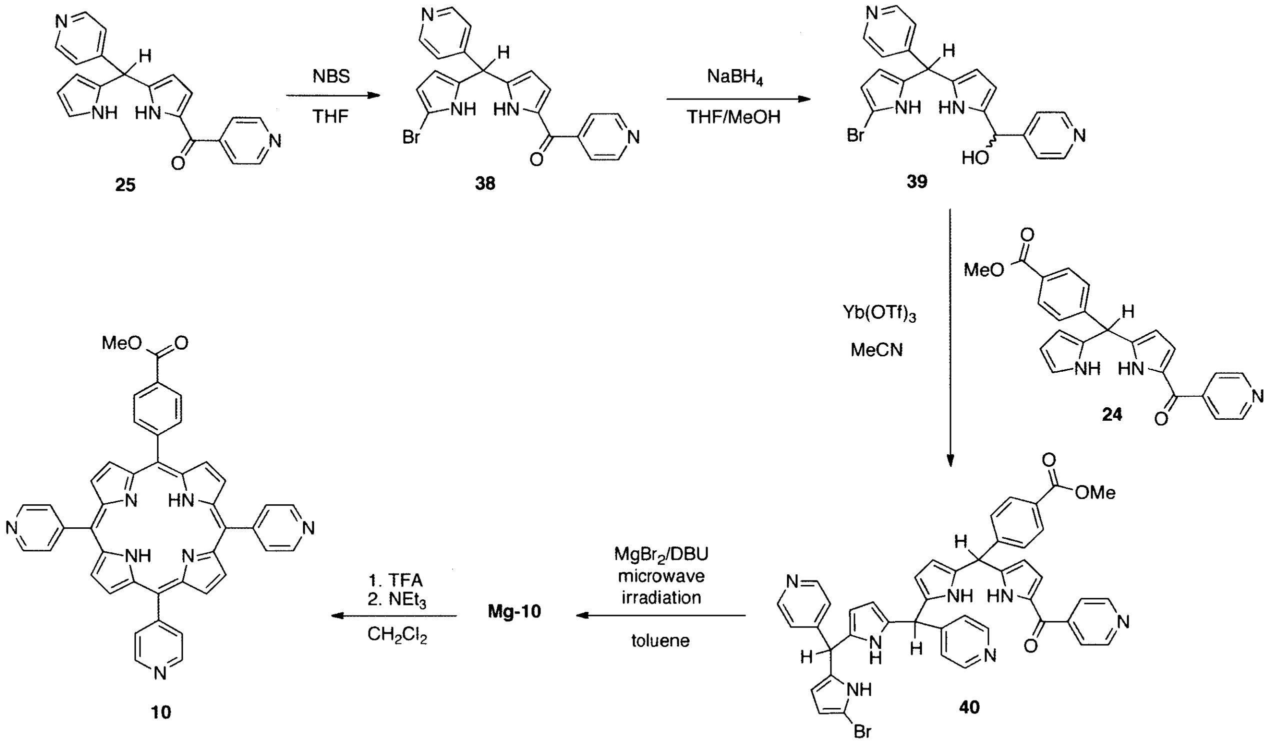
25
NBS
THF
38
NaBH4
THF/MeOH
39
Yb(OTf)3
MeCN
24
40
MgBr2/DBU
microwave
irradiation
toluene
Mg-10
1. TFA
2. NEt3
CH2Cl2
10

Scheme 2.10. Preparation of bilane **40** and subsequent cyclization under microwave irradiation to afford porphyrin **10**.

This compound is rather heat and light sensitive, although it is stable if stored at 4 °C protected from ambient light. Compound **38** was subsequently treated with $NaBH_4$ to give the corresponding carbinol **39**. Since carbinols are rather unstable, a crude solution of **39** was treated with another 1-acyldipyrromethane in a ytterbium(III)-catalyzed condensation reaction to furnish bilane **40**.[25] A large excess of $Yb(OTf)_3$ was used since the metal can coordinate to the peripheral pyridyl substituents and sequester the catalyst. TLC indicated that the reactants had been consumed and only a single spot was visible, suggesting that the crude bilane could be used without further purification. This molecule is larger and more polar than the 1,9-

diacyldipyrromethane **34**, suggesting that column chromatography of **40** would be rather difficult. The crude bilane **40** was treated with DBU and $MgBr_2$ in toluene and subjected to microwave irradiation.[26] The Lewis acid catalyst is used for metal-mediated oxidative cyclization to give the magnesium complex **Mg-10**, which was readily demetallated with TFA to give the free-base porphyrin **10** in 15% yield, based on the amount of **38** used to prepare the bilane **40**.

2.4 Water Solubilization of Pyridyl Porphyrins

Having explored several synthetic routes to pyridyl porphyrins, only two synthetic steps remain to furnish water-soluble metalloporphyrins appropriately functionalized for conjugation to quantum dots: ester hydrolysis[12] and alkylation.[32] Using the preparation of **M-3** from **M-1** as a benchmark, basic hydrolysis of **Pd-10** under microwave irradiation was performed to afford the carboxylic acid derivative **Pd-41** (Scheme 2.11). The crude reaction mixture was then treated with iodomethane to methylate the pyridyl rings, giving the water-soluble derivative **Pd-42**. However, the acidic workup of the hydrolysis reaction protonated the pyridyl rings, preventing alkylation. Indeed, the reaction mixture from the attempted preparation of **Pd-42** was soluble in CH_2Cl_2.

To circumvent this limitation, alkylation of the free-base was performed to give the water-soluble derivative **43**. The advantage to this method is that both metallation and hydrolysis reactions can then be performed in water. However, it was found that the methylation reaction was indiscriminate; the N-pyrrolic positions of the macrocycle were also methylated, thereby hindering subsequent metal insertion. However, in performing the hydrolysis reaction on the resultant species, it was found to be completely soluble in water and 6 M NaOH, enabling the hydrolysis reaction to be performed without the addition of an organic solvent. This result indicates that the hydrolysis reaction should be the final synthetic step.

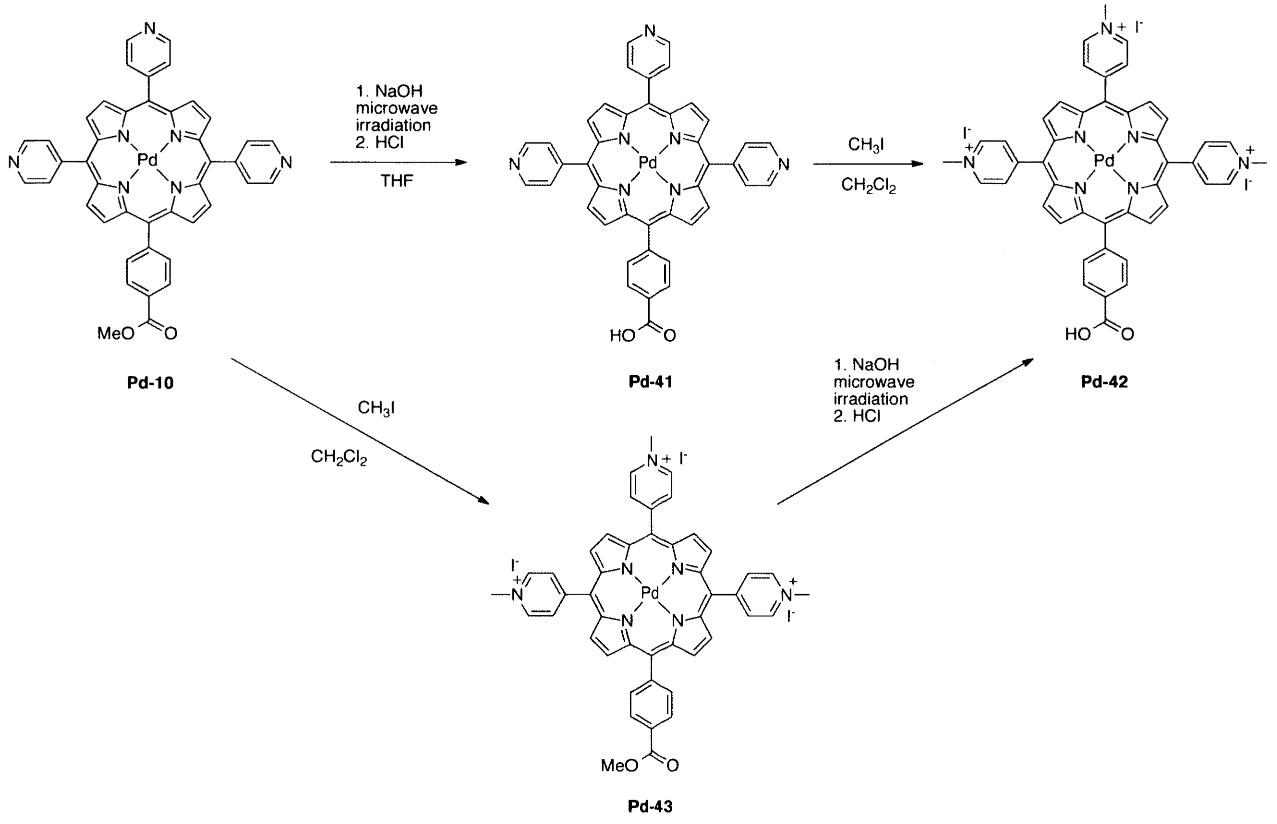
1. NaOH
microwave
irradiation
2. HCl
THF
CH_3I
CH_2Cl_2
CH_3I
CH_2Cl_2
1. NaOH
microwave
irradiation
2. HCl
Pd-10
Pd-41
Pd-42
Pd-43

Scheme 2.11. Preparation of water-soluble porphyrin derivatives of compound **Pd-10**.

To prevent methylation of the pyrrole nitrogen atoms, the zinc(II) complex **Zn-10** (Scheme 2.12) was prepared from $Zn(OAc)_2 \bullet 2H_2O$ in a mixture of CH_2Cl_2 (to solubilize the porphyrin) and MeOH (to solubilize the metal salt). Since zinc porphyrin complexes are readily demetallated under acidic conditions, zinc complexation serves as a means of protecting the macrocycle interior. This intermediate was then alkylated with iodomethane to give the water-soluble zinc complex **Zn-43**. Since this species is water soluble, it was treated with NaOH under microwave irradiation to hydrolyze the methyl ester; acidic workup demetalted the complex, giving the water-soluble free-base porphyrin **42**. Given this series of experiments, the optimal method of preparing the water soluble palladium complex **Pd-42** is alkylation of **Pd-10** to give **Pd-43** followed by ester hydrolysis of this intermediate (Scheme 2.11).

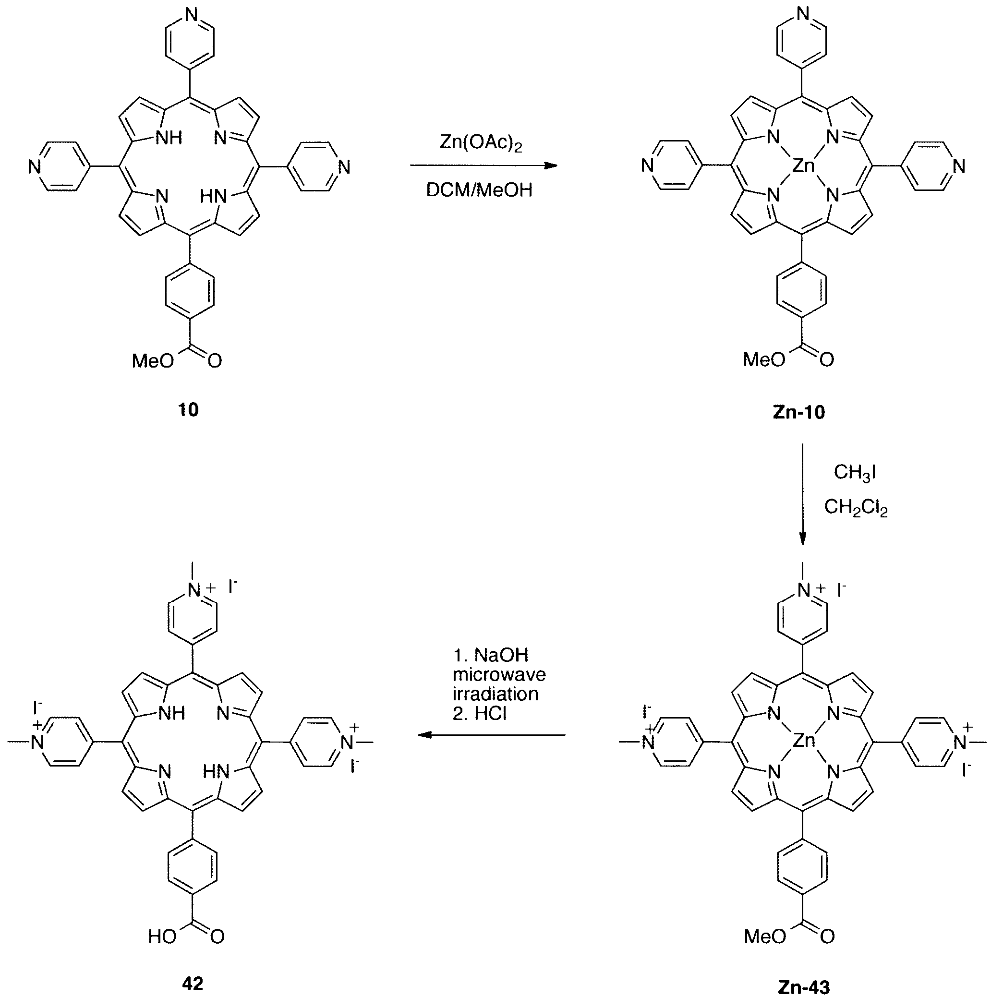

Scheme 2.12. Preparation of water-soluble porphyrin derivatives of compound **10** *via* a zinc(II) intermediate.

Photophysical studies of the methylated palladium species **Pd-42** and **Pd-43** indicate that the phosphorescence of these species is completely quenched, even after bubbling argon through the sample. This finding suggests that the iodide counterion acts as a bimolecular quencher to deactivate the electronic excited state of these molecules. To circumvent this problem, an alternative approach to N-alkylation is needed. It has been shown that pyridyl groups can be treated with 1,3-propanesultone to give a zwitterionic species bearing a sulfonate group as a result of the ring opening of the sultone.[42] Since such a species has an intramolecular counterion, bimolecular quenching of the excited state is avoided. To this end, compound **Pd-10** was treated with an excess of 1,3-propanesultone in benzene to afford the water-soluble zwitterionic porphyrin **Pd-44** in 91% yield (Scheme 2.13).

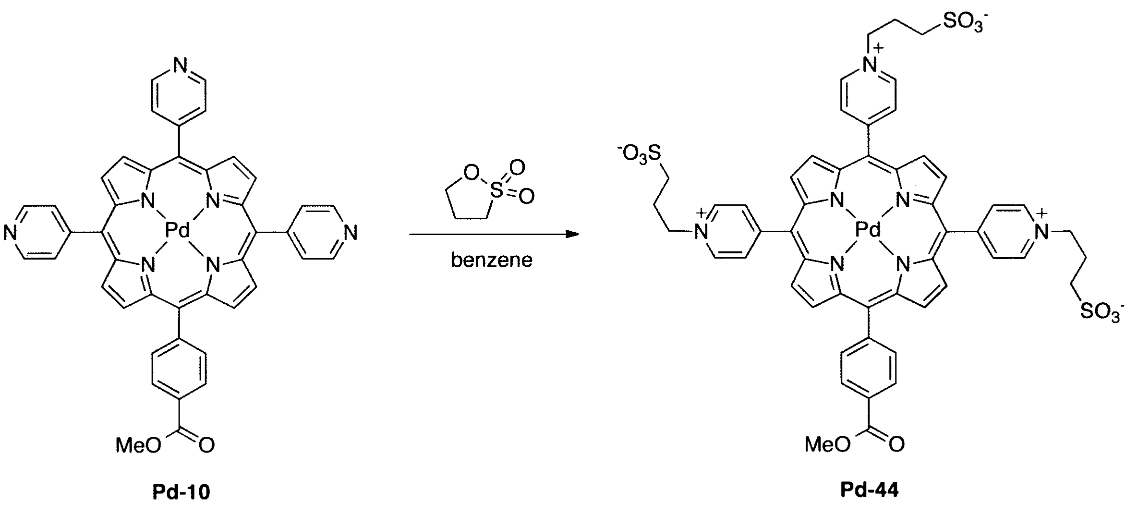

Scheme 2.13. Preparation of a zwitterionic water-soluble porphyrin **Pd-44**.

2.5 Porphyrins for *Tt* H-NOX

In addition to small molecules, protein scaffolds have been exploited for oxygen sensing. The H-NOX (heme nitric oxide/oxygen binding) domain from the thermophilic bacterium *Thermoanaerobacter tengcongensis* (*Tt* H-NOX) has been used for this purpose.[43] The unnatural porphyrin ruthenium(II) CO mesoporphyrin IX serves as the phosphor in this sensing application. However, the quantum yield of this construct is prohibitively low (1.7×10^{-4}). Additionally, the small difference in lifetime between aerated (2.9 μs) and evacuated (7.7 μs) samples limits the scope of the oxygen sensor, due to a restricted dynamic range.[43] One way to increase the quantum yield and enhance the dynamic range of the construct is to incorporate palladium and platinum porphyrins into the *Tt* H-NOX protein. To this end, palladium and platinum insertion of mesoporphyrin IX dimethyl ester (**45**) was accomplished as described above, using microwave irradiation to facilitate metallation (Scheme 2.14), giving the complexes **Pd-45** and **Pt-45** in 100% and 97% yield, respectively. Subsequent basic hydrolysis of the ester was accomplished using microwave irradiation to give the complexes **M-46** that can now be incorporated into the *Tt* H-NOX protein.

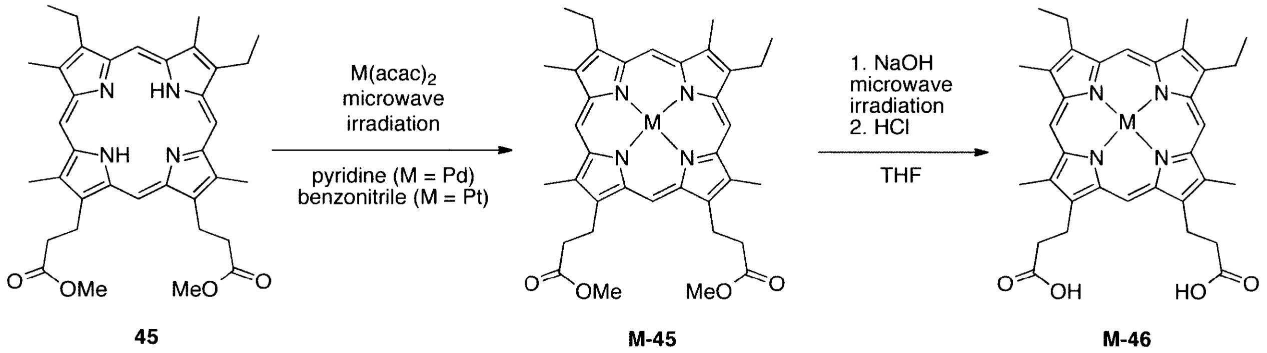

Scheme 2.14. Synthesis of palladium(II) and platinum(II) complexes of Mesoporphyrin IX dimethyl ester **45** and subsequent basic ester hydrolysis; both reactions are facilitated by microwave irradiation.

2.6 Discussion and Conclusions

In order to covalently append a porphyrin phosphor to a functionalized QD (see Chapter 1), an appropriate functional group must be incorporated into the porphyrin. Since the PIL-polymer features a terminal amine, the porphyrin features a carboxylic acid moiety to couple the phosphor to the polymer ligand *via* amide bond formation. A methyl ester, which serves as a protected carboxylic acid, is included in the porphyrin. This requires the preparation of asymmetric A_3B porphyrins because it was discovered that simple A_4 porphyrins with carboxylic acids induced aggregation, as this functional group formed cross-links to other QDs.[14]

To this end, an A_3B porphyrin with three phenyl groups and a single 4-methoxycarbonylphenyl substituent (**1**) was prepared under standard Lindsey conditions to give the target compound in good yield (~11%). Metallation, with either palladium(II) or platinum(II) salts, and subsequent ester hydrolysis reactions were facilitated by using microwave irradiation. In only three synthetic steps, phosphorescent porphyrins with an appropriate functional handle (**Pd-3** and **Pt-3**) were readily prepared in 6–7% overall yield, due to the enhanced efficiency of the last two reactions.

Unfortunately, the hydrophobic nature of these compounds prevented efficient conjugation to water-soluble quantum dots. Although attempts were made to couple **Pt-3** to the PIL ligand prior to quantum dot cap exchange (surface ligand exchange), this approach was met with limited success.[14] While this method confers water solubility to the porphyrin, the presence of the porphyrin hinders the subsequent cap exchange. To efficiently perform the conjugation reaction in aqueous media, water-soluble porphyrins are necessary. First, the incorporation of sulfonate groups was explored as a means of making these molecules water-soluble. The harsh reaction conditions (*i.e.* refluxing sulfuric acid) results in indiscriminate sulfonation that gives many inseparable products. This was corroborated by ^{1}H NMR spectroscopy in which the integration for both the β-pyrrole and 4-sulfonatophenyl protons was inconstant with the well-resolved 4-aminophenyl signals.

As an alternative to sulfonate groups, porphyrins bearing pyridyl substituents may be N-alkylated to afford water-soluble derivatives. Such alkylations are conducted under ambient conditions, thereby circumventing indiscriminate reactions like sulfonation; it can be performed in the final step to avoid difficult chromatographic separations. The preparation of the A_3B porphyrin with three phenyl groups and a single 4-methoxycarbonylphenyl substituent (**10**) could not be accomplished under standard Lindsey conditions. Both mixed aldehyde and aldehyde/dipyrromethane condensations were unsuccessful. Presumably, the Lewis acid catalyst BF_3•OEt_2 coordinates to the pyridyl nitrogen, thereby sequestering this reagent and preventing the condensation reaction from occurring. An alternative statistical methodology is the Adler-Longo method in which pyrrole and aryl aldehydes are condensed in refluxing propionic acid. While this methodology gave porphyrin **10** in ~4% yield, five other porphyrin isomers, in addition to other tetrapyrrolic macrocycles, were formed in the course of the reaction, thus requiring several chromatographic separations to obtain pure products. By making a few modifications (*i.e.* slow addition of reagents and using a toluene/propionic acid mixture as the solvent), the yield was increased to 6%.

Because of the low yield and multiple chromatographic separations, an alternative to the statistical synthesis of pyridyl porphyrins is necessary. Rational porphyrin synthesis allows for the synthesis of porphyrin isomers that are difficult to isolate under statistical conditions (*e.g.* *cis*-A_2B_2 versus *trans*-A_2B_2). Additionally, up to four different *meso* substituents can be incorporated, enabling the formation of precise porphyrin isomers that are inaccessible with statistical methods (*e.g.* *cis*-A_2BC and ABCD). Many of the early steps (synthesis of dipyrromethanes and Mukaiyama reagents) can be performed on a multi-gram scale and employ crystallization rather than chromatography as the primary means of purification. Many of the later steps are very efficient and are performed *in situ* to minimize difficult chromatographic separations.

To accomplish the rational synthesis of porphyrins, first dipyrromethanes are prepared from an aryl aldehyde and pyrrole. Next, these compounds are acylated using Mukaiyama reagents (*S*-2-pyridyl thioates) as the acylating reagent to give 1-acyldipyrromethanes. These compounds are the equivalent to one half of a porphyrin, bearing two pyrrole rings and two *meso* substituents. While formation of 9-BBN complexes of these compounds has been shown to facilitate purification of 1-acyldipyrromethanes, this reaction was unsuccessful with compounds bearing pyridyl substituents. Two different 1-acyldipyrromethanes can be used directly in a magnesium(II)-mediated [2+2] condensation reaction under microwave irradiation to give magnisum(II) porphyrin complexes. While this reaction is statistical, only three of six possible porphyrin isomers (two self-condensation products and one cross-condensation product) are formed in the course of the reaction. Thus, the term "semi-rational" may be an appropriate description of this reaction. In particular, this method is particularly convenient for the preparation of *cis*-A_2B_2 prophyrins, which are otherwise difficult to prepare or separate and differentiate from the *trans*-A_2B_2 isomer. While the conversion of 1-acyldipyrromethanes to porphyrins appears to be a straightforward reaction, there are many synthetic steps that are required to afford this transformation, although the order of these processes is unknown: formation of two C–C bonds, elimination of two molecules of water, dehydrogenation, and magnesium(II) complexation.[32] Additionally, the nature of the oxidant is unknown. While molecular oxygen is a likely species to serve this role, it has been shown the reaction proceeds under an argon atmosphere,[32] suggesting that DBU is a more likely oxidant. Using this methodology, compound **10** was prepared in 11% yield.

An alternative [2+2] condensation involves the use of a 1,9-diacyldipyrromethane (two pyrrole rings and three *meso* substituents) and a dipyrromethane to give the porphyrin. This route is completely rational, as only one porphyrin product may be formed during the course of the reaction. Due to the high polarity of the 1,9-diacyldipyrromethane with three 4-pyridyl substituents (**34**) pure product could not be obtained. To facilitate purification, *in situ* complexation with Bu_2SnCl_2 was attempted, although this reaction was unsuccessful, preventing the synthesis of compound **10** by this route.

Finally, the preparation of bilanes and their subsequent cyclization was explored as a means of preparing compound **10**. The bilane was prepared in a ytterbium(III)-catalyzed condensation between two 1-acyldipyrromethanes. However, one of the 1-acyldipyrromethanes was first subjected to a regioselective α-bromination to prevent self-condensation. Because the formation of the bilane was relatively clean and the molecule is highly polar, this intermediate was used directly in a magnesium(II)-mediated oxidative cyclization reaction under microwave irradiation to give porphyrin **10** in 15% yield, based on the amount of 1-bromo-9-acyldipyrromethane used in the preparation of the bilane. It should be noted that the bilane has three stereogenic centers, resulting in the formation of up to eight different stereoisomers of the bilane. Differences in reactivity of these species could account for the seemingly low yield of the porphyrin.[26]

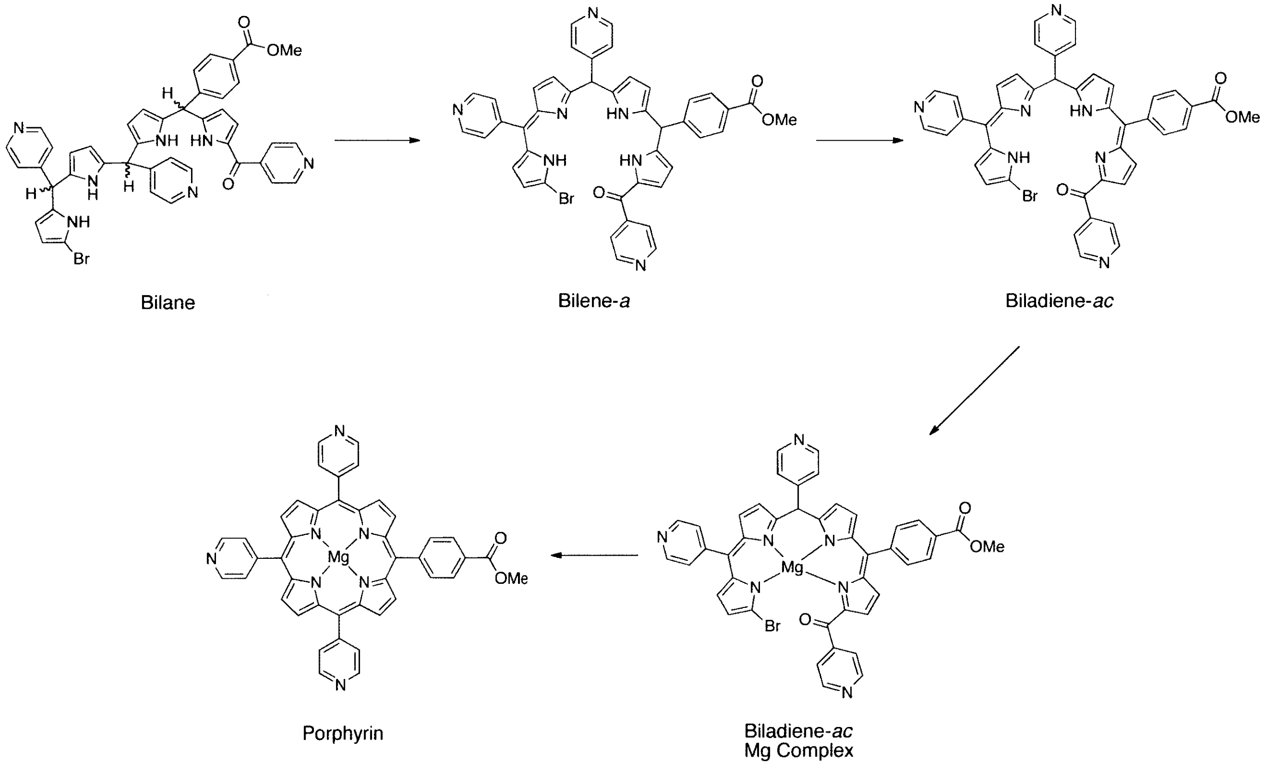

Scheme 2.15. Proposed reaction mechanism illustrating potential intermediates in the bilane to porphyrin conversion.

While this cyclization appears to be a straightforward reaction, there are many individual steps that are necessary to afford this transformation: C–C bond formation, elimination of one molecule of water, dehydrogenation, and magnesium(II) complexation. Experiments have been conducted to probe this reaction mechanism by performing some of these reactions in a stepwise manner.[25] Based on these results, Scheme 2.15 outlines a probable synthetic mechanism for this transformation. First, two reduction (dehydrogenation) steps are necessary to convert the bilane to a bilene-*a*, and subsequently a bilene-*ac*. Since this latter species is known to coordinate metal centers, magnesium(II) complexation is a likely next step. This then brings the two ends of the molecule is close proximity to facilitate cyclization and subsequent oxidation steps to give the porphyrin.

After surveying the various synthetic methods of preparing porphyrin **10**, it is concluded that the microwave-mediated [2+2] condensation of 1-acyldipyrromethanes is the most efficient synthetic route. This method gives the porphyrin in greater yield than statistical routes and circumvents the need for many chromatographic separations, as required for the purification of the porphyrin from Adler-Longo statistical routes. While the bilane route gives a nominally higher yield for the porphyrin forming reaction over the [2+2] condensation, it requires three additional synthetic steps. Having prepared various porphyrins with *meso*-pyridyl substituents, photophysical studies of these molecules and their interactions with QDs will be presented in Chapter 3.

With the pyridyl porphyrins in hand, studies to convert them to water-soluble derivatives were conducted. Three steps were necessary to give water-soluble phosphors for conjugation to quantum dots with surface amines: metallation, alkylation, and ester hydrolysis. While these reactions are straightforward, the order in which they are performed is critical. Alkylation of the free base is not viable, as alkylation of the pyrrole nitrogens also occurs. If the pyridyl substituents are not alkylated, acidic work-up of the hydrolysis reaction protonates the pyridyl nitrogen atoms and prevents subsequent alkylation. Based on these results, the metalloporphyrin must first be prepared; this intermediate is then alkylated and finally the ester is hydrolyzed. Although alkylation with iodomethane is simple and convenient, it was found to be a poor choice because the iodide counterion quenched porphyrin phosphorescence. Instead alkylation with 1,3-propanesultone was a superior strategy, thereby providing zwitterionic water-soluble species with intramolecular counterions.

2.7 Experimental Details

Materials

The following chemicals were used as received: hexanes, diethylether (Et_2O), anhydrous inhibitor-free tetrahydrofuran (THF), acetone, dichloromethane (CH_2Cl_2), chloroform ($CHCl_3$), toluene, acetonitrile (MeCN), methanol (MeOH), anhydrous methanol (MeOH), ethanol (EtOH), ethyl acetate (EtOAc), benzonitrile (PhCN), 2-mercaptopyridine, isonicotinoyl chloride hydrochloride, nicotinoyl chloride hydrochloride, pyrrole, boron trifuloride diethyl etherate ($BF_3 \bullet OEt_2$), mesitaldehyde, 4-pyridinecarboxaldehyde, 3-pyridinecarboxaldehyde, 2-pyridinecarboxaldehyde, benzaldehyde, sulfuric acid (H_2SO_4), propionic acid, methyl 4-formylbenzoate, indium(III) chloride ($InCl_3$), tin(II) chloride ($SnCl_2$), dibutyltin dichloride (Bu_2SnCl_2), sodium hydroxide beads (NaOH), sodium nitrite ($NaNO_2$), ethylmagnesium bromide 1M solution in THF (EtMgBr), mesitylmagnesium bromide 1M solution in THF (MesMgBr), 9-BBN triflate 0.5 M solution in hexanes (9-BBN-OTf), 1,3-propanesultone, iodomethane (CH_3I), *N*-bromosuccinimide (NBS), bromine (Br_2), 1,8-diazabicyclo[5.4.0]undec-7-ene (DBU), magnesium bromide ($MgBr_2$), trifluoroacetic acid (TFA), triethylamine (NEt_3), 2,3-dichloro-5,6-

dicyano-1,4-benzoquinone (DDQ), ethyl 4-chloro-4-oxobutyrate, and sodium borohydride ($NaBH_4$) from Sigma-Aldrich; sodium bicarbonate ($NaHCO_3$), sodium sulfate (Na_2SO_4), sodium hydroxide (NaOH), magnesium sulfate ($MgSO_4$), ammonium chloride (NH_4Cl), ammonium sulfate ($(NH_4)_2SO_4$), and sodium chloride (NaCl) from Mallinckrodt; potassium carbonate (K_2CO_3) and Celite 512 from Fluka; palladium(II) acetylacetonate ($Pd(acac)_2$), platinum(II) acetylacetonate ($Pt(acac)_2$), Mesoporphyrin IX dimethyl ester, and ytterbium(III) triflate ($Yb(OTf)_3$) from Strem; benzoyl chloride from J. T. Baker; pyridine, hydrochloric acid (HCl), and tetrahydrofuran (THF) from EMD; silica gel 60Å 230-400 mesh ASTM from Whatman; chloroform-*d* ($CDCl_3$), dichloromethane-d_2 (CD_2Cl_2), methanol-d_4 (CD_3OD), pyridine-d_5 (C_5H_5N), and dimethylsulfoxide-d_6 ($(CD_3)_2SO$) from Cambridge Isotope Labs; ammonium hydroxide (NH_4OH) from VWR; picolinoyl chloride hydrochloride from TCI; and zinc(II) acetate dihydrate ($Zn(OAc)_2 \bullet 2H_2O$) from Avocado Research Chemicals. Nitrogen and argon gases (Airgas) were passed over a Drierite column prior to use. All microwave reactions were performed in a CEM Discover microwave reactor.

Statistical Synthesis

5(4-Methoxycarbonylphenyl)-10,15,20-triphenylporphyrin (1)

In a 2 L two-neck flask protected from ambient light, 1 L $CHCl_3$ was degassed with argon for 45 minutes. Pyrrole (3.4 mL, 49 mmol), benzaldehyde (3.7 mL, 36 mmol), and methyl 4-formylbenzoate (2.02 g, 12 mmol) were added. After the solids were dissolved, 200 μL $BF_3 \bullet OEt_2$ (1.6 mmol) was added dropwise to the solution, which began to turn yellow, and was stirred at room temperature for 1 hour. DDQ (5.55 g, 25 mmol) was added as a solid in one portion to the red solution and stirred for an additional 1 hour under argon. To quench the reaction, 2.4 mL triethylamine (1.74 g, 17 mmol) was added and the solution was stirred for 15 minutes. Solvent was removed by rotary evaporation. The crude reaction mixture was initially purified on a silica column using CH_2Cl_2 as the eluent to remove polypyrrolic byproducts. The porphyrin-containing fractions were further purified on a silica column using 2:3 CH_2Cl_2:hexanes to remove H_2TPP and then 3:2 CH_2Cl_2:hexanes to elute the target product. Since a trace amount of H_2TPP was observed by TLC, the second porphyrin fraction was further purified on a silica gel column using the above conditions. A total of 538 mg (7.2% yield) H_2TPP was isolated in addition to 884 mg (10.8% yield) of the A_3B porphyrin. ^1H NMR (300 MHz, CD_2Cl_2, 25 °C) δ –2.80 (s, 2H), 4.08 (s, 3H), 7.78 (m, 9 H), 8.23 (m, 6H), 8.32 (d, *J* = 8.1 Hz, 2H), 8.42 (d, *J* = 8.1 Hz, 2H), 8.84 (d, *J* = 4.7 Hz, 2H), 8.89 (s, 6H).

5(4-Methoxycarbonylphenyl)-10,15,20-triphenylporphyrinatopalladium(II) (Pd-1)

In a 10 mL microwave tube, 77 mg **1** (0.11 mmol) and 105 mg $Pd(acac)_2$ (0.34 mmol) were dissolved in 3 mL pyridine. The resultant mixture was irradiated in a microwave reactor for 20 minutes at 180 °C. The crude reaction mixture was filtered through a plug of Celite and the filtrate was brought to dryness. The residue was purified on a silica gel column using CH_2Cl_2 as the eluent. The orange solution was brought to dryness by rotary evaporation to afford 85 mg (99% yield) of a red-purple solid. ^1H NMR (300 MHz, CD_2Cl_2, 25 °C) δ 4.08 (s, 3H), 7.78 (m, 9H), 8.17 (m, 6H), 8.27 (d, *J* = 8.1 Hz, 2H), 8.41 (d, *J* = 8.1 Hz, 2H), 8.79 (d, *J* = 5.0 Hz, 2H), 8.84 (s, 4H), 8.85 (d, *J* = 5.0 Hz, 2H).

5(4-Methoxycarbonylphenyl)-10,15,20-triphenylporphyrinatoplatinum(II) (Pt-1)

In a 10 mL microwave tube, 102 mg **1** (0.15 mmol) and 181 mg $Pt(acac)_2$ (0.46 mmol) were dissolved in 3 mL benzonitrile. The resultant mixture was irradiated in a microwave reactor for 20 minutes at 250 °C. The crude reaction mixture was filtered through a plug of Celite, rinsed with CH_2Cl_2 and the filtrate was brought to dryness. The residue was purified on a silica gel column using CH_2Cl_2 as the eluent. The red-orange solution was brought to dryness by rotary evaporation to afford 86 mg (66% yield) of a red-purple solid. ^{1}H NMR (500 MHz, CD_2Cl_2, 25 °C) δ 4.07 (s, 3H), 7.78 (m, 9H), 8.18 (m, 6H), 8.25 (d, $J = 8.1$ Hz, 2H), 8.40 (d, $J = 8.1$ Hz, 2H), 8.73 (d, $J = 5.0$ Hz, 2H), 8.78 (s, 4H), 8.80 (d, $J = 5.1$ Hz, 2H).

5(4-Methoxycarbonylphenyl)-10,15,20-trimesitylporphyrin (2)

In a 2 L two-neck flask protected from ambient light, 800 mL $CHCl_3$ was degassed with argon for 45 minutes. Pyrrole (3.4 mL, 49 mmol), methyl 4-formylbenzoate (2.04 g, 12 mmol), and mesitaldehyde (4.0 mL, 27 mmol) were added and the solution was degassed for 45 minutes. To this solution, 200 μL $BF_3{\bullet}OEt_2$ (1.6 mmol) was added dropwise and the solution was stirred at room temperature for 1 hour. DDQ (5.60 g, 25 mmol) was added as a solid in one portion to the red solution and stirred for an additional 1 hour under argon. To quench the reaction, 2.26 mL NEt_3 (16 mmol) was added and the solution was stirred for 10 minutes. Solvent was removed by rotary evaporation. The crude reaction mixture was initially purified on a silica column using CH_2Cl_2 as the eluent to remove polypyrrolic byproducts. The porphyrin-containing fractions were further purified on a long silica column (~ 15 inches) initially using 2:3 CH_2Cl_2:hexanes to remove 5,10,15,20-tetramesitylporphyrin and then switching to 3:2 CH_2Cl_2:hexanes to elute the target product. A total of 385 mg (7.3% yield) 5,10,15,20-tetramesitylporphyrin was isolated in addition to 560 mg (7.8% yield) of the A_3B porphyrin. ^{1}H NMR (300 MHz, CD_2Cl_2, 25 °C) δ 1.84 (s, 12H), 1.85 (s, 6H), 2.62 (s, 9H), 4.10 (s, 3H), 7.27 (s, 6H), 8.28 (d, $J = 8.0$ Hz, 2H), 8.41 (d, $J = 8.1$ Hz, 2H), 8.64 (s, 4H), 8.70 (m, 4H).

5(4-Carboxyphenyl)-10,15,20-triphenylporphyrinatopalladium(II) (Pd-3)

In a 10 mL microwave tube with three stir bars, 31 mg **Pd-1** (0.04 mmol) was dissolved in 2 mL of anhydrous inhibitor-free THF and 2 mL of 6M NaOH was added. The biphasic mixture was irradiated in a microwave reactor for 12 hours at 80 °C. Concentrated HCl(aq) was added drop-wise to the reaction mixture until all of the solid material had dissolved. The mixture was stirred for one hour in darkness. The crude reaction mixture was poured into water and the product was extracted with CH_2Cl_2, the organic layer was dried over Na_2SO_4, and brought to dryness. The crude reaction mixture was purified on a silica column using CH_2Cl_2 then 10:1 CH_2Cl_2:MeOH. The product (20 mg, 66%) was obtained as a red-orange solid. ^{1}H NMR (300 MHz, CD_2Cl_2, 25 °C) δ 7.78 (m, 9H), 8.17 (m, 6H), 8.30 (d, $J = 8.0$ Hz, 2H), 8.46 (d, $J = 8.0$ Hz, 2H), 8.80 (d, $J = 4.9$ Hz, 2H), 8.84 (s, 4H), 8.86 (d, $J = 4.9$ Hz, 2H), 10.42 (s, 1H).

5(4-Carboxyphenyl)-10,15,20-triphenylporphyrinatoplatinum(II) (Pt-3)

In a 10 mL microwave tube with three stir bars, 50 mg **Pt-1** (0.058 mmol) was dissolved in 2 mL of anhydrous inhibitor-free THF and 2 mL of 6M NaOH was added. The biphasic mixture was irradiated in a microwave reactor for 24 hours at 80 °C. Concentrated HCl(aq) was added drop-wise to the reaction mixture until all of the solid material had dissolved. The mixture was stirred for one hour in darkness. The crude reaction mixture was poured into water and the product was extracted with CH_2Cl_2, the organic layer was dried over Na_2SO_4, and brought to dryness. The crude reaction mixture was purified on a silica column using CH_2Cl_2 then 10:1 CH_2Cl_2:MeOH. The product (44 mg, 89%) was obtained as a red-orange solid. ^{1}H NMR (500 MHz, CD_2Cl_2, 25 °C) δ 7.77 (m, 9H), 8.16 (m, 6H), 8.29 (d, $J = 8.0$ Hz, 2H), 8.46 (d, $J = 8.0$ Hz, 2H), 8.74 (d, $J = 5.0$ Hz, 2H), 8.78 (s, 4H), 8.80 (d, $J = 5.1$ Hz, 2H).

5,10,15,20-Tetraphenylporphyrin (4)

The title compound was obtained as a byproduct (7.2% yield) from the synthesis of compound **1**. It was identified as the first of two porphyrin isomers on the column. ^{1}H NMR (500 MHz, $CDCl_3$, 25 °C) δ 7.76 (m, 12 H), 8.22 (m, 8H), 8.85 (s, 8H).

5,10,15,20-Tetraphenylporphyrinatopalladium(II) (Pd-4)

In a 10 mL microwave tube, 102 mg **4** (0.17 mmol) and 202 mg Pd(acac)$_2$ (0.66 mmol) were dissolved in 3 mL pyridine. The resultant mixture was irradiated in a microwave reactor for 20 minutes at 180 °C. The crude reaction mixture was filtered through a plug of silica and the filtrate was brought to dryness. The residue was purified on a silica gel column using CH_2Cl_2 as the eluent. The orange solution was brought to dryness by rotary evaporation to afford 112 mg (94% yield) of a red-orange solid. ^{1}H NMR (500 MHz, $CDCl_3$, 25 °C) δ 7.75 (m, 12 H), 8.17 (m, 8H), 8.81 (s, 8H).

5-(4-Nitrophenyl)-10,15,20-triphenylporphyrin (5)

In a 100 mL round bottom flask, 0.30 mg **4** (0.49 mmol) was dissolved in 30 mL TFA to afford a green solution. Sodium nitrite (64 mg, 0.93 mmol) was added; the solution immediately turned purple and was stirred for 3 minutes. The reaction mixture was poured into water and the product was extracted with CH_2Cl_2 until the aqueous layer was clear. The combined organics were washed with saturated $NaHCO_3$ and brine; solvent was removed by rotary evaporation. The residue was filtered through a plug of silica using CH_2Cl_2 as the eluent to remove all of the purple-red material, giving porphyrin **5**, which was used without further purification.

5-(4-Aminophenyl)-10,15,20-triphenylporphyrin (6)

The crude residue from the synthesis of **5** was dissolved in 50 mL of concentrated HCl and 0.45 g $SnCl_2$ (2.37 mmol) was added. The reaction mixture was heated at 80 °C for 1 hour under argon. The reaction mixture was poured into 300 mL of H_2O and then neutralized with aqueous ammonia. The product was extracted with CH_2Cl_2 until the organic layer was clear. The combined organics were washed with water then dried over $MgSO_4$; solvent was removed by rotary evaporation. The crude reaction mixture was filtered through a plug of silica with CH_2Cl_2

to remove a green impurity that remained adsorbed on the silica. The product was then purified on a silica column using 1:1 hexanes:CH_2Cl_2 to remove unreacted **4**. The solvent was changed to 100% CH_2Cl_2 to elute the product. Solvent was removed by rotary evaporation to afford 130 mg (42% yield, based on the starting amount of **4**) of a purple solid. ^1H NMR (500 MHz, $CDCl_3$, 25 °C) δ 4.02 (bs, 2H), 7.05 (d, J = 8.2 Hz, 2H), 7.75 (m, 9H), 7.98 (d, J = 8.2 Hz, 2H), 8.20 (m, 6H), 8.81 (s, 6H), 8.92 (d, J = 4.6 Hz, 2H).

5-(4-Aminophenyl)-10,15,20-triphenylporphyrinatopalladium(II) (Pd-6)

In a 10 mL microwave tube, 50 mg of the free-base porphyrin **6** (0.079 mmol) was dissolved in 3 mL pyridine and 132 mg Pd(acac)$_2$ (0.43 mmol) was added. The resultant solution was placed in a microwave reactor and irradiated at 180 °C for 20 minutes. The crude reaction mixture was filtered through a plug of silica and rinsed with CH_2Cl_2; the collected orange filtrate was brought to dryness. The compound was purified on a silica gel column using CH_2Cl_2 as the eluent to give 44 mg (75% yield) of the title product. ^1H NMR (500 MHz, $CDCl_3$, 25 °C) δ 4.03 (bs, 2H), 7.05 (d, J = 7.8 Hz, 2H), 7.74 (m, 9H), 7.94 (d, J = 8.1 Hz, 2H), 8.16 (m, 6H), 8.79 (s, 4H), 8.80 (overlapping d, J = 4.7 Hz), 8.91 (d, J = 5.0 Hz, 2H).

5-(4-Aminophenyl)-10,15,20-tris(4-sulfonatophenyl)porphyrin, trisammonium salt (7)

In a 100 mL round bottom flask, 75 mg **6** (0.12 mmol) was dissolved in 11 mL of concentrated H_2SO_4 and heated at 105 °C for 4.5 hours. The solution was cooled to room temperature and then poured into 100 mL of H_2O and the reaction mixture was neutralized with NH_4OH. The reaction mixture was concentrated to a volume of ~25 mL. An excess of MeOH was added to the solution and the mixture was filtered on a Büchner funnel to remove precipitated salts. The filtrate was brought to dryness and the precipitation procedure was repeated two more times to remove additional salts. The residue was dissolved in a minimal amount of MeOH and then poured over a silica plug, using MeOH as the eluent. After removal of the solvent, the residue was recrystallized from MeOH/THF and the precipitated product was collected on a frit and washed with THF. The collected solid was dried on a vacuum line overnight to afford 98 mg of material (89% yield). ^{1}H NMR (500 MHz, CD_3OD, 25 °C) δ 4.60 (bs, 2H), 7.15 (d, J = 8.2 Hz, 2H), 7.95 (d, J = 8.0 Hz, 2H), 8.27 (m, 12H), 8.84 (bs, 6H), 8.94 (bs, 2H).

5-{4-[3-(Ethoxycarbonyl)propionylamido]phenyl}-10,15,20-tris(4-sulfonatophenyl) porphyrin, trisammonium salt (8)

In a 50 mL Schlenk flask, 28 mg (0.031 mmol) of material from the synthesis of **7** was dissolved in 10 mL anhydrous MeOH. Then 76 μL NEt_3 (55 mg, 0.55 mmol) followed by 80 μL ethyl 4-chloro-4-oxobutyrate (92 mg, 0.56 mmol). The resultant mixture was stirred at room temperature for 24 hours, protected from ambient light. Solvent was removed by rotary evaporation and the residue was dissolved in ~2 mL MeOH; the solution was treated with THF and the resultant precipitate was collected on a frit. The solid material was dried under vacuum for several hours to afford 13 mg of material (41% yield). ^{1}H NMR (500 MHz, CD_3OD, 25 °C) δ 1.31 (t, 3H), 2.81 (d, 2H), 2.85 (d, 2H), 4.21 (q, 2H), 8.00 (d, J = 8.4 Hz, 2H), 8.15 (d, J = 8.5 Hz, 2H), 8.27 (m, 12H), 8.89 (bs, 8H).

5(4-Carbonylphenyl)-10,15,20-tris(4-sulfonatophenyl)porphyrin, tetrakisammonium salt (9)

In a 100 mL round bottom flask, 102 mg **1** (0.15 mmol) was dissolved in 20 mL concentrated H_2SO_4 and heated at 105 °C for 4.5 hours. The reaction mixture was cooled to room temperature and poured into 50 mL of 0 °C water; the reaction mixture was neutralized with 6 M NaOH while cooling the solution in an ice bath. The reaction mixture was concentrated to a volume of ~25 mL. An excess of MeOH was added to the solution and the mixture was filtered on a Büchner funnel to remove precipitated salts. The filtrate was brought to dryness and the precipitation procedure was repeated to remove additional salts. The green residue was dissolved in NH_4OH and stirred at room temperature for 10 minutes; solvent was removed by rotary evaporation. The purple residue was dissolved in MeOH and filtered on a Büchner funnel to remove precipitated salts. The filtrate was brought to dryness to afford 167 mg of material (>100% yield, due to the presence of inorganic salts). ^1H NMR (500 MHz, CD_3OD, 25 °C) δ 8.20 (d, J = 7.9 Hz, 2H), 8.27 (m, 12H), 8.37 (d, J = 7.9 Hz, 2H), 8.63–9.17 (bs, 6H). The very broad signal is attributed to the β-pyrrolic protons and should integrate for 8H.

5-(4-Methoxycarbonylphenyl)-10,15,20-tris(4-pyridyl)porphyrin (10)

Method 1: Adler-Longo

In a 500 mL round bottom flask, 1.60 g methyl 4-formylbenzoate (10 mmol) and 2.7 mL 4-pyridinecarboxaldehyde (29 mmol) were dissolved 160 mL propionic acid and brought to reflux. Pyrrole (2.6 mL, 37 mmol) was added and the solution was refluxed for 1.5 hours. Solvent was removed by rotary evaporation. The residue was dissolved in $CHCl_3$ and the organics were washed with saturated $NaHCO_3$ and dried over Na_2SO_4. Solvent was removed by rotary evaporation. The residue was purified on a silica column using CH_2Cl_2, then 1:1 CH_2Cl_2:EtOAc, followed by 100% EtOAc, then 10% MeOH in EtOAc, and finally 20% MeOH in EtOAc. The product was identified as the porphyrin that eluted with 20% MeOH in EtOAc; this material was further purified on a silica gel column using 100% EtOAc, then 5% MeOH in EtOAc, followed by 10% MeOH in EtOAc as the eluent. The product was then filtered through a short (~ 3 in) plug of silica gel with EtOAc. After removing the solvent, the residue was dissolved in a minimal amount of CH_2Cl_2 and subsequently precipitated with a large excess of hexanes. The purple solid was collected on a frit, washed with EtOH, and dried under vacuum to afford 225 mg of the title product (3.9% yield, based on the amount of B aldehyde). ^{1}H NMR (500 MHz, $CDCl_3$, 25 °C) δ –2.90 (bs, 2H), 4.12 (s, 3H), 8.16 (m, 6H), 8.30 (m, 2H), 8.47 (m, 2H), 8.82–8.89 (bm, 8H), 9.06 (m, 6H).

Method 2: Modified Adler-Longo

In a three-neck round bottom flask, 100 mL propionic acid and 100 mL toluene were brought to reflux. An aldehyde solution was prepared by dissolving 1.62 g methyl 4-formylbenzoate (9.9 mmol) and 2.7 mL 4-pyridinecarboxaldehyde (3.1 g, 29 mmol) in 7 mL toluene. A pyrrole solution was prepared by dissolving 2.6 mL pyrrole (2.5 g, 37 mmol) in 7 mL toluene. These two solutions were simultaneously added to the refluxing solvent dropwise *via* syringe. After the addition was complete, the solution was refluxed for 1.5 hours. The reaction mixture was then cooled to room temperature and solvents were removed by rotary evaporation. The crude residue was dissolved in 100 mL $CHCl_3$ and a saturated solution of $NaHCO_3$ was carefully added; the biphasic mixture was then stirred until bubbling had subsided. The organic layer was then washed with water, dried over Na_2SO_4, and brought to dryness. The crude reaction mixture was purified on a silica gel column using CH_2Cl_2 to elute all of the fast-moving porphyrin isomers (B_4, AB_3, and *cis-/trans-*A_2B_2 isomers). After these four products eluted, the solvent was changed to 100% ethyl acetate then 10% MeOH in EtOAc to elute the desired A_3B porphyrin. A second silica gel column, using ethyl acetate as the sole eluent, was necessary to fully purify the desired product, affording 387 mg of the title compound (5.8% yield, based on the amount of B aldehyde). ^{1}H NMR (500 MHz, $CDCl_3$, 25 °C) δ –2.90 (bs, 2H), 4.12 (s, 3H), 8.16 (m, 6H), 8.30 (m, 2H), 8.47 (m, 2H), 8.82–8.89 (bm, 8H), 9.06 (m, 6H).

5-(4-Methoxycarbonylphenyl)-10,15,20-tris(4-pyridyl)porphyrinopalladium(II) (Pd-10)

In a 10 mL microwave tube, 65 mg of the free-base porphyrin **10** (0.10 mmol) was dissolved in 3 mL pyridine and 175 mg Pd(acac)$_2$ (0.6 mmol) was added. An additional 1 mL of pyridine was added to rinse solids down the tube. The resultant solution was placed in a microwave reactor and irradiated at 180 °C for 20 minutes. The crude reaction mixture was filtered through a plug of Celite and rinsed with CH_2Cl_2; the collected orange filtrate was brought to dryness. The compound was purified using a gradient of 0–10% MeOH in EtOAc as the eluent to give 39 mg (50% yield) of the title product. ^{1}H NMR (400 MHz, $CDCl_3$, 25 °C) δ 4.12 (s, 3H), 8.12 (m, 6H), 8.25 (m, 2H), 8.45 (m, 2H), 8.80 (d, *J* = 5.1 Hz, 2H), 8.82 (s, 4H), 8.83 (d, *J* = 5.0 Hz, 2H), 9.05 (m, 6H).

5-(4-Methoxycarbonylphenyl)-10,15,20-tris(4-pyridyl)porphyrinoplatinum(II) (Pt-10)

In a 10 mL microwave tube, 50 mg of the free-base porphyrin **10** (0.074 mmol) was dissolved in 2.5 mL benzonitrile and 143 mg Pt(acac)$_2$ (0.36 mmol) was added. The resultant solution was placed in a microwave reactor and irradiated at 250 °C for 30 minutes. The crude reaction mixture was filtered through a plug of Celite and rinsed with CH_2Cl_2. The filtrate was washed with a saturated solution of $NaHCO_3$ and H_2O, then subsequently dried over Na_2SO_4 and brought to dryness by rotary evaporation. The residue was then purified on a plug of silica gel, using EtOAc then acetone as the eluent, to give an orange solution, which was brought to dryness. The oily reside was treated with a large excess of hexanes to induce precipitation of the product, which was collected on a frit and rinsed with hexanes, giving 27 mg (42% yield) of the title product. ^{1}H NMR (500 MHz, $CDCl_3$, 25 °C) δ 4.11 (s, 3H), 8.10 (m, 6H), 8.22 (d, *J* = 8.3 Hz, 2H), 8.43 (d, *J* = 8.3 Hz, 2H), 8.72 (d, *J* = 4.9 Hz, 2H), 8.75 (m, 6H), 9.02 (m, 6H).

5-(4-Methoxycarbonylphenyl)-10,15,20-tris(4-pyridyl)porphyrinozinc(II) (Zn-10)

In a 20 mL scintillation vial, 30 mg of the free-base porphyrin **10** (0.044 mmol) was dissolved in 9 mL $CHCl_3$ and 3 mL MeOH. Then $Zn(OAc)_2•2H_2O$ (248 mg, 1.13 mmol) was added and the solution was stirred at room temperature for 72 hours. The reaction mixture was washed with water (x3) and dried over Na_2SO_4; solvent was removed by rotary evaporation to afford 21 mg (65%) of product. ^{1}H NMR (500 MHz, C_5D_5N, 25 °C) δ 4.07 (s, 3H), 8.33 (m, 6H), 8.48 (d, *J* = 8.1 Hz, 2H), 8.56 (d, *J* = 8.2 Hz, 2H), 9.15 (overlapping s, 4H), 9.15 (overlapping d, *J* = 4.6 Hz, 2H), 9.19 (overlapping d, *J* = 4.6 Hz), 9.20 (m, 6H).

5,10,15,20-Tetrakis(4-methoxycarbonylphenyl)porphyrin (11)

The title product was isolated from the statistical synthesis of **10** (Method 1). It was identified as the first porphyrin fraction that eluted using 1:1 CH_2Cl_2:EtOAc as the eluent. ^{1}H NMR (500 MHz, $CDCl_3$, 25 °C) δ 4.12 (s, 12H), 8.29 (d, *J* = 8.2 Hz, 8H), 8.45 (d, *J* = 8.2 Hz, 8H), 8.82 (m, 8H).

5,15-Bis(4-methoxycarbonylphenyl)-10,20-bis(4-pyridyl) porphyrin (12)

The title product was isolated from the statistical synthesis of **10** (Method 1). It was identified as the second porphyrin fraction that eluted using 1:1 CH_2Cl_2:EtOAc as the eluent. ^{1}H NMR (500 MHz, $CDCl_3$, 25 °C) δ 4.12 (s, 6H), 8.16 (m, 4H), 8.30 (m, 4H), 8.46 (m, 4H), 8.84 (m, 8H), 9.04 (m, 4H).

5,10-Bis(4-methoxycarbonylphenyl)-15,20-bis(4-pyridyl) porphyrin (13)

The title product was isolated from the statistical synthesis of **10** (Method 1). It was identified as the first porphyrin fraction that eluted using 10% MeOH in EtOAc as the eluent. ^{1}H NMR (500 MHz, $CDCl_3$, 25 °C) δ 4.12 (s, 6H), 8.16 (m, 4H), 8.29 (m, 4H), 8.46 (m, 4H), 8.84 (m, 8H), 9.05 (m, 4H).

Semi-Rational and Rational Synthesis

5-Phenyldipyrromethane (14)

A solution of 40 mL pyrrole (38 g, 580 mmol) and 1.3 mL benzaldehyde (1.4 g, 13 mmol) were bubbled with N_2 for 10 minutes to degas the solution. Then, 280 mg $InCl_3$ (1.3 mmol) was added and the tan suspension was stirred at room temperature for 1.5 hours. Sodium hydroxide beads (2.5 g, 63 mmol) were added and the suspension was stirred for an additional 45 minutes at room temperature. The crude reaction mixture was filtered using a Büchner funnel. The flask and solids were rinsed with acetone and the filtrate was brought to dryness. The crude reaction mixture was purified on a silica gel column packed with hexanes and the product was eluted using 3:1 CH_2Cl_2:hexanes. Solvent was removed to afford 2.57 g (89% yield) of the title compound as a yellow solid. ^{1}H NMR (500 MHz, $CDCl_3$, 25 °C) δ 5.49 (s, 1H), 5.92 (m, 2H), 6.16 (m, 2H), 6.70 (m, 2H), 7.21–7.28 (m, 3H), 7.30–7.34 (m, 2H), 7.94 (bs, 2H).

5-(4-Methoxycarbonylphenyl)dipyrromethane (15)

A solution of 2.1 g methyl 4-formylbenzoate (13 mmol) in 45 mL pyrrole (44 g, 650 mmol) was bubbled with argon for 10 minutes. Then, 285 mg $InCl_3$ (1.3 mmol) was added and the mixture was stirred at room temperature for 1.5 hours. Sodium hydroxide beads (1.5 g, 38 mmol) were added and the suspension was stirred for an additional 45 minutes at room temperature. The crude reaction mixture was then filtered using a Büchner funnel. The flask and solids were rinsed with acetone; the filtrate was brought to dryness and residual pyrrole was removed by triturating with hexanes to afford a tan solid. The residue was dissolved in MeOH with the aid of a hot water bath and the product was allowed to crystallize overnight at room temperature. Solid material was collected on a frit, washed with hexanes and a minimal amount of EtOH, and dried under vacuum to afford 2.30 g (63% yield) of the title compound as a tan

solid. ^{1}H NMR (400 MHz, CDCl$_3$, 25 °C) δ 3.91 (s, 3H), 5.53 (s, 1H), 5.89 (m, 2H), 6.16 (m, 2H), 6.72 (m, 2H), 7.29 (m, 2H), 7.96 (overlapping bs, 2H), 7.98 (overlapping m, 2H).

5-(4-Pyridyl)dipyrromethane (16)

A solution of 21 mL pyrrole (20 g, 300 mmol) and 1.9 mL 4-pyridinecarboxaldehyde (2.2 g, 20 mmol) were heated at 85 °C for 15 hours. Solvent was removed by rotary evaporation. The crude residue was loaded onto a silica gel column packed with ethyl acetate. The product eluted with 100% EtOAc as the second band (orange-red). After solvent removal, the residue was dissolved in a minimal amount of EtOAc and the product was precipitated with a large excess of hexanes and collected on a frit. The collected orange-red solid was rinsed with hexanes and dried under vacuum to afford 2.27 g (51% yield) of the title compound. ^{1}H NMR (400 MHz, CDCl$_3$, 25 °C) δ 5.46 (s, 1H), 5.90 (m, 2H), 6.17 (m, 2H), 6.74 (m, 2H), 7.13 (m, 2H), 8.06 (bs, 2H), 8.52 (m, 2H).

5-(3-Pyridyl)dipyrromethane (17)

A solution of 20 mL pyrrole (19 g, 290 mmol) and 2 mL 3-pyridinecarboxaldehyde (2.3 g, 21 mmol) was heated at 85 °C for 24 hours. Solvent was removed by rotary evaporation. The crude residue was loaded onto a silica gel column packed with ethyl acetate. The product eluted with 100% ethyl acetate as the second band (orange). Solvent was removed by rotary evaporation to afford 2.41 g (51% yield) of the title compound as a tan solid. ^{1}H NMR (500 MHz, CDCl$_3$, 25 °C) δ 5.49 (s, 1H), 5.88 (m, 2H), 6.16 (m, 2H), 6.74 (m, 2H), 7.24 (m, 1H), 7.51 (m, 1H), 8.07 (bs, 2H), 8.50 (overlapping m, 2H).

5-(2-Pyridyl)dipyrromethane (18)

A solution of 20 mL pyrrole (19 g, 290 mmol) and 1.9 mL 2-pyridinecarboxaldehyde (2.14 g, 20 mmol) was heated at 85 °C for 15 hours. Solvent was removed by rotary evaporation.

The crude residue was loaded onto a silica gel column packed with hexanes. The product eluted with 1:1 EtOAc:hexanes then 100% EtOAc. A red impurity was observed by TLC. The product was further purified on a second silica gel column packed with hexanes, using this solvent as the initial eluent to remove the majority of the red impurity. The solvent was switched to 1:1 EtOAc:hexanes then 100% EtOAc. Solvent was removed by rotary evaporation to afford 1.07 g (24% yield) of the title compound as a red-brown solid. ^{1}H NMR (500 MHz, $CDCl_3$, 25 °C) δ 5.50 (s, 1H), 5.93 (m, 2H), 6.12 (m, 2H), 6.70 (m, 2H), 7.19 (m, 1H), 7.29 (m, 1H), 7.65 (m, 1H), 8.61 (m, 1H), 8.90 (bs, 2H).

S-2-Pyridyl benzoylthioate (19)

In an-oven dried flask, 5.52 g (50 mmol) 2-mercaptopyridine was dissolved in 40 mL anhydrous THF under a nitrogen atmosphere. Then 7.6 mL benzoyl chloride (9.2 g, 65 mmol) was added and the solution was stirred at room temperature for 2 hours. The yellow solid was collected on a Büchner funnel and washed with hexanes until the filtrate was clear. The solid was slowly added to a biphasic mixture of 200 mL saturated $NaHCO_3$ and 200 mL Et_2O; the mixture was stirred until bubbling subsided. The product was extracted with Et_2O (~1.5 L) and the organics were dried over Na_2SO_4. Solvent was removed by rotary evaporation to afford a yellow oil, which was isolated as a solid with the addition of a large excess of hexanes. The yellow solid was collected on a frit and washed with hexanes until the filtrate was clear to afford 6.06 g (56% yield) of the title compound. ^{1}H NMR (400 MHz, $CDCl_3$, 25 °C) δ 7.34 (m, 1H), 7.49 (m, 2H), 7.62 (m, 1H), 7.73 (m, 1H), 7.79 (m, 1H), 8.02 (m, 2H), 8.68 (m, 1H).

S-2-Pyridyl isonicotinothioate (20)

In an-oven dried flask, 11.15 g (100 mmol) 2-mercaptopyridine and 17.86 g isonicotinoyl chloride hydrochloride (100 mmol) were dissolved in 100 mL anhydrous THF and stirred at room temperature under an argon atmosphere for 2.5 hours. The yellow solid was collected on a Büchner funnel and washed with hexanes until the filtrate was clear. The solid was slowly added to a biphasic mixture of 200 mL saturated $NaHCO_3$ and 200 mL Et_2O; the mixture was stirred until bubbling subsided. The product was extracted with Et_2O and the organics were dried over Na_2SO_4. Solvent was removed by rotary evaporation to afford a pale yellow solid; the solid was collected on a frit and washed with hexanes until the filtrate was clear to afford 13.00 g (60% yield) of the title compound. ^1H NMR (400 MHz, $CDCl_3$, 25 °C) δ 7.37 (m, 1H), 7.72 (m, 1H), 7.80 (m, 2H), 7.82 (m, 1H), 8.69 (m, 1H), 8.84 (m, 2H).

S-2-Pyridyl nicotinothioate (21)

In an-oven dried flask, 5.54 g (50 mmol) 2-mercaptopyridine and 9.02 g (51 mmol) nicotinoyl chloride hydrochloride were dissolved in 40 mL anhydrous THF and stirred at room temperature under a nitrogen atmosphere for 2 hours. The yellow solid was collected on a Büchner funnel and washed with hexanes until the filtrate was clear. The solid was slowly added to a biphasic mixture of 200 mL saturated $NaHCO_3$ and 200 mL EtOAc; the mixture was stirred until bubbling subsided. The product was extracted with EtOAc (~1.5 L) and the organics were dried over Na_2SO_4. Solvent was removed by rotary evaporation to afford a yellow oil, which was isolated as a solid with the addition of a large excess of hexanes. The yellow solid was collected on a frit and washed with hexanes until the filtrate was clear to afford 4.05 g (37% yield) of the title compound. ^1H NMR (400 MHz, $CDCl_3$, 25 °C) δ 7.36 (m, 1H), 7.45 (m, 1H), 7.73 (m, 1H), 7.81 (m, 1H), 8.26 (m, 1H), 8.69 (m, 1H), 8.83 (m, 1H), 9.23 (m, 1H).

S-2-Pyridyl picolinothioate (22)

In an-oven dried flask, 2.76 g (25 mmol) 2-mercaptopyridine was dissolved in 50 mL anhydrous THF and 4.24 g picolinoyl chloride hydrochloride (24 mmol) was added; the resultant mixture was stirred at room temperature under an argon atmosphere for 1.5 hours. The yellow solid was collected on a Büchner funnel and washed with hexanes until the filtrate was clear. The solid was slowly added to a biphasic mixture of 150 mL saturated $NaHCO_3$ and 150 mL Et_2O; the mixture was stirred until bubbling subsided. The product was extracted with Et_2O and the organics were dried over Na_2SO_4. Solvent was removed by rotary evaporation to afford 3.38 g (66% yield) of the title compound. ^1H NMR (400 MHz, $CDCl_3$, 25 °C) δ 7.34 (m, 1H), 7.57 (m, 1H), 7.70 (m, 1H), 7.79 (m, 1H), 7.88 (m, 1H), 7.96 (m, 1H), 8.71 (m, 1H), 8.75 (m, 1H).

1-Benzoyl-5-phenyldipyrromethane (23)

In an oven-dried flask, 0.80 g 5-phenyldipyrromethane (**14**) (3.6 mmol) was dissolved in 10 mL anhydrous THF under a nitrogen atmosphere to afford a tan solution. Then 8 mL EtMgBr (1 M solution in THF) was slowly added and the resultant dark brown solution was stirred at room temperature for 10 minutes. The solution was cooled to –78 °C in a dry ice/acetone bath and 0.82 g *S*-2-Pyridyl benzoylthioate (**19**) (3.8 mmol) was added as a solid in one portion; the resultant mixture was stirred at –78 °C for 40 minutes. The solution was then warmed to room temperature and stirred for an additional 3.5 hours. Saturated $(NH_4)SO_4$ was added and the product was extracted with EtOAc (x3); the combined organics were washed with water and brine then dried over Na_2SO_4. Solvent was removed by rotary evaporation to afford a brown oil. The crude reaction mixture was loaded onto a silica gel column packed with CH_2Cl_2, which was also used as the initial eluent to remove unreacted dipyrromethane (first spot by TLC in 100% CH_2Cl_2, turns pink upon Br_2 staining). The eluent was then switched to 2:3 EtOAc:CH_2Cl_2 to elute the product (turns yellow-orange upon Br_2 staining). After solvent removal, the oily residue was dissolved in a minimal amount of CH_2Cl_2 and subsequently precipitated with a large excess of hexanes and the resultant solid was collected on a frit and washed with hexanes to afford 0.13

g (11% yield) of the title compound as a brown solid. ^{1}H NMR (500 MHz, $CDCl_3$, 25 °C) δ 5.56 (s, 1H), 5.99 (m, 1H), 6.09 (m, 1H), 6.17 (m, 1H), 6.69 (m, 1H), 6.81 (m, 1H), 7.20–7.23 (m, 2H), 7.28–7.34 (m, 3H), 7.43–7.48 (m, 3H), 7.80–7.83 (m, 2H), 8.19 (bs, 1H), 9.74 (bs, 1H).

1-Isonicotinoyl-5-(4-methoxycarbonylphenyl)dipyrromethane (24)

In an oven-dried flask, 1.89 g 5-(4-methoxycarbonylphenyl)dipyrromethane (**15**) (6.7 mmol) was dissolved in 15 mL anhydrous THF under an argon atmosphere to afford a tan solution. Then 17 mL EtMgBr (1 M solution in THF) was slowly added and the resultant dark brown solution was stirred at room temperature for 10 minutes. The solution was cooled to –78 °C in a dry ice/acetone bath and 1.50 g *S*-2-pyridyl isonicotinothioate (**20**) (6.9 mmol) was added as a solid in one portion; the resultant mixture was stirred at –78 °C for 1 hour. The solution was then warmed to room temperature and stirred for an additional 3 hours. Saturated NH_4Cl was added and the product was extracted with EtOAc; the combined organics were washed with water and brine then dried over Na_2SO_4. Solvent was removed by rotary evaporation to afford a brown oil. The crude reaction mixture was loaded onto a silica gel column packed with EtOAc. The product (second band, turns yellow-orange upon Br_2 staining on TLC) was eluted with 100% EtOAc. After solvent removal, the oily brown residue was dissolved in a minimal amount of EtOAc and subsequently precipitated with a large excess of hexanes and the resultant solid was collected on a frit and washed with hexanes to afford 1.67 g (65% yield) of the title compound as a tan solid. ^{1}H NMR (500 MHz, $CDCl_3$, 25 °C) δ 3.92 (s, 3H), 5.61 (s, 1H), 5.97 (m, 1H), 6.08 (m, 1H), 6.19 (m, 1H), 6.76 (m, 1H), 6.81 (m, 1H), 7.30 (m, 2H), 7.63 (m, 2H), 8.01 (m, 2H), 8.04 (bs, 1H), 8.77 (m, 2H), 9.56 (bs, 1H).

1-Isonicotinoyl-5-(4-pyridyl)dipyrromethane (25)

In an oven-dried flask, 1.51 g 5-(4-pyridyl)dipyrromethane (**16**) (6.8 mmol) was dissolved in 15 mL anhydrous THF under an argon atmosphere to afford a tan solution. Then 17 mL EtMgBr (1 M solution in THF) was slowly added and the resultant dark brown solution was stirred at room temperature for 10 minutes. The solution was cooled to –78 °C in a dry ice/acetone bath and 1.48 g *S*-2-pyridyl isonicotinothioate (**20**) (6.8 mmol) was added as a solid in one portion; the resultant mixture was stirred at –78 °C for 10 minutes. The solution was then warmed to room temperature and stirred for an additional 3 hours. Saturated NH_4Cl was added and the product was extracted with EtOAc; the combined organics were washed with water and brine then dried over Na_2SO_4. Solvent was removed by rotary evaporation to afford a brown oil. The crude reaction mixture was loaded onto a silica gel column packed with EtOAc. The product (second band, turns yellow-orange upon Br_2 staining on TLC) was eluted with 100% EtOAc. After solvent removal, the oily brown residue was dissolved in a minimal amount of EtOAc and subsequently precipitated with a large excess of hexanes and the resultant solid was collected on a frit and washed with hexanes to afford 0.66 g (30% yield) of the title compound as a tan solid. ^{1}H NMR (500 MHz, $CDCl_3$, 25 °C) δ 5.53 (s, 1H), 5.98 (m, 1H), 6.08 (m, 1H), 6.21 (m, 1H), 6.78 (m, 1H), 6.82 (m, 1H), 7.15 (m, 2H), 7.64 (m, 2H), 8.09 (bs, 1H), 8.59 (m, 2H), 8.78 (m, 2H), 9.45 (bs, 1H).

10-(9-Borabicyclo[3.3.1]non-9-yl)-1-isonicotinoyl-5-(4-pyridyl)dipyrromethane (25-BBN)

In an oven-dried flask, 0.84 g 5-(4-pyridyl)dipyrromethane (**16**) (3.8 mmol) was dissolved in 20 mL anhydrous THF under an argon atmosphere to afford a tan solution. Then 9.5 mL EtMgBr (1 M solution in THF) was slowly added and the resultant dark brown solution was stirred at room temperature for 10 minutes. The solution was cooled to –78 °C in a dry ice/acetone bath and a solution of 0.82 g *S*-2-pyridyl isonicotinothioate (**20**) (3.8 mmol) in 15 mL anhydrous THF was added; the resultant mixture was stirred at –78 °C for 10 minutes. The solution was then warmed to room temperature and stirred for an additional 4 hours. Saturated NH_4Cl was added and the product was extracted with EtOAc; the combined organics were washed with water and brine then dried over Na_2SO_4. Solvent was removed by rotary evaporation. The residue was dissolved in 13 mL CH_2Cl_2 and 1.67 mL NEt_3 (1.2 g, 12 mmol) was added; the resultant solution was purged with argon. Then 25 mL of 9-BBN-OTf solution (0.5 M in hexanes) was added and the resultant solution was stirred at room temperature for 2.5 hours. The reaction mixture was examined by TLC and it was found that an intractable mixture of products had formed.

1-Nicotinoyl-5-(3-pyridyl)dipyrromethane (26)

In an oven-dried flask, 0.65 g 5-(3-pyridyl)dipyrromethane (**17**) (2.9 mmol) was dissolved in 10 mL anhydrous THF under a nitrogen atmosphere to afford a tan solution. Then 8 mL EtMgBr (1 M solution in THF) was slowly added and the resultant dark brown solution was stirred at room temperature for 10 minutes. The solution was cooled to –78 °C in a dry ice/acetone bath and 0.69 g *S*-2-Pyridyl nicotinothioate (**21**) (3.2 mmol) was added as a solid in one portion; the resultant mixture was stirred at –78 °C for 30 minutes. The solution was warmed to room temperature and stirred for an additional 2 hours. Saturated $(NH_4)_2SO_4$ was added and the product was extracted with EtOAc (x3); the combined organics were washed with water and brine then dried over Na_2SO_4. Solvent was removed by rotary evaporation to afford a brown oil. The crude reaction mixture was loaded onto a silica gel column packed with EtOAc. The product (second fraction, turns yellow-orange upon Br_2 staining on TLC) was eluted with 100% EtOAc. After solvent removal, the oily brown residue was dissolved in a minimal amount of EtOAc and subsequently precipitated with a large excess of hexanes and the resultant solid was collected on a frit and washed with hexanes to afford 0.58 g (61% yield) of the title compound as a tan solid. ^{1}H NMR (400 MHz, $CDCl_3$, 25 °C) δ 5.57 (s, 1H), 5.96 (m, 1H), 6.09 (m, 1H), 6.19 (m, 1H), 6.77 (m, 1H), 6.83 (m, 1H), 7.27 (m, 1H), 7.43 (m, 1H), 7.53 (m, 1H), 8.10 (m, 1H), 8.34 (bs, 1H), 8.50 (m, 1H), 8.53 (m, 1H), 8.78 (m, 1H), 9.06 (m, 1H), 9.71 (bs, 1H).

1-Picolinoyl-5-(4-pyridyl)dipyrromethane (27)

In an oven-dried flask, 0.50 g 5-(4-pyridyl)dipyrromethane (**16**) (2.2 mmol) was dissolved in 10 mL anhydrous THF under an argon atmosphere to afford a tan solution. Then 5.5 mL EtMgBr (1 M solution in THF) was slowly added and the resultant dark brown solution was stirred at room temperature for 10 minutes. The solution was cooled to –78 °C in a dry ice/acetone bath and a solution of 0.39 g *S*-2-pyridyl picolinothioate (**22**) (1.8 mmol) in 10 mL anhydrous THF was added; the resultant mixture was stirred at –78 °C for 10 minutes. The solution was then warmed to room temperature and stirred for an additional 3 hours. Saturated NH_4Cl was added and the product was extracted with EtOAc; the combined organics were washed with water and brine then dried over Na_2SO_4. Solvent was removed by rotary evaporation to afford a brown oil. The crude reaction mixture was loaded onto a silica gel column packed with EtOAc. The product (second band, turns yellow-orange upon Br_2 staining on TLC) was eluted with 100% EtOAc. After solvent removal, the tan residue was dissolved in a minimal amount of EtOAc and subsequently precipitated with a large excess of hexanes and the resultant solid was collected on a frit and washed with hexanes to afford 0.23 g (39% yield) of the title compound as a tan solid. ^{1}H NMR (500 MHz, $CDCl_3$, 25 °C) δ 5.57 (s, 1H), 6.01 (m, 1H), 6.11 (m, 1H), 6.23 (m, 1H), 6.79 (m, 1H), 7.20 (m, 2H), 7.26 (m, 1H), 7.44 (m, 2H), 7.88 (m, 1H), 8.05 (bs, 1H), 8.22 (m, 1H), 8.53 (bs, 1H), 8.59 (m, 2H).

1-Isonicotinoyl-5-(3-pyridyl)dipyrromethane (28)

In an oven-dried flask, 1.52 g 5-(3-pyridyl)dipyrromethane (**17**) (6.8 mmol) was dissolved in 15 mL anhydrous THF under an argon atmosphere to afford a tan solution. Then 17 mL EtMgBr (1 M solution in THF) was slowly added and the resultant dark brown solution was stirred at room temperature for 10 minutes. The solution was cooled to –78 °C in a dry ice/acetone bath and 1.48 g *S*-2-pyridyl isonicotinothioate (**20**) (6.8 mmol) was added as a solid in one portion; the resultant mixture was stirred at –78 °C for 10 minutes. The solution was then warmed to room temperature and stirred for an additional 3 hours. Saturated NH_4Cl was added and the product was extracted with EtOAc; the combined organics were washed with water and brine then dried over Na_2SO_4. Solvent was removed by rotary evaporation to afford a brown oil. The crude reaction mixture was loaded onto a silica gel column packed with EtOAc. The product (second band, turns yellow-orange upon Br_2 staining on TLC) was eluted with 100% EtOAc. After solvent removal, the oily brown residue was dissolved in a minimal amount of EtOAc and subsequently precipitated with a large excess of hexanes and the resultant solid was collected on a frit and washed with hexanes to afford 1.35 g (60% yield) of the title compound as a tan solid. ^1H NMR (500 MHz, $CDCl_3$, 25 °C) δ 5.56 (s, 1H), 5.96 (m, 1H), 6.07 (m, 1H), 6.20 (m, 1H), 6.78 (m, 1H), 6.82 (m, 1H), 7.29 (m, 1H), 7.53 (m, 1H), 7.64 (m, 2H), 8.08 (bs, 1H), 8.53 (m, 1H), 8.56 (m, 1H), 8.78 (m, 2H), 9.42 (bs, 1H).

1-Nicotinoyl-5-(4-pyridyl)dipyrromethane (29)

In an oven-dried flask, 1.00 g 5-(4-pyridyl)dipyrromethane (**16**) (4.5 mmol) was dissolved in 10 mL anhydrous THF under an argon atmosphere to afford a tan solution. Then 11.5 mL EtMgBr (1 M solution in THF) was slowly added and the resultant dark brown solution was stirred at room temperature for 10 minutes. The solution was cooled to –78 °C in a dry ice/acetone bath and 0.98 g *S*-2-pyridyl nicotinothioate (**21**) (4.5 mmol) was added as a solid in one portion; the resultant mixture was stirred at –78 °C for 10 minutes. The solution was then warmed to room temperature and stirred for an additional 3 hours. Saturated NH_4Cl was added and the product was extracted with EtOAc; the combined organics were washed with water and brine then dried over Na_2SO_4. Solvent was removed by rotary evaporation to afford a brown oil. The crude reaction mixture was loaded onto a silica gel column packed with EtOAc. The product (second band, turns yellow-orange upon Br_2 staining on TLC) was eluted with 100% EtOAc. After solvent removal, the oily brown residue was dissolved in a minimal amount of EtOAc and subsequently precipitated with a large excess of hexanes and the resultant solid was collected on a frit and washed with hexanes to afford 0.52 g (35% yield) of the title compound as a tan solid. ^{1}H NMR (500 MHz, $CDCl_3$, 25 °C) δ 5.54 (s, 1H), 5.98 (m, 1H), 6.09 (m, 1H), 6.20 (m, 1H), 6.78 (m, 1H), 6.84 (m, 1H), 7.15 (m, 2H), 7.43 (m, 1H), 8.11 (m, 1H), 8.16 (bs, 1H), 8.57 (m, 2H), 8.78 (m, 1H), 9.06 (m, 1H), 9.56 (bs, 1H).

1-Picolinoyl-5-(3-pyridyl)dipyrromethane (30)

In an oven-dried flask, 1.52 g 5-(3-pyridyl)dipyrromethane (**17**) (6.8 mmol) was dissolved in 15 mL anhydrous THF under an argon atmosphere to afford a tan solution. Then 17 mL EtMgBr (1 M solution in THF) was slowly added and the resultant dark brown solution was stirred at room temperature for 10 minutes. The solution was cooled to –78 °C in a dry ice/acetone bath and 1.48 g *S*-2-pyridyl picolinothioate (**22**) (6.8 mmol) was added as a solid in one portion; the resultant mixture was stirred at –78 °C for 10 minutes. The solution was then warmed to room temperature and stirred for an additional 3 hours. Saturated NH_4Cl was added and the product was extracted with EtOAc; the combined organics were washed with water and brine then dried over Na_2SO_4. Solvent was removed by rotary evaporation to afford a brown oil.

The crude reaction mixture was loaded onto a silica gel column packed with EtOAc. The product (second band, turns yellow-orange upon Br_2 staining on TLC) was eluted with 100% EtOAc. After solvent removal, the oily brown residue was dissolved in a minimal amount of EtOAc and subsequently precipitated with a large excess of hexanes and the resultant solid was collected on a frit and washed with hexanes to afford 0.79 g (35% yield) of the title compound as a tan solid. ^{1}H NMR (500 MHz, $CDCl_3$, 25 °C) δ 5.59 (s, 1H), 5.98 (m, 1H), 6.09 (m, 1H), 6.22 (m, 1H), 6.79 (m, 1H), 7.26 (m, 1H), 7.28 (m, 1H), 7.43 (overlapping m, 1H), 7.44 (overlapping m, 1H), 7.56 (m, 1H), 7.87 (m, 1H), 8.20 (overlapping bs, 1H), 8.22 (overlapping bs, 1H), 8.54 (m, 1H), 8.55 (m, 2H).

1-Isonicotinoyl-5-(2-pyridyl)dipyrromethane (31)

In an oven-dried flask, 1.16 g 5-(2-pyridyl)dipyrromethane (**18**) (5.2 mmol) was dissolved in 11 mL anhydrous THF under an argon atmosphere to afford a tan solution. Then 13 mL EtMgBr (1 M solution in THF) was slowly added and the resultant dark brown solution was stirred at room temperature for 10 minutes. The solution was cooled to –78 °C in a dry ice/acetone bath and 0.98 g *S*-2-pyridyl isonicotinothioate (**20**) (4.5 mmol) was added as a solid in one portion; the resultant mixture was stirred at –78 °C for 10 minutes. The solution was then warmed to room temperature and stirred for an additional 3 hours. Saturated NH_4Cl was added and the product was extracted with EtOAc; the combined organics were washed with water and brine then dried over Na_2SO_4. Solvent was removed by rotary evaporation to afford a brown oil. The crude reaction mixture was loaded onto a silica gel column packed with EtOAc. The product (second band, turns yellow-orange upon Br_2 staining on TLC) was eluted with 100% EtOAc. After solvent removal, the oily brown residue was dissolved in a minimal amount of EtOAc and subsequently precipitated with a large excess of hexanes and the resultant solid was collected on a frit and washed with hexanes to afford 0.28 g (19% yield) of the title compound as an orange-tan solid. ^{1}H NMR (400 MHz, $CDCl_3$, 25 °C) δ 5.53 (s, 1H), 6.07 (m, 1H), 6.11 (m, 1H), 6.15 (m, 1H), 6.74 (m, 1H), 6.76 (m, 1H), 7.26 (m, 1H), 7.34 (m, 1H), 7.61 (m, 2H), 7.71 (m, 1H), 8.70 (m, 1H), 8.75 (m, 2H), 9.14 (bs, 1H), 10.01 (bs, 1H).

5-(4-Methoxycarbonylphenyl)-10,15,20-tris(4-pyridyl)porphyrin (10)

In a 10 mL microwave tube, 69 mg 1-isonicotinoyl-5-(4-pyridyl)dipyrromethane (**25**) (0.2 mmol) and 76 mg 1-isonicotinoyl-5-(4-methoxycarbonylphenyl)dipyrromethane (**24**) (0.2 mmol) were dissolved in 4 mL toluene to afford a dark brown-black suspension. After the addition of 0.6 mL DBU (0.6 g, 4.0 mmol), the suspension became a red solution and was stirred for 5 minutes at room temperature. $MgBr_2$ (420 mg, 2.3 mmol) was added and an additional 1 mL toluene was added to rinse the walls of the tube. The resultant orange-brown suspension was placed in a microwave reactor and irradiated at 115 °C for 2 hours. The reaction mixture was transferred to a flask, dissolved in THF, and the solvent was removed by rotary evaporation. The residue was dissolved in EtOAc, washed with water, and brought to dryness under rotary evaporation. The magnesium porphyrins of the crude reaction mixture were demetallated by dissolving the residue in 10 mL CH_2Cl_2 and adding 0.2 mL TFA (0.3 g, 2.6 mmol); the resulting green solution was stirred at room temperature for 30 minutes. Then 0.4 mL NEt_3 (0.3 g, 2.9 mmol) was added and the reaction mixture was washed with water and brine, dried over Na_2SO_4, and brought to dryness. The residue was loaded onto a silica gel column and eluted with EtOAc. After removal of the *trans*-A_2B_2 product, the solvent was changed to 4% MeOH in EtOAc to give 15 mg (11% yield) of the title compound. ^{1}H NMR (500 MHz, $CDCl_3$, 25 °C) δ –2.90 (bs, 2H), 4.12 (s, 3H), 8.16 (m, 6H), 8.30 (m, 2H), 8.47 (m, 2H), 8.82–8.89 (bm, 8H), 9.06 (m, 6H).

5,10-Diphenyl-15,20-bis(3-pyridyl)porphyrin (32)

In a 10 mL microwave tube, 60 mg 1-nicotinoyl-5-(3-pyridyl)dipyrromethane (**26**) (0.18 mmol) and 60 mg 1-benzoyl-5-phenyldipyrromethane (**23**) (0.18 mmol) were dissolved in 4 mL toluene to afford a dark brown-black suspension. After the addition of 0.6 mL DBU (0.6 g, 4.0 mmol), the suspension became a red solution and was then stirred for 5 minutes at room temperature. $MgBr_2$ (453 mg, 2.5 mmol) was added and an additional 1 mL toluene was added to rinse the solids down the tube and the resultant orange-brown suspension was placed in a microwave reactor and irradiated at 115 °C for 2 hours. The reaction mixture was transferred to a flask, dissolved in THF, and the solvent was removed by rotary evaporation. The residue was dissolved in EtOAc, washed with water and brine, dried over Na_2SO_4, and brought to dryness. The crude reaction mixture was purified on a silica gel column using EtOAc as the eluent to remove the first major band, Mg(TPP). The solvent was then switched to 5% MeOH in EtOAc to elute the desired product, the second fluorescent band on the column. The A_4 complex remained at the top of the column and was not isolated. The magnesium complex was demetallated by dissolving the solid in 10 mL CH_2Cl_2 and adding 0.2 mL TFA (0.3 g, 2.6 mmol); the resulting green solution was stirred at room temperature for 30 minutes. Then 0.4 mL NEt_3 (0.3 g, 2.9 mmol) was added and the reaction mixture was washed with water and brine, dried over Na_2SO_4, and brought to dryness. The free-base porphyrin (27 mg, 24% yield) was then used without further purification. ^1H NMR (500 MHz, $CDCl_3$, 25 °C) δ –2.81 (bs, 2H), 7.75–7.81 (overlapping m, 6H), 7.79 (overlapping m, 2H), 8.22 (d, J = 6.1 Hz, 4H), 8.53 (d, J = 6.8 Hz, 2H), 8.80 (d, J = 4.7 Hz, 2H), 8.84 (s, 2H), 8.87 (s, 2H), 8.91 (d, J = 4.7 Hz, 2H), 9.06 (m, 2H), 9.46 (s, 2H).

5,10-Diphenyl-15,20-bis(3-pyridyl)porphyrinatopalladium(II) (Pd-32)

In a 10 mL microwave tube, 16 mg of the free-base porphyrin **32** (0.03 mmol) was dissolved in 3 mL pyridine and 55 mg Pd(acac)$_2$ (0.2 mmol) was added. An additional 1 mL of pyridine was added to rinse solids down the tube. The resultant solution was placed in a microwave reactor and irradiated at 180 °C for 20 minutes. The crude reaction mixture was filtered through a plug of Celite and rinsed with CH_2Cl_2; the collected orange filtrate was brought to dryness. The palladium complex was purified on a silica gel column using EtOAc as the eluent to give 7 mg (32% yield) of the title product. ^{1}H NMR (500 MHz, $CDCl_3$, 25 °C) δ 7.72–7.80 (m, 8H), 8.16 (m, 4H), 8.48 (m, 2H), 8.46 (d, J = 5.1 Hz, 2H), 8.80 (d, J = 2.2 Hz, 2H), 8.84 (s, 2H), 8.87 (d, J = 5.1 Hz, 2H), 9.04 (m, 2H), 9.42 (m, 2H).

5,10-Diphenyl-15,20-bis(4-pyridyl)porphyrinatomagnesium(II) (Mg-33)

In a 10 mL microwave tube, 60 mg 1-isonicotinoyl-5-(4-pyridyl)dipyrromethane (**25**) (0.18 mmol) and 60 mg 1-benzoyl-5-phenyldipyrromethane (**23**) (0.18 mmol) were dissolved in 4 mL toluene to afford a dark brown-black suspension. After the addition of 0.6 mL DBU (0.6 g, 4.0 mmol), the suspension became a red solution and was then stirred for 5 minutes. $MgBr_2$ (444 mg, 2.4 mmol) was added and an additional 1 mL toluene was added to rinse the solids down the tube and the resultant orange-brown suspension was placed in a microwave reactor and irradiated at 115 °C for 2 hours. The reaction mixture was transferred to a flask, dissolved in THF, and the solvent was removed by rotary evaporation. The residue was dissolved in EtOAc, washed with water and brine, dried over Na_2SO_4, and brought to dryness. The crude reaction mixture was purified on a silica gel column using ethyl acetate as the eluent to remove the first major band, Mg(TPP). The solvent was then switched to 5% MeOH in EtOAc to elute the desired product, the second fluorescent band on the column. The A_4 complex with four 4-pyridyl groups remained at the top of the column and was not isolated. Solvent was removed by rotary evaporation to afford 27 mg (23% yield) of the magnesium complex. ^{1}H NMR (400 MHz, $CDCl_3$, 25 °C) δ 7.40 (bs, 4H), 7.58 (m, 2H), 7.67–7.77 (m, 6H), 8.16 (m, 4H), 8.20 (bs, 2H), 8.28 (m, 2H), 8.46 (d, *J* = 5.0 Hz, 2H), 8.79 (d, *J* = 4.6 Hz, 2H), 8.89 (s, 2H).

5,10-Diphenyl-15,20-bis(4-pyridyl)porphyrinatopalladium(II) (Pd-33)

The magnesium complex was demetallated by dissolving 11 mg of **Mg-33** (0.017 mmol) in 10 mL CH_2Cl_2 and adding 0.2 mL TFA (0.3 g, 2.6 mmol); the resulting green solution was stirred at room temperature for 30 minutes. Then 0.4 mL NEt_3 (0.3 g, 2.9 mmol) was added and the reaction mixture was washed with water and brine, dried over Na_2SO_4, and brought to dryness to give the crude free-base porphyrin **33**, which was used without further purification. The residue was dissolved in 3 mL pyridine and transferred to a 10 mL microwave tube and 51 mg $Pd(acac)_2$ (0.17 mmol) was added. An additional 1 mL of pyridine was added to rinse solids down the tube. The resultant solution was placed in a microwave reactor and irradiated at 180 °C for 20 minutes. The crude reaction mixture was filtered through a plug of Celite and rinsed with CH_2Cl_2; the collected orange filtrate was brought to dryness. The palladium complex was purified on a silica gel column packed with CH_2Cl_2 using EtOAc as the eluent followed by 10% MeOH in EtOAc to give 5 mg (40% yield) of the title product as an orange solid. ^{1}H NMR (500 MHz, $CDCl_3$, 25 °C) δ 7.72–7.79 (m, 6H), 8.11 (m, 4H), 8.14 (m, 4H), 8.74 (d, *J* = 4.9 Hz, 2H), 8.78 (s, 2H), 8.82 (s, 2H), 8.85 (d, *J* = 4.9 Hz, 2H), 9.01 (m, 4H).

1,9-Diisonicotinoyl-5-(4-pyridyl)dipyrromethane (34)

In an oven-dried flask, 1.40 g 5-(4-pyridyl)dipyrromethane (**16**) (6.3 mmol) was dissolved in 6.5 mL anhydrous THF under an argon atmosphere. Then 38 mL MesMgBr (1 M solution in THF) was slowly added and the resultant solution was stirred at room temperature for

10 minutes. Then 2.88 g isonicotinoyl chloride hydrochloride (16.2 mmol) was added as a solid in one portion and the resultant solution was stirred at room temperature for 45 minutes under argon. Saturated NH_4Cl was added and the product was extracted with EtOAc; the combined organics were washed with saturated $NaHCO_3$, water, and brine. The reaction mixture was purified on a silica gel column packed with EtOAc, using this solvent as the initial eluent. After eluting the column for two days to remove the 1-isonicotinoyl-5-(4-pyridyl)dipyrromethane (**25**) byproduct, the solvent was changed to 1:4 MeOH:EtOAc to elute the desired 1,9-diacyl dipyrromethane. Due to the polarity of the product, the product was very difficult to separate and could not readily be separated from **25**. A ^{1}H NMR of pure product could not be obtained, as signals from **25** dominated every acquired spectrum.

Dibutyl[5,10-dihydro-1,9-diisonicotinoyl-5-(4-pyridyl)dipyrrinato]tin(IV) (Sn-34)

In an oven-dried flask, 1.42 g 5-(4-pyridyl)dipyrromethane (**16**) (6.4 mmol) was dissolved in 10 mL anhydrous THF under an argon atmosphere. Then 40 mL MesMgBr (1 M solution in THF) was slowly added and the resultant solution was stirred at room temperature for 10 minutes. Then 2.89 g isonicotinoyl chloride hydrochloride (16.2 mmol) was added as a solid in one portion and the resultant solution was stirred at room temperature for 1.5 hours under argon. Saturated NH_4Cl was added and the product was extracted with EtOAc; the combined organics were washed with saturated $NaHCO_3$, water, and brine, then subsequently dried over Na_2SO_4. Solvent was removed by rotary evaporation. The residue was dissolved in 30 ml CH_2Cl_2 and 2.7 mL NEt_3 (1.96 g, 19.4 mmol) was added. The solution was then treated with 2.07 g Bu_2SnCl_2 (6.8 mmol) and stirred at room temperature overnight. During this time, the reaction mixture turned black and only decomposition products were observed by TLC.

1,9-Dibenzoyl-5-phenyldipyrromethane (35)

In an oven-dried flask, 0.41 g 5-phenyldipyrromethane (**14**) (1.8 mmol) was dissolved in 40 mL toluene under a nitrogen atmosphere to afford a tan solution. Then 9 mL EtMgBr (1 M solution in THF) was slowly added and the resultant amber solution was stirred at room temperature for 20 minutes. Then 0.7 mL benzoyl chloride (0.85 g, 6 mmol) was added and the resultant mixture was stirred for an additional hour at room temperature. Saturated $(NH_4)SO_4$ was added and the product was extracted with EtOAc (x3); the combined organics were washed with water and brine then dried over Na_2SO_4. Solvent was removed by rotary evaporation to afford a brown oil. After the addition of a large excess of hexanes, a brown solid was obtained, collected on a frit, and washed with hexanes, affording 0.16 g (20% yield) of the title product. The compound used without further purification as only one spot was visible by TLC (100% CH_2Cl_2) and the ^1H NMR spectrum indicated a nearly pure product. ^1H NMR (400 MHz, $CDCl_3$, 25 °C) δ 5.66 (s, 1H), 6.04 (m, 2H), 6.68 (m, 2H), 7.40–7.47 (m, 9H), 7.78–7.44 (m, 6H), 10.63 (bs, 2H).

5,10,15-Triphenyl-20-(4-pyridyl)porphyrin (37)

In an oven-dried flask, 90 mg 1,9-dibenzoyl-5-phenyldipyrromethane (**35**) (0.21 mmol) was dissolved in 12 mL anhydrous THF and 4 mL anhydrous MeOH under a nitrogen atmosphere to give a brown solution. Then, 0.42 g $NaBH_4$ (11 mmol) was added and the resultant tan-orange mixture was stirred at room temperature for 1 hour. Water was added to quench excess $NaBH_4$ and the product was extracted with CH_2Cl_2 and dried over K_2CO_3 to afford a solution of the corresponding dicarbinol (**36**). Since the dicarbinol is prone to decomposition, the solution was concentrated to near-dryness without heating. The residue was then dissolved in 50 mL MeCN and 45 mg 5-(4-pyridyl)dipyrromethane (**16**) (0.20 mmol) and

1.22 g Yb(OTf)$_3$ (2.0 mmol) were added; the resulting red solution was stirred at room temperature for 1 hour, protected from light. DDQ (183 mg, 0.81 mmol) was added and the solution was stirred at room temperature for an additional hour. NEt$_3$ (2 mL, 1.6 g, 16 mmol) was then added and stirred for an additional 30 minutes. Ethyl acetate was added and the reaction mixture was washed with water and brine, dried over Na$_2$SO$_4$, and brought to dryness. The product was purified on a silica gel column using EtOAc as the eluent to obtain 30 mg (24% yield) of the title compound. ^{1}H NMR (400 MHz, CDCl$_3$, 25 °C) δ –2.80 (bs, 2H), 7.75–7.80 (m, 9H), 8.17 (m, 2H), 8.22 (m, 6H), 8.80 (d, *J* = 4.5 Hz, 2H), 8.86 (s, 4H), 8.90 (d, *J* = 4.7 Hz, 2H), 9.03 (m, 2H).

5,10,15-Triphenyl-20-(4-pyridyl)porphyrinatopalladium(II) (Pd-37)

In a 10 mL microwave tube, 30 mg of the free-base porphyrin **37** (0.049 mmol) was dissolved in 3 mL pyridine and 136 mg Pd(acac)$_2$ (0.4 mmol) was added. An additional 1 mL of pyridine was added to rinse solids down the tube. The resultant solution was placed in a microwave reactor and irradiated at 180 °C for 20 minutes. The crude reaction mixture was filtered through a plug of Celite and rinsed with CH$_2$Cl$_2$; the collected orange filtrate was brought to dryness. The palladium complex was purified on a silica gel column using CH$_2$Cl$_2$ as the eluent to give 6 mg (17% yield) of the title product. ^{1}H NMR (500 MHz, CDCl$_3$, 25 °C) δ 7.72–7.80 (m, 9H), 8.13 (m, 2H), 8.16 (m, 6H), 8.75 (d, *J* = 5.1 Hz, 2H), 8.82 (s, 4H), 8.85 (d, *J* = 5.1 Hz, 2H), 9.02 (m, 2H).

1-Bromo-9-isonicotinoyl-5-(4-pyridyl)dipyrromethane (38)

In an oven-dried flask, 125 mg 1-isonicotinoyl-5-(4-pyridyl)dipyrromethane (**25**) (0.38 mmol) was dissolved in 8 mL anhydrous THF under argon. The mixture was briefly heated with a heat gun to ensure that all of the solid material had dissolved. The solution was cooled to –78

°C in a dry ice/acetone bath and 70 mg *N*-bromosuccinimide (0.39 mmol) was added as a solid in several small portions. The resultant mixture was stirred at –78 °C for 1 hour. After removing the bath, water (20 mL) and hexanes (20 mL) were added and the biphasic solution was stirred and allowed to warm to room temperature. The product was extracted with EtOAc and the combined organics were washed with water and brine then dried over K_2CO_3. Solvent was removed by rotary evaporation without heating. The crude material was filtered over a plug of silica with EtOAc to afford 134 mg (87% yield) of the title compound as a yellow solid. The product was stored at 4 °C protected from light. ^{1}H NMR (500 MHz, $CDCl_3$, 25 °C) δ 5.47 (s, 1H), 5.90 (m, 1H), 6.10 (m, 1H), 6.13 (m, 1H), 6.83 (m, 1H), 7.14 (m, 2H), 7.64 (m, 2H), 8.05 (bs, 1H), 8.61 (m, 2H), 8.79 (m, 2H), 9.43 (bs, 1H).

1-Bromo-15-(4-methoxycarbonylphenyl)-19-(isonicotinoyl)-5,10-bis(4-pyridyl)bilane (40)

In an oven-dried flask, 50 mg 1-bromo-9-isonicotinoyl-5-(4-pyridyl)dipyrromethane (**38**) (0.12 mmol) was dissolved in 7 mL anhydrous THF and 3 mL anhydrous MeOH under argon. Then, 166 mg $NaBH_4$ (4.4 mmol) was added as a solid in one portion and the resulting solution was stirred at room temperature for 45 minutes, protected from light. Saturated NH_4Cl was added to quench the excess $NaBH_4$ and the product was extracted with Et_2O; the combined organics were then washed with water and brine then dried over K_2CO_3 to afford a solution of the carbinol (**39**). Since the carbinol is not very robust, the solution was concentrated to near-dryness without heating. The residue was dissolved in 2 mL anhydrous MeCN and 47 mg 1-isonicotinoyl-5-(4-methoxycarbonylphenyl)dipyrromethane (**24**) (0.12 mmol) and 39 mg $Yb(OTf)_3$ (0.06 mmol) were added; the mixture was stirred at room temperature for 30 minutes, protected from light. Over the course of the next 3.5 hours, 666 mg $Yb(OTf)_3$ (1.0 mmol) was added in several portions. After 4 hours of total reaction time, 700 mg $Yb(OTf)_3$ (1.1 mmol) was added in one portion and the mixture was stirred at room temperature overnight. The reaction mixture was neutralized with 0.8 mL NEt_3 (0.3 g, 2.9 mmol) and the product was extracted with EtOAc. The combined organics were washed with water and brine then dried over K_2CO_3. Solvent was removed by rotary evaporation without heating to afford the crude bilane **40**. Due to the relatively clean conversion (as observed by TLC) to the bilane, the instability of the compound, and the high polarity of this species, the crude residue was used without further purification.

5-(4-Methoxycarbonylphenyl)-10,15,20-tris(4-pyridyl)porphyrin (10)

The crude bilane **40** was dissolved in 3 mL anhydrous toluene and 0.2 mL DBU (0.2 g, 1.3 mmol) was added; the mixture was transferred to a 10 mL microwave tube and stirred for 5 minutes. Then 79 mg $MgBr_2$ (0.43 mmol) was added and the resultant suspension was placed in a microwave reactor and irradiated at 115 °C for 2 hours. The reaction mixture was transferred to a flask, dissolved in THF, and the solvent was removed by rotary evaporation. The residue was dissolved in a minimal amount of EtOAc and filtered through a plug of silica, using EtOAc to elute the fluorescent porphyrin material. The porphyrin was demetalted by dissolving the residue in 10 mL CH_2Cl_2 and adding 0.2 mL TFA (0.3 g, 2.6 mmol); the resultant green solution was stirred at room temperature for 30 minutes. Then 0.4 mL NEt_3 (0.3 g, 2.9 mmol) was added and the reaction mixture was washed with water and brine, dried over Na_2SO_4, and brought to dryness. The product was then purified on a silica gel column using EtOAc then 10% MeOH in EtOAc to afford 12 mg (15% yield, based on the amount of **38** used in the bilane synthesis) of the title compound. ^1H NMR (500 MHz, $CDCl_3$, 25 °C) δ –2.90 (bs, 2H), 4.12 (s, 3H), 8.16 (m, 6H), 8.30 (m, 2H), 8.47 (m, 2H), 8.82–8.89 (bm, 8H), 9.06 (m, 6H).

Water Solubilization of Pyridyl Porphyrins

5(4-Carboxyphenyl)-10,15,20-tris(4-pyridyl)porphyrinatopalladium(II) (Pd-41)

In a 10 mL microwave tube with three stir bars, 43 mg **Pd-10** (0.55 mmol) was dissolved in 2 mL of anhydrous inhibitor-free THF and 2 mL of 6M NaOH was added. The biphasic mixture was irradiated in a microwave reactor for 12 hours at 80 °C. Concentrated HCl(aq) was added dropwise to the reaction mixture until all of the solid material had dissolved. The mixture was stirred for one hour in darkness. The crude reaction mixture was poured into water and the product was extracted with CH_2Cl_2. Since the product was suspended in the organic layer, THF was added to homogenize the organic layer. A third orange layer emerged between the two layers, suggestive of protonation of the pyridyl substitutents. As a result, a sufficient quantity of NEt_3 was added to neutralize it such that all of the material migrated to the organic layer. The combined organics were dried over Na_2SO_4 and solvent was removed by rotary evaporation. The crude material was filtered over a plug of silica using EtOAc followed by MeOH as the eluent. The collected filtrate was concentrated, dissolved in CH_2Cl_2, and concentrated HCl was added to ensure the protonation of the carboxylate; the resultant mixture was stirred in darkness at room temperature for 1 hour. The product was extracted with CH_2Cl_2 and a minimal amount of NEt_3 was added to solubilize all of the porphyrin material. The combined organics were washed with water (x2) and brine. After washing with brine, an orange precipitate formed between the two layers. This material was collected on a frit and dried in an oven (~130 °C) overnight. This material was used without further purification.

5(4-Carboxyphenyl)-10,15,20-tris(4-methylpyridin-4-ium-1-yl)porphyrin triiodide (42)

*Method 1: Starting from **43***

In a 10 mL microwave tube with three stir bars, 20 mg **43** (0.018 mmol) was dissolved in 1 mL of H_2O and 2 mL of 6M NaOH was added. The solution was irradiated in a microwave reactor for 12 hours at 80 °C. During the course of the reaction, a brown precipitate was formed. This solid was collected on a frit and was washed with water and then 1 M HCl to remove brown impurities, leaving a purple solid that was dried under vacuum.

*Method 2: Starting from **Zn-43***

In a 10 mL microwave tube with three stir bars, the residue obtained from the synthesis of **Zn-43** was dissolved in 1 mL of H_2O and 2 mL of 6M NaOH was added. The solution was irradiated in a microwave reactor for 24 hours at 80 °C. Concentrated HCl was added to the reaction mixture and the resultant solution was stirred for 2 days. The solution was subsequently neutralized with 6 M NaOH, resulting in a color change from green to purple, indicating the presence of the neutral free-base porphyrin. The solution was brought to dryness.

5(4-Carboxyphenyl)-10,15,20-tris(4-methylpyridin-4-ium-1-yl)porphyrinatopalladium(II) triiodide (Pd-42)

*Method 1: Starting from **Pd-41***

The material collected from the preparation of **Pd-41** was dissolved in 5 mL CH_2Cl_2 and a few drops of TFA were added to solubilize the material. Iodomethane (1 mL, 2.3 g, 16 mmol) was added and the resultant mixture was stirred at room temperature for 18.5 hours. Solvent was removed by rotary evaporation. It was found that the residue was soluble in CH_2Cl_2, suggesting that the alkylation reaction was unsuccessful.

*Method 2: Starting from **Pd-43***

In a 10 mL microwave tube with three stir bars, 14 mg **Pd-43** (0.012 mmol) was dissolved in 2 mL of anhydrous inhibitor-free THF and 2 mL of 6M NaOH was added. The biphasic mixture was irradiated in a microwave reactor for 24 hours at 80 °C. During the course of the reaction, a brown precipitate formed. This solid was collected on a frit and was washed with water and dried under vacuum overnight to give 27 mg of material. The brown solid was dissolved in pyridine and filtered though a 0.2 μm syringe filter and the filtrate was brought to dryness.

5(4-Methoxycarbonylphenyl)-10,15,20-tris(4-methylpyridin-4-ium-1-yl)porphyrin triiodide (43)

In a 20 mL scintillation vial, 68 mg of **10** (0.10 mmol) was dissolved in 3 mL CH_2Cl_2 and 0.8 mL iodomethane (1.8 g, 13 mmol) was added. The resultant mixture was stirred in darkness at room temperature overnight. Solvent was removed by rotary evaporation and the resultant solid was washed with CH_2Cl_2 until the filtrate was clear. The solid material was dried under vacuum overnight to afford 67 mg (61% yield) of material. ^1H NMR (500 MHz, CD_3OD, 25 °C) δ 4.05 (s, 3H), 4.73 (s, 9H), 8.29 (d, $J = 8.2$ Hz, 2H), 8.43 (d, $J = 8.1$ Hz, 2H), 8.72–9.24 (buried bs, 4H), 8.88 (m, 6H), 8.97 (m, 4H), 9.29 (m, 6H).

5(4-Methoxycarbonylphenyl)-10,15,20-tris(4-methylpyridin-4-ium-1-yl)porphyrinato-palladium(II) triiodide (Pd-43)

Beginning with 20 mg of **10** (0.030 mmol), the complex **Pd-10** was prepared using the above synthetic protocol and filtered over a plug of silica using acetone as the eluent. The filtrate was brought to dryness and the residue was dissolved in 10 mL CH_2Cl_2 and filtered. Iodomethane (0.9 mL, 2.1 g, 14 mmol) was added and the resultant mixture was stirred at room temperature for 15.5 hours. Solvent was removed by rotary evaporation and the solid residue was washed with CH_2Cl_2, affording 14 mg of material (39% yield, based on the starting amount of **10**).

5(4-Methoxycarbonylphenyl)-10,15,20-tris(4-methylpyridin-4-ium-1-yl) porphyrinatozinc(II) triiodide (Zn-43)

In a 20 mL scintillation vial, 21 mg **Zn-10** (0.028 mmol) was dissolved in 6 mL CH_2Cl_2 and 0.8 mL iodomethane (1.8 g, 13 mmol) was added and the resultant mixture was stirred in darkness at room temperature overnight. Solvent was removed by rotary evaporation and the solid residue was dissolved in water, filtered (leaving behind 18 mg of material), and the filtrate was brought to dryness.

5(4-Methoxycarbonylphenyl)-10,15,20-tris(4-[3-(pyridin-1-ium-1-yl)propane-1-sulfonate])porphyrinatopalladium(II) (Pd-44)

In a 100 mL round bottom flask, 20 mg **Pd-10** (0.026 mmol) was dissolved in 10 mL benzene. Then 0.5 mL 1,3-propanesultone (0.70 g, 5.7 mmol) was added and the solution was refluxed for 5 hours. During the course of the reaction, a red-purple precipitate formed; the solid was collected on a frit and washed with benzene to afford 27 mg of material (91% yield). ^1H NMR (400 MHz, $(CD_3)_2SO$, 25 °C) δ 2.59 (bm, 6H), 2.82 (bm, 6H), 4.05 (s, 3H), 5.06 (bm, 6H), 8.34 (m, 4H), 8.42 (m, 2H), 8.89 (m, 4H), 8.97 (m, 6H), 9.11 (m, 4H), 9.18 (m, 2H), 9.53 (m, 2H).

Porphyrins for Tt H-NOX

Palladium(II) Mesoporphyrin IX dimethyl ester (Pd-45)

In a 10 mL microwave tube, 50 mg **45** (0.084 mmol) and 90 mg $Pd(acac)_2$ (0.30 mmol) were dissolved in 3 mL pyridine. The resultant mixture was irradiated in a microwave reactor for

15 minutes at 180 °C. The crude reaction mixture was filtered through a plug of Celite and the filtrate was brought to dryness. The residue was purified on a silica gel column using CH_2Cl_2 as the eluent then increasing to 1:1 EtOAc:CH_2Cl_2. The solution was brought to dryness by rotary evaporation to afford 59 mg (100% yield) of a red-purple solid. ^1H NMR (400 MHz, $CDCl_3$, 25 °C) δ 1.86 (t, 6H), 3.28 (t, 4H), 3.58 (s, 3H), 3.59 (s, 3H), 3.61 (s, 3H), 3.62 (s, 3H), 3.68 (s, 3H), 3.69 (s, 3H), 4.04 (m, 4H), 4.38 (m, 4H), 10.07 (overlapping s, 4H).

Platinum(II) Mesoporphyrin IX dimethyl ester (Pt-45)

In a 10 mL microwave tube, 50 mg **45** (0.084 mmol) and 101 mg $Pt(acac)_2$ (0.26 mmol) were dissolved in 3 mL benzonitrile. The resultant mixture was irradiated in a microwave reactor for 15 minutes at 180 °C. The crude reaction mixture was filtered through a plug of Celite and the filtrate was brought to dryness. The residue was purified on a silica gel column using CH_2Cl_2 as the eluent then increasing to 1:1 EtOAc:CH_2Cl_2. The solution was brought to dryness by rotary evaporation to afford 64 mg (97% yield) of a red-purple solid. ^1H NMR (400 MHz, CD_2Cl_3, 25 °C) δ 1.85 (t, 6H), 3.27 (t, 4H), 3.55 (s, 3H), 3.56 (s, 3H), 3.57 (s, 3H), 3.58 (s, 3H), 3.68 (overlapping s, 6H), 4.01 (m, 4H), 4.32 (m, 4H), 10.01 (overlapping s, 3H), 10.02 (s, 1H).

Palladium(II) Mesoporphyrin IX, disodium salt (Pd-46)

In a 10 mL microwave tube with three stir bars, 59 mg **Pd-45** (0.084 mmol) was dissolved in 3 mL of anhydrous inhibitor-free THF and 3 mL of 6M NaOH was added. The biphasic mixture was irradiated in a microwave reactor for 16 hours at 80 °C. During the course of the reaction, a precipitate was formed. The solid material was collected on a frit and dried under vacuum.

Platinum(II) Mesoporphyrin IX (Pt-46)

In a 10 mL microwave tube with three stir bars, 50 mg **Pt-45** (0.063 mmol) was dissolved in 3 mL of anhydrous inhibitor-free THF and 2 mL of 6M NaOH was added. The biphasic mixture was irradiated in a microwave reactor for 12 hours at 80 °C. Concentrated HCl(aq) was added dropwise to the reaction mixture until all of the solid material had dissolved. The mixture was stirred for one hour in darkness. The crude reaction mixture was poured into water and a precipitate formed. The solid material was collected on a frit, then dissolved in MeOH, and subsequently brought to dryness to give 64 mg of material.

Physical Measurements and X-ray Crystallographic Details

^{1}H NMR spectra were recorded at room temperature on a Varian Inova-500, Bruker Avance-400, or Varian Mercury-300 NMR spectrometer at the MIT Department of Chemistry Instrumentation Facility (DCIF) and internally referenced to the residual solvent signal ($\delta = 7.26$ for $CHCl_3$ in $CDCl_3$, $\delta = 5.32$ for $CHDCl_2$ in CD_2Cl_2, $\delta = 3.31$ for CD_2HOD in CD_3OD, $\delta = 8.74$ for C_5D_4HN in C_5D_5N, $\delta = 2.50$ for $(CD_3)(CD_2H)SO$ in $(CD_3)_2SO$).[44] Low-temperature (100 K) x-ray diffraction data was collected on a Siemens Platform three-circle diffractometer coupled to a Bruker-AXS Smart Apex CCD detector with graphite-monochromated Mo Kα radiation ($\lambda = 0.71073$ Å), performing φ- and ω-scans. The data were processed and refined with the program SAINT supplied by Siemens Industrial using standard difference Fourier techniques in the SHELXL program suite (6.10 v., Sheldrick G. M., and Siemens Industrial Automation, 2000). All hydrogen atoms were included in the model at geometrically calculated positions using a riding model and refined isotropically; all non-hydrogen atoms were refined anisotropically. All thermal ellipsoid plots are drawn at the 50% probability level with hydrogen atoms omitted for clarity.

2.8 References

1. McLaurin, E. J.; Greytak, A. B.; Bawendi, M. G.; Nocera, D. G. *J. Am. Chem. Soc.* **2009,** *131*, 12994–13001.
2. Yoshihara, T.; Yamaguchi, Y.; Hosaka, M.; Takeuchi, T.; Tobita, S. *Angew. Chem. Int. Ed.* **2012**, *51*, 4148–4151.
3. Coogan, M. P.; Court, J. B.; Gray, V. L.; Hayes, A. J.; Lloyd, A. H.; Millet, C. O.; Pope, S. J. A.; Lloyd, D. *Photochem Photobiol. Sci.* **2010**, *9*, 103–109.
4. Okura, I.; Kamachi, T. Application of Porphyrins and Related Compounds as Optical Oxygen Sensors. In *Handbook of Porphyrin Science*; Kadish, K. M.; Smith, K. M.; Guilard, R., Eds.; World Scientific Publishing: Singapore, 2011; Vol. 12; pp 297–348.
5. Stern, O.; Volmer, M. *Physik. Zeitschr.* **1919**, *20*, 183–188.
6. Lakowicz, J. R.; *Principles of Fluorescence Spectroscopy*, 3rd ed.; Springer: New York, 2006.
7. Adler, A. D.; Longo, F. R.; Shergalis, W. *J. Am. Chem. Soc.* **1964**, *86*, 3145–3149.
8. Adler, A. D.; Longo, F. R.; Finarelli, J. D.; Goldmacher, J.; Assour, J.; Korsakoff, L. *J. Org. Chem.* **1967**, *32*, 476.
9. Lindsey, J. S.; Wagner, R. W. *J. Org. Chem.* **1989**, *54*, 828–836.
10. Liu, W.; Greytak, A. B.; Lee, J.; Wong, C. R.; Park, J.; Marshall, L. F.; Jiang, W.; Curtin, P. N.; Ting, A. Y.; Nocera, D. G.; Fukumura, D.; Jain, R. K.; Bawendi, M. G. *J. Am. Chem. Soc.* **2010**, *132*, 472–483.
11. Dean, M. L.; Schmink, J. R.; Leadbeater, N. E.; Brückner, C. *Dalton Trans.* **2008**, 1341–1345.

12. Dogutan, D. K.; Bediako, D. K.; Teets, T. S.; Schwalbe, M. S.; Nocera, D. G. *Org. Lett.* **2010**, *12*, 1036–1039.
13. Chang, C. J.; Yeh, C. Y.; Nocera, D. G. *J. Org. Chem.* **2002**, *67*, 1403–1406.
14. McLaurin, E. J. Ph.D. Thesis, Massachusetts Institute of Technology, Cambridge, MA, USA, **2011.**
15. Kruper, W. J.; Chamberlin, T. A.; Kochanny, M. *J. Org. Chem.* **1989**, *54*, 2753–2756.
16. Meng, G. G.; James, B. R.; Skov, K. A.; Korbelik, M. *Can. J. Chem.* **1994**, *72*, 2447–2457.
17. Rubires, R.; Crusats, J.; El-Hachemi, Z.; Jaramillo, T.; López, M.; Valls, E.; Farrera, J. A.; Ribó, J. M. *New J. Chem.* **1999**, 189–198.
18. Chen, Y.; Parr, T.; Holmes, A. E.; Nakanishi, K. *Bioconjugate Chem.* **2008**, *19*, 5–9.
19. Luguya, R.; Jaquinod, L.; Fronczek, F. R.; Vicente, M. G. H.; Smith, K. M. *Tetrahedron* **2004**, *60*, 2757–2763.
20. Lembo, A.; Tagliatesta, P.; Cicero, D.; Leoni, A.; Salvatori, A. *Org. Biomol. Chem.* **2009**, *7*, 1093–1096.
21. Ishikawa, Y.; Yamashita, A.; Uni, T. *Chem. Pharm. Bull.* **2001**, *49*, 287–293.
22. Sirish, M.; Chertkov, V. A.; Schneider, H. J. *Chem. Eur. J.* **2002**, *8*, 1181–1188.
23. Gianferrara, T.; Giust, D.; Bratsos, I.; Alessio, E. *Tetrahedron* **2007**, *63*, 5506–5013.
24. Wu, L.; Hu, P.; Xiao, Y.; Zhang, M.; Zhang, L.; Weng, X.; Wu, X.; Zhou, X.; Cao, X. *Chem. Biodivers.* **2008**, *5*, 153–161.
25. Dogutan, D. K.; Zaidi, S. H. H.; Thamyongkit, P.; Lindsey, J. S. *J. Org. Chem.* **2007**, *72*, 7701–7714.
26. Dogutan, D. K.; Lindsey, J. S. *J. Org. Chem.* **2008**, *73*, 6728–6742.

27. Gryko, D.; Lindsey, J. S. *J. Org. Chem.* **2000**, *65*, 2249–2252.

28. Laha, J. K.; Dhanalekshmi, S.; Taniguchi, M.; Ambroise, A.; Lindsey, J. S. *Org. Process Res. Dev.* **2003**, *7*, 799–812.

29. Zaidi, S. H. H.; Loewe, R. S.; Clark, B. A.; Jacob, M. J.; Lindsey, J. S. *Org. Process Res. Dev.* **2006**, *10*, 304–314.

30. Maeda, H.; Hasegawa, M.; Ueda, A. *Chem. Commun.* **2007**, 2726–2728.

31. Zaidi, S. H. H.; Muthukumaran, K.; Tamaru, S.; Lindsey, J. S. *J. Org. Chem.* **2004**, *69*, 8356–8365.

32. Dogutan, D. K.; Ptaszek, M.; Lindsey, J. S. *J. Org. Chem.* **2008**, *73*, 6187–6201.

33. Muthukumaran, K.; Ptaszek, M.; Noll, B.; Scheidt, W. R.; Lindsey, J. S. *J. Org. Chem.* **2004**, *69*, 5354–5364.

34. Milic, T. N.; Chi, N.; Yablon, D. G.; Flynn, G. W.; Batteas, J. D.; Drain, C. M. *Angew. Chem. Int. Ed.* **2002**, *41*, 2117–2119.

35. Deiters, E.; Bulach, V.; Hosseini, M. W. *New. J. Chem.* **2006**, *30*, 1289–1294.

36. Yedukondalu, M.; Ravikanth, M. *J. Chem. Sci.* **2011**, *123*, 201–214.

37. Li, Y.; Xiao, J.; Shubina, T. E.; Chen, M.; Shi, Z.; Schmid, M.; Steinrück, H. P.; Gottfried, J. M.; Lin, N. *J. Am. Chem. Soc.* **2012**, *134*, 6401–6408.

38. Rao, P. D.; Dhanalekshmi, S.; Littler, B. J.; Lindsey, J. S. *J. Org. Chem.* **2000**, *65*, 7323–7344.

39. Tamaru, S.; Yu, L.; Youngblood, J.; Muthukumaran, K.; Taniguchi, M.; Lindsey, J. S. *J. Org. Chem.* **2004**, *69*, 765–777.

40. Lipstman, S.; Goldberg, I. *Acta Crystallogr., Sect. C: Cryst. Struct. Commun.* **2008**, *C64*, m53–m57.

41. Fleischer, E. B.; Miller, C. K.; Webb, L. E. *J. Am. Chem. Soc.* **1964**, *86*, 2342–2347.

42. Gromov, S. P.; Vedernikov, A. I.; Kuz'mina, L. G.; Kondratuk, D. V.; Sazonov, S. K.; Strelenko, Y. A.; Alfimov, M. V.; Howard, J. A. K. *Eur. J. Org. Chem.* **2010**, 2587–2599.

43. Winter, M. B.; McLaurin, E. J.; Reece, S. Y.; Olea, C.; Nocera, D. G.; Marletta, M. A. *J. Am. Chem. Soc.* **2010**, *132*, 5582–5583.

44. Fulmer, G. R.; Miller, A. J. M.; Sherden, N. H.; Gottlieb, H. E.; Nudelman, A.; Stoltz, B. M.; Bercaw, J. E.; Goldberg, K. I. *Organometallics* **2010**, *29*, 2176–2179.

Chapter 3

Quantum Dot–Porphyrin Assemblies as O_2 Sensors

3.1 Background

Having prepared a series of palladium and platinum porphyrins, as described in Chapter 2, the photophysical properties and oxygen sensitivity of these compounds were studied. Following the sensing methodology outlined in Section 1.9, these porphyrins serve as phosphors in a construct with semiconductor quantum dots. In such a system, the quantum dot serves as an antenna for both one- and two-photon absorption. Through FRET, the quantum dot transfers energy to the appended porphyrin, promoting it to an excited electronic state with concomitant quenching of quantum dot luminescence. With the porphyrin in a triplet excited state, it interacts with molecular oxygen through bimolecular quenching of the excited state, thereby returning the phosphor to its electronic ground state. This chapter explores the photophysical properties of these porphyrins and their assembly with quantum dots to furnish nanoscale oxygen sensors.

Fluorescent semiconductor nanocrystals or quantum dots (QDs) have high quantum yields, photostability, narrow emission bands, and broad excitation profiles,[1] rendering them ideal scaffolds for constructing optical biosensors.[2–4] By attaching an analyte-sensitive fluorophore to the QD, Förster resonance energy transfer (FRET) may be exploited as a means of signal transduction.[5–7] Additionally, QDs exhibit high two-photon absorption cross-sections (σ_2 ~10^4 Göppert-Mayer, 1 GM = 10^{-50} cm^4•s/photon),[8–10] making them attractive fluorophores for multiphoton imaging. Near-IR excitation and detection (600–1000 nm) in the so-called therapeutic window allows for imaging with minimal background signal from cellular autofluorescence.[11] This spectral window is readily accessed using two-photon excitation; this imaging technique is nondestructive to tissue and provides high-resolution images of live tissue at depths of several hundred microns with submicron spatial resolution.[12,13] Thus, QDs offer a versatile platform from which to build supramolecular oxygen sensing assemblies.

Many oxygen sensitive phosphors have been reported in the literature: osmium,[14] iridium,[15] and ruthenium[16] polypyridine complexes as well as pyrene.[17] The most well-known and best suited for our biological O_2 sensing are platinum and palladium porphyrins due to their strong room temperature phosphorescence in the 650–800 nm range and long ($\sim 10^2$ μs) triplet lifetimes.[18] Thus far, most oxygen sensing applications have immobilized these porphyrins in polymer matrices,[18–20] on solid surfaces,[18,21] or in mesoporous silica.[18,22] Commercial palladium porphyrins (Oxyphor R2) and benzoporphyrins (Oxyphor G2), which are available as water-soluble glutamate dendrimers, have been used for solution oxygen sensing applications.[23] The long lifetimes of palladium porphyrins make them ideal for oxygen sensing in the biologically relevant 0–160 torr range. Upon optical excitation of the porphyrin, rapid intersystem crossing to a long-lived triplet state occurs. Molecular oxygen (a ground state triplet) deactivates the excited state through collisional quenching, following Stern-Volmer kinetics. By monitoring the intensity or lifetime of the triplet state of the phosphor, the amount of oxygen in a sample is quantified.[24] However, porphyrins alone have prohibitively low two-photon absorption cross-sections (σ_2 = 1–25 GM for free-base tetraphenylporphyrin).[25] An ideal oxygen sensor for biological applications would combine the oxygen-sensitive properties of porphyrins with an efficient two-photon antenna.

While Vinogradov and co-workers have reported a series of two-photon FRET-based oxygen sensors in which a platinum or platinum porphyrin is covalently linked with coumarin dyes serving as two-photon antennae,[26–29] the porphyrin/QD construct offers several advantages over theses conjugates. QDs are more efficient two-photon absorbers than coumarin dyes ($\sigma_2 \sim 10^4$ GM for QDs versus $\sigma_2 = 20$ GM for Coumarin-343[27]). The photophysical properties, namely the emission wavelength, of QDs are tunable,[1] enabling the optimization of spectral overlap with the appended phosphor and maximizing FRET efficiency; such tunability is not possible with conventional organic fluorophores, which are quite limited in both spectral features and quantum yield. Finally, our sensor features several porphyrins per QD rather than several two-photon antennae per porphyrin, giving a greater porphyrin signal on a per sensor basis. Although free-base porphyrin/QD assemblies have been previously prepared and studied as FRET systems,[30–33] these systems have not been studied under two-photon excitation nor have been explored as oxygen sensors. Both ruthenium bipyridine complexes[34] and platinum porphyrins[35,36] have been used as oxygen sensors in conjunction with QDs, but in these systems the QD merely serves as an internal intensity standard (nether a FRET donor nor a two-photon antenna). There are only three examples of authentic FRET-based oxygen sensors with a QD serving as the FRET donor and either pyrene,[17] platinum octaethylporphine ketone,[37] or osmium bipyridine complexes[14] serving as the FRET acceptor. Of these, only the osmium example has been studied under two-photon excitation. This sensor, however, suffers from low dynamic range at biologically relevant oxygen pressures (0–160 torr).[14] The optical response of the pyrene-based sensor is in the 350–400 nm range, which is outside the tissue transparency window and is not an ideal candidate for biological imaging.[17] The platinum octaethylporphine ketone sensor is embedded in a polyvinyl chloride matrix and coated on a micropipette; this is an invasive means of oxygen detection and cannot be translated to *in vivo* applications.[37]

This chapter explores the photophysical properties of palladium and platinum porphyrins as oxygen-sensitive phosphors. Additionally, supramolecular assemblies of a QD and a series of palladium(II) porphyrins have been developed to determine pO_2 in organic solvents. Porphyrins with *meso* pyridyl substituents bind to the surface of the QD to produce self-assembled nanosensors. High spectral overlap between QD emission and porphyrin absorption, results in efficient FRET for signal transduction in these sensors. The QD serves as a photon antenna, enhancing porphyrin emission under both one- and two-photon excitation. While the two-photon cross sections of porphyrins are prohibitively low, these assemblies demonstrate that palladium porphyrins may be used for oxygen sensing under two-photon excitation.

3.2 Photophysical Studies of Pd-1 and Pt-1

In order to validate the claim that palladium and platinum porphyrins are appropriate phosphors for low-pressure oxygen sensing, the photophysical properties of simple porphyrin complexes of these two metals (Chart 3.1) were studied. This porphyrin was selected because it bears a carboxylic acid group that can then be appended to the surface of a PIL-coated quantum dot with terminal amines (see Chapter 1).

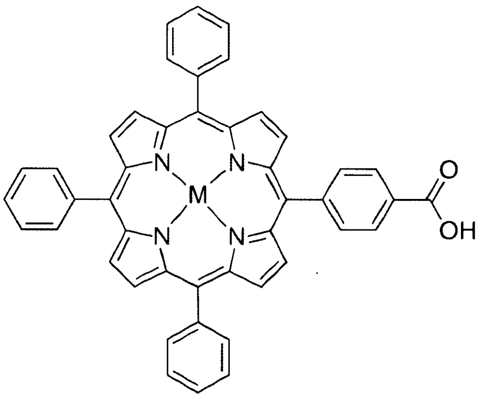

M-1

Chart 3.1. Molecular structure of the metalloporphyrins studied herein.

Compounds **Pd-1** and **Pt-1** display absorption spectra (Figure 3.1) typical of hypsoporphyrins.[38,39] The spectral features of **Pt-1** are blue-shifted by approximately 15 nm relative to **Pd-1** (Table 3.1), which is consistent with the absorption properties of related compounds.[39] Two broad features are observed in the emission spectra (Figure 3.1) and are attributed to phosphorescence transitions from the triplet state and are assigned as T(0,0) for the blue band and T(0,1) for the red band. The emission spectrum of **Pd-1** also exhibits a feature centered at 610 nm and is attributed to the Q(0,1) fluorescence transition; this is a reasonable assignment as this band is rather insensitive to oxygen, in contrast to the phosphorescent transitions. For comparison, this transition has been observed at 606 nm for PdTPP.[40] The emission intensity of **Pd-1** and **Pt-1** in air versus vacuum is drastically different, demonstrating that these compounds are responsive to the oxygen in the 0–160 torr range. Indeed, the phosphorescence emission under vacuum is over 100 times greater than under air. This effect is most pronounced for **Pd-1**, where the enhancement is 140 fold for T(0,0) and 230 fold for T(0,1); the observed increase in signal was found to be 100–120 fold for **Pt-1** at these transitions. The triplet lifetimes (λ_{ex} = 525 nm for **Pd-1** and λ_{ex} = 510 nm for **Pt-1**) were determined in 2-methyltetrahydrofuran at room temperature under both air and vacuum (τ_0). It was found that **Pd-1** exhibits triplet lifetimes of ~250 ns in air and 110 μs under vacuum; this nearly 500 fold difference in lifetime suggests that this phosphor has a sufficient dynamic range to accurately quantify oxygen in the 0–160 torr range. Although **Pt-1** exhibited a similar lifetime in air (~220 ns), the vacuum lifetime was markedly shorter (~30 μs) than the palladium analogue, exhibiting only a 100 fold difference in the lifetime. These observations are consistent with studies of other palladium and platinum porphyrins.[38,39] The shorter lifetime of the platinum complex is due to greater spin-orbit coupling with platinum than palladium,[41] as this parameter scales with atomic number. As a result, there is an enhancement of the rate of both radiative and nonradiative decay pathways, which is consistent with a shorter lifetime.

Table 3.1. Summary of Spectroscopic Data for **Pd-1** and **Pt-1**

Compound[a]	B(0,0)	Q(1,0)	Q(0,0)	T(0,0)[b]	T(0,1)[b]	τ_0 (μs)[c]	τ_{air} (ns)
Pd-1	415	523	553	695	770	110 ± 2[d]	246 ± 3[d]
Pt-1	401	509	538	663	728	26 ± 2[e]	219 ± 3[e]

[a] 2-Methyltetrahydrofuran solution, transition wavelengths are in units of nm, [b] Triplet transitions for evacuated samples (< 10^{-5} torr), [c] Natural triplet lifetime for evacuated samples (< 10^{-5} torr), [d] λ_{ex} = 525 nm, [e] λ_{ex} = 510 nm

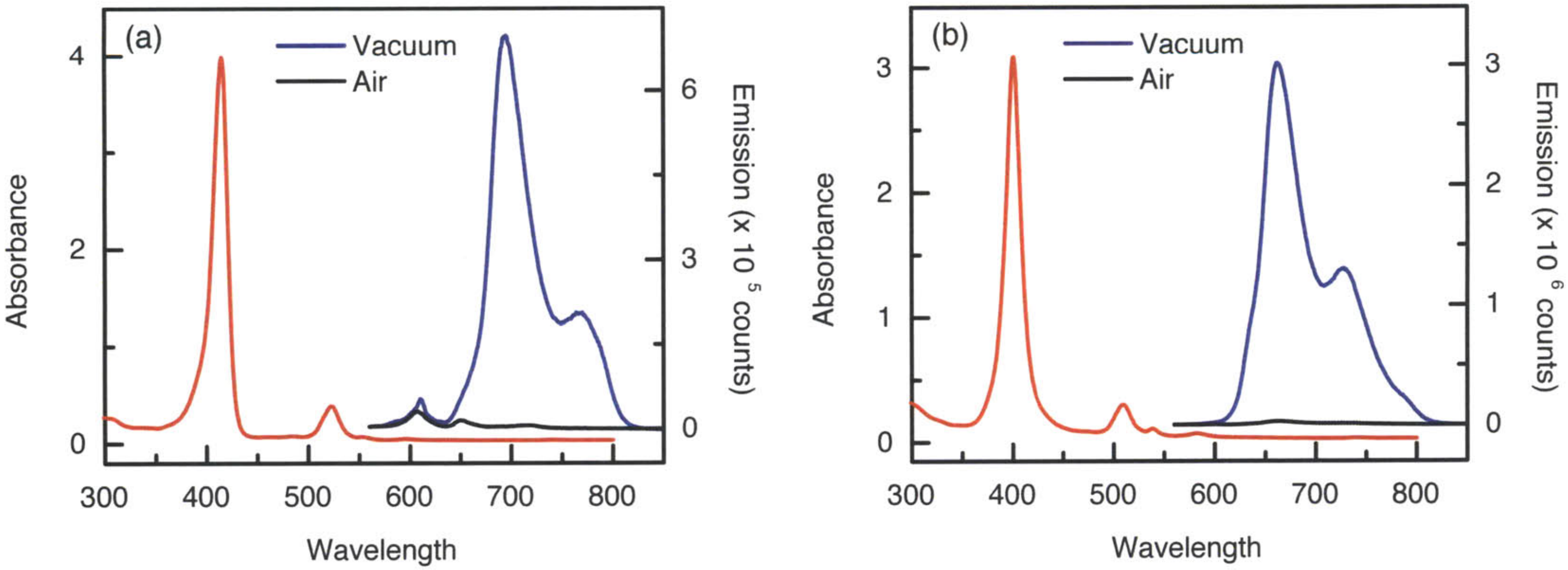

Figure 3.1. Comparison of the steady state absorption (—) and emission spectra of (a) **Pd-1** (λ_{ex} = 525 nm) and (b) **Pt-1** (λ_{ex} = 510 nm). While the emission intensity of the phosphor is almost completely quenched in the presence of air (~160 torr O_2) (—), it is greatly enhanced under vacuum (—).

3.3 Photophysical Studies of Palladium Pyridyl Porphyrins

Chapter 2 described the synthesis of porphyrins bearing *meso* pyridyl substituents. Rather than covalently conjugating these molecules to polymer-coated dots, the pyridyl ring may be exploited as a means of coordinating the porphyrin to the surface of a CdSe quantum dot. This self-assembly circumvents both the laborious synthesis of the PIL ligand and difficult coupling chemistry, resulting in the rapid preparation of oxygen sensors. Additionally, this method enables the facile preparation of sensors with variable porphyrin to quantum dot ratios and allows for high loading of the phosphor so that sufficient signal can be generated for sensing applications. In this sensing scheme (Figure 3.2), the QD is irradiated under two-photon excitation and transfers energy *via* FRET to excite the surface-bound palladium porphyrin (Chart 3.2), which is promoted to an excited triplet state that is quenched by molecular oxygen; the extent of quenching is proportional to the amount of oxygen. Since the QD is unaffected by oxygen, its emission serves as an internal standard to afford a ratiometric sensor; thus, oxygen may also be quantified using the ratio of porphyrin to QD emission.

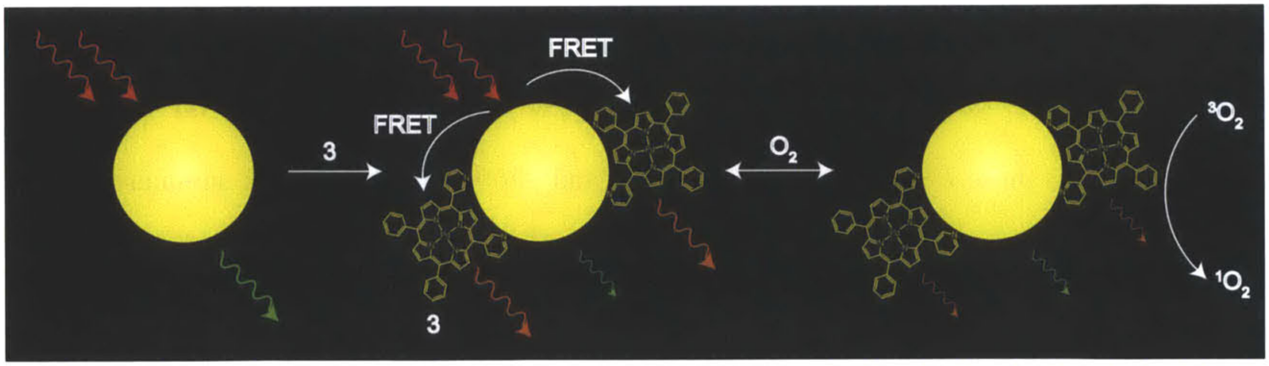

Figure 3.2. Schematic representation of the sensing methodology. The quantum dot (**QD**) is irradiated under two-photon excitation using NIR (700-1000 nm) light. QD emission is quenched in the presence of a surface-bound porphyrin (**3**) and through FRET promotes the porphyrin to an excited electronic state. The phosphorescence is then quenched in the presence of oxygen; the lifetime and intensity of the emission is a quantitative measure of O_2 concentration.

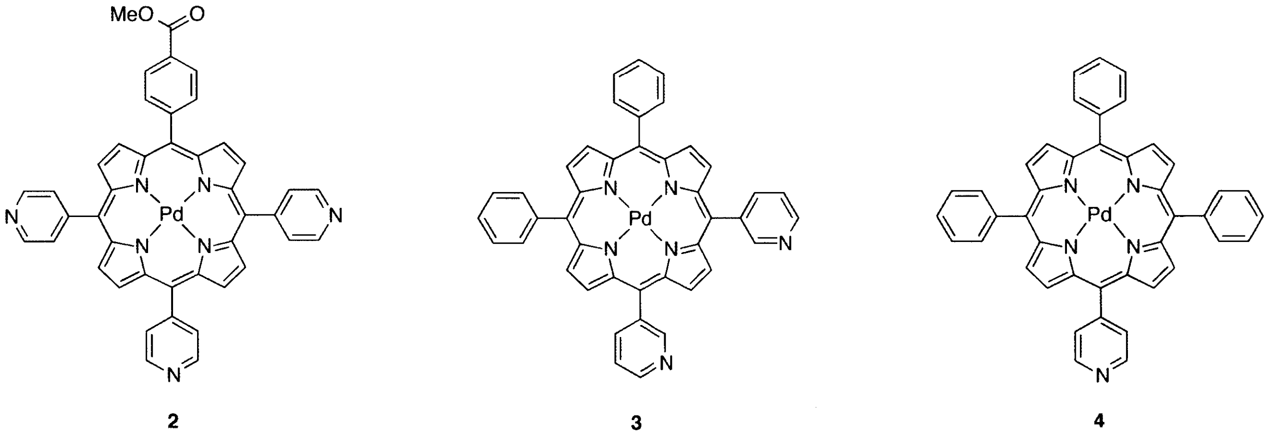

2 **3** **4**

Chart 3.2. Porphyrins bearing *meso*-pyridyl substituents that bind to the surface of CdSe quantum dots.

Porphyrins **2**–**4** display absorption spectra (Figure 3.3) typical of hypsoporphyrins,[38,39] exhibiting an intense B band (Soret) centered around 415 nm and weaker bands at 523 nm for Q(1,0) and 554 nm Q(0,0). These values are similar to other *meso*-substituted palladium porphyrins; for comparison, PdTPP (TPP = 5,10,15,20-tetraphenylporphyrin) exhibits absorbance features at 416, 522, and 551 nm.[41] Extinction coefficients were measured in CH_2Cl_2, as higher concentrations were achieved in this solvent, and fall in the typical ranges for metalloporphyrins.[38] The porphyrin emission spectra (Figure 3.3) (λ_{ex} = 525 nm) exhibit two broad emission bands with maxima observed around 690 nm for T(0,0) and 760 nm for T(0,1) and are similar to those observed for PdTPP (688 and ~760 nm).[41] Table 3.2 summarizes the static linear spectroscopic data for **2**–**4**. Each porphyrin also exhibits a small emission feature around 606 nm and is attributed to the Q(0,1) fluorescence transition. This is a reasonable assignment as this band is rather insensitive to oxygen (similar intensity under both air and vacuum) unlike the phosphorescence transitions (see below); this transition has been observed at 606 nm for PdTPP.[40]

Table 3.2. Summary of Linear Spectroscopic Data for Pd Porphyrins and QD Assemblies

Compound[a]	B(0,0), ε[b]	Q(1,0), ε[b]	Q(0,0), ε[b]	QD_{Em}	T(0,0)[c]	T(0,1)[c]	ϕ_P[d]
2	414, 240	522, 22	554, 3.6	–	684	753	0.014
3	416, 290	523, 24	554, 2.6	–	691	760	0.011
4	415, 250	523, 22	554, 2.8	–	691	760	0.014
QD2	416	523	554	517	684	754	0.040
QD3	418	524	555	518	692	763	0.027
QD4	417	523	553	516	691	761	0.018

[a] Toluene solution, transition wavelengths are in units of nm, [b] ε in 10^3 M^{-1} cm^{-1}, as determined in CH_2Cl_2,
[c] Triplet transitions for evacuated samples (< 10^{-5} torr), [d] Phosphorescence quantum yield for evacuated samples

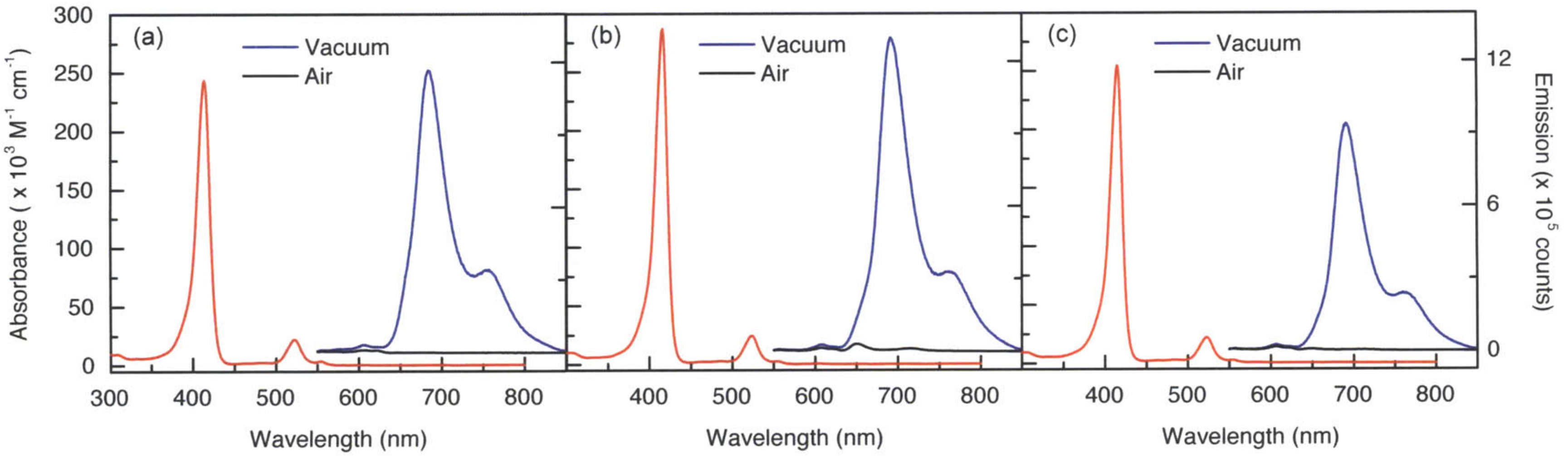

Figure 3.3. Comparison of the steady state absorption (—) and emission spectra (λ_{ex} = 525 nm) of **2** (a), **3** (b), and **4** (c) in toluene. While the emission intensity of the phosphor is almost completely quenched in the presence of air (~160 torr O_2) (—), it is greatly enhanced under vacuum (—).

One additional feature observed in the emission spectrum of **3** is a small feature centered at 650 nm and is assigned to the Q(0,0) transition of the free-base derivative of **3**. No traces of the free-base were visible by NMR and subsequent chromatography was unable to remove this species. Based on the size of the absorbance band and the ten-fold higher quantum yield ($\phi_f = 0.13$ for H_2TTP)[42] over the Pd complex ($\phi_p = 0.011$ for **3**), it is estimated that the free-base is present at most as a 1% impurity. Since the fluorescence band of the free-base porphyrin is eclipsed by the phosphorescence bands of **3** in the absence of oxygen (Figure 3.3b) and the fluorescence lifetime of the free-base ($\tau_{air} \sim 9$ ns for free-base pyridyl porphyrins)[32] is much shorter than **3** ($\tau_{air} \sim 300$ ns), the presence of this species has little impact on the results presented herein. The relative phosphorescence quantum yields were determined using $[Ru(bpy)_3]Cl_2$ as a standard and are between 1–2%, comparable to other Pd porphyrins ($\phi_p = 0.02$ for PdTPP).[43]

The emission intensity of **2**–**4** in air versus vacuum (Figure 3.3) is significantly different, demonstrating that these compounds are responsive to oxygen in the 0–160 torr range. Indeed, the phosphorescence emission under vacuum is over 100 times greater than under air. This effect is most pronounced for **2**, where the enhancement is 500 fold for T(0,0) and 300 fold for T(0,1); the observed enhancement was found to be 100-200 fold for both **3** and **4** at these transitions. The triplet lifetimes ($\lambda_{ex} = 525$ nm) of **2**–**4** were determined in toluene at room temperature under both air and vacuum (τ_0) (Table 3.3), monitoring the emission at 685 nm. Decay traces using data > 100 ns were fit to a monoexponential decay curve ($R_{adj}^2 > 0.96$). It was found that **2**–**4** exhibit triplet lifetimes of ~300 ns in air and ~150 μs under vacuum; this 500 fold difference in lifetime suggests that these phosphors have a sufficient dynamic range to accurately quantify oxygen in the 0–160 torr range.

Table 3.3. Summary of Lifetime Data for Pd Porphyrins

Compound[a]	τ_{air} (ns) linear[c]	τ_0 (μs)[b] linear[c]	τ_{air} (ns) two-photon[d]	τ_0 (μs)[b] two-photon[d]
2	332 ± 3[e]	154 ± 12	556 ± 40	157 ± 3
3	289 ± 7	133 ± 5	354 ± 14	77 ± 5
4	305 ± 6	144 ± 6	365 ± 12	80 ± 3

[a] Toluene solution, [b] Evacuated samples ($< 10^{-5}$ torr), [c] $\lambda_{ex} = 525$ nm, [d] $\lambda_{ex} = 850$ nm, [e] 95% Confidence interval

Although these compounds have low two-photon cross sections, sufficient signal was observed to measure the lifetimes of **2–4** under two-photon (λ_{Ex} = 850 nm) excitation (Table 3.3). After an extensive review of the literature, this is the first study that compares porphyrin lifetimes under one- and two-photon excitation. Due to differences in selection rules for one- and two-photon transitions, different states are accessed under these conditions. For one-photon electronic transitions, the allowed transitions involve a change in parity (*g* ↔ *u*),[44] whereas allowed two-photon transitions involve a conservation of parity (*g* ↔ *g* or *u* ↔ *u*).[45] It has been shown that differences in one- and two-photon lifetimes for linear polyenes are due to vibronic coupling.[46] Since the role of vibronic coupling in porphyrins is well-established,[38] it is not surprising that these lifetimes would be different for **2–4**.

3.4 FRET Experiments

Having characterized the photophysical properties and the oxygen sensitivity of **2–4**, the interaction of these phosphors with a QD were studied. The quantum dot was judiciously chosen such that the emission of the dot overlapped with the Q(1,0) absorbance band of **2–4**, thereby maximizing the spectral overlap integral. To this end, we selected a QD, denoted as **QD**, with a first absorbance feature at 501 nm and emission band (λ_{ex} = 450 nm) centered at 519 nm (Figure 3.4).

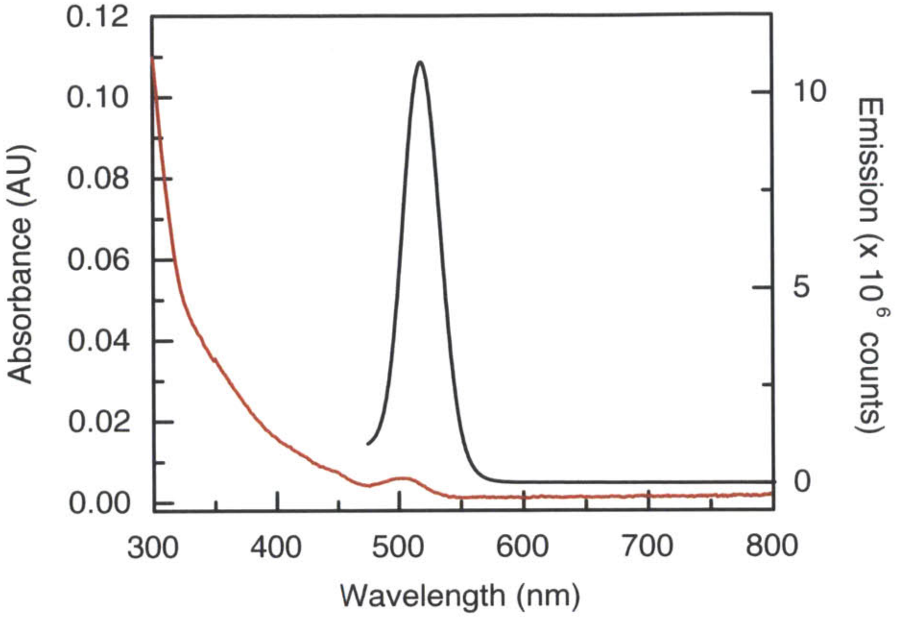

Figure 3.4. Comparison of the steady state absorption (▬) and emission spectra (▬) of **QD** (λ_{ex} = 450 nm) in toluene.

Since **2–4** possess pyridyl rings capable of surface binding to **QD**, the FRET efficiency was studied as a function of porphyrin ring geometry: two *cis* 4-pyridyl rings (**2**), two *cis* 3-pyridyl rings (**3**), and a single 4-pyridyl ring (**4**). With the presence of two adjacent pyridyl rings, the porphyrin may bind to the surface in a bidentate-like fashion. Titrations were performed in which the same amount of **QD** (~400 picomoles or ~100 nM) was treated with 1, 2, 5, or 10 equivalents of **2–4**. The interaction of **QD** and the porphyrins were monitored *via* absorption and emission spectroscopy as well as **QD** luminescence decay (Figure 3.5). Each sample point in the titration was prepared independently and incubated overnight at room temperature to ensure equilibrium of the porphyrin binding to the surface **QD**. For emission spectra and decay traces, the excitation wavelength was 450 nm where absorbance of **2–4** is minimal while that of **QD** is relatively high.

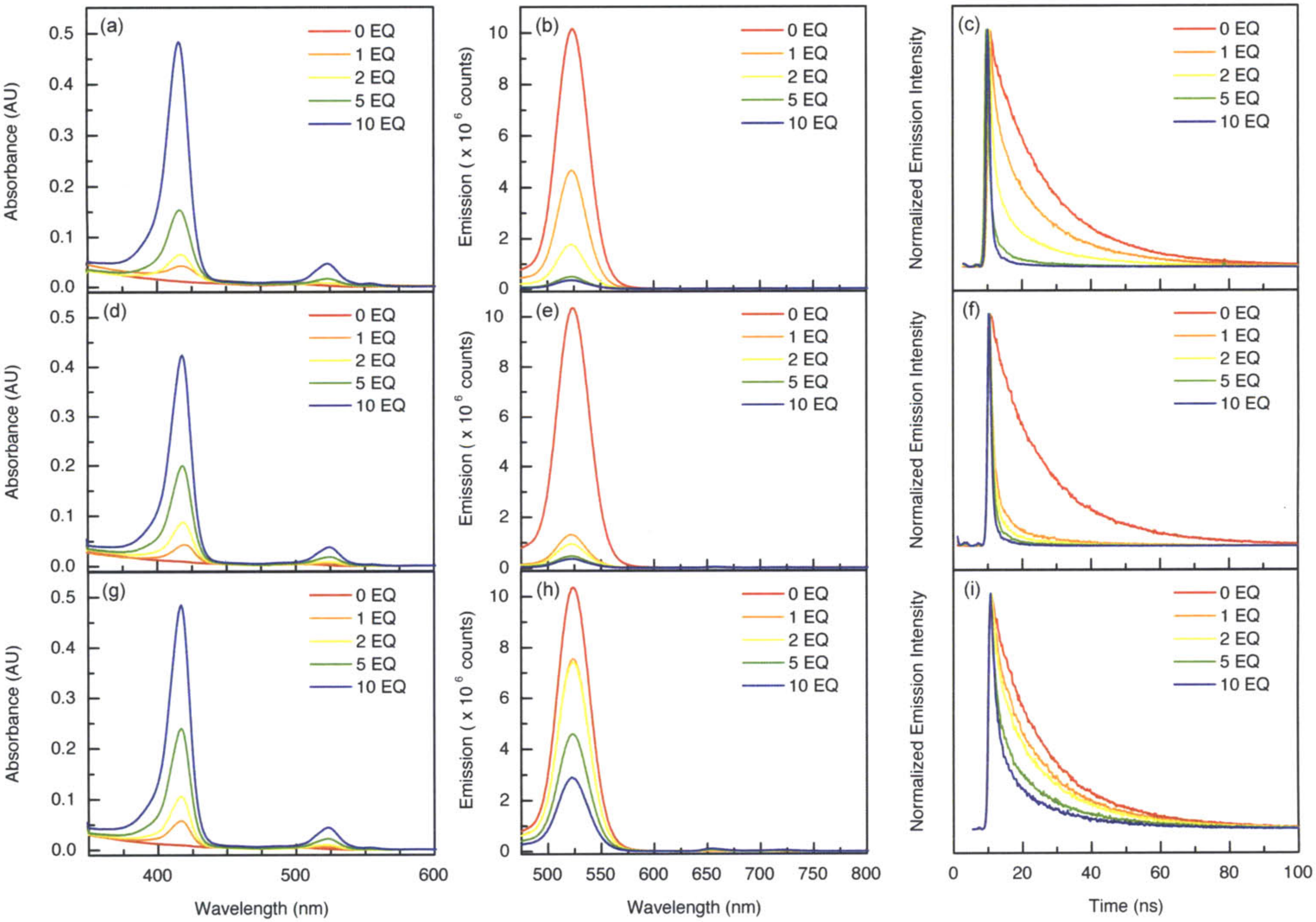

Figure 3.5. Titration of 1 (▬), 2 (▬), 5 (▬), and 10 (▬) equivalents of **2** (a–c), **3** (d–f), or **4** (g–i) into a toluene solution of **QD** (▬). The absorbance spectrum shows an increase in the Soret and Q bands with increasing porphyrin concentration (left). The emission spectrum (λ_{ex} = 450 nm) exhibits quenching of **QD** emission with increasing porphyrin concentration (center). Additionally, the **QD** lifetime (λ_{ex} = 450 nm) decreases as a function of increasing porphyrin concentration (right).

As expected, the absorbance spectra of the titrations are dominated by the B and Q bands of the porphyrin. The emission spectra and **QD** luminescence decay traces are more indicative of the energy transfer, as these demonstrate quenching of the **QD** emission as a function of porphyrin concentration. It was found that one equivalent of **3** quenched **QD** emission to the greatest extent, resulting in an 87% reduction in luminescence intensity, whereas the reduction is only 54% and 27% for a single equivalent **2** and **4**, respectively. Of these compounds, **4** is the least effective quencher as 1 and 2 equivalents have nearly an identical effect on quenching **QD** luminescence. Additionally, 10 equivalents of **4** reduced the **QD** emission by 72%, but the same amount of **2** and **3** reduced **QD** emission by 97% in both cases. This result suggests that two *cis* pyridyl rings are necessary for efficient binding to the QD surface.

This result is corroborated by the **QD** luminescence decay traces for each of the porphyrins. In the absence of porphyrin, **QD** emission follows a biexponential decay ($R_{adj}^2 > 0.99$) with components that reflect surface trapped states (17 ns) and exciton emission (5 ns).[47,48] While QD lifetimes have been fit to triexponential functions[31,49] to include Auger recombination,[50] the inclusion of a third term is an overparameterization of this data. Upon porphyrin titration (Table 3.4), the **QD** emission is quenched and the decays were fit using with a biexponential function ($R_{adj}^2 > 0.99$). The use of a triexponential function is an overparameterization of this data, giving components with lifetimes longer (> 30 ns) than **QD** alone.

Since the formation of the QD/porphyrin constructs is a dynamic self-assembly, there exists a discrete distribution of QD:porphyrin ratios at any point in the titration; this is best described using a Poisson statistics, as has been previously suggested.[32] The Poisson probability distribution provides a good model for the probability, $p(Y)$, that the number of events Y (*i.e.* the formation of assemblies with a given porphyrin:QD ratio) occur, where λ is the average value of Y (*i.e.* the number of porphyrin equivalents added to the QD solution):[51]

$$p(Y) = \frac{\lambda^Y}{Y!} e^{-\lambda} \tag{1}$$

where $Y = 0, 1, 2, \ldots,$ and $\lambda > 0$. For example, after the addition of one equivalent ($\lambda = 1$) of porphyrin, the probability that there are 0, 1, 2, or ≥ 3 porphyrins per QD is 0.368, 0.368, 0.184, and 0.080 respectively. A biexponential fit distills this distribution into two components and, given the high correlation coefficient, serves as a sufficient means of representing the lifetimes of the species in solution. The observed lifetimes and their relative amplitudes give an indication of the species in solution and can thus indicate the relative binding abilities of **2**–**4**. Indeed, for one equivalent of **2**, the two components are 14.5 ns (close to free **QD**) and 1.6 ns, suggesting that as much as 20% of **QD** may lack a surface-bound porphyrin (as determined by the reduction in the amplitude of the long component relative to free **QD**) while the other 80% may have one or more porphyrins bound. This observation is consistent with the expected value (37%) of free **QD** in solution based on the Poisson distribution. Conversely, one equivalent of **3** efficiently quenches **QD** luminescence as the calculated lifetimes are significantly shorter than **QD** alone, suggesting that this porphyrin efficiently binds to the QD surface, leaving few dots without a surface-bound porphyrin. Of the three porphyrins, **4** is the least efficient quencher. The lifetime calculations suggest that as much as 50% of **QD** lacks a surface-bound porphyrin after the addition of one equivalent of **4** while this quantity is 34% (expected value of 14% based on the Poisson distribution) after two equivalents have been added. While **2** and **3** are proposed to be relatively immobilized due to two points of attachment, porphyrin **4**, with a single 4-pyridyl group, has greater conformational flexibility, resulting in a less efficient luminescence quenching and thus a lower FRET efficiency.

Table 3.4. Lifetime data for QD titration with Pd Porphyrins **2–4**

Compound[a]	Equivalents	τ_1 (ns)	A_1 (%)[b]	τ_2 (ns)	A_2 (%)[b]	τ_{avg} (ns)[c]
QD	–	16.93 ± 0.36[d]	53	5.07 ± 0.95	47	11.30 ± 1.22
2	1	14.52 ± 0.98	10	1.63 ± 0.30	90	2.80 ± 0.91
2	2	7.55 ± 2.90	5	0.77 ± 0.16	95	1.06 ± 0.12
2	5	2.30 ± 0.45	3	0.37 ± 0.03	97	0.42 ± 0.02
2	10	1.27 ± 0.13	3	0.26 ± 0.03	97	0.29 ± 0.01
3	1	5.40 ± 2.15	2	0.70 ± 0.18	98	0.76 ± 0.18
3	2	2.47 ± 0.56	3	0.44 ± 0.05	97	0.50 ± 0.02
3	5	1.65 ± 0.32	5	0.33 ± 0.03	95	0.40 ± 0.01
3	10	1.73 ± 0.96	3	0.29 ± 0.04	97	0.34 ± 0.05
4	1	16.31 ± 0.31	24	2.54 ± 0.25	76	5.86 ± 2.60
4	2	15.89 ± 0.21	17	2.30 ± 0.08	83	4.63 ± 2.16
4	5	13.97 ± 0.99	6	1.69 ± 0.24	94	2.36 ± 0.51
4	10	12.13 ± 1.79	3	1.41 ± 0.30	97	1.66 ± 0.15

[a] Toluene solution, λ_{ex} = 450 nm, [b] Relative contribution to the biexponential fit,
[c] Weighted average lifetime, calculated as $\tau_{avg} = (A_1\tau_1 + A_2\tau_2)/100$, [d] 95% confidence interval

To describe the **QD** lifetime in a single quantity, the weighted average lifetime (τ_{avg}, based on the relative amplitudes of the lifetimes) was computed. This quantity monotonically decreases with increasing porphyrin concentration and is reflective of the quenching efficiency of **2**–**4**. Based on the data, ten equivalents of **2** and **3** reduce the QD lifetime to ~300 ps with a similar emission intensity (*vide supra*), indicating that two *cis* pyridyl groups enhance surface binding and increase **QD** quenching, resulting in efficient FRET.

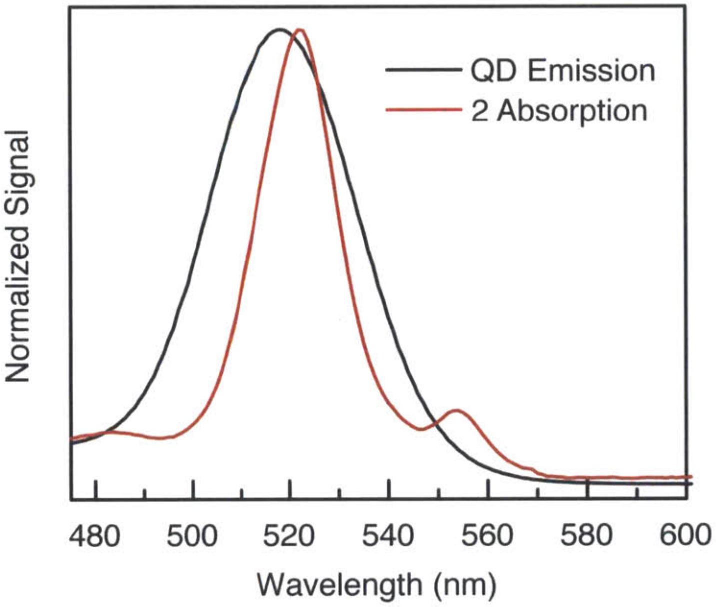

Figure 3.6. Normalized **QD** emission (**—**) (λ_{ex} = 450 nm) and absorption of **2** (**—**), illustrating spectral overlap that accounts for the high FRET efficiency in **QD2**.

In order to better understand the energy transfer in these systems, the FRET parameters (Table 3.5) were calculated based on 10 equivalents of each porphyrin (**QD2**–**QD4**). Ten equivalents maximize the amount of porphyrin per dot while still allowing for **QD** emission to serve as an internal intensity standard for ratiometric sensing. Based on the emission spectrum of **QD** and the absorption spectra of **2**–**4**, the spectral overlap integral J was determined (See Section 3.7 regarding energy transfer analysis). Figure 3.6 illustrates the spectral overlap of the donor (**QD**) and acceptor (**2**). As expected, J is quite similar for all three assemblies, although this quantity is slightly larger for **QD3** than **QD2** and **QD4** due to the greater extinction coefficients of **3** relative to **2** and **4**.

Table 3.5. Summary of Förster Energy Transfer Parameters

Compound	m	J^a (M^{-1} cm^3)	r^b (nm)	$R_0{}^a$ (nm)	E^c
QD2	10	7.96×10^{-14}	3.15	4.11	0.97
QD3	10	8.54×10^{-14}	3.19	4.15	0.97
QD4	10	7.89×10^{-14}	4.25	4.10	0.85

[a] Calculated using Eq. 5, [b] Calculated using Eq. 3, [c] Calculated using Eq. 4

The Förster distance (R_0), the donor–acceptor distance at which the FRET efficiency is 50%, may now be calculated. The relative quantum yield of **QD** (Φ_D) was determined to be 0.72 using fluorescein 27 as a reference. Using the **QD** lifetime with 10 equivalents of **2–4** (Table 3.4), the FRET efficiency for each assembly was calculated. While the Förster distance is nearly identical (4.1 nm) for each assembly, the calculated FRET efficiency varies due to differences in the porphyrin's interaction with **QD**. This is quantified by calculating r, the donor–acceptor distance, where m is taken to be 10, as the lifetimes used to calculate E were taken from titration data at 10 equivalents. The calculated FRET parameters are similar to those observed for free-base porphyrin/QD assemblies.[30] It is seen that r is approximately 3 nm for **QD2** and **QD3** whereas it is over 1 nm longer for **QD4**, thus demonstrating that two *cis* pyridyl rings enable better surface binding that a single pyridyl moiety. Since the parameters for **QD2** and **QD3** are nearly identical, the substitution motif (4-pyridyl versus 3-pyridyl) seems to be independent of the FRET efficiency. This result is in contrast to other studies,[30] which showed that QD luminescence was more efficiently quenched with 4-pyridyl-substituted free-base porphyrins than 3-pyridyl analogues. These results indicate that one equivalent of **3** has a more drastic effect on the quenching of **QD** than **2** (Figure 3.5), although the net quenching with 10 equivalents of both is nearly identical.

3.5 Characterization of QD Assemblies

Self-assembled sensors **QD2–QD4** were prepared by equilibrating 10 equivalents of porphyrin with **QD** and then studied using steady-state absorption and emission spectroscopy (Table 3.2). The absorbance spectrum of these assemblies is a composite of porphyrin and **QD** spectra, as demonstrated with **QD2** in Figure 3.7; the increased absorbance at $\lambda < 400$ nm in **QD2–QD4** relative to **2–4** is due to **QD** absorbance, which increases with decreasing wavelength.

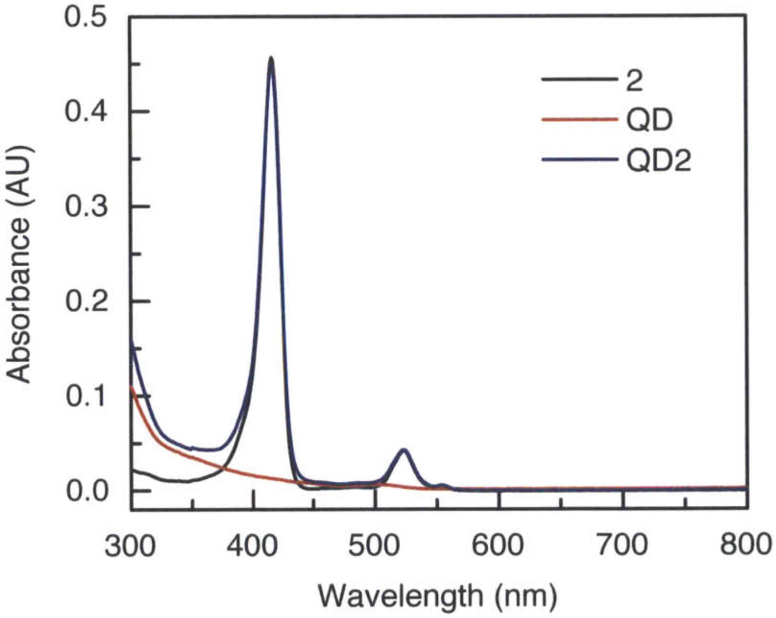

Figure 3.7. Comparison of the absorption spectra of **2** (—), **QD** (—), and **QD2** (—) in toluene. The spectrum of **QD2** represents a composite of the two constituent spectra. The increased absorbance due to **QD** is pronounced in the 300-400 nm region.

Additionally, the emission spectra (λ_{ex} = 450 nm) presented in Figure 3.8 exhibit features from both the porphyrin and **QD**. A slight red shift (1–2 nm) was observed in the porphyrin absorbance and emission bands of **QD2–QD4** relative to **2–4**; this phenomenon has been observed with both free-base porphyrins[30] and pyrene[17] bound to a QD surface. It is attributed to an increase in the average dielectric constant, ε, of the medium solvating the porphyrin:[33] ε = 2.379 for toluene versus ε_{11} = 9.70 and ε_{33} = 10.65 for CdSe.[67] The emission of the QD in **QD2**–**QD4** is slightly blue-shifted (1–3 nm) relative to **QD**; such modulation of the QD surface states has been previously observed[52,53] with the surface binding of amines and is attributed to electronic effects of the ligand.[54] Using a similar argument for the observed red-shift of porphyrin absorbance and emission, the blue-shift is likely due to a decrease in the dielectric constant of the medium solvating the QD: ε = 35.5 for triethylphosphine oxide[67] (as an analogue for the surface trioctylphosphineoxide ligand) versus ε = 13.26 for pyridine[67] and ε = 2.0 for H_2TPP[55] (as analogues for **2**–**4**).

For evacuated samples, the intensity of the T(0,0) emission in **QD2** and **QD3** is comparable to the QD emission signal in these samples, indicating that these assemblies have sufficient signal to serve as sensors. This is in stark contrast to **QD4** where the porphyrin emission is only 6% of the QD emission, due to the inefficient surface binding and quenching of **QD** luminescence, making it an inferior sensor. This result is also corroborated by the excitation spectra (Figure 3.9), which were recorded by monitoring the porphyrin emission at 685 nm. These plots are qualitatively similar to the absorbance spectra and serve as a means of probing FRET interactions. Concentration-matched solutions of **QD2**–**QD4** show that **QD4** produces the least emission signal, having an intensity that is approximately 50% of **QD2**. Because of the similar extinction coefficients of **2**–**4**, the excitation spectra of these compounds should be the same in the absence of other effects. The variation in intensities is thus due to differences in QD/porphyrin interactions and FRET efficiency. Upon binding to **QD**, the phosphorescence quantum yield of the porphyrin increases relative to free species in solution (Table 3.2).

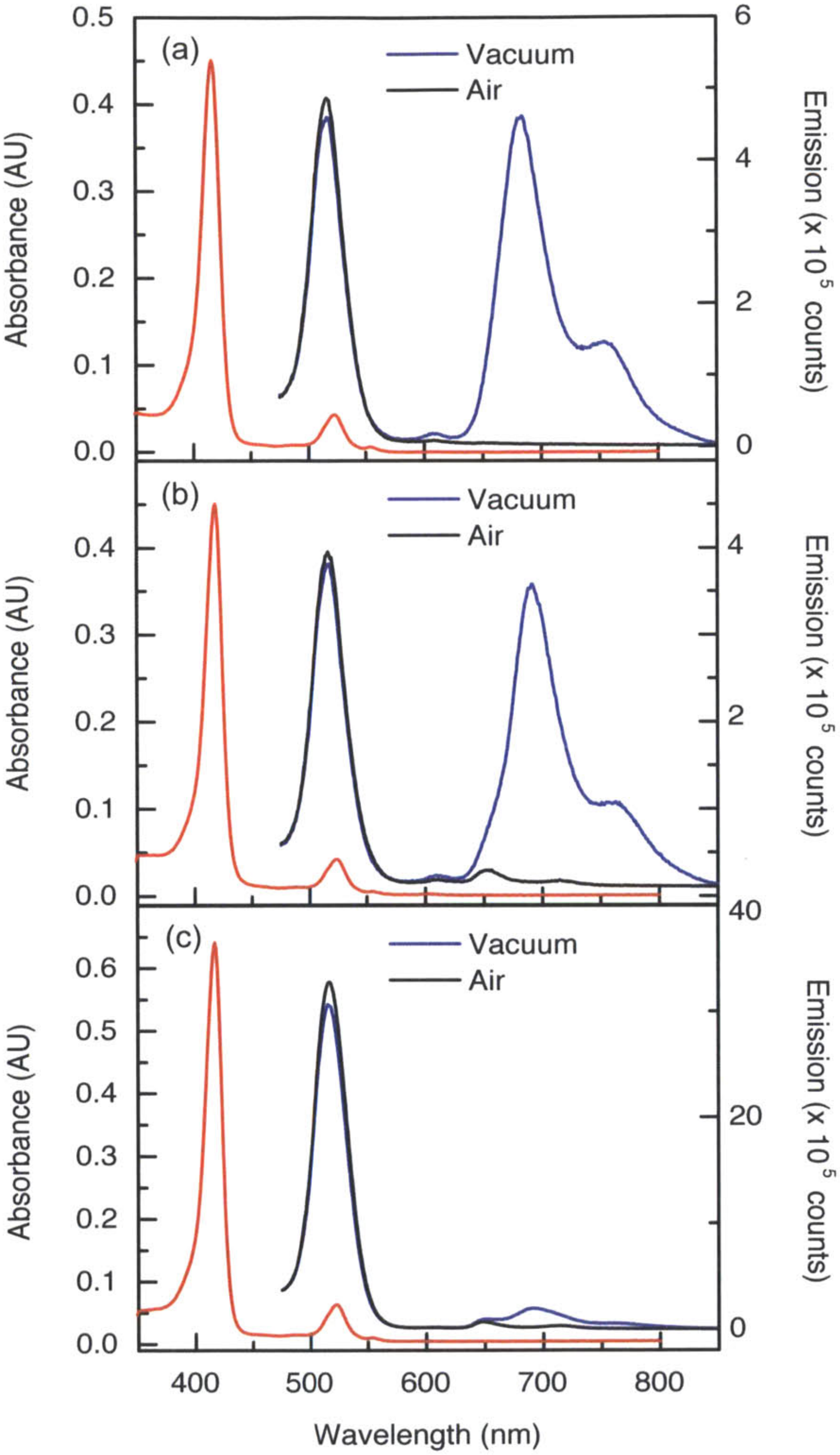

Figure 3.8. Comparison of the steady state absorption (▬) and emission spectra (λ_{ex} = 450 nm) of **QD2** (a), **QD3** (b), and **QD4** (c) in toluene. While the emission intensity of the phosphor is almost completely quenched in the presence of air (~160 torr O_2) (▬), it is greatly enhanced under vacuum (▬).

This phenomenon has been previously observed[14] and is attributed to the porphyrin intercalating in the capping ligand and preventing deactivation of the excited state *via* non-radiative pathways. This effect also accounts for the enhanced lifetime of the surface-bound porphyrin relative to free porphyrin (*vide infra*), as has been observed for other fluorophore systems.[14,17,48,56] Of these assemblies, **QD2** shows the greatest enhancement (nearly a three-fold increase) in quantum yield upon surface binding. **QD3** shows a similar increase, suggesting that these two assemblies exhibit similar surface binding and corroborating the results of other experiments. **QD4** only shows a nominal increase in the phosphorescence quantum yield, indicating that this species does not bind to the surface as efficiently and does not protect the phosphor from non-radiative decay pathways.

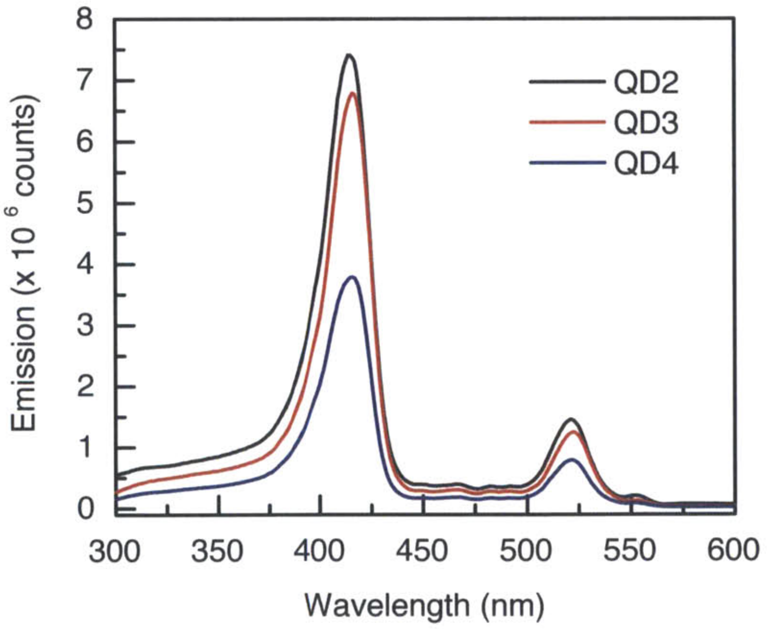

Figure 3.9. Excitation spectra of concentration-matched evacuated toluene solutions of **QD2** (—), **QD3** (—), and **QD4** (—) monitoring the emission at 685 nm; excitation light was removed using a 590 nm long pass filter. The increased emission of these species in the 300-400 nm region is due to **QD** absorbance at these wavelengths.

In these assemblies, the role of the QD is to serve as an antenna for photon absorption, manifesting in an enhancement of porphyrin emission. Under linear excitation (λ_{ex} = 450 nm), a nearly four-fold enhancement in emission is observed when **QD** is present (Figure 3.10). This is indicative of FRET excitation of the porphyrin since **QD** has a greater absorbance at 450 nm relative to **2**.

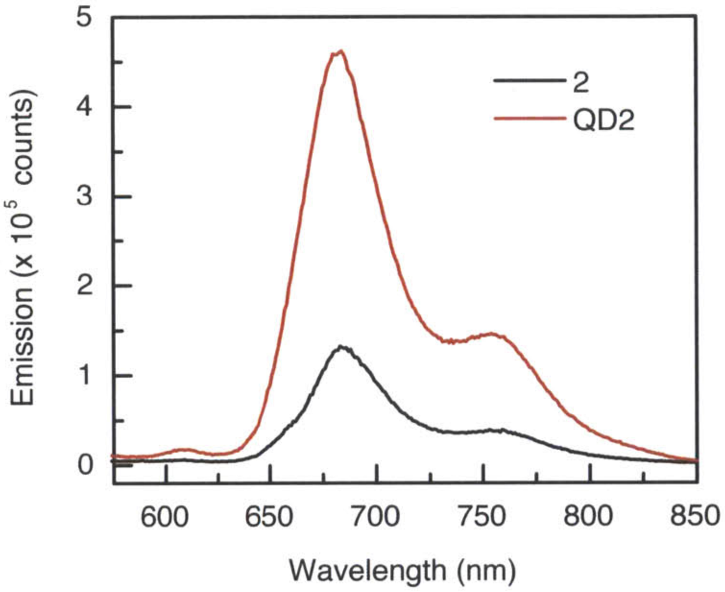

Figure 3.10. Emission spectra (λ_{ex} = 450 nm) of concentration-matched toluene solutions of **2** (—) and **QD2** (—) under vacuum. The enhancement of the emission intensity of **QD2** is attributed to FRET excitation of the porphyrin, as the QD has a greater absorbance at 450 nm relative to **2**.

While **2–4** still absorb under 450 nm excitation, the FRET enhancement with **QD** is more dramatic under two-photon excitation (λ_{ex} = 800 nm), as the two-photon absorption cross-section for **QD** is ~10^4 times greater than for **2** (*vide supra*). Figure 3.11 shows the two-photon emission spectrum for concentration-matched solutions in three different 140 nm spectral windows (a–c) in addition to a qualitative spectrum (d) that has been scaled to include all of the data on a single plot. A significant 10-fold enhancement of the porphyrin emission in **QD2** relative to **2** was observed in addition to a 70% reduction in QD emission for **QD2** relative to **QD**. Additionally, the two-photon lifetime decay traces (λ_{ex} = 850 nm) show a 3–4 fold increase in signal for **QD2** relative to **2**. These results indicate that the QD serves as an absorption antenna and FRET donor, resulting in enhanced porphyrin emission under both one- and two-photon excitation.

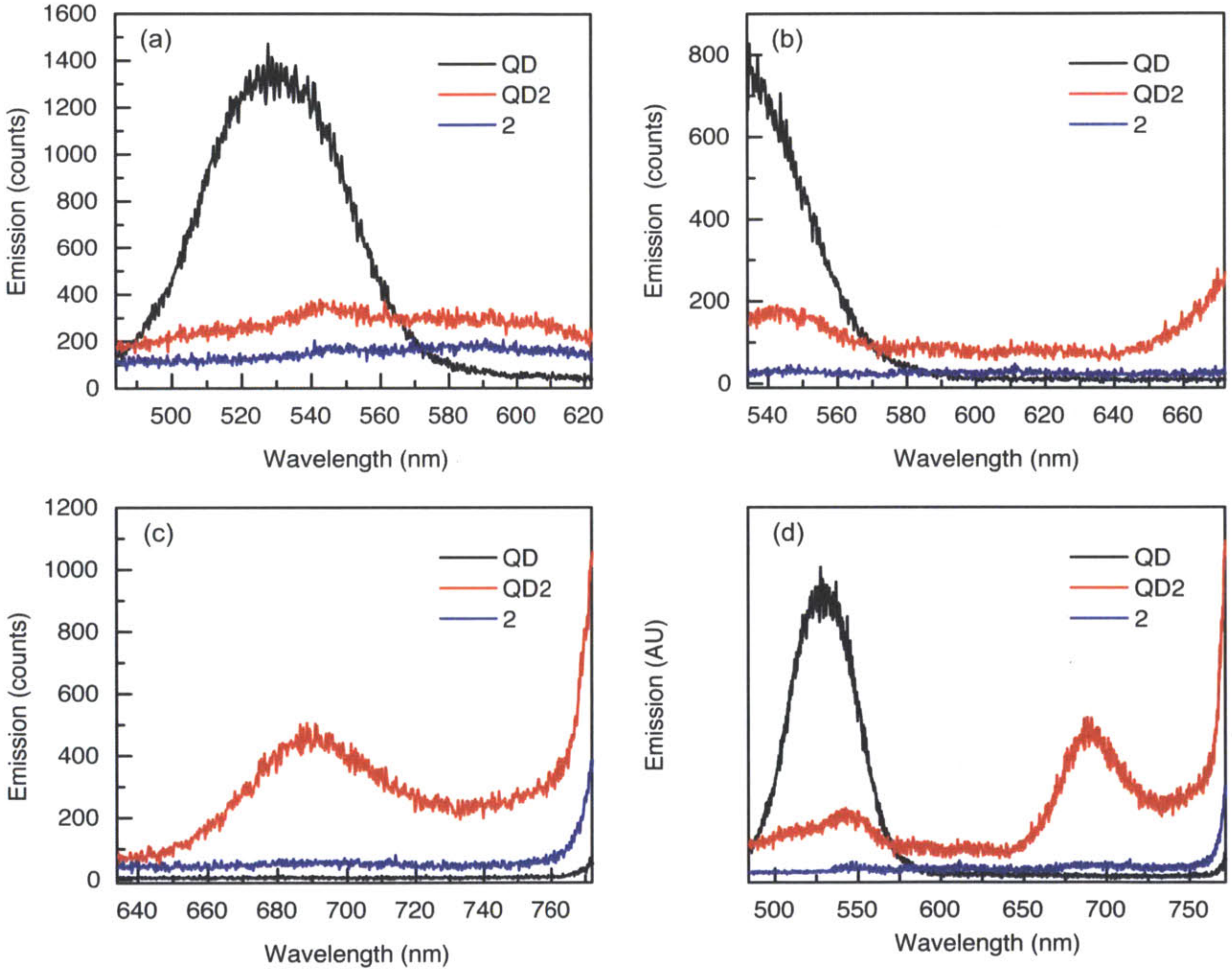

Figure 3.11. Two-photon emission spectra (λ_{ex} = 800 nm) of concentration-matched toluene solutions of **QD** (—) and evacuated samples of **2** (—) and **QD2** (—) in three different spectral windows: 500 nm (a), 550 nm (b), and 650 nm (c). The emission intensity of the dot is quenched in the presence of porphyrin, as observed in (b). **2** does not emit under two-photon excitation and emission is only observable in the presence of **QD**, as shown in (c). (d) Qualitative two-photon emission spectra constructed by concatenating (a), (b), and (c) and rescaling the emission intensity. This is a qualitative representation of the data so that all of the data may be visualized in a single plot.

As shown in Figure 3.8, **QD2**–**QD4** have similar oxygen sensitivity as **2**–**4**, as evidenced by the difference in the emission intensity in air versus vacuum. However, the extent of the enhancement is markedly diminished relative to free porphyrin; this is attributed to the overall lower amount of signal due to the FRET excitation of the porphyrin in **QD2**–**QD4** relative to direct excitation of Q(1,0) in **2**–**4**. It was found that the greatest difference was observed for **QD2**, where the enhancement is 100 fold for T(0,0) and 50 fold for T(0,1) and is consistent with the result that **2** exhibits the greatest emission intensity enhancement. **QD3** is somewhat less sensitive with approximately a 50 fold enhancement for both triplet transitions whereas only a 10 fold enhancement is observed for **QD4**, presumably due to the lower FRET efficiency and thus lower amount of total signal.

Triplet lifetimes (λ_{ex} = 450 nm) of **QD2**–**QD4** were determined in toluene at room temperature under both air and vacuum (τ_0) (Table 3.6); decay traces using data > 100 ns were fit to a biexponential decay curve ($R_{adj}^2 > 0.96$). In air, it was observed that the average lifetimes for the assemblies were significantly shorter than observed for the porphyrins alone. This may be due to self-quenching of the porphyrin on the surface of the quantum dot; this conclusion is corroborated by the observed decrease in emission intensity after laser irradiation. Since the porphyrin can absorb 450 nm light, it could be that the irradiation is inducing molecular motions that are causing the formation of π-stacked dimers on the dot surface, resulting in significant porphyrin quenching. The long component of the decay, albeit a rather small contribution, is due to intercalation of the porphyrin in the capping ligands of the QD, protecting it from oxygen and thereby lengthening the excited state lifetime, as has been observed previously.[14,17,48] Under vacuum, it appears that the shorter component is likely to be free porphyrin as this lifetime is comparable to free porphyrin in solution (~ 150 μs, Table 3.3).

Table 3.6. Summary of Lifetime Data for QD Assemblies

Compound[a]	Sample	Excitation	τ_1	A_1 (%)[b]	τ_2	A_2 (%)[b]	τ_{avg}[c]
QD2	Air	450 nm	638 ± 64 ns[d]	17	69 ± 11 ns	83	174 ± 92 ns
QD3	Air	450 nm	575 ± 5 ns	1	29 ± 1 ns	99	37 ± 1 ns
QD4	Air	450 nm	550 ± 6 ns	6	41 ± 1 ns	94	72 ± 7 ns
QD2	Vacuum[e]	450 nm	590 ± 79 μs	75	149 ± 51 μs	25	479 ± 26 μs
QD3	Vacuum	450 nm	482 ± 41μs	65	143 ± 34 μs	35	363 ± 15 μs
QD4	Vacuum	450 nm	578 ± 111 μs	69	166 ± 51μs	31	386 ± 106 μs
QD2	Air	850 nm	537 ± 14 ns	100	–[f]	–	537 ± 14 ns
QD3	Air	850 nm	401 ± 4 ns	100	–[f]	–	401 ± 4 ns
QD4	Air	850 nm	430 ± 5 ns	100	–[f]	–	430 ± 5 ns
QD2	Vacuum	850 nm	270 ± 11 μs	62	60 ± 10 μs	38	190 ± 16 μs
QD3	Vacuum	850 nm	203 ± 8 μs	60	57 ± 15 μs	40	145 ± 11 μs
QD4	Vacuum	850 nm	101 ± 5 μs	100	–[g]	–	101 ± 5 μs

[a] Toluene solution, [b] Relative contribution to the biexponential fit, [c] Weighted average lifetime, calculated as $\tau_{avg} = (A_1\tau_1 + A_2\tau_2)/100$, [d] 95% Confidence interval, [e] Evacuated samples (< 10^{-5} torr), [f] Due to instrumental limitations, the fast component could not be resolved and the data was fit to a monoexponential decay,
[g] A biexponential fit was found to be an overparameterization of the data and was thus fit to a monoexponential

The significantly longer component may be attributed to the intercalation of the porphyrin in the passivating ligand; this protects it from molecular collisions and other non-radiative decay processes, thereby extending the radiative lifetime.

In addition to the one-photon lifetimes, the air and vacuum lifetimes of **QD2**–**QD4** were measured under two-photon irradiation (λ_{ex} = 850 nm) (Table 3.6). The observed lifetimes for **QD2** and **QD3** are consistent with the phenomena observed in the one-photon case. The vacuum data exhibits a shorter component (~ 50 μs) due to self-quenching on the quantum dot surface and a longer component (~ 200 μs) due to screening from non-radiative decay processes. It is noteworthy that the average lifetime of the assemblies is quite similar to free porphyrin. This suggests that, under two-photon excitation, the sensor behaves similarly to the porphyrin alone under one-photon excitation. This is somewhat expected because the amount of energy transferred from **QD** to porphyrin via FRET should be approximately 525 nm worth of energy and the poprhyrin should behave similarly to direct excitation with 525 nm light under these conditions. For **QD4**, a biexponential fit was found to be an overparameterization of the data. The observed lifetime is rather similar to the two-photon lifetime of **4** and quite disparate from the lifetimes of the other assemblies, indicating that binding to QD is less efficient than **QD2** and **QD3**; this result is consistent with titration experiments and calculated FRET efficiency (*vide supra*). Presumably the air data for **QD2** and **QD3** would show a second component corresponding to porphyrin self-quenching. Due to the bin size used for data acquisition (40 ns), the second component could not be resolved and smaller bin sizes are not possible given the instrumentation.

3.6 Discussion and Conclusions

Preliminary photophysical studies of compounds **Pd-1** and **Pt-1** showed that both of these compounds exhibit favorable properties for use in biological oxygen sensing: emission in the tissue transparency window and a significant difference in triplet emission lifetime and intensity in the 0–160 torr of O_2 range. Due to the more red emission and longer τ_0 of **Pd-1** relative to **Pt-1**, palladium complexes were selected as the compounds of choice. It was found that compounds **2–4** have similar absorption and emission spectral features, oxygen sensitivity, and triplet lifetimes to **Pd-1**, suggesting that the nature of the *meso* substituent has little effect on these properties.

Having studied the properties of compounds **2–4** alone, titrations of these compounds with a solution of a quantum dot **(QD)** were performed. It was found that increasing the porphyrin concentration resulted in a decrease of both the emission intensity and luminescence lifetime of **QD**. This is due to a FRET interaction in which there is an energy transfer from the **QD** to the porphyrin. The pyridyl substituents enable the porphyrin to bind to the surface of the quantum dot. It was found that quenching of **QD** luminescence was least efficient with compound **4**, presumably due to the presence of a single pyridyl substituent. Both **2** and **3** exhibit similar effective quenching with ten equivalents with the porphyrin, suggesting that the bidentate-like or chelating nature of the porphyrin as a surface ligand is more important than the substitution pattern of the *meso* substituent (3-pyridyl versus 4-pyridyl). Because of superior spectral overlap and efficient surface binding, the FRET efficiency in these systems **(QD2–QD4)** is 89–98%. The presence of the quantum dot serves as an efficient photon antenna, enhancing porphyrin emission under both one- and two-photon excitation. This effect is more dramatic for two-photon excitation, as the porphyrin alone has a low cross-section for two-photon absorption and minimal signal is observed in this case. While all of these assemblies **QD2**–**QD4** are also responsive to oxygen in the 0–160 torr range, **QD2** possesses the best properties, exhibiting the greatest enhancement in porphyrin emission under vacuum relative to air. This system has the greatest phosphorescence quantum yield and the largest differences in the air and vacuum lifetimes. Chapter 4 explores the modification of **QD2** so that this sensor can be used in aqueous media for biological oxygen sensing.

3.7 Experimental Details

Materials

The following chemicals were used as received: tris(2,2′-bipyridyl)dichlororuthenium(II) hexahydrate ([Ru(bpy)]Cl_2), 2′,7′-dichlorofluorescein (fluorescein 27), toluene, acetonitrile, and ethanol from Sigma-Aldrich; and sodium hydroxide (NaOH) from Mallinckrodt. 2-methyltetrahydrofuran from Sigma-Aldrich was dried over sodium metal and benzophenone; sample solutions were prepared by vacuum transfer of the solvent. Cadmium selenide core/shell quantum dots (518 nm emission, QD Vision) were twice precipitated from toluene using EtOH and redissolved in toluene prior to use. The following compounds were prepared as presented in Chapter 2: 5(4-carboxyphenyl)-10,15,20-triphenylporphyrinatopalladium(II) (**Pd-1**), 5(4-carboxyphenyl)-10,15,20-triphenylporphyrinatoplatinum(II) (**Pt-1**), 5-(4-methoxycarbonyl-phenyl)-10,15,20-tris(4-pyridyl)porphyrinopalladium(II) (**2**), 5,10-diphenyl-15,20-bis(3-pyridyl) porphyrinatopalladium(II) (**3**), and 5,10,15-triphenyl-20-(4-pyridyl)porphyrinatopalladium(II) (**4**).

Preparation of QD/Porphyrin Assemblies

Toluene stock solutions of each palladium porphyrin **2**–**4** (~100 μM) and **QD** (~10 μM) were prepared. The concentration of the **QD** stock solution was calculated using $\varepsilon_{350} = 4.34 \times 10^5$

M^{-1} cm^{-1}, as estimated using an empirical formula based on the first absorbance feature ($\lambda = 501$ nm).[57] An aliquot of the **QD** stock (typically containing ~1 nmol of dots) was dissolved in 4 mL of toluene; an appropriate volume of the porphyrin stock was then added to give 10 molar equivalents of porphyrin per **QD**. The resultant mixture was stirred overnight at room temperature to allow equilibration of the porphyrin on the **QD** surface, to give assemblies **QD2**–**QD4**.

Physical Measurements

UV–vis absorption spectra were acquired using a Cary 5000 spectrometer. Steady-state emission and excitation spectra were recorded on a SPEX FluoroMax-3 spectrofluorimeter. Relative quantum yields of porphyrins (Φ_{sam}) were calculated using $[Ru(bpy)_3]Cl_2$ in MeCN as the reference according to the following equation:

$$\Phi_{sam} = \Phi_{ref}\left(\frac{A_{ref}}{A_{sam}}\right)\left(\frac{I_{sam}}{I_{ref}}\right)\left(\frac{\eta_{sam}}{\eta_{ref}}\right)^2 \qquad (2)$$

where A is the measured absorbance, η is the refractive index of the solvent, I is the integrated emission intensity, and Φ_{ref} is the emission quantum yield of the reference. Φ_{ref} was taken to be 0.094 for an evacuated sample of $[Ru(bpy)_3]Cl_2$ in MeCN.[58] The quantum yield of **QD** was similarly determined using fluorescein 27 in 0.1 M NaOH ($\Phi = 0.87$, $\eta = 1.335$)[59] as the standard. Porphyrin samples for quantum yield measurements, vacuum lifetime (τ_0) measurements, and evacuated steady-state emission spectra were prepared using three cycles of freeze–pump–thaw to pressures below 10^{-5} torr.

Nanosecond time-resolved emission measurements of porphyrin lifetimes were acquired using a previously reported system.[60,61] Pump light was provided by the third harmonic (355 nm) of a Quanta-Ray Nd:YAG laser (Spectra-Physics) operating at 10 Hz. The pump light was passed through a BBO crystal in an optical parametric oscillator (OPO), yielding a visible frequency that was tuned to 510 nm to excite **Pt-1**, 525 nm to excite **Pd-1** and **2–4**, or 450 nm to excite the assemblies **QD2–QD4**. Excitation light was attenuated to 1–4 mJ per pulse for all experiments using neutral density filters. Emitted light was first passed through a series of long pass filters to remove excitation light and then entered a Triax 320 monochromator (Jobin Yvon Horiba) and was dispersed by a blazed grating (500 nm, 300 grooves/mm) centered at 685 nm. The entrance and exit slits of the monochromator were set to 0.36 mm in all experiments herein, corresponding to a spectral resolution of 4.5 nm. The signal was amplified by a photomultiplier tube (R928, Hamamatsu) and collected on a 1 GHz digital oscilloscope (9384CM, LeCroy); acquisition was triggered using a photodiode to collect scattered laser excitation light.

Femtosecond time-resolved emission measurements of QD lifetimes were acquired using a Libra-F-HE (Coherent) chirped-pulse amplified Ti:sapphire laser system. Sub-100 fs laser pulses were generated in a mode-locked Ti:sapphire oscillator (Coherent Vitesse) which was pumped by a 5 W cw Coherent Verdi solid-state, frequency-doubled Nd:YVO_4 laser. The 80-MHz output was amplified in a regenerative amplifier cavity, pumped by a diode-pumped, frequency-doubled Nd:YLF laser (Coherent Evolution-30) to generate a 1 kHz pulse train with a wavelength of 800 nm. This was then used to pump an OperA Solo (Coherent) optical parametric amplifier (OPA), which is able to generate frequencies between 285 and 2600 nm. Excitation pulses of 450 nm were produced *via* fourth harmonic generation of the idler using a BBO crystal; the pulse power was attenuated to 2.5 mW at the sample. Emission lifetimes were measured on a Hamamatsu C4334 Streak Scope streak camera, which has been described elsewhere.[62] The emission signal was collected over a 140 nm window centered at 475 nm using 100, 50, 20, 10, or 5 ns time windows. Delays in the 100 ns time window were generated using a Hamamatsu

C1097-04 delay unit, whereas a Stanford Research Systems DG535 delay generator was used to generate delays for the other time windows.

Two-photon emission spectra were generated using the aforementioned Libra-F-HE (Coherent) chirped-pulse amplified Ti:sapphire laser system. Excitation pulses of 800 nm were used directly from the Libra output; the pulse power was attenuated to 6 mW using neutral density filters and the beam was focused onto the sample using a 500 mm focal length lens. The emission spectrum was collected using a Hamamatsu C4334 Streak Scope streak camera in 140 nm windows centered at 500 nm, 550 nm, and 650 nm.

Two-photon lifetime measurements were made using a custom-built multiphoton laser-scanning microscope (MPLSM) in the Edwin L. Steel Laboratory, Department of Radiation Oncology at Massachusetts General Hospital, as previously described.[63] Additions to the MPLSM system[64] were made such that lifetime measurements could be performed. Sub-100 fs laser pulses were generated at a repetition rate of 80 MHz in a mode-locked Ti:sapphire oscillator (Spectra-Physics Mai Tai HP) which was pumped by a 14 W cw Spectra-Physics Millennia diode-pumped solid-state (DPSS) laser operating at 532 nm; the output of the Mai Tai laser is tunable in the 690–1040 nm range. The 850 nm laser output was adjusted using a 10RP52-2 zero-order half-wave plate (Newport) and a 10GL08AR.16 Glan-Laser polarizer (Newport) to attenuate the power to 700–800 mW for air samples and 400 mW for evacuated samples. The beam was passed through a 350-50 KD*P Pockels cell (Conoptics) that amplified and switched the triggering pulses from a DG535 digital delay generator (Stanford Research Systems). The experimental square wave trigger pulse from the delay generator defined the repetition rate while a second delayed pulse defined the excitation pulse, which was 1.6 μs in duration for air samples and 15.36, 30.72, or 51.20 μs in duration for evacuated samples. At the rejection site of the Pockels cell, a TDS-3052 oscilloscope (Tektronix) and photodiode were used to monitor the applied voltage and the optical response; the Pockels cell attenuated the beam to 10% of the incident power. The beam was then directed into a custom-modified multiphoton microscope based on the Olympus Fluoview 300 laser scanner. The output beam from the scanner was collimated through a scan lens into the back of an Olympus BX61WI microscope. An Olympus LUMPlanFL 20×, 0.95 NA water immersion objective lens was used to focus the excitation light and collect the emission light. NIR laser excitation light and visible emission were separated using a 750SP-2P AR-coated dichroic mirror (Chroma Technology). A 690/90 bandpass filter (Chroma Technology) and a focusing lens were used in front of the GaAs H7421-50 photomultiplier tube (Hamamatsu) to collect phosphorescent emission. Photon counting was performed using a SR430 multichannel scaler (Stanford Research Systems) to histogram the counts in 1024 or 2048 bins of 40 ns for air samples or 2.56 or 5.12 μs for evacuated samples.

Energy Transfer Analysis

The efficiency of energy transfer from the QD to the porphyrin was evaluated using Förster analysis:[24,65]

$$E = \frac{mk_{D-A}}{mk_{D-A} + \tau_D^{-1}} = \frac{mR_0^6}{mR_0^6 + r^6} \qquad (3)$$

where k_{D-A} is the rate of energy transfer, r is the distance between the donor and acceptor, R_0 is the Förster distance or the distance at which the energy transfer efficiency is 50%, and m is the number of acceptor molecules per donor. This quantity (E) can be measured experimentally:

$$E = 1 - \frac{\tau_{D-A}}{\tau_D} \qquad (4)$$

where τ_D is the lifetime of the QD alone and τ_{D-A} is the lifetime of the QD with surface-bound porphyrin (**QD2**–**QD4**). Although the efficiency can be experimentally determined from the excited-state lifetime quenching, additional information is needed to quantify the parameters R_0, r, and m. The Förster distance is calculated using the following equation:

$$R_0^6 = \frac{9000(\ln 10)\kappa^2\Phi_D}{128\pi^5 N n^4}\int_0^{\infty} F_D(\lambda)\varepsilon_A(\lambda)\lambda^4 \mathrm{d}\lambda \qquad (5)$$

where κ^2 is the relative orientation factor of the dipoles, taken to be 0.476 for static donor-acceptor orientations,[24,66] Φ_D is the quantum efficiency of the donor, N is Avogadro's number, and n is the index of refraction of the medium, which is taken to be 1.4961 for toluene.[67] The latter half of the equation represents the spectral overlap integral, often represented as J, where $F_D(\lambda)$ is the normalized intensity of the donor and $\varepsilon_A(\lambda)$ is the extinction coefficient of the acceptor at wavelength λ. Thus, R_0 may be calculated from the experimentally determined emission spectrum of the donor and the absorption spectrum of the acceptor.

3.8 References

1. Murray, C. B.; Norris, D. J.; Bawendi, M. G. *J. Am. Chem. Soc.* **1993**, *115*, 8706–8715.
2. Alivisatos, P. *Nat. Biotechnol.* **2004**, *22*, 47–52,
3. Xia, Z.; Rao, J. *Curr. Opin. Biotechnol.* **2009**, *20*, 37–44.
4. Baltazar, R.; Vistas, C. R.; Ferreira, G. N. M. Biosensing Applications Using Nanoparticles. In *Nanocomposite Particles for Bio-Applications: Materials and Bio-Interfaces*; Trindade, T.; da Silva, A. L. D., Eds.; Taylor & Francis: Boca Raton, FL, 2012; pp 265–282.
5. Medintz, I. L.; Clapp, A. R.; Mattoussi, H.; Goldman, E. R.; Fisher, B.; Mauro, J. M. *Nat. Mater.* **2003**, *2*, 630–638.
6. Somers, R. C.; Bawendi, M. G.; Nocera, D. G. *Chem. Soc. Rev.* **2007**, *36*, 579–591.

7. Suzuki, M.; Husimi, Y.; Komatsu, H.; Suzuki, K.; Douglas, K. T. *J. Am. Chem. Soc.* **2008**, *130*, 5720–5725.

8. Blanton, S. A.; Dehestani, A.; Lin, P. C.; Guyot-Sionnest, P. *Chem. Phys. Lett.* **1994**, *229*, 317–322.

9. Larson, D. R.; Zipfel, W. R.; Williams, R. M.; Clark, S. W.; Bruchez, M. P.; Wise, F. W.; Webb, W. W. *Science* **2003**, *300*, 1434–1436.

10. Pu, S. C.; Yang, M. J.; Hsu, C. C.; Lai, C. W.; Hsieh, C. C.; Lin, S. H.; Cheng, Y. M.; Chou, P. T. *Small* **2006**, *2*, 1308–1313.

11. Richards-Kortum, R.; Sevick-Muraca, E. *Annu. Rev. Phys. Chem.* **1996**, *47*, 555–606.

12. Zipfel, W. R.; Williams, R. M.; Webb, W. W. *Nat. Biotechnol.* **2003**, *21*, 1369–1377.

13. Jain, R. K.; Booth, M. F.; Padera, T. P.; Munn, L. L.; Fukumura, D.; Brown, E. Applications of Nonlinear Intravital Microscopy in Tumor Biology. In *Handbook of Biomedical Nonlinear Optical Microscopy*; Masters, B. R.; So, P. T. C., Eds.; Oxford University Press: New York, 2008; pp 735–756.

14. McLaurin, E. J.; Greytak, A. B.; Bawendi, M. G.; Nocera, D. G. *J. Am. Chem. Soc.* **2009**, *131*, 12994–13001.

15. Yoshihara, T.; Yamaguchi, Y.; Hosaka, M.; Takeuchi, T.; Tobita, S. *Angew. Chem. Int. Ed.* **2012**, *51*, 4148–4151.

16. Coogan, M. P.; Court, J. B.; Gray, V. L.; Hayes, A. J.; Lloyd, A. H.; Millet, C. O.; Pope, S. J. A.; Lloyd, D. *Photochem Photobiol. Sci.* **2010**, *9*, 103–109.

17. Amelia, M.; Lavie-Cambot, A.; McClenaghan, N. D.; Credi, A. *Chem. Commun.* **2011**, *47*, 325–327.

18. Okura, I.; Kamachi, T. Application of Porphyrins and Related Compounds as Optical Oxygen Sensors. In *Handbook of Porphyrin Science*; Kadish, K. M.; Smith, K. M.; Guilard, R., Eds.; World Scientific Publishing: Singapore, 2011; Vol. 12; pp 297–348.

19. Tripathi, V. S.; Lakshminarayana, G.; Nogami, M. *Sens. Actuators, B* **2010**, *147*, 741–747.

20. Wang, X.; Meier, R. J.; Link, M.; Wolfbeis, O. S. *Angew. Chem. Int. Ed.* **2010**, *49*, 4907–4909.

21. Amao, Y.; Miyakawa, K.; Okura, I. *J. Mater. Chem.* **2000**, *10*, 305–308.

22. Zhang, H.; Sun, Y.; Ye, K.; Zhang, P.; Wang, Y. *J. Mater. Chem.* **2005**, *15*, 3181–3186.

23. Dunphy, I.; Vinogradov, S. A.; Wilson, D. F. *Anal. Biochem.* **2002**, *310*, 191–198.

24. Lakowicz, J. R.; *Principles of Fluorescence Spectroscopy*, 3rd ed.; Springer: New York, 2006.

25. Kruk, M.; Karotki, A.; Drobizhev, M.; Kuzmitsky, V.; Gael, V.; Rebane, A. *J. Lumin.* **2003**, *105*, 45–55.

26. Briñas, R. P.; Troxler, T.; Hochstrasser, R. M.; Vinogradov, S. A. *J. Am. Chem. Soc.* **2005**, *127*, 11851–11862.

27. Finikova, O. S.; Troxler, T.; Senes, A.; DeGrado, W. F.; Hochstrasser, R. M.; Vinogradov, S. A. *J. Phys. Chem. A* **2007**, *111*, 6977–6990.

28. Finikova, O. S.; Lebedev, A. Y.; Aprelev, A.; Troxler, T.; Gao, F.; Garnacho, C.; Muro, S.; Hochstrasser, R. M.; Vinogradov, S. A. *ChemPhysChem* **2008**, *9*, 1673–1679.

29. Sinks, L. E.; Robbins, G. P.; Roussakis, E.; Troxler, T.; Hammer, D. A.; Vinogradov, S. A. *J. Phys. Chem. B* **2010**, *114*, 14373–14382.

30. Zenkevich, E.; Cichos, F.; Shulga, A.; Petrov, E. P.; Blaudeck, T.; von Borczyskowski, C. *J. Phys. Chem. B* **2005**, *109*, 8679–8692.

31. Zenkevich, E. I.; Sagun, E. I.; Yarovoi, A. A.; Shulga, A. M.; Knyukshto, V. N.; Stupak, A. P.; von Borczyskowski, C. *Opt. Spectrosc.* **2007**, *103*, 958–968.

32. Zenkevich, E. I.; Sagun, E. I.; Knyukshto, V. N.; Stasheuski, A. S.; Galievsky, A. V.; Stupak, A. P.; Blaudeck, T.; von Borczyskowski, C. *J. Phys. Chem. C* **2011**, *115*, 21535–21545.

33. Blaudeck, T.; Zenkevich, E. I.; Abdel-Mottaleb, Szwaykowska, K.; Kowerko, D.; Cichos, F.; von Borzyskowski, C. *ChemPhysChem* **2012**, *13*, 959–972.

34. Jorge, P. A. S.; Mayeh, M.; Benrashid, R.; Caldas, P.; Santos, J. L.; Farahi, F. *Appl. Opt.* **2006**, *45*, 3760–3767.

35. Collier, B. B.; Singh, S.; McShane, M. *Analyst* **2011**, *136*, 962–967.

36. Wang, X.; Chen, X.; Xie, Z.; Wang, X. *Angew. Chem. Int. Ed.* **2008**, *47*, 7450–7453.

37. Zhang, C.; Ingram, J.; Schiff, S.; Xu, J.; Xiao, M. *Proc. SPIE* **2011**, *7947*, 79470B-1–79470B-6.

38. Gouterman, M. Optical Spectra and Electronic Structure of Porphyrins and Related Rings. In *The Porphyrins*; Dolphin, D., Ed.; Academic Press: New York, 1978; Vol. 3; pp 1–165.

39. Kalyanasundaram, K. *Photochemistry of Polypyridine and Porphyrin Complexes*; Academic Press: San Diego, CA, 1992; pp 498–502.

40. Callis, J. B.; Gouterman, M.; Jones, Y. M.; Henderson, B. H. *J. Mol. Spectrosc.* **1971**, *39*, 410–420.

41. Eastwood, D.; Gouterman, M. *J. Mol. Spectrosc.* **1970**, *35*, 359–375.

42. Quimby, D. J.; Longo, F. R. *J. Am. Chem. Soc.* **1975**, *97*, 5111–5117.

43. Faure, S.; Stern, C.; Guilard. R.; Harvey, P. D. *Inorg. Chem.* **2005**, *44*, 9232–9241.

44. Figgis, B. N.; Hitchman, M. A. *Ligand Field Theory and Its Applications*; Wiley-VCH: New York, 2000; pp 181–183.

45. Bonin, K. D.; McIlrath, T. J. *J. Opt. Soc. Am. B: Opt. Phys.* **1984**, *1*, 52–55.

46. Petek, H.; Bell, A. J.; Choi, Y. S.; Yoshihara, K.; Tounge, B. A.; Christensen, R. L. *J. Chem. Phys.* **1995**, *102*, 4726–4739.

47. Javier, A.; Magana, D.; Jennings, T.; Strouse, G. F. *Appl. Phys. Lett.* **2003**, *83*, 1423–1425.

48. Wen, Y.; Liu, Y.; Yang, Y.; An, L.; Song, W.; Yang, Z. *J. Micro/Nanolith. MEMS MOEMS* **2010**, *9*, 031003-1–031003-4.

49. Jones, M.; Lo, S. S.; Scholes, G. D. *Proc. Natl. Acad. Sci. USA* **2009**, *106*, 3011–3016.

50. Klimov, V. I.; Mikhailovsky, A. A.; Branch, D. W.; Leatherdale, C. A.; Bawendi, M. G. *Science* **2000**, *287*, 1011–1013.

51. Wackerly, D. D.; Mendenhall, W.; Scheaffer, R. L. *Mathematical Statistics with Applications*, 6th ed.; Duxbury: Pacific Grove, CA, 2002; pp 124–126.

52. Talapin, D. V.; Rogach, A. L.; Kornowski, A.; Hasse, M.; Weller, H. *Nano Lett.* **2001**, *1*, 207–211.

53. Balogh, L.; Zhang, C.; O'Brien, S.; Turro, N. J.; Brus, L. *Chim. Oggi* **2002**, *20*, 45–51.

54. Bullen, C.; Mulvaney, P. *Langmuir* **2006**, *22*, 3007–3013.

55. Kampas, F. J.; Gouterman, M. *J. Phys. Chem.* **1977**, *81*, 690–695.

56. Sagun, E. I.; Zenkevich, E. I.; Knyukshto, V. N.; Shulga, A. M.; Starukhin, D. Z.; von Borczyskowski, C. *Chem. Phys.* **2002**, *275*, 211–230.

57. Leatherdale, C. A.; Woo, W. K.; Mikulec, F. V.; Bawendi, M. G. *J. Phys. Chem. B* **2002**, *106*, 7619–7622.

58. Suzuki, K.; Kobayashi, A.; Kaneko, S.; Takehira, K., Yoshihara, T.; Ishida, H.; Shiina, Y.; Oishi, S.; Tobita, S. *Phys. Chem. Chem. Phys.* **2009**, *11*, 9850–9860.

59. Grabolle, M.; Spieles, M.; Lesnyak, V.; Gaponik, N.; Eychmüller, A.; Resch-Genger, U. *Anal. Chem.* **2008**, *81*, 6285–6294.

60. Pizano, A. A.; Lutterman, D. A.; Holder, P. G.; Teets, T. S.; Stubbe, J.; Nocera, D. G. *Proc. Natl. Acad. Sci. USA* **2012**, *109*, 39–43.

61. Holder, P. G.; Pizano, A. A.; Anderson, B. L.; Stubbe, J.; Nocera, D. G. *J. Am. Chem. Soc.* **2012**, *134*, 1172–1180.

62. Loh, Z. H.; Miller, S. E.; Chang, C. J.; Carpenter, S. D.; Nocera, D. G. *J. Phys. Chem. A* **2002**, *106*, 11700–11708.

63. Brown, E. B.; Campbell, R. B.; Tsuzuki, Y.; Xu, L.; Carmeliet, P.; Fukumura, D.; Jain, R. K. *Nat. Med.* **2001**, *7*, 864–868.

64. Lanning, R. M. Ph.D. Thesis, Massachusetts Institute of Technology, Cambridge, MA, USA, **2009**.

65. Förster, T. *Ann. Phys.* **1948**, *437*, 55–75.

66. Steinberg, I. Z. *Annu. Rev. Biochem.* **1971**, *40*, 83–114.

67. *CRC Handbook of Chemistry and Physics*, 84th ed.; CRC Press: Boca Raton, FL, 2003.

Chapter 4

Micelle Encapsulation of Assemblies for O_2 Sensing

4.1 Background

In Chapter 3, supramolecular assemblies consisting of a QD and a palladium(II) porphyrin were described; these have now been solublized *via* micelle encapsulation to quantify oxygen (pO_2) in aqueous media. Palladium porphyrins are sensitive in the 0–160 torr range, making them ideal phosphors for measuring O_2 levels *in vivo*. FRET is exploited as a means of signal transduction in this system to enhance porphyrin emission with concomitant quenching of quantum dot emission. This chapter presents the synthesis and characterization of these micelle sensors as well as their photophysical properties under both linear and two-photon excitation. Since quantum dot emission is unaffected by oxygen concentration, the sensor is ratiometric, enabling the use of emission intensity to quantify oxygen in aqueous samples. Having fully characterized this sensor, preliminary *in vivo* multiphoton imaging and oxygen measurements were conducted using mice with chronic dorsal skinfold chambers or cranial windows. Together, the properties of this sensor establish a ratiometric two-photon oxygen sensor for applications in probing biological microenvironments.

4.2 Preparation of Micelles

In this construct (Figure 4.1), the preformed assembly of a quantum dot and **1** (Chart 4.1) is encapsulated in a phospholipid micelle. The micelle is irradiated under two-photon conditions to selectively excite the quantum dot. Through FRET, the porphyrin is promoted to an excited electronic state. Upon interaction with molecular oxygen, the porphyrin returns its ground state and singlet oxygen is generated; the emission intensity of the porphyirn as well as its lifetime are quantitative measures of oxygen concentration. Quantum dot emission is unaffected by O_2, thereby serving as an intensity standard for ratiometric sensing.

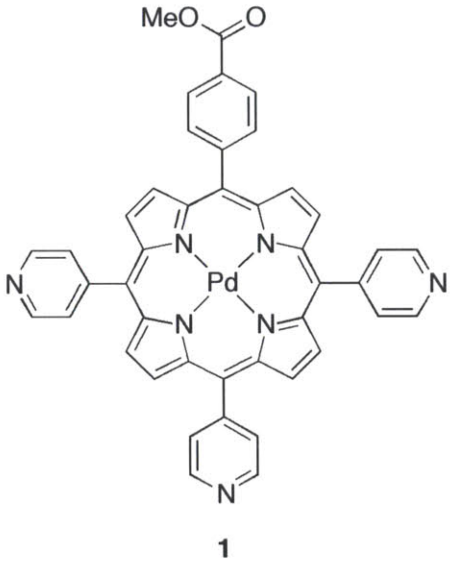

1

Chart 4.1. Molecular structure of porphyrin **1** incorporated into lipid micelles.

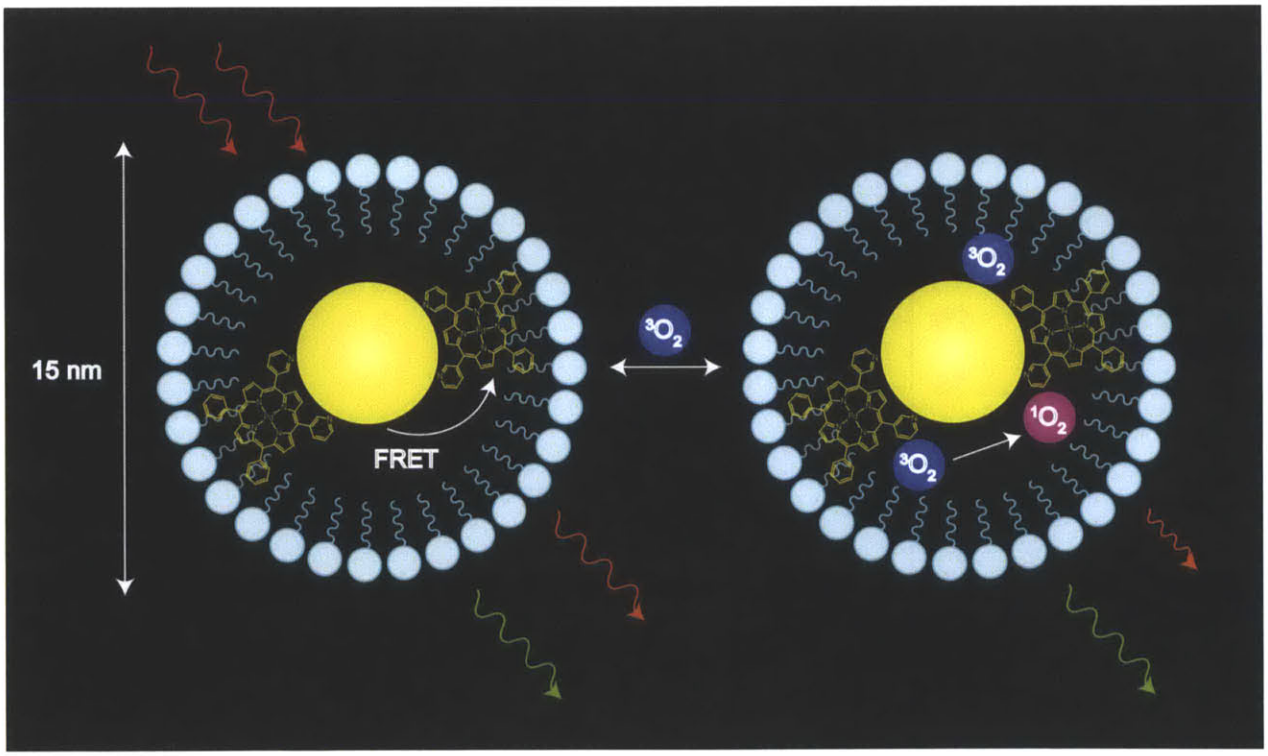

Figure 4.1. Schematic representation of the sensing methodology. The quantum dot–porphyrin assembly, encapsulated in a lipid micelle is irradiated under two-photon excitation using NIR (700-1000 nm) light. Through FRET, the porphyrin is promoted to an excited electronic state. Oxygen can freely diffuse into the micelle and reversibly quench porphyrin emission; the lifetime and intensity of the emission is a quantitative measure of O_2 concentration.

Encapsulation of quantum dots in lipid or amphiphilic polymer micelles is a well-established method of solubilizing hydrophobic dots in aqueous buffer.[1–9] While these constructs have been used extensively for biological imaging, there have been only two reports in which micelle-encapsulated quantum dots have been used for sensing analytes: nitric oxide[10] and bovine serum albumin.[11] This represents the first oxygen sensor as well as the first sensor that is ratiometric and functional under two-photon excitation that exploits micelle encapsulation. This provides a direct translation of the self-assembled supramolecular sensor of Chapter 3 from toluene to an aqueous environment. A lipid functionalized with a PEG-2000 chain was chosen to impart water solubility. While the vast majority of synthetic procedures for micelle formation involve heating and evaporation of an organic solvent[1,3,5,6] or dissolution of an organic film in aqueous media or a similar method of phase transfer,[2,4,7,8] sonication offers and alternative method to assemble micelles.

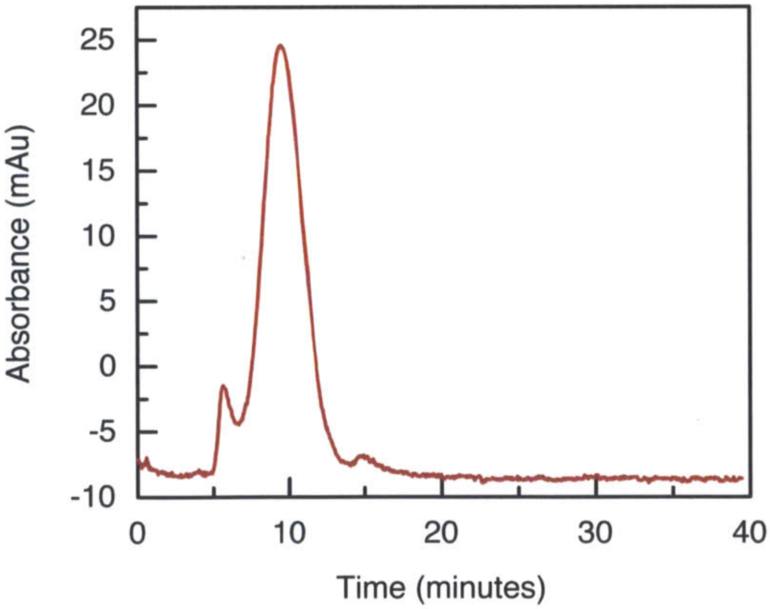

Figure 4.2. A typical GFC trace of the **QD1-MC** assembly. The eluent of the column was monitored by recording the absorbance at 280 nm.

In contrast to other sonication protocols,[9] this procedure is conducted at room temperature, yielding a rapid (~ 5 minutes) and facile method of producing nanosensors of a consistent size. The quantum dot serves as a template for micelle formation. Indeed, micelles cannot form in the absence of QD; when a porphyrin solution in the absence of QD was treated in an identical manner, the solution remained turbid and inhomogeneous. Because of the template effect in the synthesis of these sensors, a Gaussian distribution of particles is achieved, as evidenced by gel filtration chromatography (GFC) and dynamic light scattering (DLS) (see Figures 4.2 and 4.3, respectively).

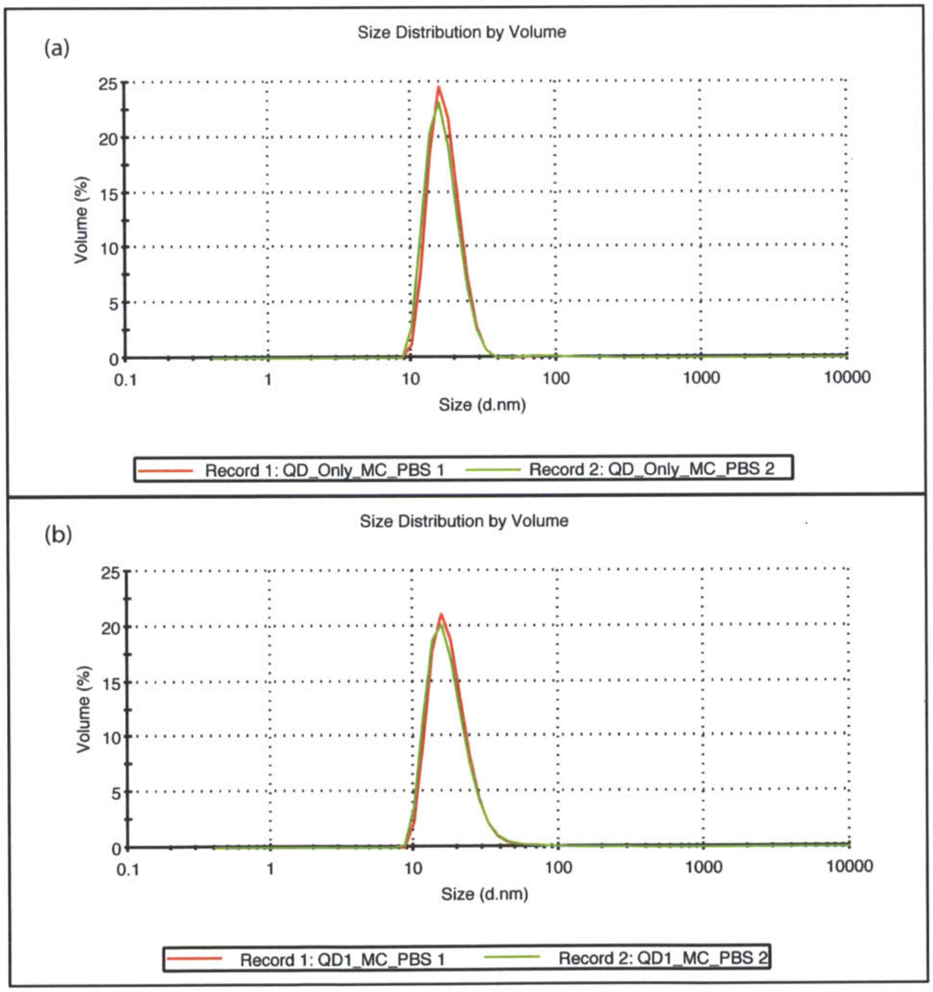

Figure 4.3. Representative DLS traces of **QD-MC** (a) and **QD1-MC** (b). Based on this data, the diameter of these particles is 16.8 nm and 18.2 nm, respectively.

Based on DLS, the average particle size for a typical synthetic preparation is 16.8 ± 0.7 nm for micelles containing the QD alone (**QD-MC**) while particles with the porphyrin (**QD1-MC**) are slightly larger at 18.2 ± 0.7 nm. Presumably, the appended porphyrins on the surface of the dot increase the radius of the assembly relative to the dot alone, resulting in a larger micelle particle. These particles are a few nanometers larger than previously reported polymeric ligands with dihydrolipoic acid (DHLA)[12] or poly-imidazole ligands (PIL),[13] both of which exhibit particle sizes of ~11.5 nm by DLS. Micelle encapsulation represents a scalable method of synthesizing water-soluble nanosensors and circumvents laborious multi-step polymer syntheses. Additionally, these micelles are stable for several months when stored at 4°C.

4.3 Photophysical Properties of Micelles

The photophysical properties of these micelles, both **QD-MC** and **QD1-MC** are comparable to their toluene-soluble analogues **QD** and **QD1**, with a few notable exceptions (*vide infra*). The absorbance spectrum (Figure 4.4) is dominated by the Soret and two Q bands of porphyrin **1**, while the emission spectrum features both QD luminescence at 527 nm and emission from **1**: triplet transitions centered at 682 and 754 nm and a singlet transition at 608 nm. The photophysical properties, including the phosphorescence quantum yield, of **QD1-MC** in PBS are nearly identical to the assembly **QD1** in toluene (Table 4.1), suggesting that the porphyrin largely resides in a hydrophobic environment of QD capping ligand and lipid. The sensor **QD1-MC** exhibits oxygen dependent emission. Under 450 nm excitation where the QD is the primary photon absorber, there is a ten-fold enhancement in the intensity of the T(0,0) transition of the evacuated sample relative to the same sample exposed to air. It should be noted that the enhancement is not nearly as great as the toluene-soluble assembly **QD1**, which exhibited a 100 fold enhancement of the T(0,0) transition.

Table 4.1. Comparison of Linear Spectroscopic Data for **1**, **QD1**, and **QD1-MC**

Compound	B(0,0)	Q(1,0)	Q(0,0)	QD_{Em}	T(0,0)[a]	T(0,1)[a]	ϕ_P[b]
1[c]	414	522	554	–	684	753	0.014
QD1[c]	416	523	554	517	684	754	0.040
QD1-MC[d]	414	523	555	527	682	754	0.012

[a] Phosphorescence transitions observed in evacuated samples (< 10^{-5} torr), [b] Phosphorescence quantum yield for evacuated samples using Eq. 11, [c] Toluene solution, [d] PBS solution

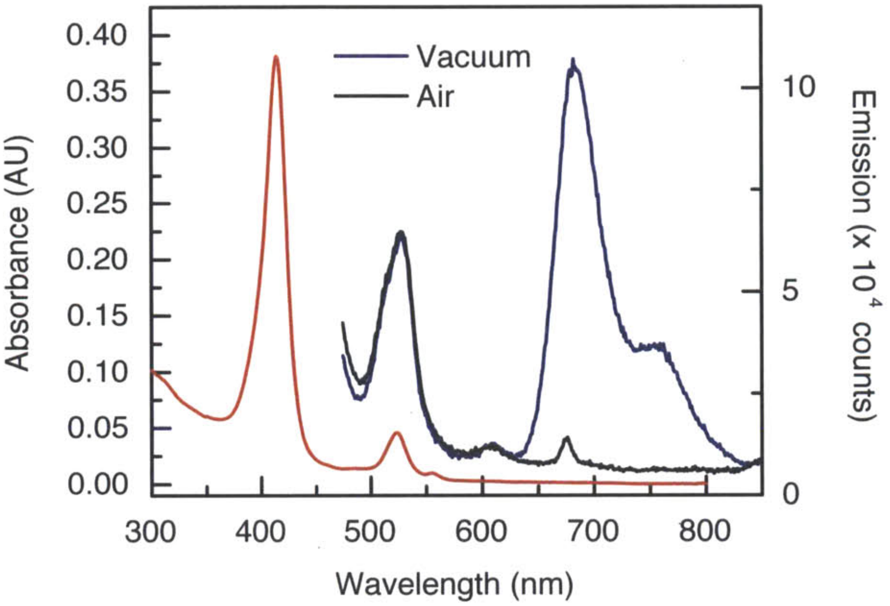

Figure 4.4. The steady state absorption (▬) and emission spectra of **QD1-MC** (λ_{ex} = 450 nm) in PBS buffer. While the emission intensity of the phosphor is almost completely quenched in the presence of air (~160 torr O_2) (▬), it is greatly enhanced under vacuum (▬). The emission of the QD in **QD1-MC** is unchanged in air and vacuum, thereby establishing a ratiometric sensor.

The absorption and emission spectra (λ_{ex} = 450 nm) of **QD-MC** (Figure 4.5) are red-shifted relative to **QD** in toluene; the first absorption feature shifts from 501 nm for **QD** to 503 nm for **QD-MC** while the emission maximum shifts from 519 nm to 523 nm. This spectral shift is due to an increase in dielectric constant of the solvent[14] from toluene to aqueous solution (ε = 2.379 for toluene versus ε = 80.20 for water at 20°C)[15]. An increase in the lifetime (λ_{ex} = 450 nm) of the QD in the micelle versus toluene solution (see Table 4.2) was observed. This is due a modulation of the surface states of the QD; indeed, the lifetime of the surface-trapped states is increased by ~4 ns while the exciton emission lifetime is nearly identical.

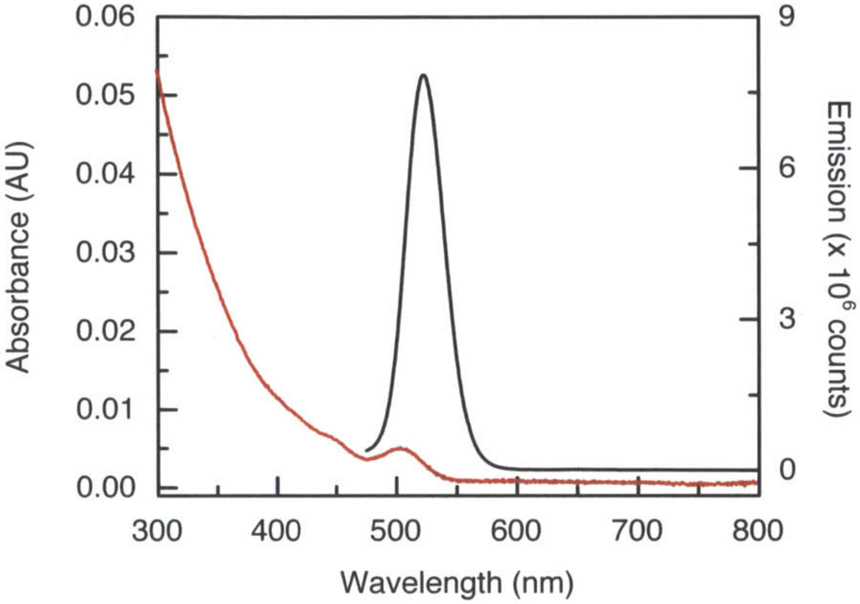

Figure 4.5. Comparison of the steady state absorption (—) and emission spectra (—) (λ_{ex} = 450 nm) of **QD-MC** in PBS solution.

The energy transfer and FRET efficiency of these micelles was also studied. Experimentally, the lifetime of the QD in **QD1-MC** is dramatically diminished (~80 ps) relative to **QD-MC** (~13 ns), corresponding to a FRET efficiency of 99% (Table 4.2). The excitation spectrum (Figure 4.6) is also indicative of a FRET interaction, as demonstrated by the increased emission in the 300–400 nm region, where the QD absorbance dominates. Additionally, the red shift in **QD-MC** emission (*vide supra*) results in greater spectral overlap with the absorption of **1** (Figure 4.7), resulting in an increase of FRET efficiency. A summary of FRET parameters is presented in Table 4.3. It should be noted that the observed number of porphyrins per quantum dot is lower than the number of added porphyrin equivalents, presumably due to intercalation of the hydrophobic porphyrin in the excess lipid used to prepare the micelles, which is subsequently washed away. Also, a decrease in the quantum yield of the QD was observed, dropping from Φ = 0.72 in toluene to Φ = 0.42 for the micelle **QD-MC** in PBS. However, this construct has a superior quantum yield to micelles with the same lipid and similar dots (Φ = 0.24),[1] suggesting that synthesis of the micelle (sonication versus heating) may have an effect on the quantum yield.

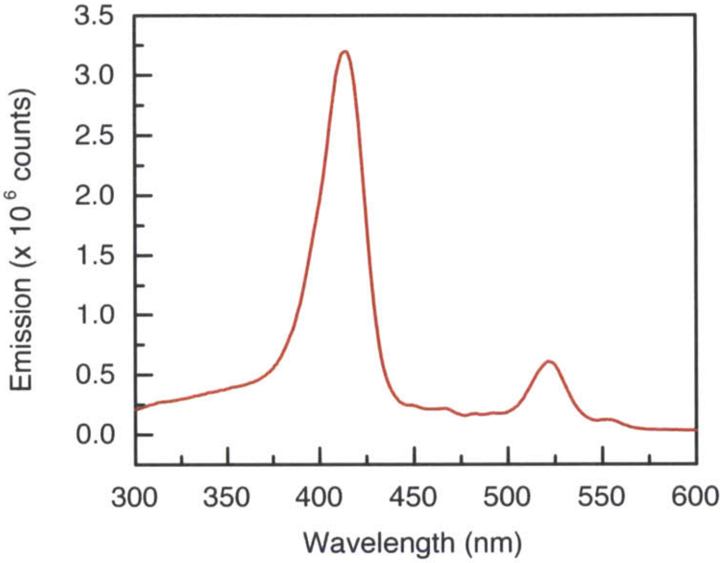

Figure 4.6. Excitation spectrum of **QD1-MC** in PBS solution, monitoring the emission at 685 nm. Excitation light was removed using a 590 nm long-pass filter.

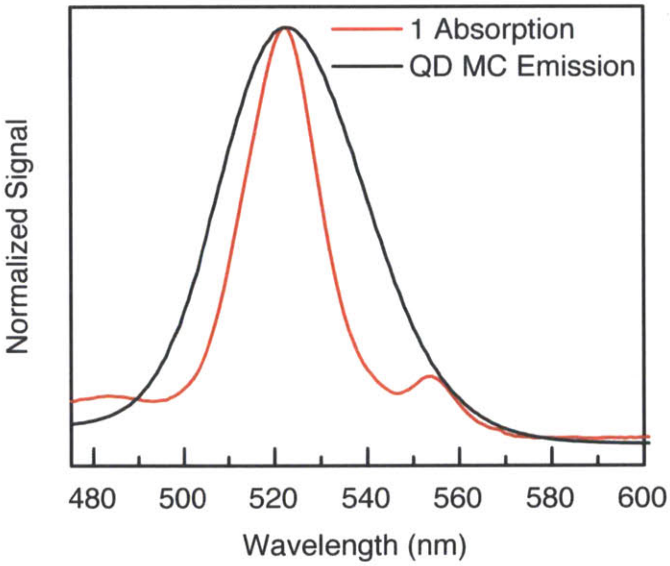

Figure 4.7. Normalized **QD-MC** emission (—) (λ_{ex} = 450 nm) and absorption of **1** (—), illustrating the spectral overlap that accounts for high FRET efficiency in **QD1-MC**.

Table 4.2. Comparison of QD Lifetime Data for Micelles in PBS

Compound[a]	Solvent	τ_1 (ns)	A_1 (%)[b]	τ_2 (ns)	A_2 (%)[b]	τ_{avg} (ns)[c]
QD	toluene	16.93 ± 0.36[d]	53	5.07 ± 0.95	47	11.30 ± 1.22
QD-MC	PBS	20.62 ± 1.74	56	4.38 ± 1.43	44	13.38 ± 1.44
QD1	toluene	1.27 ± 0.13	3	0.26 ± 0.03	97	0.29 ± 0.01
QD1-MC	PBS	0.386 ± 0.035	<1	0.078 ± 0.002	>99	0.079 ± 0.002

[a] $\lambda_{ex} = 450$ nm, [b] Relative contribution to the biexponential fit, [c] Weighted average lifetime, calculated as $\tau_{avg} = (A_1\tau_1 + A_2\tau_2)/100$, [d] 95% Confidence interval

Table 4.3. Comparison of Förster Energy Transfer Parameters

Compound	m	J[a] (M^{-1} cm^3)	r[b] (nm)	R_0[a] (nm)	E[c]
QD1	10	7.96×10^{-14}	3.15	4.11	0.97
QD1-MC	8	8.07×10^{-14}	2.67	4.06	0.99

[a] Calculated using Eq. 14, [b] Calculated using Eq. 12, [c] Calculated using Eq. 13

In this sensor, the role of the QD is to serve as an antenna for two-photon absorption, as QDs are known to have high two-photon absorption cross-sections;[16–18] both **QD-MC** and **QD1-MC** were studied under two-photon excitation. It was found under the experimental conditions (5–8 mW of focused 800 nm light), the PBS solvent is an effective medium for generating white light. This is in stark contrast to toluene, which enabled the collection of two-photon spectra of **QD**, **1**, and **QD1** (see Chapter 3). Due to the high two-photon cross section and quantum yield of **QD-MC**, it was possible to collect a two-photon emission spectrum of this species (Figure 4.8), as the green emission of the sample greatly exceeded the generated white light.

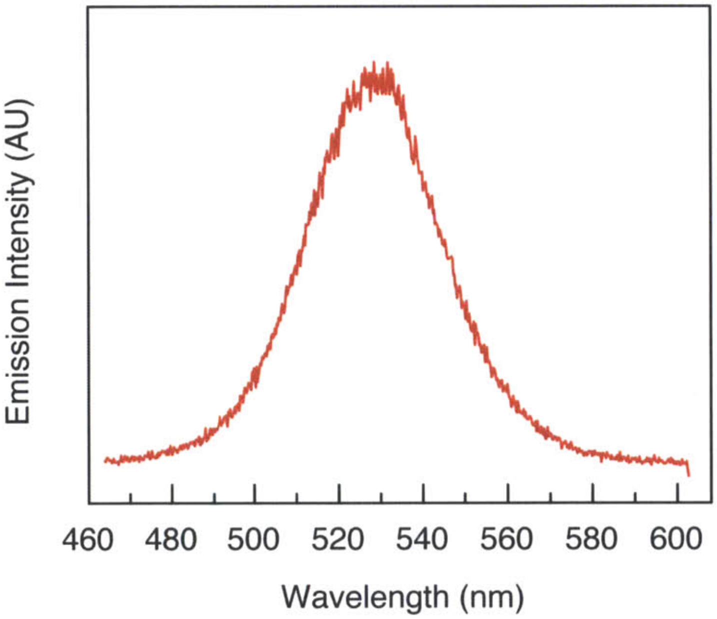

Figure 4.8. Steady state emission spectrum of **QD-MC** in PBS solution under two-photon excitation ($\lambda_{ex} = 800$ nm).

However, the low quantum yield of the porphyrin and the dramatically quenched quantum dot emission in the assembly **QD1-MC** resulted in low signal that was much less than the generated white light, even in the absence of oxygen. Increasing the laser power only resulted in more efficient white light generation. While a two-photon emission spectrum of **QD1-MC** could not be obtained, visible red-orange emission of the evacuated sample could be observed, thereby qualitatively demonstrating the function of the assembly: two-photon excitation of the quantum dot, energy transfer to the porphyrin, followed by porphyrin emission. Other experiments (*vide infra*) demonstrate that this assembly is functional under two-photon excitation.

The excited state lifetimes of **1** in **QD1-MC** under both linear and two-photon excitation were measured and the results are presented in Table 4.4. Under both one- and two-photon excitation, the lifetime of **QD1-MC** in air is enhanced relative to **QD1**. Indeed, under linear excitation the lifetime of the porphyrin in air of **QD1-MC** (~ 4 μs) is enhanced by a factor of 10 relative to **QD1** (~ 0.2 μs). This enhancement is concomitant with a decrease in the average natural lifetime (τ_0) under vacuum, resulting in a smaller 0–160 torr O_2 lifetime range of 206 μs for **QD1-MC** versus 480 μs for **QD1** under 450 nm excitation. This phenomenon has been previously observed when the solution lifetime of palladium porphyrins were compared to those in asolectin vesicles. It was found that the air lifetime was enhanced for the vesicle while the lifetime under nitrogen was diminished relative to the same compound free in solution.[19] Under two-photon excitation with 850 nm light, both **QD1** and **QD1-MC** show nearly identical oxygen sensitivity as the average values of $\tau_0 - \tau_{air}$ for these two species are 190 μs and 165 μs, respectively. This is in stark contrast to 450 nm excitation where $\tau_0 - \tau_{air}$ is 479 μs for **QD1** and 205 μs for **QD1-MC**, a difference of 274 μs. This suggests that the two-photon excitation mechanism (sequential QD excitaiton, FRET, porphyrin emission) is the same for both sensors. It is clear that the micelle structure is engendering a perturbation of the assembly, as evidenced by the differences in lifetime of **QD1** and **QD1-MC** under linear excitation.

Table 4.4. Comparison of Porphyrin Lifetimes for **QD1-MC**

Sample	Environment	Excitation	τ_1 (μs)	A_1 (%)[a]	τ_2 (μs)	A_2 (%)[a]	τ_{avg}[b] (μs)
QD1-MC[c]	Air	450 nm	6.01 ± 0.43[d]	49	2.35 ± 0.23	51	4.13 ± 0.23
QD1-MC	Vacuum[e]	450 nm	411 ± 27	48	29 ± 5	52	209 ± 10
QD1-MC	Air	850 nm	5.50 ± 0.36	1	0.69 ± 0.03	99	0.73 ± 0.05
QD1-MC	Vacuum	850 nm	325 ± 35	40	60 ± 6	60	165 ± 19
QD1[f]	Air	450 nm	0.638 ± 0.064	17	0.069 ± 0.011	83	0.174 ± 0.092
QD1	Vacuum	450 nm	590 ± 79	75	149 ± 51	25	479 ± 26
QD1	Air	850 nm	0.537 ± 0.014	100	–[g]	–	0.537 ± 0.014
QD1	Vacuum	850 nm	270 ± 11	62	60 ± 10	38	190 ± 16

[a] Relative contribution to the biexponential fit, [b] Weighted average lifetime, calculated as $\tau_{avg} = (A_1\tau_1 + A_2\tau_2)/100$, [c] PBS solution, [d] 95% Confidence interval, [e] Evacuated samples (< 10^{-5} torr), [f] Toluene solution, [g] Due to instrumental limitations, the fast component could not be resolved and the data was fit to a monoexponential decay

Since the observed difference in $\tau_0 - \tau_{air}$ for **QD1-MC** is similar to that of free porphyrin **1** in toluene, it appears that the porphyrin in the micelle is behaving as though it is free in solution. A physical interpretation of this observation is that the poprhyrin is now residing in a "solution" of the hydrophobic phospholipid rather than bound to the surface of the quantum dot. During the process of micelle formation, it could be that the porphyrin of the preformed assembly dissociates from the surface of the quantum dot and is now dispersed in the oleate groups of the phospholipid; this process is likely facilitated by the force of sonication used to form the micelles. This is consistent with the observation that the photophysical properties of **QD1-MC** (wavelength of the Soret band and quantum yield) are more similar to **1** than to **QD1**.

4.4 Oxygen Sensitivity and Quenching Kinetics

In order to rigorously study the oxygen sensitivity of these micelle sensors and probe the quenching kinetics, oxygen-dependent emission spectra and lifetime measurements were acquired. Both intensity and lifetime data are necessary to elucidate the details of the oxygen dependence in the system. First, emission spectra (λ_{ex} = 450 nm) of **QD1-MC** were collected after exposure to various concentrations of dissolved oxygen (Figure 4.9a). The emission intensity at 682 nm of each sample (I), normalized to the emission intensity in the absence of oxygen (I_0) was plotted as a function of oxygen concentration to give an intensity Stern-Volmer plot (Figure 4.9b). This nonlinear response also manifests in the ratio of porphyrin to quantum dot emission, I_{682}/I_{528} (Figure 4.10a); this phenomenon has also been observed in ratiometric sensors consisting of a platinum porphyrin as the oxygen-sensitive phosphor and a quantum dot as an intensity reference embedded in a polymer hydrogel.[20] If only simple bimolecular quenching was operative, the data should exhibit a linear relationship:

$$\frac{I_0}{I} = 1 + K_{SV}[\mathrm{O_2}] \qquad (1)$$

where K_{SV} is the Stern-Volmer quenching constant and is defined as $K_{SV} = k_q\tau_0$, where k_q is the bimolecular quenching constant and τ_0 is the natural lifetime of the phosphor in the absence of quencher.

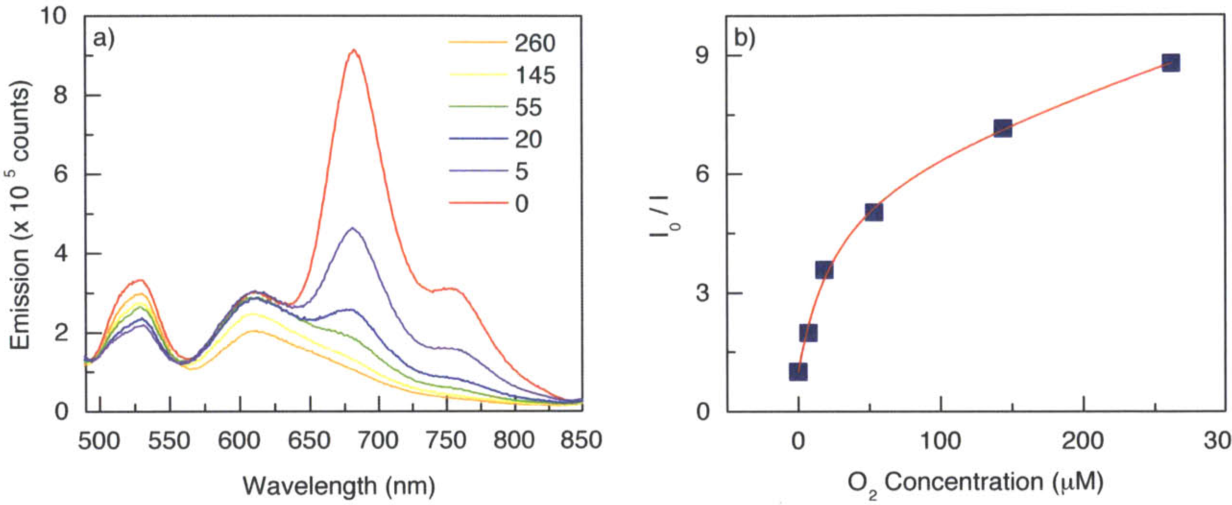

Figure 4.9. (a) The steady state emission spectra of **QD1-MC** (λ_{ex} = 450 nm) in PBS buffer with various oxygen concentrations: 0 (—), 5 (—), 20 (—), 55 (—), 145 (—), and 260 (—) μM O_2. (b) An intensity Stern-Volmer plot constructed from the data obtained in (a) at 682 nm. The data was fit (—) to a two-component model.

However, the nonlinear oxygen response indicates that the quenching mechanism is more complicated. Nonlinear Stern-Volmer plots are rather common,[21–25] especially for phosphors embedded in a polymer matrix.[26–31] Two common sources of nonlinearity are the presence of static quenching or a heterogeneous distribution of phosphors with different quenching constants.[14] If the data could be explained as a combination of both static and dynamic quenching, the mathematical description of this situation is as follows:

$$\frac{I_0}{I} = \left(1 + K_D[\mathrm{O}_2]\right)\left(1 + K_S[\mathrm{O}_2]\right) \tag{2}$$

where K_D is the dynamic quenching constant and K_S is the association constant for the complex formation between the ground-state phosphor and molecular oxygen (*i.e.* static quenching).

Thus, if static quenching were operative, a plot of $\left[\frac{I_0}{I}-1\right]/[O_2]$ versus $[O_2]$ should result in a linear relationship in which the slope of the line is $K_D K_S$ and the intercept is $K_D + K_S$. However, the treatment of the data in this manner (Figure 4.10c) gives a nonlinear plot, indicating that static quenching is not occurring this system.

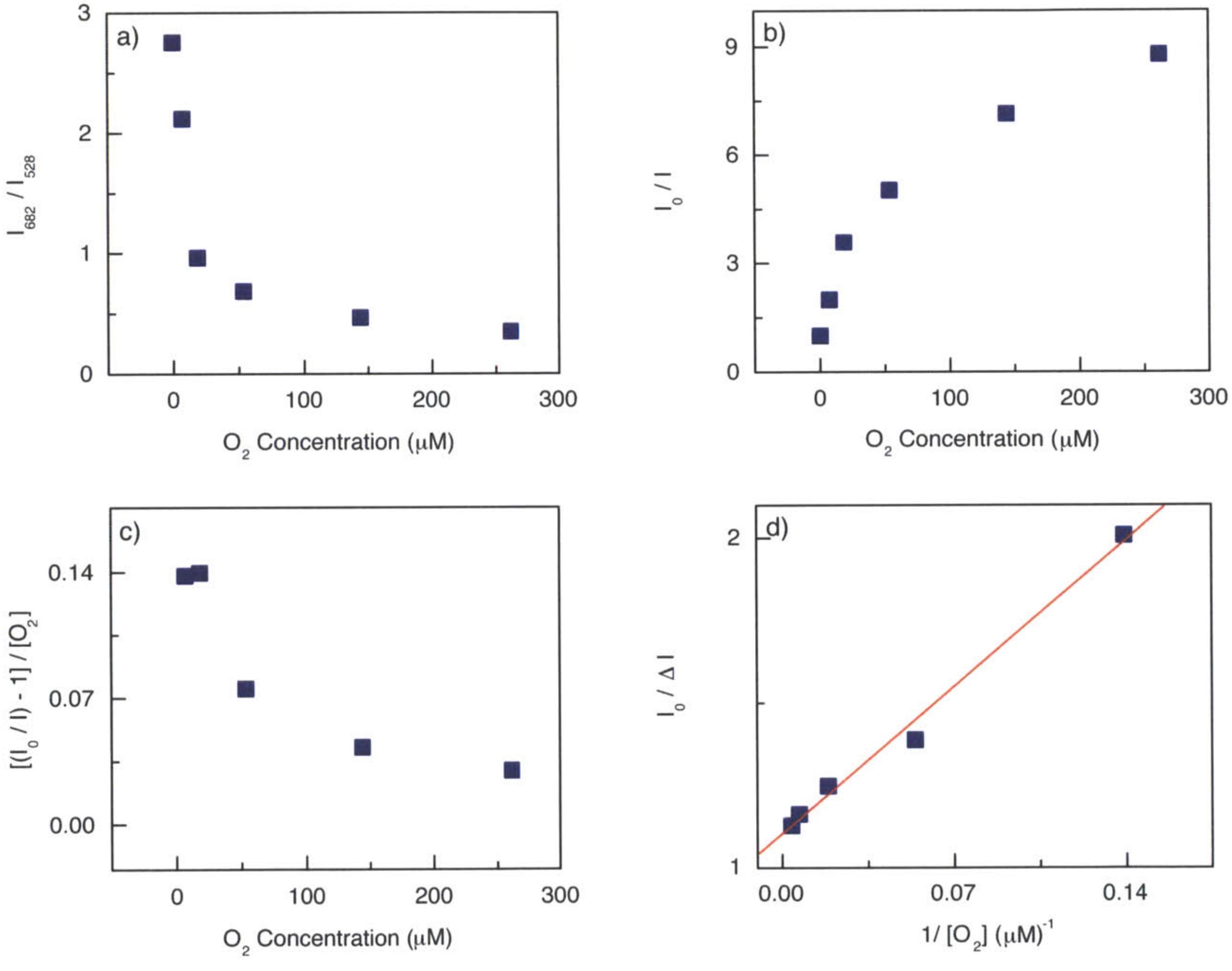

Figure 4.10. (a) A plot of the ratio of porphyrin emission at 682 nm to quantum dot emission at 528 nm (I_{682}/I_{528}) as a function of oxygen concentration. (b) The raw data obtained from the oxygen-dependent emission spectra presented in Figure 4.9b. (c) A plot of $\left[\frac{I_0}{I}-1\right]/[O_2]$ versus $[O_2]$ to determine if static quenching is present in **QD1-MC**. (d) A plot of $\frac{I_0}{\Delta I}$ versus $[O_2]^{-1}$ to determine if a two-component system is a sufficient means of explaining the nonlinearity of (b).

Alternatively, if the system exhibits microheterogeneity, as has been well-established for fluorophores in polymer supports and micelles,[32] the individual components of the system exhibit unique Stern-Volmer quenching constants. As a simple case, assume that there are two types of phosphors in the system: one that is accessible to the quencher and one that is not. In this case, the quenching can be described using the following mathematical model:

$$\frac{I_0}{\Delta I} = \frac{1}{f_a K_a [\mathrm{O_2}]} + \frac{1}{f_a} \tag{3}$$

where $\Delta I = I_0 - I$, K_a is the Stern-Volmer quenching constant for the accessible fraction of phosphors, and f_a is the fractional amount of the phosphor that is accessible to quencher. Thus, if this model were a reasonable description of the data, a plot of $I_0/\Delta I$ versus $[\mathrm{O_2}]^{-1}$ would yield a linear relationship with a slope of $(f_a K_a)^{-1}$ and an intercept of f_a^{-1}.[14] This analysis of the intensity data (Figure 4.10d) gives a linear fit to the data ($R^2 = 0.98749$), resulting in $f_a = 0.906$ and $K_a = 0.174 = \mu\mathrm{M}^{-1}$. This analysis suggests that the data is explained by the presence of two populations of palladium porphyrins in the micelle. A more general treatment of the data is to assume that these two populations each have a distinctive Stern-Volmer quenching constant;[22,27–30] the assumptions of Eq. 3 represent a limiting case of this two-component scenario. If it is assumed that the phosphors reside in two distinct environments, the corresponding mathematical model is:

$$\frac{I_0}{I} = \left[\frac{f_1}{1 + K_1[\mathrm{O_2}]} + \frac{f_2}{1 + K_2[\mathrm{O_2}]} \right]^{-1} \tag{4}$$

where the fractions of the two components are f_1 and f_2, the Stern-Volmer quenching constants are K_1 and K_2, and there is the constraint that $f_1 + f_2 = 1$. The intensity data in Figure 4.9b was fit to Eq. 4 ($R^2 = 0.99625$) to give the following parameters: $f_1 = 0.854$, $K_1 = 0.242\ \mu\mathrm{M}^{-1}$, $f_2 = 0.146$, and $K_2 = 0.00173\ \mu\mathrm{M}^{-1}$. Since lifetime measurements have been made (Table 4.4), the bimolecular quenching constants may be determined. Using the average lifetime under vacuum (209 μs), as the static intensity measurements are representative of an average of the lifetimes in the micelle ensemble, the quenching rate constants are determined to be $k_{q1} = 1.16 \times 10^9$ M^{-1} s^{-1} and $k_{q2} = 8.28 \times 10^6$ M^{-1} s^{-1}. The difference in the two values of K (~10^3) is consistent with other reports in which this analysis has been applied to systems in which platinum(II) porphyrins have been used as the oxygen-sensitive phosphor.[23,31]

As a more rigorous measurement of the oxygen sensitivity, oxygen-dependent lifetimes were measured; a representative example of the decay traces as a function of oxygen concentration is presented in Figure 4.11. Each trace was fit to a biexponential decay, as this is identical to the fitting regimes used to generate the data in Table 4.4. It has been shown[27,29,30] that the most appropriate treatment of the data is to define a pre-exponential factor weighted lifetime:

$$\tau_{\mathrm{M}} = \sum_{i=1}^{N} a_i \tau_i / \sum_{i=1}^{N} a_i \qquad (5)$$

where a_i is the pre-exponential factor and τ_i is the lifetime of the ith component of the fit and the sum is taken over the total number of components in the fit N, which is equal to two for a biexponential fit. In the absence of static quenching or other effects, this representation of the lifetime data should match the intensity data as described in Eq. 4 such that $\tau_{\mathrm{M0}}/\tau_{\mathrm{M}} = I_0/I$.[27] In principle, each of the components should still follow Stern-Volmer kinetics, giving a linear relationship in a plot of τ_{i0}/τ_i versus $[\mathrm{O_2}]$. In practice, multiexponential fits are merely mathematical models that distill a complex distribution of excited state lifetimes in a microheterogeneous system into a few components, giving rise to lifetimes and pre-exponential factors that may have no physical basis.[33] Thus, a plot of τ_{M0}/τ_M versus $[O_2]$ should describe the overall quenching dynamics that are operative in the system.

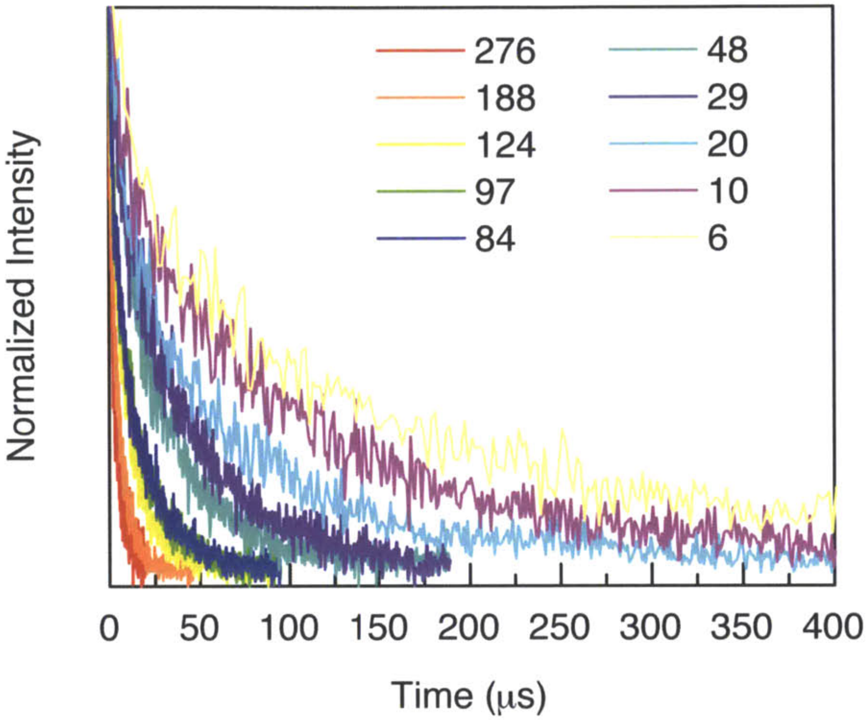

Figure 4.11. Representative series of lifetime decay traces of **QD1-MC** as a function of oxygen concentration. The lifetime of the porphyin emission was monitored at 685 nm.

Analysis of a typical oxygen-dependence series for a given sample of **QD1-MC** is presented in Figures 4.12 and Figure 4.13, which were conducted at 25°C and 37°C, respectively. In each series of lifetime measurements, the plot of τ_{M0}/τ_M versus $[O_2]$ exhibits upward curvature, directed toward the y-axis. If the system were simply represented by two components, each should exhibit typical Stern-Volmer behavior:

$$\frac{\tau_0}{\tau} = 1 + k_q \tau_0 [O_2] \tag{6}$$

For each dataset, the long component is well behaved and exhibits a typical Stern-Volmer relationship (*vide infra*). Alternatively, the short component is much less consistent and a typical series of measurements displays several anomalous points in which the computed lifetime does not monotonically decrease with increasing oxygen concentration (see Figure 4.12a); this demonstrates that the two-component representation may merely be a mathematical construct with no real physical meaning. Indeed, the normalized pre-exponential factors show a dependence on the oxygen concentration. For a typical set of experiments, the short component tends to dominate at low oxygen concentrations, but when $[O_2] > 100$ μM, the long component dominates with an approximately 60% contribution to the fit.

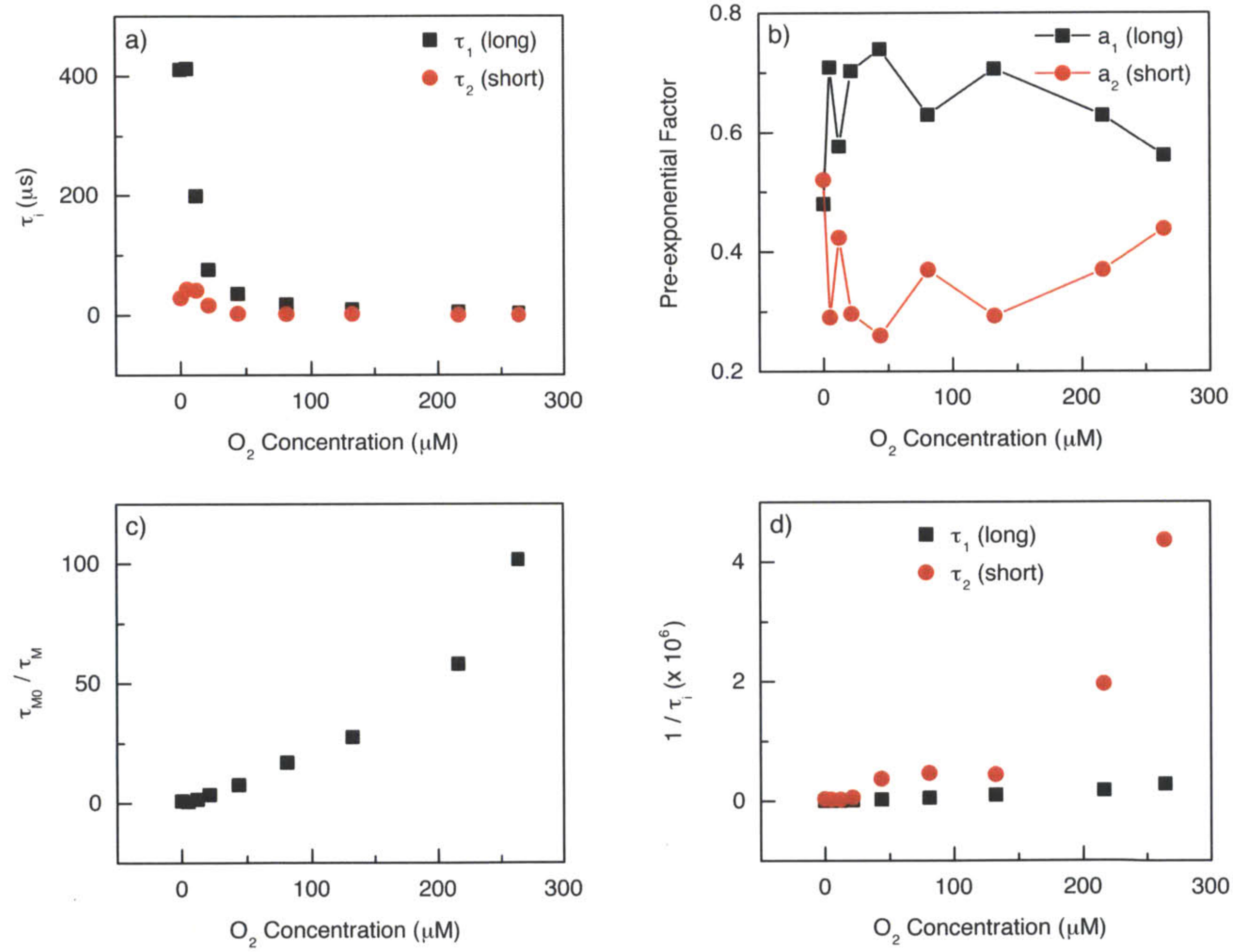

Figure 4.12. Representative analysis of a set of lifetime data of **QD1-MC** as a function of oxygen concentration at 25°C. (a) A plot of the lifetime components (τ_i) as a function of $[O_2]$ (b) A plot of the pre-exponential factors (a_i) as a function of $[O_2]$. Ideally, the contribution of each component of the fit should not exhibit a dependence on $[O_2]$. (c) A plot of τ_{M0}/τ_M as a function of $[O_2]$, illustrating the upward curvature (toward the y-axis) of the data at high $[O_2]$. (d) A plot of $1/\tau_i$ as a function of $[O_2]$, illustrating that long component exhibits a linear dependence while the short component shows an exponential dependence.

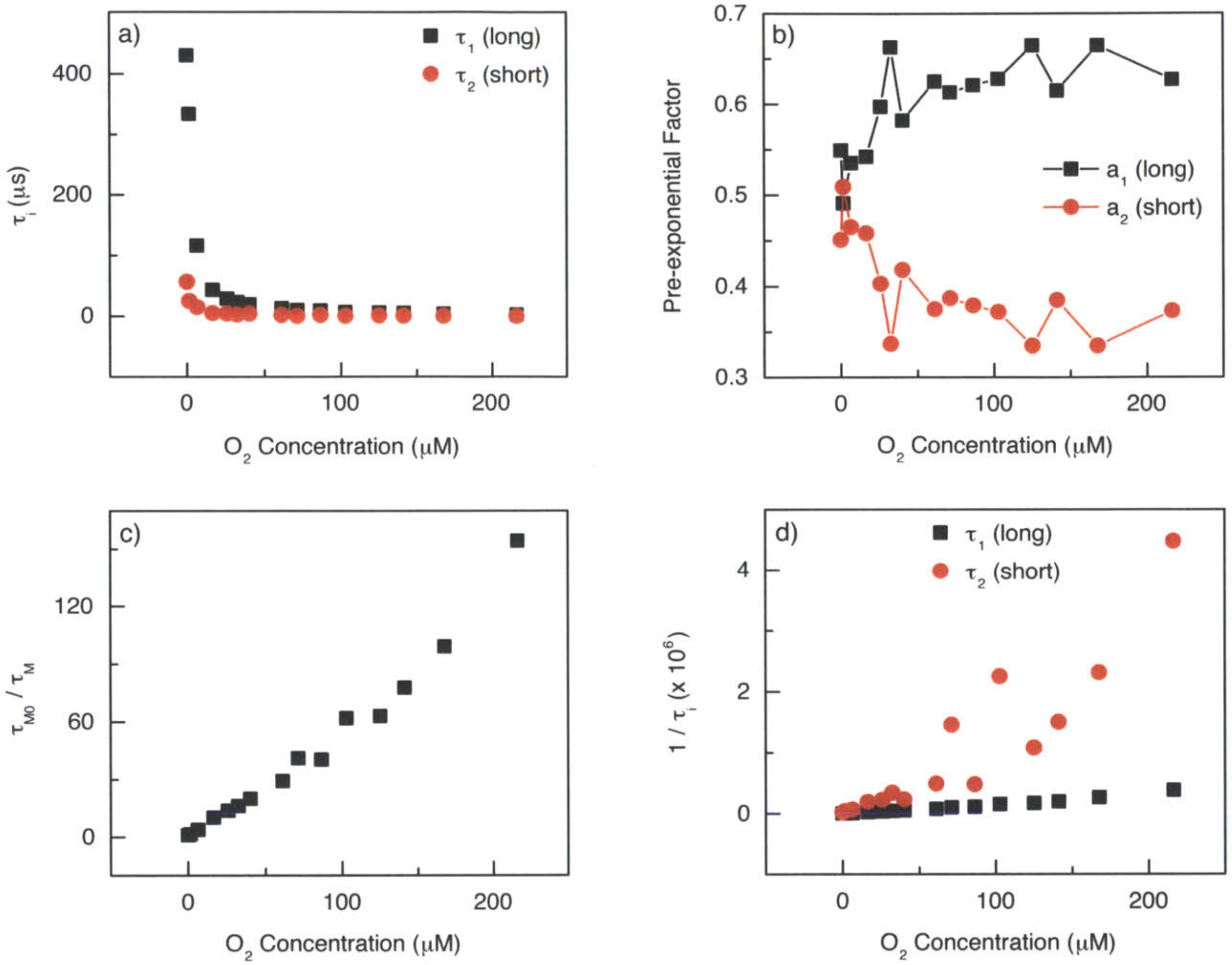

Figure 4.13. Representative analysis of a set of lifetime data of **QD1-MC** as a function of oxygen concentration at 37°C. (a) A plot of the lifetime components (τ_i) as a function of [O_2]. It should be noted that, while the long component decreases monotonically with increasing oxygen concentration, the short component does not; this is more clearly illustrated in (d). (b) A plot of the pre-exponential factors (a_i) as a function of [O_2]. Ideally, the contribution of each component of the fit should not exhibit a dependence on [O_2]. (c) A plot of τ_{M0}/τ_M as a function of [O_2], illustrating the upward curvature (toward the y-axis) of the data at high [O_2]. (d) A plot of $1/\tau_i$ as a function of [O_2], demonstrating that while the long component exhibits a linear dependence on oxygen concentration, the short component shows an exponential dependence.

Since the data does not display the expected behavior and there is a strange oxygen dependence on the pre-exponential factor, an alternative model to interpret the data may be necessary. Lippitsch and co-workers have reported nonlinear lifetime Stern-Volmer relationships with ruthenium(II) phenanthroline complexes embedded in polymer matrices.[33] After fitting the decay traces to a multiexponential function, they too observe a dependence of the pre-exponential factors on the oxygen concentration and conclude that this finding is indicative of a distribution of relaxation rates. The phosphor can interact with the polymer matrix, thereby affecting both the radiative and non-radiative decay pathways of the excited state. Because the polymer is microheterogeneous, a distribution of phosphor and polymer interactions exist, giving rise to decay kinetics that cannot appropriately be attributed to a multiexponential function. In this construct, the relaxation probability of a single fluorophore is determined by the interactions with the surrounding polymer in a distance dependent fashion and is mathematically described by the following differential equation:

$$\frac{dp_j}{dt} = k^{(i)} + \sum_k k_j^{(e)}\left(r_{jk}\right) \qquad (7)$$

where p_j is the probability for the jth excited molecule to be found in the excited state at time t, $k^{(i)}$ is the internal relaxation rate of the molecule and is assumed to be constant for all fluorophores, $k_j^{(e)}(r_{jk})$ is an external decay rate that is dependent on the jth excited molecule with the kth site of the polymer with a dependence on the distance r_{jk} between them. If it is assumed that the interaction between the phosphor and polymer site is dipolar in nature with an r^{-6} dependence in three dimensions, it has been shown[34–36] that the solution to Eq 7 is the following probability function:

$$p_j(t) = p_j(0)\exp\left[-a\sqrt{t/\tau} - t/\tau\right] \qquad (8)$$

where $p_j(0)$ is the initial probability for the jth molecule to be in the excited state, a is an interaction parameter, and $\tau = 1/\, k^{(i)}$. When the molecule is quenched by an exogenous species, another term is added to Eq. 7 to describe the quenching interaction: $k_j^{(Q)}[Q]$. If it is assumed that the quenching rate is the same for all molecules and the density of interaction sites is independent of quencher concentration, then Eq. 8 then becomes:

$$f(t) = \exp\left[-a\sqrt{t/\tau} - t/\tau(1+c)\right] \tag{9}$$

where $f(t)$ is the time-dependent fluorescence intensity, which is proportional to $p_j(t)$ of Eq. 8, and c is a quenching parameter that is dependent on the oxygen concentration and is related to $k_j^{(Q)}[Q]$.[33] It should be noted that given the definition of the parameter τ, it represents the natural lifetime of the molecule in the absence of quencher (τ_0) and should not exhibit a dependence on the oxygen concentration. Using this mathematical model, Lippitsch and co-workers demonstrated that this description was more appropriate than multiexponential decays to describe ruthenium(II) phenanthroline complexes embedded in polymer matrices. Each sample displayed a consistent value for τ and a, with only c exhibiting a dependence on the oxygen concentration.[33]

The distribution of the porphyrin **1** in the hydrophobic capping ligands of the quantum dot and the oleate groups of the micelle phospholipid is akin to a phosphor distributed in a polymer matrix. The hydrophobic residues can interact with the excited state of **1**, thereby perturbing the decay dynamics of the molecule. To test this model, a representative data set of oxygen-dependent decays (presented in Figure 4.11) was fit to Eq 9. The residuals of the fit for each oxygen-dependent decay showed a regular trend, suggesting that the model doesn't completely capture the data; this is corroborated by the higher value of the χ^2 statistic for the fit of Eq 9 relative to the biexponential. Also the calculated correlation coefficients were inferior to the biexponential fit (0.94–0.97 for Eq 9 compared to 0.99 for a biexponential). Additionally, the calculated error in each of the parameters exceeded the value of the parameter itself. For each oxygen concentration, all three parameters of the fit (τ, a, and c) varied. Based on the theory, the values for both τ and a should remain constant and only c should vary. However, it was found that only τ showed a dependence on the oxygen concentration. Despite the inferiority of the fits and deviations from theory, a plot of τ_0/τ versus $[O_2]$ exhibited remarkable linearity (Figure 4.14), with $R^2 = 0.98741$. This treatment of the data distills a distribution of excited state lifetimes into a single parameter τ and gives an overall description of the quenching kinetics: $K_{SV} = 1.27\ \mu M^{-1}$ with $k_q = 3.18 \times 10^8\ M^{-1}\ s^{-1}$. Interestingly, this value is comparable to the arithmetic mean of the two k_q values obtained from the analysis of the intensity data, $5.84 \times 10^8\ M^{-1}\ s^{-1}$.

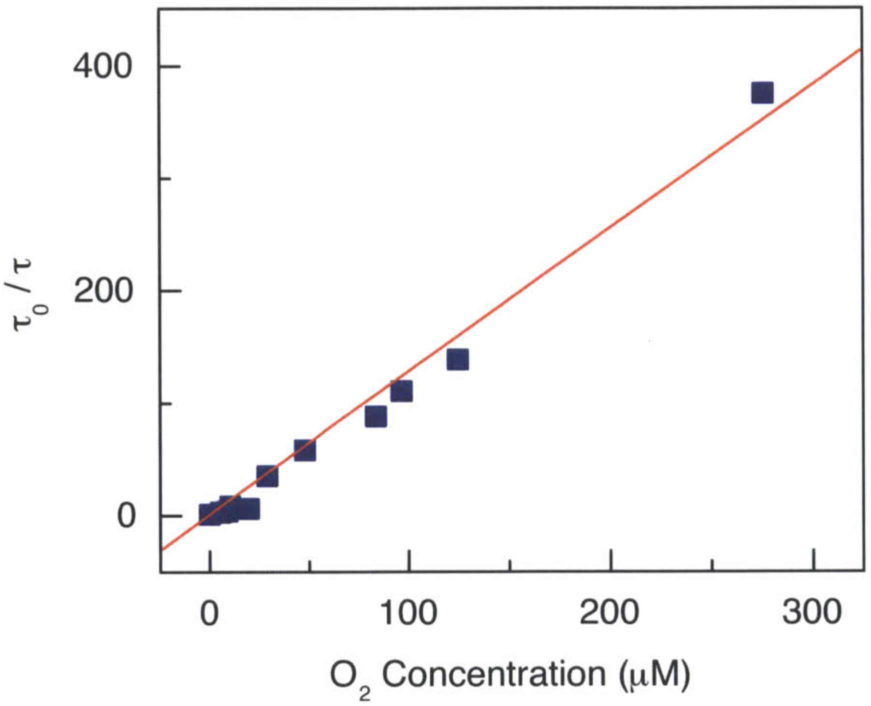

Figure 4.14. A Stern-Volmer plot using an alternative fitting regime in which it is assumed that the porphyrin phosphor interacts with the micelle, giving a distribution of lifetimes. Each decay trace with fit to Eq. 9. The above plot is derived from the τ parameter of each decay trace (the raw data is illustrated in Figure 4.11). Based on the theory behind this model, the a and τ should be constant and only the c term, which represents the quenching parameter, should exhibit an oxygen dependence. Despite these limitations and unexpected results, a reasonable Stern-Volmer plot could be obtained ($R^2 = 0.98741$) that does not exhibit an upward curvature at high oxygen concentrations and is wholly representative of all the data, rather than just a single component of a biexponential fit. However, the deviation from theory and the inferior fits relative to the biexponential decay discredit this model to explain the data.

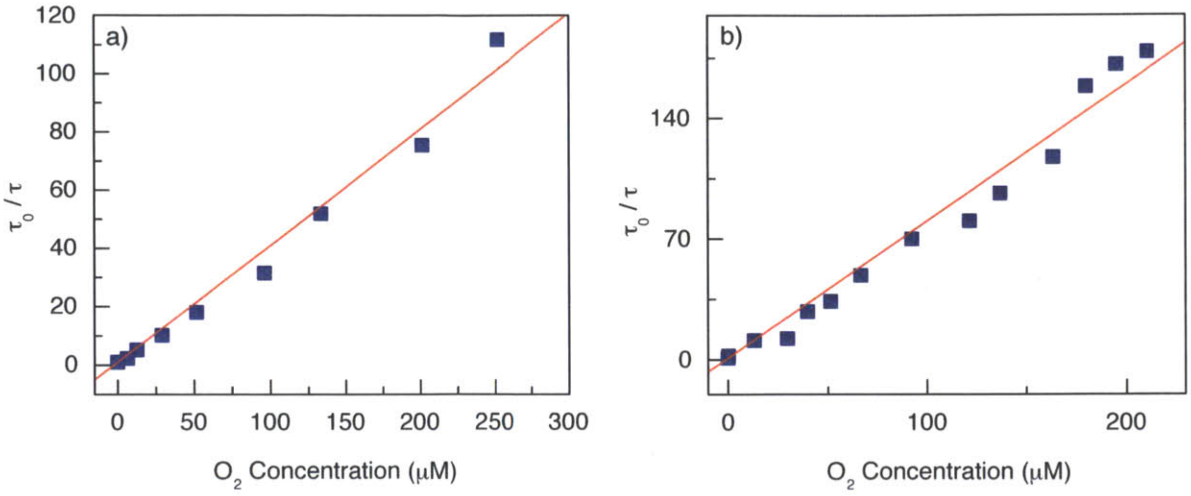

Figure 4.15. A representative example of the long lifetime component of the biexponential fit as a function of [O$_2$] for one sample of **QD1-MC** at (a) 25°C and (b) 37°C. (a) The line of best fit ($R^2 = 0.98839$) gives $K_{SV} = 0.400\ \mu M^{-1}$ and $k_q = 9.73 \times 10^8\ M^{-1}\ s^{-1}$ at 25°C. (b) The line of best fit ($R^2 = 0.98728$) gives $K_{SV} = 0.794\ \mu M^{-1}$ and $k_q = 1.84 \times 10^9\ M^{-1}\ s^{-1}$ at 37°C.

Due to the unsatisfactory fits of the data and the deviations from theory, it is clear that the above model (Eq. 9) does not appropriately describe the data. Returning to a biexponential analysis of the data, the long component exhibits a typical Stern-Volmer relationship (Eq 6) and gives consistent values for K_{SV} (Figure 4.15). For five independent samples at 25°C, the average $K_{SV} = 0.412\ \mu M^{-1}$ with a standard deviation of $0.047\ \mu M^{-1}$, giving $k_q = 1.00 \times 10^9\ M^{-1}\ s^{-1}$; this is consistent with a global fit of all five samples (Figure 4.16a) in which $K_{SV} = 0.410\ \mu M^{-1}$ with $k_q = 9.96 \times 10^8\ M^{-1}\ s^{-1}$. It should be noted that these quenching constants are consistent with the major component of the intensity data analysis (*vide supra*), which gave $k_{q1} = 1.16 \times 10^9\ M^{-1}\ s^{-1}$. Similarly for measurements conducted at 37°C, which were studied for the purposes of calibrating *in vivo* lifetimes, it was found that for five independent samples the average $K_{SV} = 0.693\ \mu M^{-1}$ with a standard deviation of $0.083\ \mu M^{-1}$, giving $k_q = 1.61 \times 10^9\ M^{-1}\ s^{-1}$; a global fit of all data acquired at 37°C (Figure 4.16b) gives $K_{SV} = 0.723\ \mu M^{-1}$ with $k_q = 1.67 \times 10^9\ M^{-1}\ s^{-1}$. This observed change in k_q as a function of temperature is consistent with observations of temperature-dependent values of k_q that were reported for oxygen quenching of a palladium(II) porphyrin. Using the reported empirical relationship between k_q and temperature (T), $k_q = (6.4 + 0.21T)^2$, the rate constant at 37°C should be faster than that at 25°C by a factor of 1.5.[37] This result is consistent with these observations, in which k_q increased by a factor of 1.6.

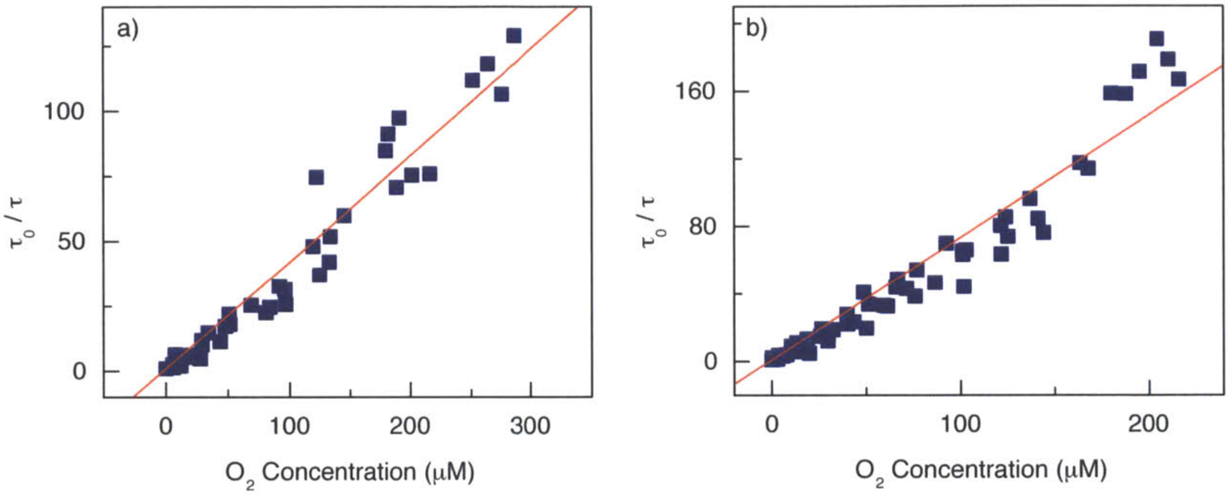

Figure 4.16. Global fits of the long lifetime component of the biexponential fit as a function of [O_2] for five independent samples of **QD1-MC** at (a) 25°C and (b) 37°C. (a) The line of best fit ($R^2 = 0.97354$) gives $K_{SV} = 0.410\ \mu M^{-1}$ and $k_q = 9.96 \times 10^8\ M^{-1}\ s^{-1}$ at 25°C. (b) The line of best fit ($R^2 = 0.96525$) gives $K_{SV} = 0.723\ \mu M^{-1}$ and $k_q = 1.67 \times 10^9\ M^{-1}\ s^{-1}$ at 37°C.

While the long component is easily explained and serves as an appropriate means of calibrating **QD1-MC** as an oxygen sensor, the short component is more complicated. In many of the observed samples, the short component exhibits an upward curvature, toward the y-axis. Such an observation in a Stern-Volmer plot is usually attributed to static quenching. However, the intensity data discredited the presence of static quenching (*vide supra*). Additionally, the nonlinearity is observed in a Stern-Volmer plot constructed from lifetime data, which is a dynamic measurement, and cannot be attributed to a static component. An alternative explanation of this observation is the presence of a so-called quenching sphere of action.[14] This is derived from a formalism that was first introduced by Perrin.[38,39] This apparent static quenching arises from the quencher being adjacent to the phosphor at the moment of excitation; this is contrasted with true static quenching in which a complex is formed between the ground state phosphor and quencher.[14] Within a sphere of volume V around the phosphor, the probability of quenching is unity, resulting in a modified Stern-Volmer relationship:

$$\frac{I_0}{I} = \left(1 + K_{SV}[\mathrm{O}_2]\right)\exp\left(V[\mathrm{O}_2]\right) \tag{10}$$

As the concentration of quencher increases, the probability that it is in the first solvent shell of the phosphor at the moment of excitation increases exponentially. This model has been used to describe quenching kinetics in microheterogeneous systems.[40] Simulations have demonstrated that this model is appropriate to describe data (both intensity and lifetime) with an upward curvature, regardless of the cause of the apparent static effect.[41]

Using this model, plots of τ_0/τ for the short component versus $[\mathrm{O}_2]$ were fit to Eq. 10 (Figure 4.17). It should be noted that two anomalous points, in which the calculated lifetime of the short component increased rather than decreased with increasing $[\mathrm{O}_2]$, have been removed from Figure 4.17b; the full data set and corresponding analysis is presented in Figure 4.18. For data acquired at 25°C, it was found that $K_{SV} = 0.0129\ \mu\mathrm{M}^{-1}$ or $k_q = 4.45 \times 10^8\ \mathrm{M}^{-1}\ \mathrm{s}^{-1}$ with a corresponding sphere of action with $V = 0.0127\ \mu\mathrm{M}^{-1}$. As expected, the rate constant increases to $K_{SV} = 0.168\ \mu\mathrm{M}^{-1}$ or $k_q = 2.95 \times 10^9\ \mathrm{M}^{-1}\ \mathrm{s}^{-1}$ for data acquired at 37°C. However, the sphere of action $V = 0.00889\ \mu\mathrm{M}^{-1}$ is rather similar to that observed at 25°C. This result is quite satisfying because this parameter should not vary with temperature, as it is inherent to the nature of the interaction between the phosphor and quencher; this suggests that the sphere of action formalism is an appropriate model with which to treat the data.

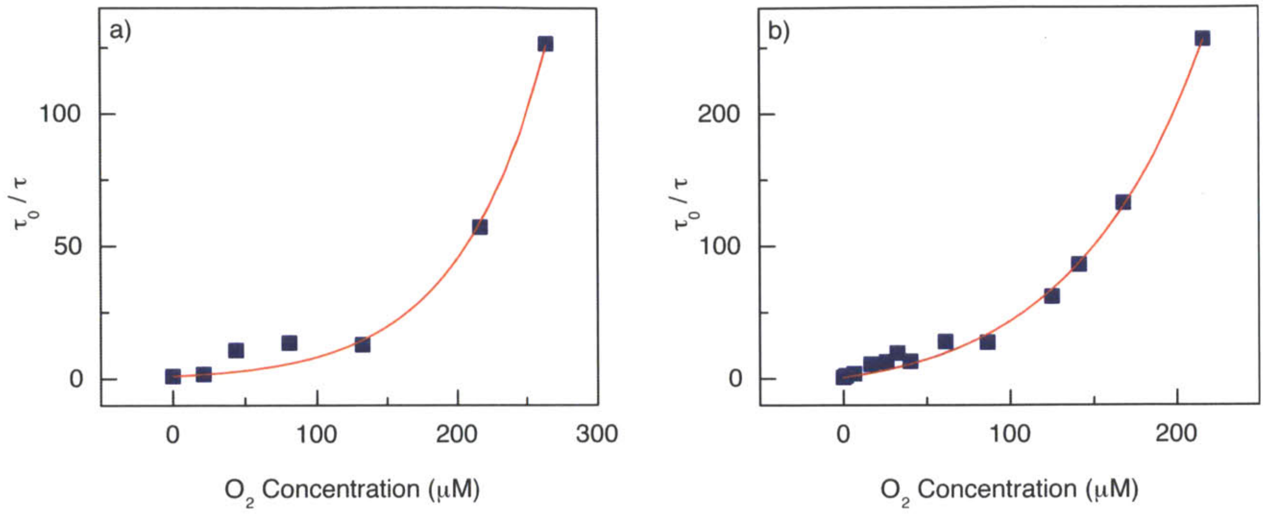

Figure 4.17. A representative example of the short lifetime component of the biexponential fit as a function of [O$_2$] for one sample of **QD1-MC** at (a) 25°C and (b) 37°C. (a) The curve of best fit ($R^2 = 0.98731$) yields $V = 0.0127\ \mu\text{M}^{-1}$ and $K_{\text{SV}} = 0.0129\ \mu\text{M}^{-1}$, which translates to $k_q = 4.45 \times 10^8\ \text{M}^{-1}\ \text{s}^{-1}$ at 25°C. (b) The curve of best fit ($R^2 = 0.994$) yields $V = 0.00889\ \mu\text{M}^{-1}$ and $K_{\text{SV}} = 0.168\ \mu\text{M}^{-1}$, which translates to $k_q = 2.95 \times 10^9\ \text{M}^{-1}\ \text{s}^{-1}$ at 37°C.

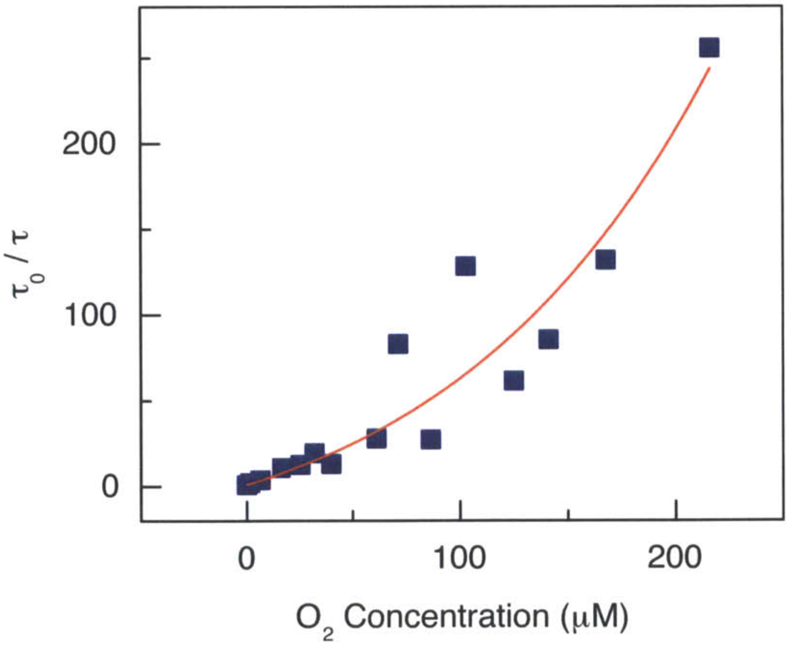

Figure 4.18. A plot of the short component of the biexponential decay as a function of oxygen concentration at 37°C. This represents the full set of data that is presented in Figure 4.17b. The curve of best fit ($R^2 = 0.87353$) yields $V = 0.00512\ \mu\text{M}^{-1}$ and $K_{\text{SV}} = 0.368\ \mu\text{M}^{-1}$, which corresponds to $k_q = 6.45 \times 10^9\ \text{M}^{-1}\ \text{s}^{-1}$.

Based on the observed data, a physical model for the molecular structure of the micelle may now be proposed (Figure 4.19). Since the porphyrin **1** is hydrophobic, there are a multitude of conformations in which it could exist in the core of the micelle **QD1-MC**. Chapter 3 demonstrated that this compound binds to the surface of the QD in toluene solution. Upon encapsulation of the assembly with phospholipids to form the micelle, **1** may diffuse away from the QD surface and into the oleate groups of the phospholipid; additionally, this process may be facilitated under the sonication conditions required to prepare the micelles. As a result, there are two major environments in which the porphyrin can reside: the QD surface and capping ligand or the oleate groups of the micelle phospholipids. This is satisfying, given that the two-component model was the best description of both the intensity and lifetime Stern-Volmer data. Indeed, the model of Eq 9 that assumes a distribution of porphyrin and polymer interactions was an inferior treatment of the data, suggesting that the porphyrin is not homogeneously distributed in the micelle. Since the **QD1-MC** bulk measurements of absorption spectroscopy and phosphorescence quantum yield, as well as the observed lifetime differential between air and vacuum measurements (*vide supra*), are more consistent with those of **1** rather than **QD1**, it can be concluded that the majority the porphyrin resides in the phospholipids of the micelle. This environment can be attributed to the long-lived component of the biexponential fit, as this term dominates the fit (~60%), especially at high oxygen concentrations. Also, this component exhibits a typical Stern-Volmer relationship, which would be expected for a phosphor dissolved in a liquid solution, which is akin to the molecule being well dispersed in a hydrophobic lipid "solution." Conversely, the short component is attributed to the porphyrin bound to the surface of the quantum dot. The shorter lifetimes may be attributed to self-quenching of adjacent porphyrins on the dot surface. Since these molecules are static, as they are surface bound and intercalated in the capping ligand, they are not freely mobile to encounter oxygen molecules as readily, potentially giving rise to anomalous oxygen responses and nonlinear Stern-Volmer behavior. Perhaps the porphyrin's interaction with the quantum dot and the surrounding capping ligand engenders a quenching sphere of action, as the molecule is now exposed to quencher in two dimensions rather than three for an unbound molecule.

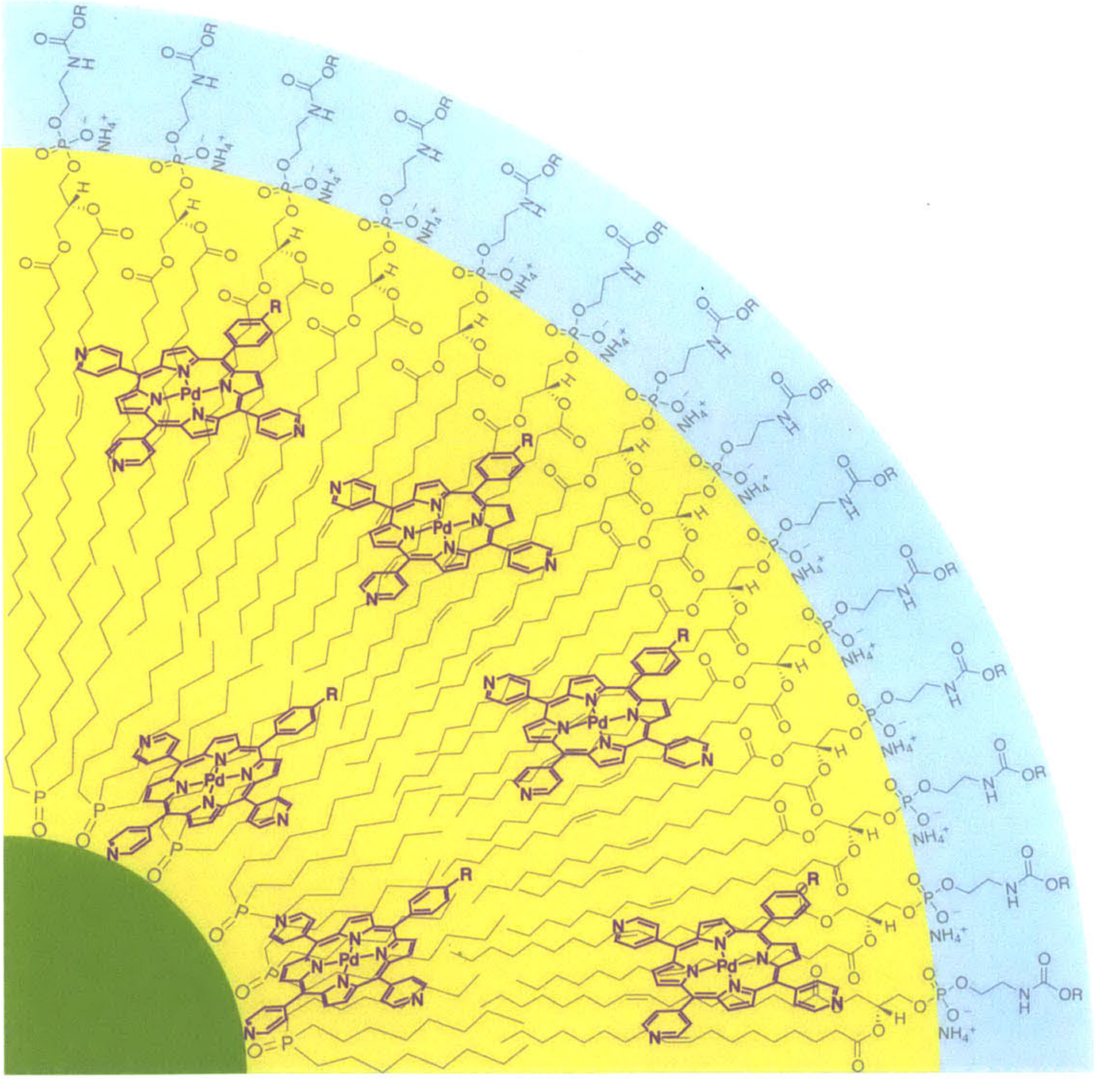

Figure 4.19. Schematic representation of the proposed structure of **QD1-MC**. The hydrophobic QD, represented in green, is encapsulated by phospholipids, to give a hydrophobic interior (yellow) and a hydrophilic exterior (blue). It is proposed that the long lifetime component, which exhibits well-behaved Stern-Volmer kinetics, is due to **1** dispersed in the oleate groups of the phospholipids. Alternatively, the short component is attributed to **1** bound to the QD surface.

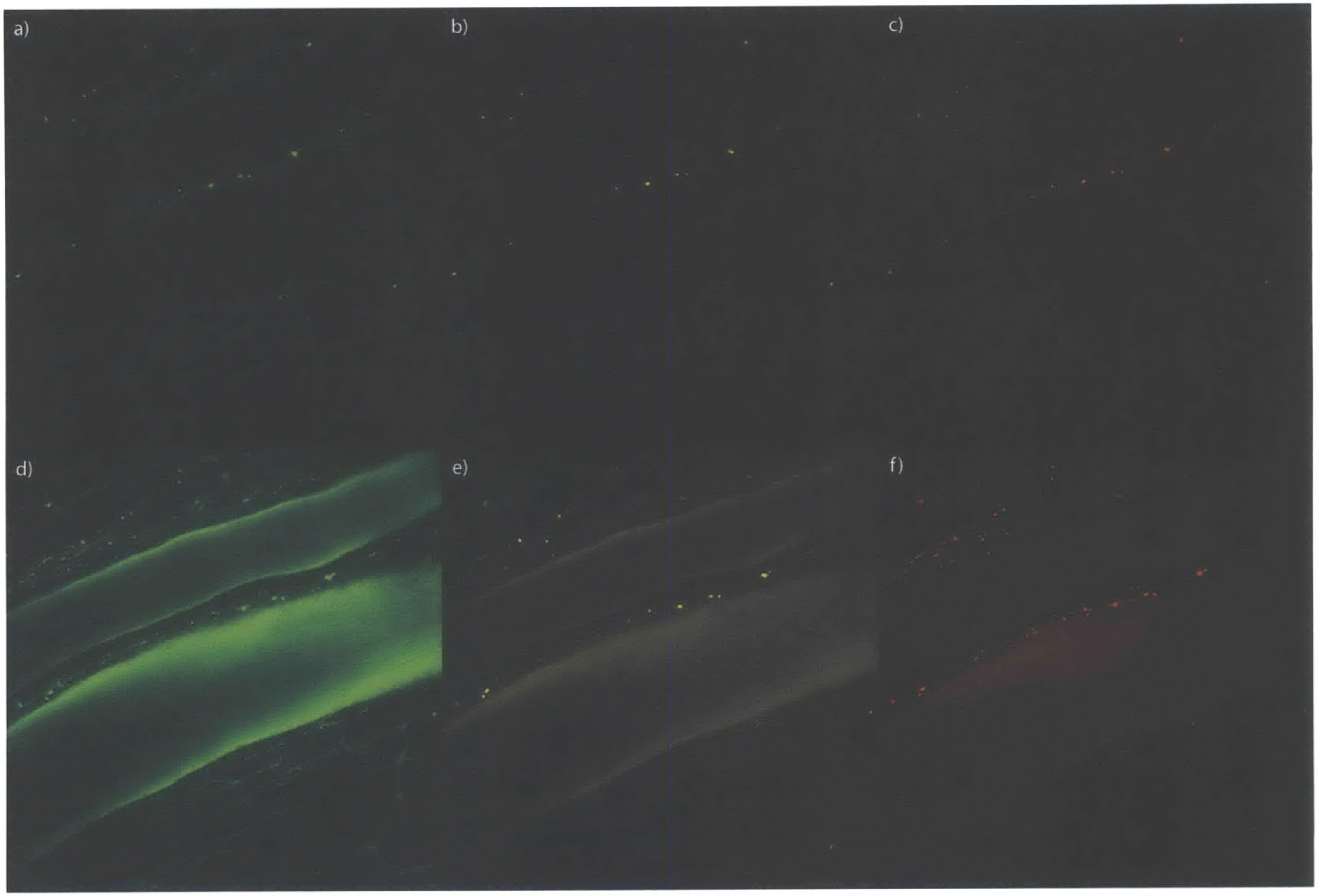

Figure 4.20. Two-photon images of a SCID mouse with a dorsal skinfold chamber (DSC) at a depth of 70 μm, comparing the vasculature without the sensor (a–c) and with **QD1-MC** (d–f). Collected light was separated into three channels: green (a & d) for **QD** emission using a 565 nm dichroic mirror and a 535/40 bandpass filter, yellow (b & e) for autofluorescence using a 585 nm dichroic mirror, and red (c & f) for emission of **1** using a 690/90 bandpass filter.

4.5 Preliminary *In Vivo* Imaging

Having demonstrated that the sensor **QD1-MC** shows oxygen sensitivity in the biologically relevant 0–160 torr range, multiphoton images of severe combined immunodeficient (SCID) mice with surgically implanted dorsal skinfold chambers (DSC) or cranial windows (CW) were obtained. Under typical imaging conditions (400 mW of 850 nm excitation light), a substantial signal after systemic injection of the sensor was observed, while background signal was minimial prior to injection (Figure 4.20). Although QD emission is low based on *in vitro* experiments, significant signal was observed in the green channel to serve as a suitable means of tracking the location of the sensor. Imaging of the brain vasculature shows that the sensor is evenly distributed in the vessels, as evidenced by the green channel, while the intensity of the red channel is variable, illustrating differences in oxygen levels of arteries and veins (Figure 4.21).

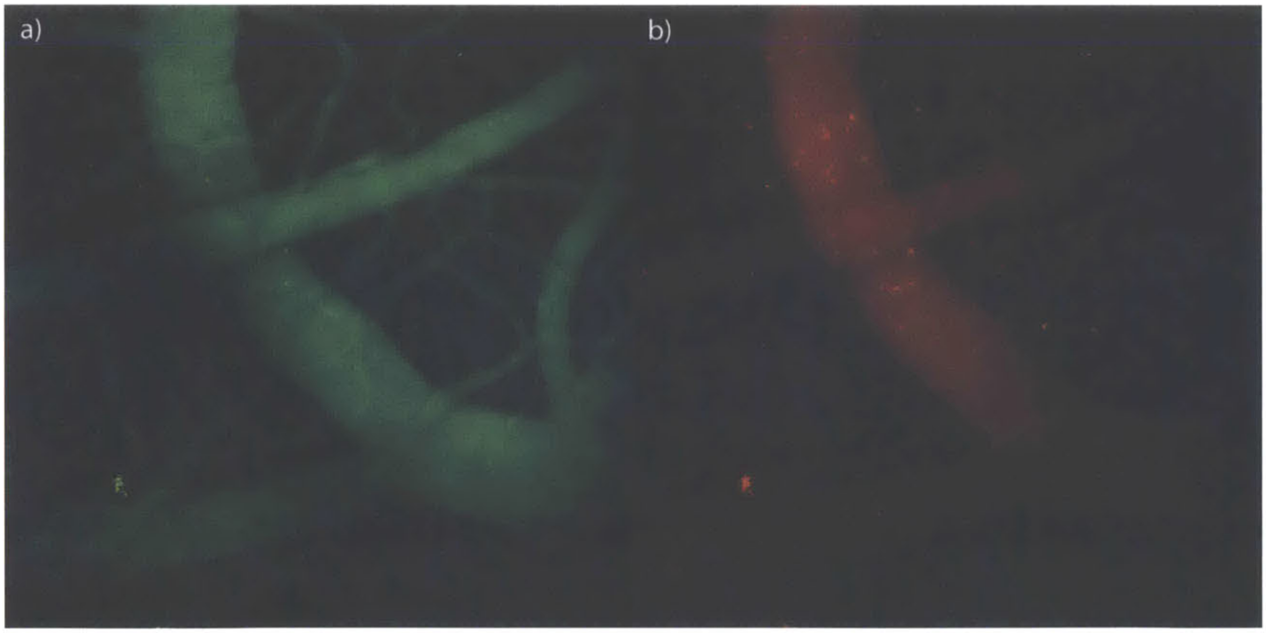

Figure 4.21. Three-dimensional projections of brain vasculature under two-photon excitation of a SCID mouse with a cranial window (CW). Images were collected over a depth of 200 μm in 10 μm increments and combined into a projection using the ImageJ software package. Collected light was separated into three channels: green (a) for **QD** emission using a 570 nm dichroic mirror and a 535/40 bandpass filter, yellow (not pictured) for autofluorescence using a 585 nm dichroic mirror, and red (b) for emission of **1** using a 690/90 bandpass filter.

Oxygen levels were quantified *in vivo* and used to differentiate veins from arteries using lifetime measurements. Figure 4.22 shows a composite image of a dorsal skinfold chamber at a depth of 70 μm (a) and a cranial window at a depth of 115 μm (b). Lifetime measurements were made at the indicated points (1–8) and this data is summarized in Table 4.5. Using the long component of the biexponential fit, the oxygen levels at these points were determined using Eq. 6 in which $\tau_0 = 325$ μs (see Table 4.4) and $k_q = 1.67 \times 10^9$ M^{-1} s^{-1} from the global fit of all data acquired at 37°C (Figure 4.17b). The calculated oxygen levels fall within reported ranges for the same type of mice using the same anesthetic: 11.3–31.3 torr for arterioles and 7.4–29.2 torr for venules.[42] Based on the size of the vessels in Figure 4.22a, the top vessel bearing points 1 and 3 is an artery while the lower one is a vein; the measured lifetimes and corresponding oxygen levels are consistent with this observation. The average intensity of red signal (see Figure 4.20f) in the vein is 1.25 times greater than it is in the artery, demonstrating that **QD1-MC** has promise as a ratiometric sensor *in vivo*. Points 1 and 3 have nearly the same oxygen concentration while points 2 and 4 exhibit a slight difference (~ 4 torr). This difference may be attributed to differing distances to the vessel wall, as it is known that radial oxygen gradients from a vessel into the tissue exist.[43] While point 2 is definitively in the lumen of the vein, point 4 may actually be above the vessel, as the vein is coming out of the image plane. The CW image (Figure 4.22b) demonstrates a known feature of oxygen levels in the vasculature: the partial pressure of oxygen decreases as the diameter of the vessel decreases.[44,45] The partial pressure of oxygen increases when the smaller vein bearing point 8 joins the larger one with points 5 and 7, increasing the partial pressure by about 2 torr; the observed increase is consistent with previously reported values for small veins flowing to larger ones.[43]

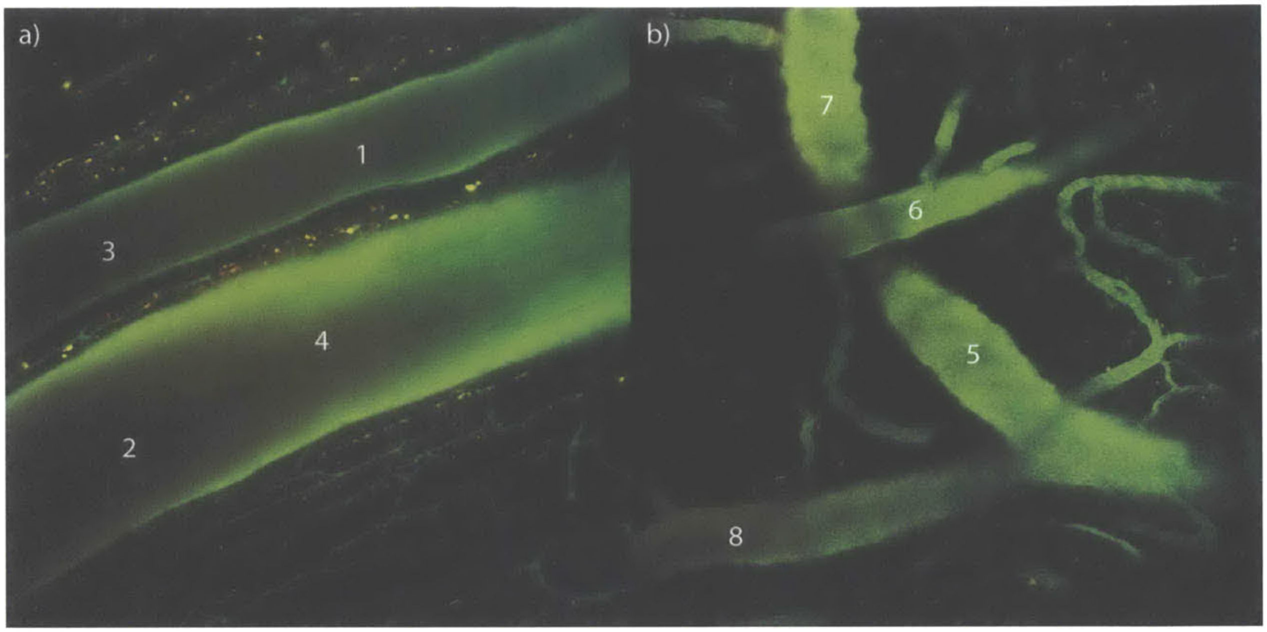

Figure 4.22. Composite two-photon images of SCID mice with either (a) a dorsal skinfold chamber (DSC) at a depth of 70 μm or (b) a cranial window (CW) at a depth of 115 μm. Collected light was separated into three channels: green for **QD** emission using a 565 nm or 570 nm dichroic mirror, for (a) and (b), respectively and 535/40 bandpass filter, yellow for autofluorescence using a 585 nm dichroic mirror, and red for emission of **1** using a 690/90 bandpass filter. These images are an overlay of all three optical channels. The indicated points (1–8) represent locations at which *in vivo* lifetimes were measured and the associated data is presented in Table 4.5.

Table 4.5. *In vivo* Lifetime Measurements

Point[a]	τ_1 (μs)	A_1 (%)[b]	τ_2 (μs)	A_2 (%)[b]	$[O_2]$ (μM)	pO_2 (torr)
1	16.5	< 1	3.0	> 99	34.2	25.2
2	25.1	< 1	3.0	> 99	21.9	16.1
3	16.6	< 1	3.1	> 99	34.0	25.0
4	31.6	< 1	3.1	> 99	17.0	12.5
5	27.7	< 1	2.8	> 99	19.7	14.5
6	15.5	< 1	3.2	> 99	36.6	26.9
7	22.4	< 1	2.7	> 99	24.7	18.2
8	30.9	< 1	2.7	> 99	17.4	12.8

[a] See Figure 4.22, [b] Relative contribution to the biexponential fit, [c] Determined using Eq. 6, [d] See Section 4.7 on oxygen solubility determination

4.6 Discussion and Conclusions

In summary, a micelle-encapsulated construct for oxygen sensing in aqueous has been developed. The synthesis of these sensors is rapid and scalable; sonication processing provides consistently sized particles without the need for chromatography. The small size of the particles permits their use in probing biological microenvironments. Using both one and two-photon techniques, the oxygen sensitivity of these sensors has been demonstrated in the biologically-relevant 0–160 torr range. One salient feature of this sensor is that QD emission is largely unaffected by oxygen, providing an internal reference for signal intensity and establishing a ratiometric sensor. The oxygen-dependent emission intensity exhibited nonlinear Stern-Volmer behavior and was attributed to a two-component system. Oxygen-dependent lifetime data fit best to a two component model, as a biexponential fit was superior to a model reflective of a distribution of lifetimes in the micelle (Eq. 9). The long component exhibited typical Stern-Volmer behavior, giving $k_q = 1.00 \times 10^9$ M^{-1} s^{-1} at 25°C and $k_q = 1.67 \times 10^9$ M^{-1} s^{-1} 37°C and is consistent with the quenching constant obtained from the intensity data. Because the long component is consistent over many independent samples, it serves as a reliable means of calibrating **QD1-MC**. While the short component exhibits some anomalous points, a typical data set exhibits an exponential dependence on the oxygen concentration and is best described using a quenching sphere of action model. Based on the analysis, the quenching volume is independent of temperature while the quenching constant k_q is affected. This two-component model may be rationalized by recognizing that porphyrin **1** can reside in two distinct hydrophobic environments: bound to the quantum dot surface and dispersed in the oleate groups of the phospholipids that form the micelle. Preliminary studies have shown that **QD1-MC** provides sufficient signal to collect *in vivo* images and lifetime-based oxygen measurements that are consistent with known values. Currently, studies are being conducted to exploit the ratiometric nature of this sensor such that oxygen concentrations may be determined using intensity data rather than lifetime measurements, enabling faster data acquisition and affording the possibility to rapidly detect real time changes in oxygen levels of biological systems.

4.7 Experimental Details

Materials

The following chemicals were used as received: chloroform ($CHCl_3$), ethanol (EtOH), 2′,7′-dichlorofluorescein (fluorescein 27), and tris(2,2′-bipyridyl)dichlororuthenium(II) hexahydrate ([Ru(bpy)]Cl_2) from Sigma-Aldrich; 1,2-dioleoyl-*sn*-glycero-3-phosphoethanolamine-N-[methoxy(polyethylene glycol)-2000] ammonium salt, 25 mg/mL solution in chloroform from Avanti Polar Lipids Inc.; Dulbecco's phosphate-buffered saline (PBS) without calcium and magnesium from Mediatech Inc.; and argon from Airgas. Cadmium selenide core/shell quantum dots (QD) obtained from QD Vision were twice precipitated from toluene using EtOH and redissolved in toluene prior to use. Porphyrin **1** [**5-(4-Methoxycarbonylphenyl)-10,15,20-tris(4-pyridyl)porphyrinopalladium(II)**] was prepared as described in Chapter 2.

Preparation of Sensors

Toluene stock solutions of the porphyrin (~100 μM) and QD (~10 μM) were prepared. The concentration of the QD stock solution was calculated using $\varepsilon_{350} = 4.34 \times 10^5$ M^{-1} cm^{-1}, as estimated using an empirical formula based on the first absorbance feature (λ = 501 nm).[46] To prepare the sensor, an aliquot of the QD stock (typically containing ~10 nmol of dots) was dissolved in 4 mL of chloroform and an appropriate volume of the porphyrin stock was then added to give 10 molar equivalents of porphyrin per QD. The resultant mixture was stirred overnight at room temperature in a 20 mL scintillation vial to allow equilibration of the porphyrin on the QD surface. Solvent was removed by rotary evaporation and the residue was dissolved in 750 μL of the lipid solution (1,2-dioleoyl-*sn*-glycero-3-phosphoethanolamine-N-[methoxy(polyethylene glycol)-2000] ammonium salt, 25 mg/mL solution in chloroform). Solvent was removed by rotary evaporation and 4 mL PBS were added. The mixture was then sonicated for 5 minutes using a Microson XL 2000 ultrasonic liquid processor (Qsonica LLC) with an output power of 2 W to give an orange, non-turbid solution. Aggregates were removed by filtering the solution through a 0.45 μm and then 0.22 μm syringe filter (Millipore). Solutions for *in vivo* imaging were prepared by combining four independent batches and concentrating the solution using 50,000 MW centrifuge filters to a final volume of 500–700 μL.

Physical Measurements

UV–vis absorption spectra were acquired using a Cary 5000 spectrometer. Steady-state emission and excitation spectra were recorded on a SPEX FluoroMax-3 spectrofluorimeter. Relative quantum yields of samples (Φ_{sam}) were calculated according to the following equation:

$$\Phi_{\mathrm{sam}} = \Phi_{\mathrm{ref}}\left(\frac{A_{\mathrm{ref}}}{A_{\mathrm{sam}}}\right)\left(\frac{I_{\mathrm{sam}}}{I_{\mathrm{ref}}}\right)\left(\frac{\eta_{\mathrm{sam}}}{\eta_{\mathrm{ref}}}\right)^2 \qquad (11)$$

where A is the measured absorbance, η is the refractive index of the solvent, I is the integrated emission intensity, and Φ_{ref} is the emission quantum yield of the reference. Φ_{ref} was taken to be 0.094 for an evacuated sample of $[\mathrm{Ru(bpy)_3}]\mathrm{Cl_2}$ in MeCN.[47] The quantum yield of **QD** was similarly determined using fluorescein 27 in 0.1 M NaOH (Φ = 0.87, η = 1.335)[48] as the standard. Porphyrin samples for quantum yield measurements, vacuum lifetime (τ_0) measurements, and evacuated steady-state emission spectra were prepared using three cycles of freeze–pump–thaw to pressures below 10^{-5} torr. Gel filtration chromatography (GFC) was performed on an Akta Prime system (GE) with a Superose 6 cross-linked dextran column, using PBS as the eluent; the UV absorbance at 280 nm was monitored over the course of the column. Dynamic light scattering (DLS) measurements were made using a Zetasizer Nano S90 (Malvern). For measurements conducted at 37°C, a TC 125 temperature controller (Quantum Northwest) equipped with a circulating water bath was used to maintain the sample temperature. Samples were equilibrated at 37°C for one hour before measurements were made. Solution oxygen measurements were made using an Ocean Optics NeoFox Phase Measurement system equipped with a FOXY-HPT-1-PNA fiber optic probe. The sensor was calibrated using a two-point calibration: an air-equilibrated PBS solution and a PBS solution purged with argon for one hour. The probe was re-calibrated before each set of data was collected; the measured lifetime of the sensor was used to determine the amount of dissolved oxygen in the sample (see section on oxygen solubility below).

Nanosecond time-resolved emission measurements of porphyrin lifetimes were acquired using a previously reported system.[49,50] Pump light was provided by the third harmonic (355 nm) of a Quanta-Ray Nd:YAG laser (Spectra-Physics) operating at 10 Hz. The pump light was passed through a BBO crystal in optical parametric oscillator (OPO) yielding a visible frequency that was tuned to 450 nm. Excitation light was attenuated to 1–3 mJ per pulse for all experiments using neutral density filters. Emitted light was first passed through a series of long pass filters to remove excitation light then to a Triax 320 monochromator (Jobin Yvon Horiba) and dispersed by a blazed grating (500 nm, 300 grooves/mm) centered at 685 nm. The entrance and exit slits of the monochromator were set to 0.36 mm in all experiments herein, corresponding to a spectral resolution of 4.5 nm. The signal was amplified by a photomultiplier tube (R928, Hamamatsu) and collected on a 1 GHz digital oscilloscope (9384CM, LeCroy); acquisition was triggered using a photodiode to collect scattered laser excitation light.

Femtosecond time-resolved emission measurements of QD lifetimes were acquired using a Libra-F-HE (Coherent) chirped-pulse amplified Ti:sapphire laser system. Sub-100 fs laser pulses were generated in a mode-locked Ti:sapphire oscillator (Coherent Vitesse) which was pumped by a 5 W cw Coherent Verdi solid-state, frequency-doubled Nd:YVO_4 laser. The 80-MHz output was amplified in a regenerative amplifier cavity, pumped by a diode-pumped, frequency-doubled Nd:YLF laser (Coherent Evolution-30) to generate a 1 kHz pulse train with a wavelength of 800 nm. This was then used to pump an OperA Solo (Coherent) optical parametric amplifier (OPA), which is able to generate frequencies between 285 and 2600 nm. Excitation pulses of 450 nm were produced *via* fourth harmonic generation of the idler using a BBO crystal; the pulse power was attenuated to 0.4–1 mW at the sample. Emission lifetimes were measured on a Hamamatsu C4334 Streak Scope streak camera, which has been described elsewhere.[51] The emission signal was collected over a 140 nm window centered at 480 nm using 100 and 2 ns time windows; time delays for these time windows were generated using a Hamamatsu C1097-04 delay unit. A 495 nm long pass filter was used to remove laser excitation light.

Two-photon emission spectra were generated using this Libra-F-HE (Coherent) laser system. Excitation pulses of 800 nm were used directly from the Libra output; the pulse power was attenuated to 5–8 mW using neutral density filters and the beam was focused onto the sample using a 200 mm focal length lens. The emission spectrum was collected using a Hamamatsu C4334 Streak Scope streak camera in 140 nm windows centered at 480 nm.

Two-photon lifetime measurements were made using a custom-built multiphoton laser-scanning microscope (MPLSM) in the Edwin L. Steels Laboratory, Department of Radiation

Oncology at Massachusetts General Hospital, as previously described.[52] Additions to the MPLSM system[53] were made such that lifetime measurements could be performed. Sub-100 fs laser pulses were generated at a repetition rate of 80 MHz in a mode-locked Ti:sapphire oscillator (Spectra-Physics Mai Tai HP) which was pumped by a 14 W cw Spectra-Physics Millennia diode-pumped solid-state (DPSS) laser operating at 532 nm; the output of the Mai Tai laser is tunable in the 690–1040 nm range. The 850 nm laser output was adjusted using a 10RP52-2 zero-order half-wave plate (Newport) and a 10GL08AR.16 Glan-Laser polarizer (Newport) to attenuate the power to 700 mW for air samples and 400 mW for evacuated samples. The beam was passed through a 350-50 KD*P Pockels cell (Conoptics) that amplified and switched the triggering pulses from a DG535 digital delay generator (Stanford Research Systems). The experimental square wave trigger pulse from the delay generator defined the repetition rate while a second delayed pulse defined the excitation pulse, which was 1.60 μs in duration for air samples and 15.36 μs in duration for evacuated samples. At the rejection site of the Pockels cell, a TDS-3052 oscilloscope (Tektronix) and photodiode were used to monitor the applied voltage and the optical response; the output of the Pockels cell was ~10% of the incident power. The beam was then directed into a custom-modified multiphoton microscope based on the Olympus Fluoview 300 laser scanner. The output beam from the scanner was collimated through a scan lens into the back of an Olympus BX61WI microscope. An Olympus LUMPlanFL 20×, 0.95 NA water immersion objective lens was used to focus the excitation light and collect the emission light. NIR laser excitation light and visible emission were separated using a 750SP-2P AR-coated dichroic mirror (Chroma Technology). A 690/90 bandpass filter (Chroma Technology) and a focusing lens were used in front of the GaAs H7421-50 photomultiplier tube (Hamamatsu) to collect phosphorescent emission. Photon counting was performed using a SR430 multichannel scaler (Stanford Research Systems) to histogram the counts in 1024 or 2048 bins of 40 ns for air samples or 2.56 μs for evacuated samples.

This MPLSM system was also used to collect two-photon *in vivo* images of severe combined immunodeficient (SCID) mice with surgically implanted dorsal skinfold chambers (DSC)[54] or cranial windows (CW),[55] as previously described. Prior to imaging, mice were with anesthetized with Ketamine/Xylazine (10/1 mg/mL) and subsequently treated with 150–200 μL of the concentrated sensor solution *via* retro-orbital injection. For imaging, 850 nm excitation light was used at a power of 400 mW. Collected light was split into three channels: green for QD emission using either a 565 or 570 nm dichroic mirror and a 535/40 bandpass filter, yellow for autofluorescence using a 585 nm dichroic mirror, and red for porphyrin emission using a 690/90 bandpass filter. For *in vivo* porphyrin emission lifetimes, the excitation pulse was 15.36 μs in duration and photon counts were histogramed in 1024 bins of 2.56 μs. After imaging, mice were sacrificed with a systemic injection of Fatal-Plus.

Energy Transfer Analysis

The efficiency of energy transfer from the QD to the porphyrin was evaluated using Förster analysis:[14,56]

$$E = \frac{mk_{D-A}}{mk_{D-A} + \tau_D^{-1}} = \frac{mR_0^6}{mR_0^6 + r^6} \qquad (12)$$

where k_{D-A} is the rate of energy transfer, r is the distance between the donor and acceptor, R_0 is the Förster distance or the distance at which the energy transfer efficiency is 50%, and m is the number of acceptor molecules per donor. This quantity (E) can be measured experimentally:

$$E = 1 - \frac{\tau_{D-A}}{\tau_D} \qquad (13)$$

where τ_D is the lifetime of the QD alone and $\tau_{D\text{-}A}$ is the lifetime of the QD with surface-bound porphyrin. Although the efficiency can be experimentally determined from the excited-state lifetime quenching, additional information is needed to quantify the parameters R_0, r, and m:

$$R_0^6 = \frac{9000(\ln 10)\kappa^2\Phi_D}{128\pi^5 N n^4}\int_0^\infty F_D(\lambda)\varepsilon_A(\lambda)\lambda^4 \mathrm{d}\lambda \tag{14}$$

where κ^2 is the relative orientation factor of the dipoles, taken to be 0.476 for static donor-acceptor orientations,[14,57] Φ_D is the quantum efficiency of the donor, N is Avogadro's number, and n is the index of refraction of the medium, which is taken to be 1.334 for PBS.[58] The latter half of the equation represents the spectral overlap integral, often represented as J, where $F_D(\lambda)$ is the normalized intensity of the donor and $\varepsilon_A(\lambda)$ is the extinction coefficient of the acceptor at wavelength λ. Thus, R_0 may be calculated using the overlap of the experimentally determined spectra. The average number of porphyrins attached to the QD, m, can be determined from the optical cross-sections of the spectra of QD, the porphyrin, and the corresponding assembly. The absorption spectra of the assemblies may be taken as the sum of the individual absorbance spectra of the donor and acceptor, as previously demonstrated with these assemblies (See Chapter 3 Figure 3.7). The value for m and the concentration of the assemblies may be calculated using the individual donor and acceptor absorption spectra, their known ε values, and Beer's law. To this end, the absorbance of the Soret was used to determine the concentration of poprhyrin while the absorbance at 350 nm was used to determine the concentration of QD.

Oxygen Solubility

In order to calibrate the fiber optic oxygen sensor and accurately measure oxygen concentrations in solution, the solubility of oxygen in pure water as a function of temperature was calculated using the following empirical equation:[59]

$$\ln c = -52.16764 + 84.59929/\tau + 23.41230\ln\tau \tag{15}$$

where c is in units of mL of gas at STP per liter of solution and $\tau = T/100$ where T is the temperature in K. This gives $c = 5.951$ at 25°C and $c = 4.999$ at 37°C. The using the ideal gas law, where 1 mol = 22.42 L at STP, the solubility of oxygen is then 265 μM and 223 μM for pure water at 25°C and 37°C, respectively. Since the solvent used for these experiments is PBS buffer and not pure water, a perturbation of this value was made to account for the solute using the following equation:[59]

$$k_{sc\alpha} = \left(\frac{1}{c_2}\right)\ln\left(\frac{c^{o}}{c}\right) \tag{16}$$

where $k_{sc\alpha}$ is the salt effect parameter, c_2 is the concentration of solute, c° is the solubility of oxygen in pure water, and c is the solubility of oxygen in the electrolyte solution. Since the primary component of this buffer is NaCl at a concentration of 137 mM,[60] this was used as the correction to approximate the solubility of oxygen in PBS buffer. Using Eq. 16 and $k_{sc\alpha} = 0.145$ L mol^{-1} for NaCl,[59] the solubility of oxygen was determined to be 5.711 mL/L (255 μM) and 4.775 mL/L (213 μM) at 25°C and 37°C, respectively. For the solubility of oxygen in blood, the following equation was used to convert a molar concentration to a partial pressure:

$$c = \alpha P \tag{17}$$

where c is the concentration of dissolved oxygen, P the partial pressure of oxygen, and α is the solubility parameter, taken to be 0.0031 mL dL^{-1} torr^{-1} or 1.39×10^{-3} mmol L^{-1} torr^{-1} for blood at 37°C.[61]

4.8 References

1. Dubertret, B.; Skourides, P.; Norris, D. J.; Noireaux, V.; Brivanlou, A. H.; Libchaber, A. *Science* **2002**, *298*, 1759–1762.

2. Fan, H.; Leve, E. W.; Scullin, C.; Gabaldon, J.; Tallant, D.; Bunge, S.; Boyle, T.; Wilson, M. C.; Brinker, C. J. *Nano Lett.* **2005**, *5*, 645–648.

3. Carion, O.; Mahler, B.; Pons, T.; Dubertret, B. *Nat. Protoc.* **2007**, *2*, 2383–2390.

4. Lee, Y. K.; Hong, S. M.; Kim, J. S.; Im, J. H.; Min, H. S.; Subramanyam, E.; Huh, K. M.; Park, S. W. *Macromol. Res.* **2007**, *15*, 330–336.

5. Ducongé, F.; Pons, T.; Pestourie, C.; Hérin, L.; Thézé, B.; Gombert, K.; Mahler, B.; Hinnen, F.; Kühnast, B.; Dollé, F.; Dubertret, B.; Tavitian, B. *Bioconjugate Chem.* **2008**, *19*, 1921–1926.

6. Cormode, D. P.; Skajaa, T.; an Schooneveld, M. M.; Koole, R.; Jarzyna, P.; Lobatto, M. E.; Calcagno, C.; Barazza, A.; Gordon, R. E.; Zanzonico, P.; Fisher, E. A.; Fayad, Z. A.; Mulder, W. J. M. *Nano Lett.* **2008**, *8*, 3715–3723.

7. Papagiannaros, A.; Levchenko, T.; Hartner, W.; Mongayt, D.; Torchilin, V. *Nanomed. Nanotechnol. Biol. Med.* **2009**, *5*, 216–224.

8. Yong, K. T.; Roy, I.; Law, W. C.; Hu, R. *Chem. Commun.* **2010**, *46*, 7136–7138.

9. Liu, J.; Yang, X.; Wang, K.; He, Y.; Zhang, P.; Ji, H.; Jian, L.; Liu, W. *Langmuir* **2012**, *28*, 10602–10609.

10. Wang, S.; Han, M. Y.; Huang, D. *J. Am. Chem. Soc.* **2009**, *131*, 11692–11694.

11. Ge, S.; Lu, J.; Yan, M.; Yu, F.; Yu, J.; Sun, X. *Dyes Pigm.* **2011**, *91*, 304–308.

12. Liu, W.; Howarth, M.; Greytak, A. B.; Zheng, Y.; Nocera, D. G.; Ting, A. Y.; Bawendi, M. G. *J. Am. Chem. Soc.* **2008**, *130*, 1274–1284.

13. Liu, W.; Greytak, A. B.; Lee, M.; Wong, C. R.; Park, J.; Marshall, L. F.; Jiang, W.; Curtin, P. N.; Ting, A. Y.; Nocera, D. G.; Fukumura, D.; Jain, R. K.; Bawendi, M. G. *J. Am. Chem. Soc.* **2010**, *132*, 472–483.

14. Lakowicz, J. R.; *Principles of Fluorescence Spectroscopy*, 3rd ed.; Springer: New York, 2006.

15. *CRC Handbook of Chemistry and Physics*, 84th ed.; CRC Press: Boca Raton, FL, 2003.

16. Blanton, S. A.; Dehestani, A.; Lin, P. C.; Guyot-Sionnest, P. *Chem. Phys. Lett.* **1994**, *229*, 317–322.

17. Larson, D. R.; Zipfel, W. R.; Williams, R. M.; Clark, S. W.; Bruchez, M. P.; Wise, F. W.; Webb, W. W. *Science* **2003**, *300*, 1434–1436.

18. Pu, S. C.; Yang, M. J.; Hsu, C. C.; Lai, C. W.; Hsieh, C. C.; Lin, S. H.; Cheng, Y. M.; Chou, P. T. *Small* **2006**, *2*, 1308–1313.

19. Losev, A. P.; Aghion, J. *J. Photochem. Photobiol., B* **1990**, *7*, 181–187.

20. Collier, B. B.; Singh, S.; McShane, M. *Analyst* **2011**, *136*, 962–967.

21. Keizer, J. *J. Am. Chem. Soc.* **1983**, *105*, 1491–1498.

22. Carraway, E. R.; Demas, J. N.; DeGaff, B. A.; Bacon, J. R. *Anal. Chem.* **1991**, *63*, 337–342.

23. Amao, Y.; Miyakawa, K.; Okura, I. *J. Mater. Chem.* **2000**, *10*, 305–308.

24. Eaton, K.; Douglas, P. *Sens. Actuators, B* **2002**, *82*, 94–104.

25. Zhang, H.; Sun, Y.; Ye, K.; Zhang, P.; Wang, Y. *J. Mater. Chem.* **2005**, *15*, 3181–3186.

26. Bacon, J. R.; Demas, J. N. *Anal. Chem.* **1987**, *59*, 2780–2785.

27. Carraway, E. R.; Demas, J. N.; DeGraff, B. A. *Anal. Chem.* **1991**, *63*, 332–336.

28. Klimant, I.; Wolfbeis, O. S. *Anal. Chem.* **1995**, *67*, 3160–3166.

29. Xu, W.; Schmidt, R.; Whaley, M.; Demas, J. N.; DeGraff, B. A.; Karikari, E. K.; Farmer, B. L. *Anal. Chem.* **1995**, *67*, 3172–3180.

30. Hartmann, P.; Leiner, M. J. P.; Lippitsch, M. E. *Sens. Actuators, B* **1995**, *29*, 251–257.

31. Chu, C. S.; Lo, Y. L.; Sung, T. W. *Talanta* **2010**, *82*, 1044–1051.

32. Kalyanasundaram, K.; *Photochemistry in Microheterogeneous Systems*; Academic Press: Orlando, 1987.

33. Draxler, S.; Lippitsch, M. E.; Klimant, I.; Kraus, H.; Wolfbeis, O. *J. Phys. Chem.* **1995**, *99*, 3162–3167.

34. Blumen, A.; Manz, J. *J. Chem. Phys.* **1979**, *71*, 4694–4702.

35. Baumann, J.; Fayer, M. D. *J. Chem. Phys.* **1986**, *85*, 4087–4107.

36. Sienicki, K.; Blonski, S.; Durocher, G. **1991**, *95*, 1576–1579.

37. Sinaasappel, M.; Ince, C. *J. Appl. Physiol.* **1996**, *81*, 2297–2303.

38. Perrin, F. *C. R. Acad. Sci. Paris* **1924**, *178*, 1978–1980.

39. Perrin, F. *C. R. Acad. Sci. Paris* **1924**, *178*, 2252–2254.

40. Castanho, M. A. R. B.; Prieto, M. J. E. *Biochim. Biophys. Acta* **1998**, *1373*, 1–16.

41. Eftink, M. R. In *Topics in Fluorescence Chemistry*; Lakowicz, J. R., Ed.; Plenum Press: New York **1991**; Vol. 2, pp. 53–126.

42. Filho, I. P. T.; Leunig, M.; Yuan, F.; Intaglietta, M.; Jain, R. K. *Proc. Natl. Acad. Sci. USA* **1994**, *91*, 2081–2085.

43. Tsai, A. G.; Johnson, P. C.; Intaglietta, M. *Physiol. Rev.* **2003**, *83*, 933–963.

44. Filho, I. P. T.; Kerger, H.; Intaglietta, M. *Microvasc. Res.* **1996**, *51*, 202–212.

45. Intaglietta, M.; Johnson, P. C.; Winslow, R. M. *Cardiovasc. Res.* **1996**, *32*, 632–643.

46. Leatherdale, C. A.; Woo, W. K.; Mikulec, F. V.; Bawendi, M. G. *J. Phys. Chem. B* **2002**, *106*, 7619–7622.

47. Suzuki, K.; Kobayashi, A.; Kaneko, S.; Takehira, K., Yoshihara, T.; Ishida, H.; Shiina, Y.; Oishi, S.; Tobita, S. *Phys. Chem. Chem. Phys.* **2009**, *11*, 9850–9860.

48. Grabolle, M.; Spieles, M.; Lesnyak, V.; Gaponik, N.; Eychmüller, A.; Resch-Genger, U. *Anal. Chem.* **2008**, *81*, 6285–6294.

49. Pizano, A. A.; Lutterman, D. A.; Holder, P. G.; Teets, T. S.; Stubbe, J.; Nocera, D. G. *Proc. Natl. Acad. Sci. USA* **2012**, *109*, 39–43.

50. Holder, P. G.; Pizano, A. A.; Anderson, B. L.; Stubbe, J.; Nocera, D. G. *J. Am. Chem. Soc.* **2012**, *134*, 1172–1180.

51. Loh, Z. H.; Miller, S. E.; Chang, C. J.; Carpenter, S. D.; Nocera, D. G. *J. Phys. Chem. A* **2002**, *106*, 11700–11708.

52. Brown, E. B.; Campbell, R. B.; Tsuzuki, Y.; Xu, L.; Carmeliet, P.; Fukumura, D.; Jain, R. K. *Nat. Med.* **2001**, *7*, 864–868.

53. Lanning, R. M. Ph.D. Thesis, Massachusetts Institute of Technology, Cambridge, MA, USA, **2009**.

54. Leunig, M.; Yuan, F.; Menger, M. D.; Boucher, Y.; Goetz, A. E.; Messmer, K.; Jain, R. K. *Cancer Res.* **1992**, *52*, 6553–6560.

55. Yuan, F.; Salehi, H. A.; Boucher, Y.; Vasthare, U. S.; Tuma, R. F.; Jain, R. K. *Cancer Res.* **1994**, *54*, 4564–4568.

56. Förster, T. *Ann. Phys.* **1948**, *437*, 55–75.

57. Steinberg, I. Z. *Annu. Rev. Biochem.* **1971**, *40*, 83–114.

58. Chen, F. C.; Chen, S. J. *Opt. Lett.* **2006**, *31*, 187–189.

59. Battino, R.; Rettich, T. R.; Tominaga, T. *J. Phys. Chem. Ref. Data* **1983**, *12*, 163–178.

60. Dulbecco, R.; Vogt, M. *J. Exp. Med.* **1954**, *99*, 167–182.

61. Saltzman, H. A.; Brown, I. W. *Annu. Rev. Med.* **1965**, *16*, 253–262.

Acknowledgements

First and foremost, I need to thank Dan Nocera for allowing me to work in your group. You were the only faculty member at MIT that genuinely showed in interest in speaking to me in January of 2010, when I was a first year graduate student out of sync with the rest of my class. I appreciate all of the opportunities that you have given me in your lab. The Nocera group is a lab full of colleagues that bring a diverse knowledge base to the group and makes it a great place to work. Most importantly, thank you for all of your support and the freedom to execute my own ideas to move the research project forward.

Thanks to Emily McLaurin and Andrew Greytak for getting me started on the sensing project. I am grateful for all that you both taught me, even though we only overlapped for a short while. I am extremely indebted to Elizabeth Karnas for helping to guide me to a more fruitful series of experiments that has ultimately led to this thesis. Thank you for all of your help and guidance. I'm sorry that we didn't have the opportunity to work together longer.

I would like to thank all of the people that have helped me with experiments in the lab related to this thesis: Pat and Arturo for teaching me how to use the nanosecond; Bryce for taking time to teach me to use the femtosecond; Casandra, Andrew M., and Christina for assistance with the femtosecond; Andrew U. and Matt for help with crystallography; Xiaoxing and Vikash at MGH for helping with the two-photon microscope and lifetime measurements.

Thanks to my classmates in the Nocera lab: Andrew U., Lisa, Kwabena, and Christina. It was great taking classes with you guys and I really appreciate the support from you all. Thanks to my buddies in the DIC house: Ben, Michael, and Eric. You guys are awesome and I've loved every minute we've lived together. I appreciate all of the fun times, the emotional support, and the scientific discussions that make it like an episode of "The Big Bang Theory."

Finally, I would like to thank all of the members of the Nocera lab, past and present. It has been a pleasure to get to know you and work with you all. I've enjoyed all of the discussions, coffees, lunches, and even some of the drama because it makes life interesting. Since this is only a master's thesis, I'm writing an abbreviated set of acknowledgements; I'll write a more complete one for my PhD thesis. Thanks!

Curriculum Vitae

Christopher M. Lemon
77 Massachusetts Avenue 18-172, Cambridge, MA 02139

EDUCATION

PhD in Inorganic Chemistry: Expected May 2015
Harvard University, Cambridge, MA

MSc in Inorganic Chemistry: Expected February 2013
Massachusetts Institute of Technology, Cambridge, MA
GPA: 5.0/5.0
Thesis (Submitted January 2013)
Supramolecular Quantum Dot–Porphyrin Assemblies for Biological Oxygen Sensing

BSc(Hon) in Chemistry with First Class Honours: May 2010
The Univeristy of Auckland, Auckland, New Zealand
GPA: 9.0/9.0 (A+ average)
Thesis (Submitted November 2009):
The Synthesis and Characterisation of Metallocorroles: Period 6 Late Transition and Main Group Metals

B.S. Biochemistry (ACS Certified) and Physics with High Distinction: May 2008
Ohio Northern University, Ada, OH
GPA: 3.97/4.0
Senior Chemistry Seminar (Presented January 2007):
Boron Neutron Capture Therapy: Historical Foundations and Modern Perspectives
Senior Physics Capstone (Presented May 2008):
Surface Physics: LEED Study of a Stepped Cu(511) Surface

B.A. Mathematics/Statistics with High Distinction: May 2008
Ohio Northern University, Ada, OH
GPA: 3.97/4.0
Senior Capstone (Presented February 2008):
Markov Chains and the Heat Bath Monte Carlo Algorithm for the Ising Model of Ferromagnetism

Honors Program
Honors Project (Presented May 2008):
Markov Chains and the Heat Bath Monte Carlo Algorithm for the Ising Model of Ferromagnetism

RESEARCH EXPERIENCE

Spring 2010-Present	Inorganic Chemistry Prof. Daniel Nocera, Massachusetts Institute of Technology CdSe quantum dot based oxygen sensors • Synthesis of Pt and Pd porphyrins as oxygen-sensitive dyes • Laser studies to quantify oxygen dependence
Spring 2009-Winter 2009	Inorganic Chemistry Prof. Penelope Brothers, The University of Auckland Synthesis and characterization of period 6 metallocorroles • Devised several ways of inducing complex formation

	• Design and synthesis of picket-fence corroles
Fall 2007-Spring 2008	Statistics and Probability Prof. Ronald Johns, Ohio Northern University Markov chains and the Ising model of ferromagnetism • MatLab program to model spin interactions • Correctly predicts presence of ferromagnetic domains and Curie temperature
Fall 2007-Spring 2008	Physical Chemistry Prof. Jeffrey Gray, Ohio Northern University Fluorescence spectroscopy of molecular iodine • Design laser experiments to improve an undergraduate experiment • Statistical analysis of experimental data
Summer 2007	Inorganic Chemistry Prof. Richard Eisenberg, University of Rochester (REU Program) Synthesis and characterization of platinum complex for the generation of H_2 • Synthesis and purification of dithiolene and diimine ligands • Synthesis of platinum complexes and studied their ability to produce H_2
Summer 2006	Bioinorganic Chemistry Prof. Janet Morrow, SUNY at Buffalo (REU Program) Spectroscopic studies of europium(III) binding to DNA oligomers • DNA melting experiments (T_m determination of oligomers) • Laser fluorescence experiments and data analysis
Summer 2006	Biophysics Prof. Andrea Markelz, SUNY at Buffalo (REU Program) Terahertz spectroscopy of nucleotide monophosphates • THz Laser absorbance experiments and data analysis • Monitor avidin and biotin binding by THz spectroscopy
Winter 2005-Fall 2007	Inorganic Synthesis Prof. E. Alan Sadurski, Ohio Northern University Synthesis and characterization of aryl substituted silanes • Air and water sensitive reactions • ^1H & ^{13}C NMR and FTIR analysis
Winter 2005-Spring 2008	Solid State Physics Prof. Mellita Caragiu, Ohio Northern University Structural determination of atomic adsorption geometries on metal surfaces • Performing calculations to determine atom coordinates • Use of the TLEED software package for calculations
Winter 2004-Fall 2005	Pharmacy Prof. Jim Kuykendall, Ohio Northern University Interaction of DNA and the anti-cancer drug calicheamicin • DNA and drug sample preparation • Agarose gel electrophoresis

PUBLICATIONS

Lemon, C.M.; Dogutan, D.K.; Nocera, D. G. Porphyrin and Corrole Platforms for Water Oxidation, Oxygen Reduction, and Peroxide Dismutation. In *Handbook of Porphyrin Science*; Kadish, K.M.; Smith, K.M.; Guilard, R., Eds.; World Scientific Publishing: Singapore, 2012; Vol 21; pp 1-143.

Lemon, C.M.; Brothers, P.J. "The synthesis, reactivity, and peripheral functionalization of corroles." *J. Porphyrins Phthalocyanines* **2011**, *15*, 809-834.

Lemon, C.M.; Brothers, P.J.; Boitrel, B. "Porphyrin complexes of the period 6 main group and late transition metals." *Dalton Trans.* **2011**, *40*, 6591-6609.

PRESENTATIONS

Lemon, C.M.; Dogutan, D.K.; Nocera, D.G. "The Rational Synthesis of Water Soluble A_3B Pyridyl Porphyrins." Oral Presentation, Tetrapyrrole Discussion Group, University of Glamorgan, Cardiff, Wales, UK, April 13-14, 2011.

Lemon, C.M., Johns, R. "Simulation of Ferromagnetic Properties of the Two-Dimensional Ising Model." Oral Presentation, Ohio Section of the American Physical Society Fall Meeting, Wright State University, Dayton OH, October 10-11, 2008.

Lemon, C.M., Johns, R. "The Heat Bath Monte Carlo Algorithm for the Ising Model of Ferromagnetism." Poster Presentation, Ohio Section of the American Physical Society Fall Meeting, Wright State University, Dayton OH, October 10-11, 2008.

Du, P., Lemon, C.M., Schneider, J., Jarosz, P.R., Lazaidis, T., Brennessel, W., Eisenberg, R. "Studies Involving Heavy Metal Dithiolene complexes: Revisiting Old Observations and Presenting New Ones." Poster Presentation, 236 ACS Meeting, Philadelphia, PA, August 17-21, 2008.

Lemon, C.M. "Markov Chains and the Heat Bath Monte Carlo Algorithm for the Ising Model of Ferromagnetism." Oral Presentation, Ohio Section of the Mathematical Association of America Spring Meeting, Marietta College, Marietta OH, April 11-12, 2008.

Lemon, C.M., Canagatarana, S., Gray, J. "Rotationally Resolved Fluorescence Spectroscopy of Molecular Iodine: Using Inexpensive DPSS Lasers to Enhance a Familiar P-chem Lab Experiment." Poster Presentation, 235 ACS Meeting, New Orleans LA, April 6-10, 2008.

Lemon, C.M., Canagatarana, S., Gray, J. "Rotationally Resolved Fluorescence Spectroscopy of Molecular Iodine: Using Inexpensive DPSS Lasers to Enhance a Familiar P-chem Lab Experiment." Poster Presentation, Ohio Section of the American Physical Society Spring Meeting, Youngstown State University, Youngstown OH, March 28-29, 2008.

Lemon, C.M., Caragiu, M., Diehl, R.D., Hanna, K.J., Li, H.I., Wan, R. "Low-Energy Electron Diffraction Investigation of the Clearn, Stepped Cu(511) Surface." Oral Presentation, Ohio Section of the American Physical Society Spring Meeting, Youngstown State University, Youngstown OH, March 28-29, 2008.

Lemon, C.M., Du, P., Eisenberg, R. "Applications of Inorganic Platinum Complexes for the Production of H_2 as an Energy Source." Poster Presentation, Ohio Section of the American Physical Society Fall Meeting, Miami University, Oxford OH, October 19-20, 2007.

Lemon, C.M., Caragiu, M., Diehl, R., Hanna, K., Li, H., Wan, R. "Low-Energy Electron Diffraction Investigation of the Cu(511) Stepped Surface." Poster Presentation, Ohio Section of the American Physical Society Spring Meeting, Eastern Michigan University, Ypsilanti MI, May 4-5, 2007.

Lemon, C.M., Mathews, R.A., Morrow, J.R., Switala, B. "Spectroscopic Investigation of Metal Ion Binding to DNA Hairpin Loops." Poster Presentation, 233 National ACS Meeting, Chicago IL, March 25-29, 2007.

Lemon, C.M., Knab, J., He, Y., Markelz, A.G., Morrow, J.R. "Application of Terahertz Spectroscopy to the Analysis of DNA." Poster Presentation, Ohio Section of the American Physical Society Fall Meeting, University of Akron, Wayne College, Orrville OH, October 13-14, 2006.

Lemon, C.M., Pan, F.M., Caragiu, M., Ferralis, N., Diehl, R.D. "Substitutional Adsorption Geometry for Pb(111)-($\sqrt{3}$ x $\sqrt{3}$)R30°-K." Poster Presentation, Ohio Section of the American Physical Society Spring Meeting, Wayne State University, Detroit MI, March 31- April 1, 2006.

TEACHING EXPERIENCE

2010-2011	Teaching Assistant, Department of Chemistry, MIT, Cambridge, MA Conducted recitation sessions, held office hours, graded homework and exams Prepared lecture notes and clicker questions, presented clicker questions during lecture • 5.111 (Introductory Chemistry), Head TA
2006-2008	Tutor, College of Arts and Sciences, Ohio Northern University, Ada, OH Conducted tutoring sessions, reviewed key concepts, assisted with homework problems • All chemistry department courses • Mathematics and statistics courses
2006-2007	Teaching Assistant, Department of Physics, Ohio Northern University, Ada, OH Coordinated laboratory materials, conducted lab sessions, graded lab reports • Electricity and Magnetism • Heat Light and Sound
2004-2008	Teaching Assistant, Department of Chemistry, Ohio Northern University, Ada, OH Coordinated laboratory materials, conducted lab sessions, graded lab reports • Introductory Chemistry 1, 2, and 3 • Organic Chemistry 1, 2, and 3 • Physical Chemistry 2

AWARDS & HONORS

- Fulbright Scholarship (New Zealand) 2008-2009
  Project: The Synthesis and Anti-cancer Analysis of Metal-based Compounds
- Barry M. Goldwater Scholarship, 2006-07 School Year
- MIT Teaching Award, 2011
- Grace Phillips Memorial Bursary (University of Auckland), 2010
- Biochemistry Departmental Honors, 2008
- Physics Departmental Honors, 2008
- Honors Council, Vice President 2007, President 2008
- NSF REU Travel Award, 2007
- Chemistry Alumni Scholarship, 2005-06 School Year

- Linda Schultz Scheuerman Award, 2006-07 & 2007-08 School Year
- Sophomore (2005), Junior (2006), and Senior (2007) Chemistry Class Honors
- College of Pharmacy Centennial Award, 2005
- ONU Presidential Merit Scholarship, 2003-08
- Phi Lambda Upsilon Chemical Honorary Society Award
- Mortar Board Aurora Award

PROFESSIONAL AFFILIATIONS & ACTIVITIES

- MIT Chemistry Department EH&S Committee, 2011-2012
- MIT Chemistry Student Seminar Series, Co-organizer, 2011-2012
- American Chemical Society 2005-Present
- ONU Student Affiliate Chapter of ACS 2004-2008, Secretary 2007-08
- American Physical Society 2006-Present
- Ohio Section of the American Physical Society 2006-Present, Executive Board Student Member at Large Elected 2007
- Society of Physics Students 2005-Present, Secretary 2007-08
- American Statistical Association 2007-Present
- Mathematical Association of America 2007-Present
- Phi Kappa Phi 2007-2008, Vice President 2007-08 (Senior Honors Society), Chapter delegate for the triennial convention in Orlando, FL (August 2007)
- Sigma Pi Sigma 2006-2008, President 2006-08 (Physics Honorary)
- Phi Lambda Sigma 2006-2008 (Pharmacy Leadership Honorary)
- Mortar Board 2006-2008, Vice President of Membership 2007-08 (Senior Honors Society)
- Kappa Mu Epsilon 2005-2008, Treasurer 2007-08 (Mathematics Honorary)
- Sigma Xi (Research Honorary) 2008